Coarse Grid Approaches for the Shallow Water Model

vorgelegt von
Dipl.-Ing.
Ilhan Özgen
geb. in Berlin

von der Fakultät VI – Planen Bauen Umwelt
der Technischen Universität Berlin
zur Erlangung des akademischen Grades

Doktor der Ingenieurwissenschaften
– Dr.-Ing. –

genehmigte Dissertation

Promotionsausschuss:

Vorsitzender:	Prof. Dr.-Ing. Matthias Barjenbruch
Gutachter:	Prof. Dr.-Ing. Reinhard Hinkelmann
Gutachter:	Prof. Dr. Philippe Gourbesville
Gutachter:	apl. Prof. Dr.-Ing. Frank Molkenthin
Gutachter:	Dr. Dongfang Liang

Tag der wissenschaftlichen Aussprache: 17. Juli 2017

Berlin 2017

Preface

This thesis summarises my efforts as a PhD student at Technische Universität Berlin during the years from 2014 to 2017.

Gratitude is expressed to my supervisors, Reinhard Phillip Hinkelmann and Dongfang Liang, for guidance and supervision, to Frank Molkenthin for his helpful suggestions and to Philippe Gourbesville for his insightful comments and support.

Gratitude is expressed to my parents, my brother, my aunts, my uncles and my cousins for their support.

Much love to my girlfriend, Anna Hong Xian, for everything.

Berlin
September 13, 2017

Publications of cumulative doctoral thesis

Journal papers

1. Özgen, I., Zhao, J., Kim, B., Liang, D., and Hinkelmann, R. (nd) A robust well-balanced anisotropic porosity shallow water model with a novel drag force discretization. *International Journal for Numerical Methods in Fluids* (submitted) [preprint version]
2. Özgen, I., Zhao, J., Liang, D., and Hinkelmann, R. (2016) Urban flood modeling using shallow water equations with depth-dependent anisotropic porosity. *Journal of Hydrology* 541, pp. 1165–1184 [postprint version].
   doi: 10.1016/j.hydrol.2016.08.025
3. Özgen, I., Liang, D., and Hinkelmann, R. (2016) Shallow water equations with depth-dependent anisotropic porosity for subgrid-scale topography. *Applied Mathematical Modelling* 40, pp. 7447–7473 [postprint version].
   doi: 10.1016/j.apm.2015.12.012
4. Özgen, I., Teuber, K., Simons, F., Liang, D., and Hinkelmann, R. (2015) Upscaling the shallow water model with a novel roughness formulation. *Environmental Earth Sciences* 74, pp. 7371–7386 [postprint version].
   doi: 10.1007/s12665-015-4726-7

Supplementary contributions

Journal papers

1. Jahanbazi, M., Özgen, I., Aleixo, R., and Hinkelmann, R. (2017) Development of a diffusive wave shallow water model with a novel stability condition and other new features. *Journal of Hydroinformatics*, 19, pp. 405–425 [postprint version]. doi: 10.2166/hydro.2017.108
2. Fišer, M., Özgen, I., Hinkelmann, R. and Vimmr, J. (2016) A mass conservative well-balanced reconstruction at wet/dry interfaces for the Godunov-type shallow water model. *International Journal for Numerical Methods in Fluids* 82, 893–908 [postprint version]. doi: 10.1002/fld.4246
3. Liang, D., Özgen, I., Hinkelmann, R., Xiao, Y., and Chen, J.M. (2015) Shallow water simulation of overland flows in idealised catchments. *Environmental Earth Sciences* 74, pp. 7307–7318 [postprint version]. doi: 10.1007/s12665-015-4744-5

Conference papers

1. Özgen, I. (2017) A coarse grid approach-based model chain for fast rainfall-runoff predictions in natural and urban areas. In: Proceedings of the 37th IAHR World Congress 2017, Kuala Lumpur, Malaysia [postprint version].
2. Özgen, I., Liang, D., Om, J., and Hinkelmann, R. (2016) Shallow water model with anisotropic porosity: A case study of dambreak flow in city environment. In: Proceedings of 12th International Conference on Hydroinformatics 2016, Incheon, South Korea.
3. Özgen, I., Teuber, K., Liang, D., and Hinkelmann, R. (2015) Surface roughness parameterization to account for subgrid scale topography in shallow water flow modeling. In: Proceedings of the 36th IAHR World Congress 2015, The Hague, the Netherlands.
4. Özgen, I., Liang, D., and Hinkelmann, R. (2015) Anisotropic porosity shallow water equations for inundated areas. In: Workshop on Advances in Numerical Modelling of Hydrodynamics, Sheffield, UK.

Conference posters

1. Özgen, I., Serrano-Taslim, M., Zhao, J., Liang, D., and Hinkelmann, R. (2016) Coarse grid shallow water simulations of rainfall runoff in small catchments with modified friction law to account for unresolved microtopography. In: European Geophysical Union General Assembly 2016, Vienna, Austria.

Conference presentations

1. Özgen, I., Zhao, J., Liang, D., and Hinkelmann, R. (2016) Comparison of an isotropic porosity shallow water model with an anisotropic porosity shallow water model. Nordic Water Network – Conference 2016, Berlin, Germany.
2. Özgen, I., Zhao, J., Liang, D., and Hinkelmann, R. (2016) Towards an anisotropic porosity shallow water model for computationally efficient rainfall-runoff simulation. AG Hydrologische Modellierung, Berlin, Germany.

Abstract

Developments in survey technology such as light detection ranging and laser-scanning are able to provide high-resolution topography data sets. In shallow water equations based modeling, the use of high-resolution topography data is generally desirable, because it is considered to be a more accurate representation of the "real world". Indeed, high-resolution discretization of topography leads to more accurate representation of preferential flow paths and obstructions which influence the global flow behaviour inside the domain.

However, the integration of these data into the numerical model is often challenging because of finite computer resources. The challenge comes from the scale difference between the computational domain and the topographical features. If each topographical feature was discretized explicitly, the cell number of the resulting mesh and consequently the simulation wall-time would be unfeasibly high. Instead of explicitly discretizing the small-scale topography, its influence can be conceptually accounted for on coarser meshes to reduce the computational cost. These approaches are commonly referred to as "coarse grid approaches" or "scaling approaches".

Aim of this doctoral thesis is the development of coarse grid approaches for the shallow water model. Hereby, two approaches will be investigated: (1) friction-law based coarse grid approach, (2) porosity-based coarse grid approach. The approaches allow simulations on a coarser resolution while still maintaining an acceptable accuracy. The development of such approaches is of interest in engineering applications, such as the fast prediction of flood inundation areas in case of a fast flood wave or the relatively new field of physical modeling based catchment hydrology.

The friction-law based coarse grid approach uses an artificially increased roughness coefficient, two additional calibration parameters that describe the geometry of the topographical features and the so-called "inundation ratio", which is the ratio between water depth and roughness height. Using automated calibration, good agreement between the scaled shallow water model and high-resolution reference solutions and measurement data was achieved.

Further, in this thesis a porosity-based coarse grid approach was developed, which enables full inundation of unresolved features by means of water depth-dependent porosity terms. A Godunov-type method for the solution of the equations was developed, whereby the reconstruction of cell values at the cell interfaces was identified as a source of spurious oscillation. A monotonicity treatment was suggested to address this issue.

The friction-law based as well as the porosity-based coarse grid approach yield results with comparable accuracy to high-resolution classical shallow water models for water depths and flood areas. However, flow velocities can not be reproduced with the same accuracy. Further, processes at subgrid-scale can not be reproduced.

The benefit of the developed approaches was demonstrated in this work. In the investigated cases, utilizing coarse grid approaches reduced the wall-time of the simulation 2 up to 3 orders of magnitude.

Zusammenfassung

Aktuelle Entwicklungen in der Fernerkundung wie LIDAR (light detection and ranging) und Laserscanning sind in der Lage, hochaufgelöste topographische Datensätze zu erzeugen. Für die Modellierung von Fließprozessen anhand der Flachwassergleichung ist es von Vorteil, Gebrauch von diesen Datensätzen zu machen. Das hochaufgelöste Diskretisieren der Topographie ermöglicht eine bessere Abbildung der Fließwege und Hindernisse, welche Einfluss auf das gesamte Fließverhalten im Gebiet haben.

Aufgrund begrenzter Computerkapazitäten ist die Einbindung hochaufgelöster Datensätze in einem numerischen Modell oft eine große Herausforderung, da die Bandbreite der in einem Untersuchungsgebiet zu berücksichtigenden Skalen topographischer Strukturen in der Regel sehr groß ist. Eine explizite Diskretisierung dieser Strukturen führt zu Netzen mit extrem hoher Zellanzahl und nicht vertretbaren Rechenzeiten. Anstatt die kleinskaligen topographische Strukturen explizit zu diskretisieren, kann deren Einfluss konzeptionell in das Modell integriert werden. Dies hat den Vorteil, dass Simulationen auf gröberen Netzen durchgeführt werden können, was zu einer erheblich verminderten Rechenzeit führt. Ansätze dieser Art werden als Grobgitterverfahren oder Skalierungsansätze bezeichnet.

Im Rahmen dieser Arbeit werden zwei neue Grobgitteransätze für die Flachwassergleichungen entwickelt: (1) ein auf einem Reibungsgesetz basierender Ansatz und (2) ein auf der Porosität basierender Ansatz. Die entwickelnden Ansätze ermöglichen Simulationen auf gröberen Gittern mit vertretbaren Genauigkeiten. Die Entwicklung solcher Ansätze ist zum Beispiel für Ingenieuranwendungen im Bereich der Hochwasservorhersage sowie im relativ neuen Bereich der physikalisch basierten Niederschlag-Abfluss-Simulation höchst interessant.

Der hier entwickelte, auf einem Reibungsgesetz basierende Ansatz benutzt einen erhöhten Reibungskoeffizienten, zwei weitere Kalibrierungsparameter, welche die geometrischen Eigenschaften der topographischen Struktur beschreiben, sowie den sogenannten "Überflutungsanteil", der das Verhältnis zwischen Wassertiefe und charakteristischer Rauheitshöhe angibt. Mit Hilfe einer automatisierten Kalibrierung wurde eine gute Übereinstimmung zwischen dem Grobgitter-Flachwassermodell und hochaufgelösten Referenzlösungen und Messdaten erzielt.

In dieser Arbeit wurde auch ein Porositäts-basierter Grobgitteransatz entwickelt, welcher eine Überflutung der unaufgelösten Strukturen ermöglicht, indem die Porositäten in Abhängigkeit der Was-

sertiefe in jedem Zeitschritt neu berechnet werden. Ein Godunov-Verfahren zur Lösung der Gleichungen wurde entwickelt, wobei die Rekonstruktion der Zellvariablen an den Kanten als eine mögliche Quelle von Oszillationen identifiziert wurde. Daher wurde auch ein Ansatz zur Erhaltung der Monotonie des Verfahrens entwickelt.

Sowohl der Reibungsgesetz-basierte als auch der Porositäts-basierte Ansatz liefern vergleichbare Genauigkeiten mit hochaufgelösten Rechnungen für die Wasserstände und Überflutungsflächen im Gebiet. Fließgeschwindigkeiten können jedoch nicht mit der gleichen Genauigkeit berechnet werden. Des Weiteren werden Prozesse unterhalb der Netzauflösung nicht abgebildet.

Die Vorteile der entwickelten Verfahren konnten im Rahmen dieser Arbeit deutlich herausgestellt werden. In den untersuchten Fällen wurde die Rechenzeit durch Grobgitterverfahren um 2 bis 3 Größenordnungen vermindert.

Contents

List of Figures

Chapter 1

Introduction

> "... surface water and subsurface are *multiscale* systems. In surface water systems, the space scales range from one hundred kilometers and more via meters to micrometers, while the time scales range from more than days via minutes to milliseconds, depending on whether *currents*, *waves* or *turbulences* are of major interest."
>
> – Hinkelmann (2005) [56]

1.1 Motivation

On the global scale, 54% of the world's population is living in urban areas and by 2050, the value is projected to be 66% [145, 146]. At the same time, the globally averaged combined land and ocean surface temparature data show a warming of 0.85 °C, mostly caused by human influence [68]. A major impact of the global warming is an increase in the number of heavy precipitation events in a number of regions, whereby the number of these extreme weather events is very likely to further increase in many regions in the future (projection for 2081-2100) [68].

Climate change and rapid urbanization has increased the number of urban flood events in the past two decades [147], leading to an estimated number of 539811 casualties and 361974 injuries (most likely underestimated) worldwide [30]. A definition of floods is given by the European

Union Floods Directive [34] as "the temporary covering by water of land not normally covered by water". In urban environment, several reasons may lead to flooding, i.e. high tides and tsunamies in coastal areas, dambreaks, backwater caused by ice, heavy rainfall (pluvial urban flooding) in combination with overflow of the sewer system or flooding of rivers and flow over breaking dikes (fluvial urban flooding). The focus of this work is on the latter two, i.e. pluvial and fluvial urban flooding.

Pluvial urban flooding is a consequence of urbanization as buildings, roads, infrastructure and paved areas prevent rainfall from infiltrating into the soil and lead to an increase in surface runoff. Usually, surface runoff in urban environment is collected in a drainage system which aims to discharge the stormwater as quickly as possible, however the drainage system might be overwhelmed by extreme rainfall events [147]. A recent example of pluvial flooding is the flooding of Gleim tunnel on July 27, 2016, in Berlin, Germany, where heavy rainfall caused the drainage system to fail, resulting in significant damage in property and the closing of the tunnel until January 13, 2017. In the same time period, on July 30, 2016, heavy rainfall after a preceding heat wave caused an overflow of the sewer system and flooded several basements in the district Wilmersdorf, Berlin, Germany. Worldwide, many other examples with much more devastating consequences can be found. In contrast to the other reasons of floods, which only pose a threat to cities at certain locations, all urban areas are at risk of pluvial urban flooding [147]. The European Union Floods Directive [34] does not directly address pluvial flooding, e.g. standard reoccurence periods for precipitation events to be used in the design of urban flood protection structures is not defined in the directive.

Fluvial urban flood events are divided in flooding of bigger rivers and local flash flood events. Flood events at bigger rivers usually cause extensive damage in property but due to the long reaction time (time between forecasting and arrival of the flood wave) result in less casualties compared to flash floods. An example for a large river flood event is the Elbe river flood of 2002, which resulted in 21 casualties, and a total damage of 11 billion Euro. Heavy rainfalls in the catchment of the Elbe river with durations of several hours caused a high groundwater table and excess runoff which concentrated in the river. Meanwhile, the sewer system in Dresden, Germany, failed due to heavy rainfall. The flood wave propagating in the Elbe river caused flooding of smaller rivers connected to the Elbe river and flooded the city Dresden, Germany. The forecast of this event happened on August 9, 2002. Dresden was flooded two days later, on August 11, 2002. Flash flood events are usually caused by short, localized heavy rainfall events and are characterized by a short reaction time (usually below 6 hours) and high

flow velocities [9]. An example for this type of fluvial flood is the Braunsbach flash flood of May 29, 2016 in Baden-Württemberg, Germany. Heavy rainfall saturated the soil in the catchment of Braunsbach, produced excess runoff and due to the high flow velocities resulted in erosion and bedload transport in the river (Orlacher Bach) as well as in the natural areas in the catchment. The flood wave, consisting of a mixture of water and rocks, arrived in Braunsbach with a high flow velocity and water depths up to 3 m, causing high damage in the city [8]. The duration of the whole flood event was about 2 hours [8]. Another example is the Panke flood of August 22, 2012, where after a heavy rainfall, tree branches and grass (that had been mowned in a nearby park) blocked a screen inside the heavily modified Panke river, Berlin, resulting in the river bursting its banks. Several basements of houses near to the blocked area were flooded and cars were damaged. As before, more devastating examples of fluvial flooding can be found worldwide.

Numerical models are an important tool for flood protection measures, which the European Floods Directive [34] defines as comprising three pillars: precautionary measures, technical flood protection and water retention in the catchment. As precautionary measures, numerical models can be applied for fast predictions, forecasting and nowcasting of flood events for early warning systems. Numerical models can further be used to assess the effect of technical flood protection measures as well as measures for water retention in the catchment, e.g. the effect of restoration of streams and rivers [82], serving as an additional tool in decision making processes. In recent years, the shallow water model has been widely used for these purposes.

1.2 The shallow water model

The flow of Newtonian fluids can be described by combining the continuity equation and the Navier-Stokes equations, which express balance laws for mass and momentum in three dimensions, respectively.

For applications that are dominated by horizontal processes (i.e. long waves), the two-dimensional shallow water equations can be derived as a special case of the continuity and Navier-Stokes equations for incompressible flow with a free surface over generally slow bottom inclinations. If the flow is dominated by long waves, i.e. the ratio of water depth to wave length is smaller than 1/20, the vertical pressure function can safely be approximated with a hydrostatic pressure distribution. Then, neglecting vertical acceleration, vertical velocities and vertical viscous forces and assuming a

logarithmic vertical flow velocity profile, the continuity and Navier-Stokes equations can be integrated over the water depth, resulting in the depth-averaged two dimensional shallow water equations that can be written in conservative form as

$$\frac{\partial h}{\partial t} + \frac{\partial q_x}{\partial x} + \frac{\partial q_y}{\partial y} = s_h, \tag{1.1}$$

$$\frac{\partial q_x}{\partial t} + \frac{\partial}{\partial x}\left(\frac{q_x^2}{h} + \frac{\partial}{\partial x}\nu\frac{q_x^2}{h}\right) + \frac{\partial}{\partial y}\left(\frac{q_x q_y}{h} + \frac{\partial}{\partial y}\nu\frac{q_x^2}{h}\right) = s_{q,x}, \tag{1.2}$$

$$\frac{\partial q_y}{\partial t} + \frac{\partial}{\partial x}\left(\frac{q_x q_y}{h} + \frac{\partial}{\partial x}\nu\frac{q_y^2}{h}\right) + \frac{\partial}{\partial y}\left(\frac{q_y^2}{h} + \frac{\partial}{\partial y}\nu\frac{q_y^2}{h}\right) = s_{q,y}, \tag{1.3}$$

where Eq. 1.1 is the mass balance and Eq. 1.2 and Eq. 1.3 are the momentum balance in x- and y-direction of the Cartesian coordinate system, respectively. Further, t denotes the time axis. The conserved variables of the shallow water equations are the water depth h and the unit discharges in x- and y-direction, q_x and q_y, respectively. ν is the sum of the molecular and turbulent viscosity of water. For most shallow water flow applications, the turbulent viscosity is orders of magnitude larger than the molecular one. s_h is the mass source term and $s_{q,x}$ and $s_{q,y}$ are the momentum source terms in x- and y-direction, respectively. The mass source term accounts for sources and sinks in the mass balance. For example, it may be written as

$$s_h = r - i, \tag{1.4}$$

where r is the rainfall intensity and i is the infiltration rate of water into the subsurface. The momentum source terms $s_{q,x}$ and $s_{q,y}$ contain terms that result from the depth-integration and external momentum sources. Most commonly, they are written as

$$s_{q,x} = -g\frac{\partial}{\partial x}(h+z) - \frac{g}{C^2}h^{-2}q_x||\mathbf{q}|| + f_x, \tag{1.5}$$

$$s_{q,y} = -g\frac{\partial}{\partial y}(h+z) - \frac{g}{C^2}h^{-2}\rho q_y||\mathbf{q}|| + f_y, \tag{1.6}$$

with g being the gravity, z being the bottom elevation, C being the Chézy-friction coefficient, ρ being the fluid density and $||\mathbf{q}||$ being the Euclidian norm of the unit discharge vector $\mathbf{q} = [q_x, q_y]^T$. The first term of $s_{q,x}$ is the bottom slope source term that describes the gravity effect on the water and the second term is the friction source term that describes momentum losses due to the effect of roughness. f_x is the external source term. The definitions apply analogously to the terms of $s_{q,y}$. Depending on the scale

and the nature of the investigated problem, the external source term may contain wind shear stress, air-pressure gradient and Coriolis force [56].

The shallow water equations in this present form (Eqs. 1.1–1.3) are a mixed-type hyperbolic-parabolic system of partial differential equations. The first term of the space derivative at the left hand-side in Eq. 1.2, i.e. q_x^2/h, is the convection term and is the hyperbolic part of the equation. The second term of the space derivative, i.e. $\partial(\nu q_x^2/h)/\partial x$, is the diffusion term and is the parabolic part of the equation. The same definition applies in y-direction for Eq. 1.3. Depending on whether the convection terms or the diffusion terms are dominant, the equations behave hyperbolic or parabolic. The important implication of this classification is that for parabolic problems, the solution at one point in the domain depends on all other points while for hyperbolic problems the solution at one point in the domain depends on a limited number of points in the domain [96].

Other formulations of the shallow water equations exist. For example, velocities are sometimes used instead of unit discharges, or the free water elevation is used instead of the water depth. A special form of the shallow water equations usually found in ocean or atmosphere modeling is obtained by using vorticities as primary variables.

Following a common simplification found in literature, e.g. [86, 142, 47], the diffusive terms, i.e. the terms associated with molecular or turbulent viscosity, and external forces f_x and f_y are neglected in this work. This yields a hyperbolic system of equations that can be written in conservative vector form as

$$\frac{\partial \mathbf{q}}{\partial t} + \frac{\partial}{\partial x}\mathbf{f}(\mathbf{q}) + \frac{\partial}{\partial y}\mathbf{g}(\mathbf{q}) = \mathbf{s}, \tag{1.7}$$

$$\mathbf{q} = \begin{bmatrix} h \\ q_x \\ q_y \end{bmatrix}, \ \mathbf{f}(\mathbf{q}) = \begin{bmatrix} q_x \\ q_x^2/h + gh^2/2 \\ q_x q_y/h \end{bmatrix},$$

$$\mathbf{g}(\mathbf{q}) = \begin{bmatrix} q_y \\ q_x q_y/h \\ q_y^2/h + gh^2/2 \end{bmatrix}, \ \mathbf{s} = \begin{bmatrix} s_h \\ -gh\partial z/\partial x + s_{f,x} \\ -gh\partial z/\partial y + s_{f,y} \end{bmatrix}, \tag{1.8}$$

which is the preferred way to express the equations in this work and will be referred to as the classical shallow water equations. With $s_{f,x}$ and $s_{f,y}$ being the friction source terms, in x- and y-direction, respectively, it is easy to verify that the rows of the vectors in Eq. 1.8 evaluated in Eq. 1.7 correspond to Eqs. 1.1, 1.2 and 1.3, respectively, if the aforementioned simplifications are made and simple algebraic manipulation is carried out.

In hyperbolic problems, the solution travels in wave form through the domain. The wave speed at which the information travels can be determined

with an eigenvalue analysis which is usually conducted for the homogeneous system, i.e. by neglecting the source term $\mathbf{s}$. The Jacobian matrices in x- and y-direction of system 1.7, i.e. matrices $\mathbf{J}_x$ and $\mathbf{J}_y$ that allow rewriting system 1.7 as

$$\frac{\partial \mathbf{q}}{\partial t} + \mathbf{J}_x \frac{\partial \mathbf{q}}{\partial x} + \mathbf{J}_y \frac{\partial \mathbf{q}}{\partial y} = \mathbf{s}, \tag{1.9}$$

can be written as

$$\begin{aligned} \mathbf{J}_x &= \begin{bmatrix} 0 & 1 & 0 \\ c^2 - q_x^2/h^2 & 2q_x/h & 0 \\ -q_x q_y/h^2 & q_y/h & q_x/h \end{bmatrix}, \\ \mathbf{J}_y &= \begin{bmatrix} 0 & 0 & 1 \\ -q_x q_y/h^2 & q_y/h & q_x/h \\ c^2 - q_y^2/h^2 & 0 & 2q_y/h \end{bmatrix}, \end{aligned} \tag{1.10}$$

where c is the celerity $c = \sqrt{gh}$. Due to hyperbolicity, the eigenvalues of $\mathbf{J}_x$ are distinct and real, and can be calculated as

$$\lambda_x^{(1)} = \frac{q_x}{h} - c,\ \lambda_x^{(2)} = \frac{q_x}{h},\ \lambda_x^{(3)} = \frac{q_x}{h} + c, \tag{1.11}$$

and the same applies to $\mathbf{J}_y$, where the eigenvalues are

$$\lambda_y^{(1)} = \frac{q_y}{h} - c,\ \lambda_y^{(2)} = \frac{q_y}{h},\ \lambda_y^{(3)} = \frac{q_y}{h} + c. \tag{1.12}$$

This means, that for the shallow water equations, for each direction, the solution can be decomposed in three invariants that travel as waves with the speed of $\lambda^{(1)}$, $\lambda^{(2)}$ and $\lambda^{(3)}$ through the domain. At any time and at any point, the solution in terms of conserved variables can be reconstructed by linear superposition of these three waves.

Some problems are faced during the numerical solution of hyperbolic systems. A major problem is the computation of discontinuous solutions, which requires sophisticated methods. In addition, first order accurate methods lead to smeared results in regions near discontinuities, yet higher order accurate methods tend to produce spurious oscillations in the results. These challenges are related to the occurance of shock waves in the solution, which is a wave-type that propagates a discontinuity. In literature, e.g. [85], two ways have been proposed to approach the problem: (1) shock tracking and (2) shock capturing. Shock tracking methods aim to track the location of discontinuities and apply special treatment at these locations. This approach becomes very complicated and is not very present in literature. On the other hand, shock capturing methods aim to produce sharp approximations of discontinuities automatically, without additional treatment and

location tracking. Currently, shock capturing methods are considered state of the art.

Given the numerical challenges, the preferred method in current literature for spatial discretization of the shallow water equations is the finite-volume method [14], which has the advantages of being locally conservative and allowing discontinuous solutions. Here, the Godunov-type finite-volume method [44] is favored because of its shock capturing property. The essence of Godunov-type methods is to solve the Riemann problem [124] across cell edges. Because the solution of the Riemann problem depends on the eigenvalues of the equation, Godunov-type methods naturally include the physics of the problem in the flux calculation. In recent years, the Discontinuous Galerkin method, which can be considered a mixture of the finite-element and the finite-volume method, has reemerged in literature, cf. [75] and cited references within. The advantage of the Discontinuous Galerkin method is that the order of accuracy can be increased arbitrarily by increasing the order of the shape functions. In contrast to the conventional finite-element method, these shape functions are defined locally at each cell and are discontinuous at the edges. Across cell edges, the Riemann problem is solved.

Other numerical challenges that are specific to the shallow water model are wetting and drying of cells, the occurence of transcritical flow conditions and very small water depths, preservation of a quiescent state and maintaining a steady state in the presence of source terms and the time integration of source terms. In recent years, significant development on these issues has been made, cf. e.g. [59, 61, 60] and cited references within.

1.3 Integration of the work into research field

The Godunov-type shallow water model with explicit time integration has been applied to a wide range of hydraulic and environmental flows that range from river hydraulics [82, 111], flood modeling caused by dam- or dike-break [165, 156, 153], urban flood modeling [98, 91, 127, 126, 16, 119] and rainfall-runoff processes in natural catchments [128, 114, 14], among many others, cf. [63] and cited references within. The focus of this work is rainfall-runoff and flood modeling with an emphasis on urban systems.

The graph in Fig. 1.1 lists some application fields of shallow water models, namely the classical application field of river hydraulics, flood modeling and the new application field of rainfall-runoff modeling. River hydraulics and other applications are not emphasized in this work and thus are ex-

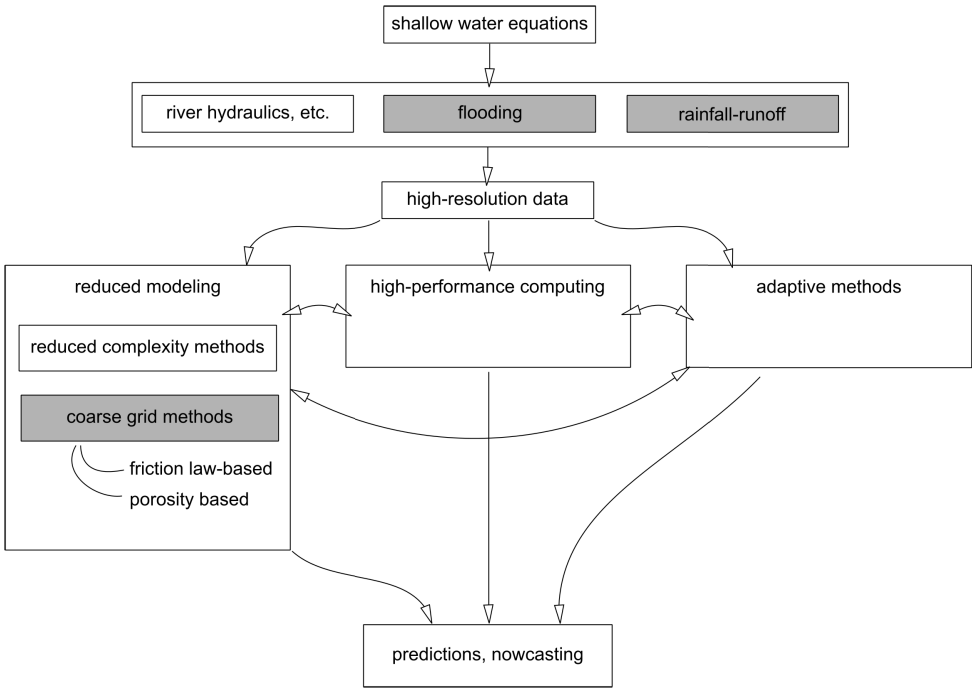

Figure 1.1: Motivation for coarse grid methods

cluded from the discussion. Flood modeling and rainfall-runoff modeling end in engineering applications, e.g. predictions and nowcasting of flood events for early warning systems. Hydraulic and environmental systems are multiscale systems, which means that relevant processes have different spatial scales [56]. The existence of small natural and man-made features may significantly influence the flow field [14]. For example in natural catchments that span up to several hundred kilometers, local depressions with horizontal scales smaller than a meter may act as surface storage and significantly reduce the hydrograph at the outlet of the catchment. Similarly, in urban catchments the scale of buildings is exceeded by the scale of the city by several orders of magnitude. Current developments in survey technology such as airborne and terrestrial LIDAR enable the collection of high-resolution topography data sets with a resolution of centimeters down to millimeters. Because of the aforementioned effect of small scale features, the incorporation of these data sets into shallow water models is desirable. This is indicated in Fig. 1.1, where the path from the flood or rainfall-runoff simulation passes through the high-resolution data set. However, due to finite computer resources, running simulations at the resolution of these data sets is currently hardly feasible, except of simulations running on supercomput-

ers [129]. The challenging question then becomes, whether and how the whole bandwidth of scales ranging from millimeters to kilometers can be properly taken into account.

One of the possible paths in Fig. 1.1 that connects the high-resolution data set with engineering applications is high-performance scientific computing, which is mainly based on parallelization of algorithms. Here, different parallelization strategies exist. Most parallel programs follow the single program multiple data strategy, which executes the same program with different data on each processor. Here, two different programming models are distinguished; the data parallel model and the message-passing model. In the data parallel model the exchange of data is steered by the compiler. This model is suitable for shared-memory machines, i.e. data is stored globally and can be accessed by every processor at the same time. The message-passing model is developed for distributed-memory machines, i.e. data is stored locally and local data can only be accessed by the processor it is stored on. Processors exchange data by means of communication routines. Generally speaking, the message-passing model scales over a much larger number of processors than the data parallel model. A more in-depth discussion of parallelization techniques is found in [56]. Recently, high performance computing has been carried out on graphical processor units (GPUs), e.g. [129, 80, 81]. Finally, it has to be mentioned that the speedup, i.e. the reduction of computational time, of the simulation due to parallelization, is limited by Amdahl's law.

Another path in Fig. 1.1 is using adaptive methods. The most common adaptivity in shallow water models is the h-adaptivity, which adjusts the mesh resolution depending on the solution. The adjustment is usually steered by an error-estimator [56], which in shallow water models is related to the gradients of the flow field. Recent development in adaptive methods has replaced the error-estimator with multiresolution analysis [103, 40, 52, 73, 15].

The third and final path in Fig. 1.1 is reduced modeling, which aims to reduce the number of floating point operations by either reducing the number of equations or reducing the cell number while conceptually accounting for subgrid-scale information. The first approach is referred to as reduced complexity approach and the latter approach is referred to as coarse grid approach.

Reduced complexity approaches are usually based on a simplified version of the shallow water equations. Common reduced complexity approaches are the diffusive wave approximation, e.g. [69], which neglects the inertia terms in the shallow water model and the kinematic wave approximation, e.g. [22], which neglects the inertia terms and the pressure terms. Because

the calculation of the inertia terms is the most computationally expensive part of the equation, neglecting these terms results in significant decrease of computational cost. Yet, these simplified models have limitations for applications in cases of flow over flat slopes, flow into large reservoirs, flow reversals and strong backwater conditions [79, 78]. It should also be mentioned that neglecting the convection terms in the shallow water model changes the property of the system of partial differential equations, which becomes parabolic. A more in-depth discussion of the diffusive and kinematic wave approximations is found in [157]. The reduced complexity approach is sometimes applied in combination with an adaptive method, using m-adaptivity, which switches between model concepts during the simulation. In [157], the fully dynamic shallow water model is reduced to the kinematic wave approximation, depending on the kinematic wave number. A similar approach is adopted in [159], where the switch between fully dynamic shallow water model and kinematic wave approximation depends on the water depth. Another reduced complexity approach is the cellular automata, which solves the continuity equation in combination with very simple rules that replace the momentum balance to mimic the behaviour of water flow to some extent [97]. A very well-known cellular automata is being developed at the University of Exeter, UK, e.g. [4, 43, 19, 20]. A discussion of this branch of research is omitted, and the reader is referred to [97, 31].

Coarse grid approaches reduce the cell number of the computational mesh by using a coarse mesh resolution. Subgrid-scale information is recovered by means of conceptual approaches. In literature, methods based on a friction-law, e.g. [106, 88, 114], methods based on the definition of a porosity term, e.g. [26, 55, 51], and subgrid methods, [138, 155, 121], are found. An overview of the state of the art is given in the next section.

Aim of this work is to study and develop coarse grid methods (also referred to as scaling methods) for the shallow water model to enable efficient computation of rainfall-runoff and flood events with application to fast predictions and nowcasting (cf. Fig. 1.1). Two approaches are considered: (1) friction law-based coarse grid approach, (2) porosity-based coarse grid approach.

Following steps had been identified to achieve the main objective: the development and verification of a friction-law based coarse grid approach, then the development and verification of a porosity-based coarse grid approach and finally application of both model concepts to rainfall-runoff and flood prediction as a proof of concept.

1.4 A review of relevant literature

Classical shallow water models

The shallow water equations are usually solved using an Eulerian approach within the framework of a finite-difference, finite-volume or finite-element method.

The finite-difference method is one of the oldest methods for solving partial differential equations and is based on Taylor-series approximation of the differentials [56]. It is usually restricted to structured, rectangular meshes and is not necessarily conservative. While the classical finite-difference method fails in the presence of shocks, sophisticated shock-capturing finite-difference schemes such as the TVD MacCormack method [95] have been derived.

The finite-element method uses shape functions to interpolate discrete variables at nodes inside the element and an error due to this approximation with discrete variables is calculated. In a second step, the errors are multiplied with weighting functions, whereby the choice of the weighting functions gives different finite-element schemes. The essential idea is to integrate the weighted error over the domain and force the integral to zero, i.e. the integral approximation error vanishes globally. The finite-element method is suitable for unstructured meshes, and is globally but not locally conservative [56]. In shallow water modeling, weighting functions that incorporate more upstream information, e.g. the Petrov-Galerkin and the Streamline-Upwind/Petrov-Galerkin finite-element method, are preferred, cf. [56].

The finite-volume method, sometimes referred to as integral-finite-difference method, can be formulated in a cell-centered or node-centered way. In the finite-volume method, each computational cell is considered a Eulerian control volume and the conservation law is solved locally in each cell. The method is applicable to unstructured meshes and is both locally and globally conservative [56]. The main difficulty of the finite-volume method is the calculation of the numerical flux over the edge. Classical approaches for the numerical flux calculation are the central method, the upwind method and the QUICK method, which may fail in the presence of a strong shock wave. A better way to calculate the numerical flux is to solve a local Riemann problem over the edge, which results in a shock-capturing finite-volume scheme, which is referred to as Godunov-type finite-volume scheme [44].

Some well-known shallow water codes are the open TELEMAC-MASCARET suite (finite-element) [54], [108], the DHI-Mike models (finite-

difference) [24], the Delft models by Deltares (finite-difference). Many of these models face instabilities or even fail in cases with complex hydraulic conditions, i.e. wetting and drying, small water depths, transcritical flow.

Shallow water models that overcome these numerical difficulties are referred to as robust shallow water models, and usually use a Godunov-type finite volume scheme to solve the equations, e.g. a well-known commercial robust shallow water model is Hydro_AS-2D [108]. Some lesser-known academic Godunov-type shallow water models are the FullSWOF model [29], the HiPIMS model by the Newcastle University [129] and the Hydroinformatics Modeling System by the Chair of Water Resources Management and Modeling of Hydrosystems, Technische Universität Berlin [128]. Another academic robust shallow water model is DIVAST [35], which uses a TVD MacCormack finite-difference method [95].

Friction law-based coarse grid approaches

The friction coefficient in shallow water models expresses a parameterization of subgrid topography [130], more specifically it represents the shear stress at the bottom of the water column but is often used to account for all unresolved processes, e.g. turbulence and depth-averaging effects [101]. Therefore, the idea of calibrating the friction coefficient to account for subgrid-scale effects is very straight-forward.

Néelz & Pender [106] and Liang *et al.* [88] investigated the possibility of using an increased friction coefficient to account for unresolved buildings. Néelz & Pender [106] report that while the high-resolution model solution can be recovered to some extent, preferential flow paths inside the city could not be reproduced. Liang *et al.* [88] point out the difficulty of interpreting the calibrated friction coefficient. Instead of calibrating existing friction laws, specialized friction laws have been presented in literature. Jain *et al.* [70] present a variable Manning law that accounts for vegetation. Another specialized friction law is reported by Razafison *et al.* [123] that conceptually accounts for furrows. Özgen *et al.* [114] presented a generalized friction law that accounts for subgrid-scale obstacles of any kind, e.g. microtopography, pavement structure, buildings.

It can be concluded that there is no systematic development in this methodology, and research is reported in single publications without continuity.

Porosity-based coarse grid approaches

In coarse grid approaches, the porosity term is adopted from porous media flow modeling and describes the fraction of a cell that is available for water flow. The first porous shallow water equations were derived in 1994 by Defina *et al.* [27] with application to rainfall-runoff in natural catchments. Six years later, in 2000, an improved version of the first porous shallow water equations was presented by Defina [26] and solved using a finite-element method. The porosity is calculated by means of an error function that depends on the water depth and accounts for the subgrid-scale microtopography. In the same year, Hervouet *et al.* [55] applied the porous shallow water equations to urban flood modeling using a finite-element method. Here, the porosity terms account for unresolved buildings and are constant values assigned to each cell based on the geometry of the urban catchment.

Another six years later, in 2006, Guinot & Soares-Frazão [51] published a Godunov-type finite-volume scheme to solve the porous shallow water equations for urban flood modeling. The equations were rederived using a representative elementary volume (REV) assumption, again assigning each cell a single porosity that accounted for the subgrid-scale buildings. Lhomme [87] developed porous Riemann solvers for these equations and in [132], some contributions to the momentum-loss formulation were reported. A limitation of this isotropic porosity shallow water model is its incapability of representing directionality of buildings and street networks. Thus, in 2008, Sanders *et al.* [125] removed the REV assumption by deriving the porous shallow water equations in integral differential form. This allowed defining conveyance porosities at the edges, which introduced directionality to the flow. As the porosity in these equations is not isotropic anymore, these equations are referred to as anisotropic porosity shallow water equations. Meanwhile, further studies of the isotropic porosity shallow water equations using the numerical scheme of [51] were carried out between 2009 and 2012 in [18, 39, 152, 151].

In 2012, Le [84] presented a finite-volume shallow water model with porosity for overland flow, similar to the one proposed in Defina [26]. In the same year, Guinot [48] proposed the multiple porosity shallow water model to address the issue of directionality. Here, multiple porosities representing different storage effects are defined in each cell. For each porosity, conservation of mass and momentum is solved and mass is exchanged via source terms. Meanwhile, Chen *et al.* [19, 20] presented a diffusive wave model that defined storage reduction factors (SRF) in the cell and conveyance reduction factors at the cell edges (CRF). These factors can be viewed as the opposite of the porosity terms, as they represent the fraction

of the cell or edge that is blocked by obstacles.

More recently, in 2014, Mohamed [100] presented a Rusanov scheme to solve the isotropic porosity shallow water equations of Guinot & Soares-Frazão [51]. Kim *et al.* [77] carried out numerical studies of the anisotropic porosity shallow water equations using the same numerical method as Sanders *et al.* [125]. The anisotropic porosity shallow water model was reported to be mesh-dependent and suitable meshing techniques were investigated. Viero *et al.* [154] applied the equations of Defina [26] to long term simulations in large natural catchments, using an implicit finite-element method.

In 2015, Kim *et al.* [76] carried out a case study to quantify the model errors in the presence of porosity, comparing the anisotropic porosity shallow water model with the isotropic porosity shallow water model in a laboratory experiment. The anisotropic porosity model was found to be more accurate. Henonin *et al.* [53] presented an isotropic porosity model with variable porosity that allowed full inundation of unresolved obstacles.

In 2016, Özgen *et al.* [110] derived an anisotropic porosity shallow water model that allowed full inundation of subgrid-scale obstacles. In contrast to the model of Sanders *et al.* [125], the porosities were defined as functions of the water depth. In the same year, Özgen *et al.* [116] published a Godunov-type finite-volume method to solve these equations.

In 2017, Özgen *et al.* [115] introduced a dual conveyance porosity concept to the anisotropic porosity shallow water model to enhance the model accuracy. At about the same time, Guinot *et al.* addressed similar issues in [50].

In addition, there is ongoing research on the anisotropic porosity shallow water model at the Université de Liège, Belgium, that has not been published yet (M. Bruwier, private communication, 14 Oct 2016).

It can be concluded that the research of this methodology is carried out more systematically than the friction law-based approach and that continuous developments are reported.

1.5 Document structure

This document is structured in eight chapters, comprising an introduction, four peer-reviewed journal articles (three published, one submitted), one supplementary peer-reviewed conference contribution, further related work and a synthesis.

The first chapter gives a short introduction to the topic of coarse grid methods for the shallow water model. The second chapter presents a friction-law based coarse grid approach suitable for rainfall-runoff simula-

tions in natural catchments. The third chapter presents the mathematical model of a porosity-based coarse grid approach that allows full inundation of subgrid-scale obstacles. The fourth chapter discusses the numerical methods used to solve the mathematical model of the third chapter. The fifth chapter presents improvements of the numerical model that enhance the stability and accuracy of the model. The sixth chapter shows an application case, where the friction-law based model is coupled with the porosity-based model to simulate rainfall-runoff concentration in a natural catchment that leads to a flood in urban environment. The seventh chapter presents supplementary work of the author that is related to the presented research. The eighth chapter draws conclusions, points out open research questions and gives an outlook.

Chapter 2

Friction law-based coarse grid approach

Published as:

[114] Özgen, I., Teuber, K., Simons, F., Liang, D., and Hinkelmann, R. (2015) Upscaling the shallow water model with a novel roughness formulation. *Environmental Earth Sciences* 74, pp. 7371–7386.
doi: 10.1007/s12665-015-4726-7

This is the postprint version of the publication. The final publication is available at Springer via `https://doi.org/10.1007/s12665-015-4726-7`.

2.1 Abstract

This study presents a novel roughness formulation to conceptually account for microtopography and compares it to four existing roughness models from literature. The aim is to increase the grid size for computational efficiency, while capturing subgrid scale effects with the roughness formulation to prevent the loss in accuracy associated with coarse grids. All roughness approaches are implemented in the Hydroinformatics Modeling System and compared with results of a high resolution shallow water model in three test cases: rainfall-runoff on an inclined plane with sine-wave shaped microtopography, flow over an inclined plane with random microtopography and rainfall-runoff in a small natural catchment. Although the high resolution results can not be reproduced exactly by the coarse grid model,

e.g. local details of flow processes can not be resolved, overall good agreement between the upscaled models and the high resolution model has been achieved. It is concluded that the accuracy increases with the number of calibration parameters available, however the calibration process becomes more difficult. Using coarser grids results in significant speedup in comparison with the high resolution simulation. In the presented test cases the speedup varies from 20 up to 2520, depending on the size and complexity of the test case and the difference in cell sizes. The proposed roughness formulation generally shows the best agreement with the reference solution, compared to the other models investigated in this study.

2.2 Introduction

Recent developments in survey technology such as light detection and ranging (LIDAR) and laser scanning are able to provide high-resolution elevation data sets, e.g. in [38, 163, 122], yet the integration of these data into numerical models is often challenging because of finite computer resources [46, 97, 31]. The use of high-resolution elevation data is generally desirable, because it allows a better representation of spatial heterogeneity and localized flow processes. However, high-resolution simulations of practical interest, e.g. across catchment or city scales, are often unfeasible without supercomputers because they are computationally very demanding [129, 62, 81]. Therefore, high-resolution elevation data is usually averaged over relatively coarse grid cells [71] which results in loss of model accuracy [160].

The accuracy of coarse grid models can be improved by conceptually accounting for subgrid-scale effects by calibrating the roughness coefficient [106]. This is a valid natural approach because by definition, a roughness coefficient expresses a parameterization of subgrid topography [130]. In principle, the roughness coefficient in shallow water models represents the shear stress at the bottom of a water column but it is often used to account for all unresolved processes, e.g. turbulence, depth-averaging effects, and therefore may lose its physical meaning [101]. The value of the calibrated roughness coefficient is usually heavily dependent on the calibration conditions, e.g. water depth, grid size, and can not be transferred easily to different conditions [67, 158].

Upscaling is the approximation of a system of partial differential equations by another system of partial differential equations that can be solved with fewer computing resources [36]. The upscaling process usually requires the determination of a set of coefficients, which conceptually account for

properties of the original system. The main advantage of using roughness formulations instead of more sophisticated upscaling approaches for shallow water models, e.g. [51, 155, 67, 97, 88], is their easy implementation into existing models without the need to modifiy the governing equations or numerical methods.

This study presents a novel roughness formulation to account for the effects of microtopography and investigates limits and capabilities of upscaling shallow water equations based overland flow models using roughness formulations. The proposed new formulation uses the experimental studies in [83, 136, 144] as theoretical basis and is to some extent inspired by the roughness models in [123, 70]. The distribution function of the subgrid-scale bottom elevation and the water depth are used to calculate a dimensionless inundation ratio, which is then used to calculate a roughness coefficient. Further, the bottom slope is taken into account. The formulation is compared with four different roughness models: Manning's model with constant roughness coefficient; Lawrence's model [83]; Manning's model with a waterdepth dependent roughness coefficient [102] and Razafison's furrow roughness model [123]. All approaches are implemented in the Hydroinformatics Modeling System (hms), which is an in-house cell-centered finite-volume code developed at the Chair of Water Resources and Modeling of Hydrosystems, Technische Universität Berlin [128]. Three test cases are presented to evaluate the proposed approach: rainfall-runoff on an inclined plane with sine-wave shaped microtopography; surface flow over an inclined plane with random microtopography; and rainfall-runoff in a small Alpine catchment.

2.3 Governing equations

Shallow water equations

The depth-averaged shallow water equations can be written in a conservative form as

$$\frac{\partial \mathbf{q}}{\partial t} + \frac{\partial \mathbf{f}}{\partial x} + \frac{\partial \mathbf{g}}{\partial y} = \mathbf{s}, \tag{2.1}$$

where t is time, x and y are the Cartesian coordinates, $\mathbf{q}$, $\mathbf{f}$ and $\mathbf{g}$ denote the vectors of conserved flow variables, fluxes in the x- and y-directions, respectively. $\mathbf{S}$ is the source vector including bed slope source $\mathbf{s}_b$ and friction

source term $\mathbf{s}_f$. $\mathbf{q}$, $\mathbf{f}$ and $\mathbf{g}$ are usually expressed as

$$\mathbf{q} = \begin{bmatrix} h \\ q_x \\ q_y \end{bmatrix}, \ \mathbf{f} = \begin{bmatrix} q_x \\ uq_x + 0.5gh^2 \\ uq_y \end{bmatrix}, \ \mathbf{g} = \begin{bmatrix} q_y \\ vq_x \\ vq_y + 0.5gh^2 \end{bmatrix}. \tag{2.2}$$

Here, h, u, v are the water depth and depth-averaged velocity in x- and y-directions, respectively; q_x and q_y are the unit-width discharges in x- and y-directions, and $q_x = uh$, $q_y = vh$; g represents the gravity acceleration. The source vector $\mathbf{s}$ can be splitted into

$$\mathbf{s} = \mathbf{s}_b + \mathbf{s}_f + \mathbf{s}_o. \tag{2.3}$$

Here $\mathbf{S}_o$ accounts for additional source terms, e.g. rainfall, wind shear on the free surface, Coriolis-force. It is noted that the first entry of the vector $\mathbf{s}$ is the mass source, the second entry and third entry are momentum source terms in x- and y-direction, respectively. Writing out the vectors leads to

$$\mathbf{s} = \begin{bmatrix} 0 \\ s_{b,x} \\ s_{b,y} \end{bmatrix} + \begin{bmatrix} 0 \\ s_{f,x} \\ s_{f,y} \end{bmatrix} + \begin{bmatrix} i \\ 0 \\ 0 \end{bmatrix}, \tag{2.4}$$

$$\mathbf{s} = \begin{bmatrix} 0 \\ -gh\partial z_b/\partial x \\ -gh\partial z_b/\partial y \end{bmatrix} + \begin{bmatrix} 0 \\ -gu|\mathbf{v}|/C^2 \\ -gv|\mathbf{v}|/C^2 \end{bmatrix} + \begin{bmatrix} i \\ 0 \\ 0 \end{bmatrix}. \tag{2.5}$$

z_b stands for bottom elevation; $\mathbf{v} = \{u, v\}$ is the vector of velocity; $|\cdot|$ denotes the vector norm and C is the so-called Chézy coefficient accounting for flow resistance and i is the rainfall intensity. As shown in, e.g. [128, 131], every friction law coefficient can be transformed into the Chézy coefficient and therefore can be incorporated in Equation 2.1. Viscosity of the fluid, turbulence, wind shear stress on the free surface and Coriolis-force are neglected in this study. The incorporation of these effects into the shallow water equations can be found in, e.g. [56].

Existing roughness formulations

Friction laws can be written in a generalized form as

$$\mathbf{s}_f = -Kh^{\alpha}|\mathbf{v}|^{\beta}\mathbf{v} \tag{2.6}$$

where α and β are positive real numbers and K is the proportionality constant. Well known friction laws such as, e.g. Manning's law and the

Darcy-Weisbach law, can be obtained by a certain choice for α and β. When formulating a friction law, the choice of α and β is arbitrary [123], however the choice is usually related to experimental data sets.

Manning's law with constant roughness can be obtained by choosing $\alpha = -1/3$ and $\beta = 1$ in Equation 2.6:

$$\mathbf{s}_f = -\,g\,n^2\,h^{-1/3}|\mathbf{v}|\mathbf{v} \tag{2.7}$$

Here, n is the Manning roughness coefficient, which relates to the Chézy coefficient as

$$C = \frac{h^{1/6}}{n}. \tag{2.8}$$

In Lawrence's roughness model [83], different flow regimes associated with different roughness formulations are identified for different inundation ratios. The inundation ratio Λ is calculated as

$$\Lambda = \frac{h}{k} \tag{2.9}$$

by using a characteristic roughness length k, which is identified as the mean grain size of the river bed. For increasing Λ, the influence of the subgrid-scale topography decreases. The frictional resistance f is calculated for $\Lambda < 1$ with a drag force approach

$$f = \frac{8\phi C_d}{\pi}\min\left(\frac{\pi}{4}, \Lambda\right), \tag{2.10}$$

where C_d stands for the drag coefficient for roughness elements, and ϕ is the fraction of the surface covered by roughness elements. For the drag coefficient, $C_d = 1$ is assumed [83]. The operator $\min(\cdot)$ is the minimum function, which outputs the smallest value of all input values. For $1 \leq \Lambda \leq 10$, a power law in the form of

$$f = \frac{10}{\Lambda^2} \tag{2.11}$$

is suggested. For $\Lambda > 10$, f is calculated with

$$f = \frac{1}{(1.64 + 0.803\ln\Lambda)^2}. \tag{2.12}$$

The suggested calibration parameters of this model are ϕ (cf. Equation 2.10) and k (cf. Equation 2.9) [102]. f can be transformed into the Chézy coefficient by using

$$C = \sqrt{\frac{8\,g}{f}}. \tag{2.13}$$

The depth-dependent variable Manning's coefficient has been developed for rainfall-runoff models in [70] and is calculated as follows:

$$n\left(h\right) = \begin{cases} n_0 \left(\frac{h}{h_0}\right)^{-\epsilon} & \text{for} \quad h < h_0, \\ n_0 & \text{for} \quad h \geq h_0 \end{cases} \tag{2.14}$$

In this model, n_0 is defined as the Manning's roughness occuring at flow depth h_0 beyond which n is assumed constant and ϵ is a parameter accounting for vegetation. The transformation into the Chézy coefficient is done according to Equation 2.8. The variable Manning's coefficient model has three calibration parameters: n_0, h_0 and ϵ.

Finally, a roughness formulation to account for unresolved furrows is derived by Razafison et al. in [123]. Here, Equation 2.6 is rewritten as

$$\mathbf{s}_f = -\, g\, n^2\, h^{-1/3} |\mathbf{v}| \mathbf{v} - K_{\mathrm{R}} h \mathbf{v} \tag{2.15}$$

where the first term is the classical Manning's equation and the second term is an additional friction term accounting for the furrows. The coefficient K_{R} in this model is calculated as follows:

$$K_{\mathrm{R}} = K_{0,\mathrm{R}} \exp\left(\frac{-h + \langle h_F \rangle}{C \cdot \langle h_F \rangle}\right) \tag{2.16}$$

Here, $K_{0,\mathrm{R}}$ and C are unitless model parameters; and $\langle h_F \rangle$ is the average height of water trapped in furrows which may be calculated with

$$\langle h_F \rangle = \frac{V}{L_F \cdot L}, \tag{2.17}$$

whereby V is the volume of trapped water in a furrow, L_F is its wavelength and L is the length of the domain. Razafison suggests to approximate $\langle h_F \rangle$ numerically (personal communication, August 4, 2014). The model is calibrated with C and $K_{0,\mathrm{R}}$.

In summary, common roughness formulations usually express a relationship between water depth and roughness, often in the form of a power law, e.g. [102, 144, 70, 123]. In the authors' opinion, a more general approach can be obtained for free surface flows by using the inundation ratio instead of the water depth and by including the unitless bottom slope into the formulation.

Novel roughness formulation

$\alpha = 0$ and $\beta = 1$ are chosen in Equation 2.6, which allows to rewrite the friction source term in Equation 2.5 as

$$\mathbf{s}_f = -\left(\frac{g}{C_0^2} + K\right)|\mathbf{v}|\mathbf{v}. \tag{2.18}$$

Here, subgrid-scale topography is accounted for with the parameter K from Equation 2.6 which is here interpreted as a variable dimensionless roughness value, which increases the roughness of the model in dependency of the inundation ratio, and the Chézy coefficient C_0. The index 0 implies that the value of C_0 differs from the value of the Chézy coefficient in the classical formulation of Equation 2.5. C_0 is a model calibration parameter. In this study, a constant Manning formulation (Equation 2.8) is used to calculate C_0.

Experimental results reported in [136] show that the bottom slope I reduces the influence of tillage significantly. This findings certainly can be extended to microtopography in general, as increasing the slope is associated with a loss of surface storage [141].

Equation 2.18 is required to satisfy the following requirements:

1. If Λ increases, the influence of the subgrid-scale topography decreases significantly, hence K should converge to 0.

2. If I increases, the influence of the subgrid-scale topography should decrease, hence K should decrease.

3. For large Λ, only C_0 should account for subgrid-scale effects.

Based on preliminary numerical studies by the authors [140], the following formulation for K is proposed, which satisfies these requirements:

$$K = \alpha_0 \exp\left(-\alpha_1\ (\Lambda - 1)\right) \tag{2.19}$$

Here, $\exp(\cdot)$ stands for the natural exponential function. The inundation ratio is calculated by a modified expression of Equation 2.9 to take the effect of bottom slope into account:

$$\Lambda = \frac{h}{(1 - I)\ k} \tag{2.20}$$

The inundation ratio has been used before in literature to derive friction laws, e.g. [83]. It stands for the ratio of the water depth h to the characteristic roughness length k. If the inundation ratio is smaller than 1, the water

depth is smaller than the characteristic roughness length, which indicates a partially dry area. in this case the flow will be influenced significantly by the subgrid-scale topography. Consequently, a high inundation ratio states that the water depth is relatively high when related to the characteristic roughness length and the flow will not be influenced strongly by the subgrid-scale topography. Both cases are illustrated in Figure 2.1. The choice which value should be used as characteristic roughness is not trivial. Suggestions in literature range from standard deviation of elevations to grain size percentiles [129]. In this study, the standard deviation of microtopography, hereinafter referred to as σ, is used as the characteristic roughness length k. σ represents a summary of topographic irregularity and is often used as a roughness indicating parameter [131, 130], hence it is reasonable to use it as the characteristic roughness length. The relationship between σ and the maximum value of the distribution a_r can be approximated by $a_r = 2\,\sigma$ [26], which means that $\Lambda = 1$ does not indicate full inundation but marks the point, where the majority of the subgrid-scale topography has been inundated. For the derivation of the depth-averaged shallow water equations, I is required to be very small. In shallow water flow simulations, I is usually in the range of 0 to 0.1.

Equations 2.18, 2.19 and 2.20 together represent the proposed roughness formulation. To provide some physical interpretation on the calibration parameters, α_0 can be regarded as a dimensionless friction coefficient. α_1 can be interpreted as a geometric conveyance parameter. It accounts for the influence of the spatial distribution of the subgrid-scale elevations, e.g. blockade effects due to clustering mentioned in [160]. A large α_1 indicates that the conveyance of the spatial distribution is high, so K decreases faster. In the applications presented in this work, α_0 and α_1 are model calibration parameters. Thus, in total three parameters are used for model calibration; C_0, α_0, and α_1. However, as C_0 is calculated via Equation 2.8, the model is actually calibrated using a Manning's coefficient n.

2.4 Numerical implementation

The shallow water equations, shown in Equation 2.1, are discretized with cell-centered finite volumes. The discretized equations are solved numerically with a second order monotonic-upstream-centered scheme for conservation laws (MUSCL). The implementation can be applied to both structured and triangular meshes, however in this work structured grids with square-shaped cells were used. A brief overview of the implementation is given below. For more detailed information, the reader is referred to [128].

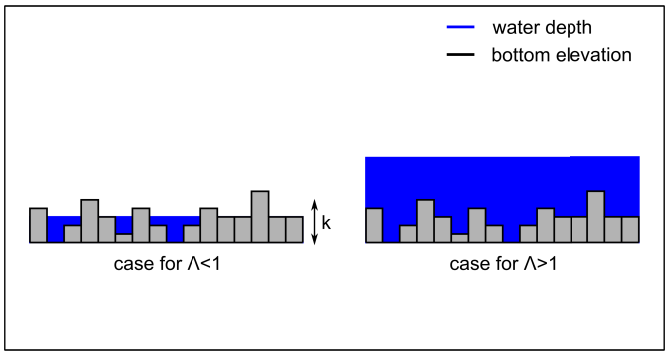

Figure 2.1: Illustration of the concept of the inundation ratio Λ.

Interface flux calculation

The fluxes at cell interfaces, given by the vectors $\mathbf{f}$ and $\mathbf{g}$ in Equation 2.2, are functions of the state variables h and $\mathbf{v}$. Appropriate values for the state variables are calculated by solving the Riemann problem on the interface via a Harten, Lax and van Leer approximate Riemann solver with the contact wave restored (HLLC) [143]. The Riemann states at the left and right side of the interface, namely h_L, h_R and $\mathbf{v}_L$, $\mathbf{v}_R$ where L and R stand for the left and right side of the interface, respectively, are extrapolated from the cell center with a three-point-stencil with slope limiters, shown in [64, 65]. In this study, the min-mod limiter is used to suppress spurious oscillations.

To well preserve the C-property, non-negative hydrostatic reconstruction of the bottom elevation at the interface by [2] is used. The water depth and bottom elevation are modified prior to the Riemann solution [60]. Discussion of the non-negative hydrostatic reconstruction method is given in [66, 28].

Slope and friction source term treatment

The bottom slope source term $\mathbf{s}_b$ of a cell (cf. Equation 2.3) is transformed into fluxes through the cell faces [60].

The friction source term is discretized with the splitting point-implicit method derived in [93], which allows a fully implicit integration of the friction source term.

In order to avoid numerical instabilites caused by too high friction source terms, the entries $s_{f,x}$ and $s_{f,y}$ of the vector $\mathbf{s}_f$ (cf. Equation 2.5) are limited

as shown in [93]:

$$s_{f,i} \begin{cases} \geq -q_i^n \Delta t & \text{if } q_i^n \geq 0 \\ \leq -q_i^n \Delta t & \text{if } q_i^n < 0 \end{cases} \tag{2.21}$$

Here, the subscript i stands for either x or y, denoting the direction in cartesian coordinates. With this limitation, friction no longer changes the direction of the flow [60].

2.5 Computational examples

All simulations were carried out with the Hydroinformatics Modeling System (hms). The proposed roughness approach is compared with different roughness models. Results of high-resolution simulations with explicitly discretized microtopography (HR) are used as reference solutions. All models use the same numerical scheme. The parameters of all models are optimized with the SciPy library [149] by minimizing the root mean square deviation (RMSD) of the model results in regard to the HR model, using either Brent's method [7] for one free parameter or the Limited-memory Broyden, Fletcher, Goldfarb and Shanno algorithm (L-BFGS-B) [12, 164] for more parameters.

The RMSD is calculated as:

$$\text{RMSD} = \sqrt{\frac{\sum_{t=1}^{n} \left(\hat{q}_t - q_t\right)^2}{n}} \tag{2.22}$$

Here, $\hat{q}_t$ is the unit discharge obtained by the roughness model, q_t stands for the unit discharge of the reference solution of a HR model; t is a sample index and n is the number of samples. The normalized root mean square deviation NRMSD is calculated as

$$\text{NRMSD} = \frac{\text{RMSD}}{q_{\max} - q_{\min}}, \tag{2.23}$$

where $q_{\max}$ and $q_{\min}$ are the maximum and minimum values of the reference solution calculated by the HR model, respectively.

The computational benefit gained by the coarse grids is quantified with the speedup, which is calculated as

$$\text{SPEEDUP} = \frac{T}{\hat{T}}, \tag{2.24}$$

whereby T is the walltime duration of the HR model and $\hat{T}$ is the walltime duration of the upscaled model.

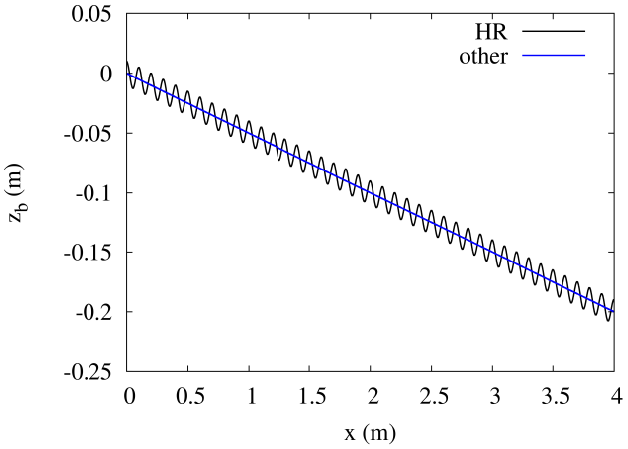

Figure 2.2: Rainfall-runoff over an inclined plane with sine-wave shaped microtopography: Computational domain of different models: HR (black), all other models (blue).

Rainfall-runoff over an inclined plane with sine-wave shaped microtopography

Rainfall-runoff over a one-dimensional inclined plane with sine-wave shaped microtopography is simulated. Although synthetic, this test case is suitable to study the capability of roughness models because in the limit, any theory for complex microtopography has to converge to the solution of this idealized set up [141]. The domain is 4 m long and its topography is described by

$$z_b = -0.05\,x + 0.01 \sin\left(20\pi\,x + \frac{\pi}{2}\right) \tag{2.25}$$

for a high-resolution model with explicitly discretized microtopography (HR) on a 0.01 m grid. The standard deviation of the microtopography is $\sigma = 0.01$ m. If the microtopography is not explicitly discretized, which is the case in the upscaled models, the bottom elevation is described by

$$z_b = -0.05\,x. \tag{2.26}$$

The side-view of the domain with microtopography (HR) and without (other) is plotted in Figure 2.2. Simulation parameters, initial and boundary conditions for this simulation are summarized in Table 2.1.

Results for the proposed roughness model (RM), Lawrence's model (LAW), constant Manning's coefficient model (CM), variable Manning's co-

Table 2.1: Rainfall-runoff over an inclined plane with sine-wave shaped microtopography: Simulation parameters, initial and boundary conditions.

Symbol	Meaning	Value
σ	Standard deviation	$0.01\,\mathrm{m}$
I	Slope	0.05
n	Manning's coefficient (HR)	$0.04\,\mathrm{sm}^{-1/3}$
i	Rainfall intensity	$8 \cdot 10^{-4}\,\mathrm{m/s}$
T	Simulation time	$22.5\,\mathrm{s}$
BC_0	Boundary condition at $x = 0$	closed boundary
BC_4	Boundary condition at $x = 4\,\mathrm{m}$	open boundary
h_0	Initial water depth	0

Table 2.2: Rainfall-runoff over an inclined plane with sine-wave shaped microtopography: Calibrated parameter values and corresponding RMSD for each model (CM: Constant Manning, VM: Variable Manning, LAW: Lawrence, RA: Razafison, RM: proposed approach).

Model	Calibrated parameter(s)	RMSD
CM	$n = 0.22\,\mathrm{sm}^{-1/3}$	0.081
VM	$n_0 = 0.018\mathrm{sm}^{-1/3}$;$h_0 = 0.04\mathrm{m}$;$\epsilon = 2.4$	0.014
LAW	$\phi = 5.6\,\%$; $k = 0.06\,\mathrm{m}$	0.040
RA	$C = 0.4$; $K_{0,\mathrm{R}} = 0.02$	0.058
RM	$n = 0.15\,\mathrm{sm}^{-1/3}$;$\alpha_0 = 28.57$;$\alpha_1 = 7.26$	0.007

efficient model (VM) and Razafison's furrow roughness model (RA) using a grid size of 0.1 m are calculated.

Optimization was carried out regarding the discharge at the outlet of the domain. The optimized parameters for each model together with the resulting RMSDs are given in Table 2.2. The optimal parameters of the RA model for this test case were taken from the literature [123].

The unit discharges at the outlet of the domain divided by the total unit discharge of the rain $q_{\mathrm{rain}} = 3.2 \cdot 10^{-3}\,\mathrm{m}^2/\mathrm{s}$ are plotted in Figure 2.3. The CM model poorly reproduces the HR model result by overshooting it in the early stage of the simulation and undershooting it in the later stage. The VM model with three free parameters shows very good agreement. The RM model shows the best agreement. At the beginning, the RM model slightly overshoots the solution of the HR model, however in the later stages the curves show very good agreement. The LAW model with two calibration

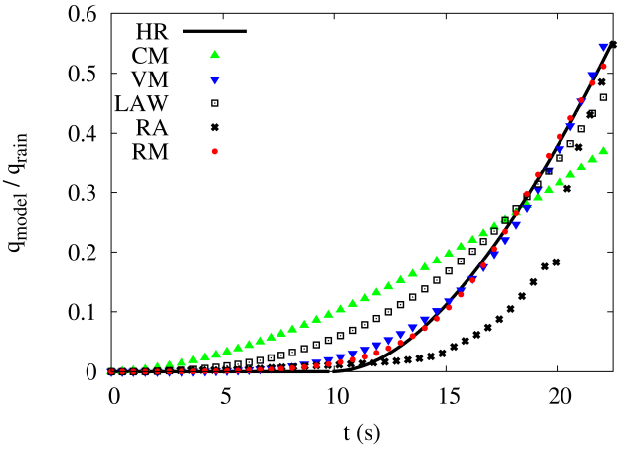

Figure 2.3: Rainfall-runoff over an inclined plane with sine-wave shaped microtopography: Unit discharges compared at the outlet (HR: High-resolution, CM: Constant Manning, VM: Variable Manning, LAW: Lawrence, RA: Razafison, RM: proposed approach).

parameters shows good agreement with the HR model. The discharge in the early stages of the simulation is overshot by the LAW model, however the later stages are captured well. The discharge calculated by the RA model rises later than all other models and keeps undershooting the HR model results. A discontinuity occurs at about $t = 20\,\mathrm{s}$, which marks the time for $\langle h_F \rangle < h$. At the end of the simulation, the RA model catches up with the HR model.

All models can be calibrated to match the HR results to some extent. However, it could be argued that the VM model parameter h_0 and the LAW model parameter k are geometric parameters and should not be used for calibration. From their conceptual point of view, h_0 and k should either be set to the standard deviation of microtopography, i.e. 0.01 m, or the amplitude of the microtopography, i.e. 0.02 m. It was found out that using these values for h_0 and k significantly reduces these models accuracy. Especially the LAW model can not be calibrated to satisfactory accuracy using only ϕ, because ϕ represents a fraction and therefore is bounded between 0 and 1 and is not very sensitive. The simulation of the coarse models runs on a mesh with 40 cells in average 50 times faster than the HR model simulation, which runs on a mesh with 400 cells.

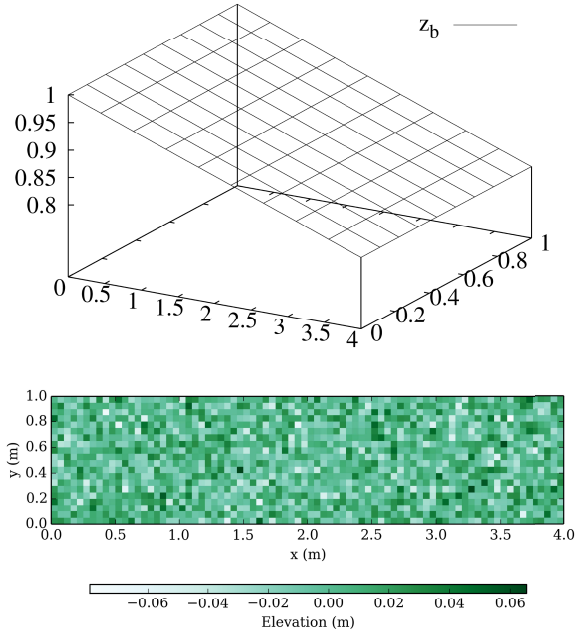

Figure 2.4: Flow over an inclined plane with random microtopography: Global topography for $I = 0.05$ (top); microtopography (bottom).

Flow over an inclined plane with random microtopography

Study area

The following example is inspired by similar simulation runs carried out in [89] and simulates a run-dry process of an inclined surface with random microtopography. The study area is a $4\,\mathrm{m} \times 1\,\mathrm{m}$ inclined plane (cf. Figure 2.4 (top)). Random microtopography is generated as square blocks with a horizontal length of 0.05 m and a vertical elevation according to a Gaußian distribution with a standard deviation of $\sigma = 0.02$ m (cf. Figure 2.4 (bottom)). The maximum value of the microtopography is about 0.07 m and the minimum value about -0.08 m. The domain is initially ponded with water which is then discharged during the simulation at the outlet of the domain. Several simulations with different slope and initial water depth are carried out.

Table 2.3: Flow over an inclined plane with random microtopography: Simulation parameters, initial and boundary conditions.

Symbol	Meaning	Value
σ	Standard deviation	$0.02\,\mathrm{m}$
I	Slope	$0.01 - 0.14$
n	Manning's coefficient (HR)	$0.04\,\mathrm{sm}^{-1/3}$
i	Rainfall intensity	0
T	Simulation time	$60\,\mathrm{s}$
BC_0	Boundary condition at $x = 0$	closed
BC_4	Boundary condition at $x = 4\,\mathrm{m}$	open
$\mathrm{BC}_\parallel$	Boundary conditions at $y = 0$; 1m	closed
h_0	Initial water depth	$0.005 - 0.08\,\mathrm{m}$

The slope I and the initial water depth h_0 are varied for different simulation runs. For each different slope, different simulation runs. The slope is increased in steps of 0.01 and the water depth is increased in steps of $0.005\,\mathrm{m}$. For example, for $I = -0.01$, simulation runs with $h_0 = 0.005\,\mathrm{m}$, $h_0 = 0.01\,\mathrm{m}$, $h_0 = 0.015\,\mathrm{m}$ until $h_0 = 0.08\,\mathrm{m}$ are carried out, and after that the slope is set to $I = -0.02$ and again simulation runs with varying h_0 are carried out. Table 2.3 shows the simulation parameters, initial and boundary conditions for this simulation.

Four different roughness models are compared for every possible combination of I and h_0 with results of a high-resolution model explicitly discretizing the microtopography (HR): a model using a calibrated constant Manning's coefficient (CM); a model using a variable Manning's coefficient (VM), Lawrence's model (LAW); and the proposed roughness approach (RM). The HR model uses quadratic grid cells with an edge length of $0.01\,\mathrm{m}$, all other models use grids with coarser cells.

Uncalibrated model on coarse grid

First, an uncalibrated simulation on a coarse grid is carried out to show the effects of increasing the grid size without using an upscaling approach. The simulation is run on a $0.05\,\mathrm{m} \times 0.05\,\mathrm{m}$ grid using the same roughness coefficient as the HR model ($n = 0.02\,\mathrm{sm}^{-1/3}$) for $I = -0.02$, $h_0 = 0.04\,\mathrm{m}$. Results for the unit discharge at the outlet for the uncalibrated model (UCM) are plotted in Figure 2.5 (top). The peak of the discharge curve of the UCM model is about 20 times higher than the HR model. After the peak is reached, the UCM model discharge decreases too quickly which indicates

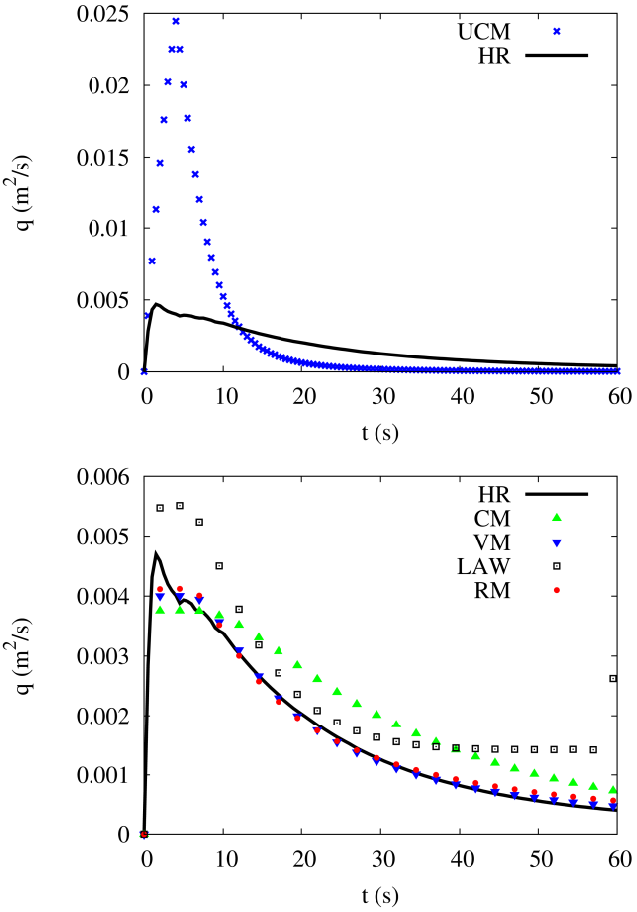

Figure 2.5: Flow over an inclined plane with random microtopography, 0.05 m grid size: Unit discharges of the uncalibrated model (UCM) and HR models (top) and model comparison at the outlet for $h_0 = 0.04$ m and $I = 0.02$ (bottom) (HR: High-resolution, CM: Constant Manning, VM: Variable Manning, LAW: Lawrence, RM: proposed approach).

that the roughness is overall underestimated. A NRMSD of 1.0 is calculated.

Application to different hydraulic conditions

In this section, the applicability of the roughness models to different hydraulic conditions is tested. In a first step, the models are calibrated for a fixed I-Λ_0 combination and in a second step these calibrated models are

Table 2.4: Flow over an inclined plane with random microtopography, 0.05 m grid size: Calibrated parameter values and corresponding NRMSD for $h_0 = 0.04$ m and $I = 0.02$ for each model (CM: Constant Manning, VM: Variable Manning, LAW: Lawrence, RM: proposed approach).

Model	Calibrated parameter(s)	NRMSD
CM	$n = 0.18\,\mathrm{sm}^{-1/3}$	0.120
VM	$n_0 = 0.14\mathrm{sm}^{-1/3}$;$h_0 = 0.045$m;$\epsilon = 1.4$	0.026
LAW	$\phi = 50\,\%$; $k = 0.023\,\mathrm{m}$	0.173
RM	$n = 0.112\mathrm{sm}^{-1/3}$;$\alpha_0 = 5.52$;$\alpha_1 = 2.61$	0.030

applied to different I-Λ_0 combination.

All models were calibrated on a $0.05\,\mathrm{m} \times 0.05\,\mathrm{m}$-grid with regard to the unit discharge calculated by the HR model at the outlet of the domain for a slope of $I = -0.02$ and an initial water depth of $h_0 = 0.04\,\mathrm{m}$, i.e. an initial inundation ratio of $\Lambda_0 = h_0/\sigma = 2$. The calibrated parameters of all models with the corresponding NRMSDs are given in Table 2.4. The unit discharges at the outlet are plotted in Figure 2.5 (bottom). While the LAW model is showing the worst agreement with the HR model, the VM model agrees the best, followed by the RM model. Although the first peak of the HR model can not be captured by any of the models, overall the VM and RM models capture the HR model results very well. The CM model undershoots the HR solution significantly at the beginning of the simulation and starts to overshoot it after about $t = 12\,\mathrm{s}$. The overall agreement is not satisfactory. Additional calibrations which were carried out with different initial conditions suggest that all models except the LAW model should be calibrated for $\Lambda_0 \geq 2$, because for $\Lambda_0 < 2$ the calibration may fail to deliver good results. One reason for this may be, that for $\Lambda_0 < 2$ the blockade effects of the microtopgraphy outweigh its roughness effects, i.e. the flow depends on the spatial configuration and geometric properties of single microtopography elements. Then, spatial heterogeneity significantly influences the flow and therefore the roughness effects can not be averaged over the domain. For $h_0 = 0.04\,\mathrm{m}$, the LAW model uses Equation 2.11 to calculate the roughness and therefore has no calibration parameters. The calibrated values in Table 2.4 effect only the stage of the simulation when the inundation ratio becomes smaller than 1. Calibrating the LAW model for smaller Λ_0 might deliver better results, however the calibration difficulties regarding the LAW model mentioned in the test case before still remain.

To study the transferability of the calibrated parameters to different hydraulic conditions, the calibrated parameters in Table 2.4 are used to

simulate the unit discharge for every I-Λ_0 combination. The grid cell size used by the models is 0.05 m. Results are compared with HR model results. Figure 2.6 shows the NRMSD of all models in dependency of I and Λ_0, where each cell is the result of a simulation run of a certain I-Λ_0 combination. The main focus of Figure 2.6 is the change of the NRMSD in dependency of I and Λ_0 within one model. Because of this reason and the significant differences in the NRMSDs of different models, the range of the legends are not set equal. The I-Λ_0 combination used for the calibration is denoted with a black rectangle. High NRMSD in the CM model results occur for small Λ_0 combined with small I. As Λ_0 or I increase, the NRMSD decreases as the influence of the microtopography decreases. The minimum NRMSD occurs for the calibration conditions, i.e. $\Lambda_0 = 2$ and $I = -0.02$. Except for the region around $\Lambda_0 = 0.75$ and $I = -0.01$, which is the location of the maximum NRMSD, the transfer of the calibrated parameters to different I and Λ_0 does not significantly alter the NRMSD. It stays almost constant around the mean value of 0.133. The NRMSD distributions of the VM model and the RM model are qualitatively very similar. High NRMSD occurs for small Λ_0 combined with large I. For the VM model, the minimum NRMSD occurs for the calibration conditions, but for the RM model smaller NRMSD is calculated for other simulation runs. For both models, transfering the calibrated parameters to hydraulic conditions with $\Lambda_0 > 1.5$ leads to increased NRMSDs, but transfering the parameters to conditions with higher Λ_0 has not a significant influence on the NRMSD. The LAW model has the highest NRMSD of all considered models. The NRMSD increases significantly for $\Lambda_0 < 1$, for $\Lambda_0 > 1$ the NRMSD is about 0.15 and remains constant. With increasing Λ_0, the NRMSD decreases. The maximum NRMSD, the minimum NRMSD and the mean NRMSD of all simulations for each model are given in Table 2.5. Here it is seen that the RM model calculates a smaller minimum, maximum, and mean NRMSD than the VM model, but the VM model can be locally calibrated to show better agreement (cf. Figure 2.5 (bottom)).

Application to different cell size

Grid size is increased from 0.05 m to 0.1 m and to 0.2 m to study the transferability of the calibrated parameters to different mesh resolutions. It is desirable, that the RMSD decreases with decreasing cell size (also called grid convergence) because this allows to efficiently calibrate the model on coarser cells and then transfer the calibrated parameters to a model with the desired spatial resolution [58]. If this can not be achieved, it is desirable that at least the RMSD stays the same for different cell sizes. Table

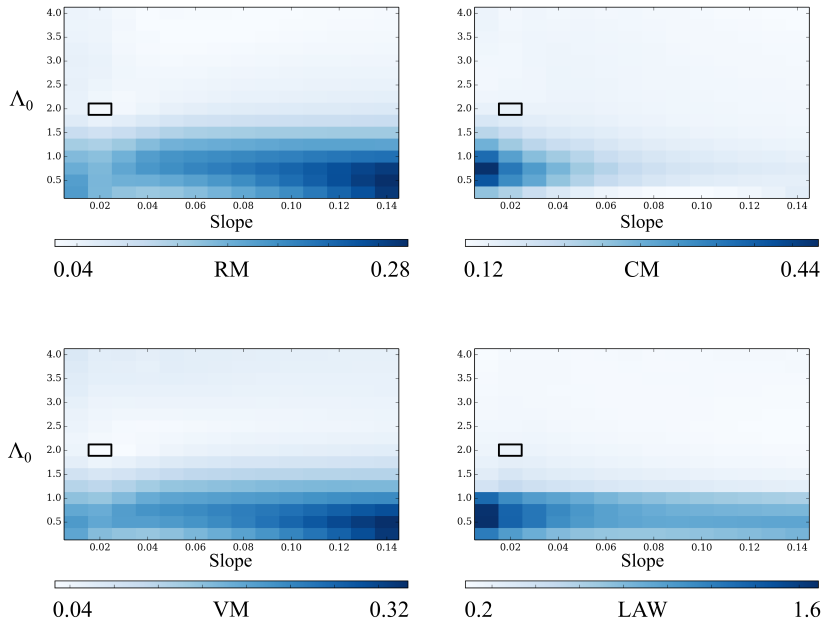

Figure 2.6: Flow over an inclined plane with random microtopography, 0.05 m grid size: Normalized root mean square deviation in relation to initial inundation ratio Λ_0 and slope I.

Table 2.5: Flow over an inclined plane with random microtopography, 0.05 m grid size: Minimum (min), maximum (max) and mean NRMSD values of all I-Λ_0-combinations for different models (CM: Constant Manning, VM: Variable Manning, LAW: Lawrence, RM: proposed approach).

Model	min	max	mean
CM	0.095	0.468	0.133
VM	0.026	0.347	0.105
LAW	0.093	1.688	0.335
RM	0.022	0.304	0.091

Table 2.6: Flow over an inclined plane with random microtopography: Computational benefit for different grid sizes Δx (HR: high-resolution, other: all upscaled roughness models).

Model	Δx	cell number	SPEEDUP
HR	0.01 m	40000	1
other	0.05 m	1600	20
other	0.1 m	400	40
other	0.2 m	100	70

Table 2.7: Flow over an inclined plane with random microtopography: Mean NRMSD in dependency of grid cell length averaged over all I-Λ_0-combinations (CM: Constant Manning, VM: Variable Manning, LAW: Lawrence, RM: proposed approach).

Model	0.05 m	0.1 m	0.2 m
CM	0.133	0.133	0.133
VM	0.105	0.105	0.105
LAW	0.336	0.336	0.335
RM	0.092	0.092	0.091

2.7 shows the NRMSD in dependency of grid cell length averaged over all I-Λ_0-combinations. For all models, the calibrated parameters were transferred between the investigated scales with negligibly small change in the NRMSD. Oddly, coarsening the grid size to 0.2 m improves the NRMSD. The reason for this negligibly small improvement may be due to numerical round-off somehow benefiting the accuracy of the solution, yet this has not been further investigated. The inclined plane as a study area is not very sensitive to grid size, because the geometry is captured perfectly accurate by the second order discretization in combination with the non-negative hydrostatic reconstruction (cf. [128]). The plane has no other spatial heterogeneities than the subgrid-scale microtopography, which is accounted for by the roughness formulation, i.e. the model domain is a smooth inclined plane. Therefore, increasing grid size is not associated with further loss of geometric information and only reduces accuracy because of numerical diffusion. The HR model simulation runs on a mesh with 40000 cells. The speedup (Equation 2.24) in relation to the cell number is shown in Table 2.6. As the cell number decreases, the speedup increases. The speedup of the different upscaled roughness models did not differ significantly.

Rainfall-runoff in a small alpine catchment

Study area and preliminary studies

Hortonian overland flow in a natural catchment, the Heumöser slope, Vorarlberg Alps, Austria, is simulated. The study area is a 100 000 m^2 large subcatchment of the Heumöser slope. Bottom elevation of the area is provided in 1 m × 1 m resolution by a digital elevation model of the Austrian department Torrent and Avalanche Control. This bottom elevation is used for the high-resolution model. Figure 2.7 (top) shows the topography of the domain and the location of the outlet, where discharge was measured. Rainfall is imposed according to a time series measured in July 2008 with a resolution of 10 min (Figure 2.7 (middle)). The simulation runs for $t = 120$ h, i.e. 5 days.

Extensive numerical simulations of the surface and subsurface runoff for this domain were carried out in [128, 137] within Research Unit 'Coupling of flow and deformation processes for modelling the movement of natural slopes' funded by the German Research Foundation [57]. During these simulations, the model was calibrated with a runoff coefficient $\Psi = 0.3$ in combination with a linear reservoir model to account for the slower discharge component in the subsurface, which was identified as a crucial contributor to the discharge at the outlet of the domain. The linear reservoir is described by the following equations:

$$\frac{\mathrm{d}S(t)}{\mathrm{d}t} = I(t) - Q(t) \tag{2.27}$$

$$S(t) = KQ(t) \tag{2.28}$$

Here, $S(t)$ stands for the storage at time t; $I(t)$ for the inflow; and $Q(t)$ for the outflow of the reservoir. K is the constant of proportionality which can be obtained by calibration. A calibration in [128] resulted in a constant of proportionality $K = 6$ h and a Manning coefficient of $n = 0.067$ $\mathrm{sm}^{-1/3}$. Because the same numerical model (hms) as in [128] is used in this study, the same values for Ψ and K are used in all models. For reference, the results of a high-resolution simulation with these parameters on a 1 m × 1 m grid (HR) is plotted in Figure 2.7 (bottom).

In the simulations grids with cell sizes of 5 m, 10 m and 20 m are used. The bottom elevation inside a cell is set to the arithmetic average of all DEM points located inside the cell. The discretized bottom elevation for the studied cases is given in Figure 2.8. As expected, the discretization with a cell size of 5 m (Figure 2.8 (top)) has the most information about local

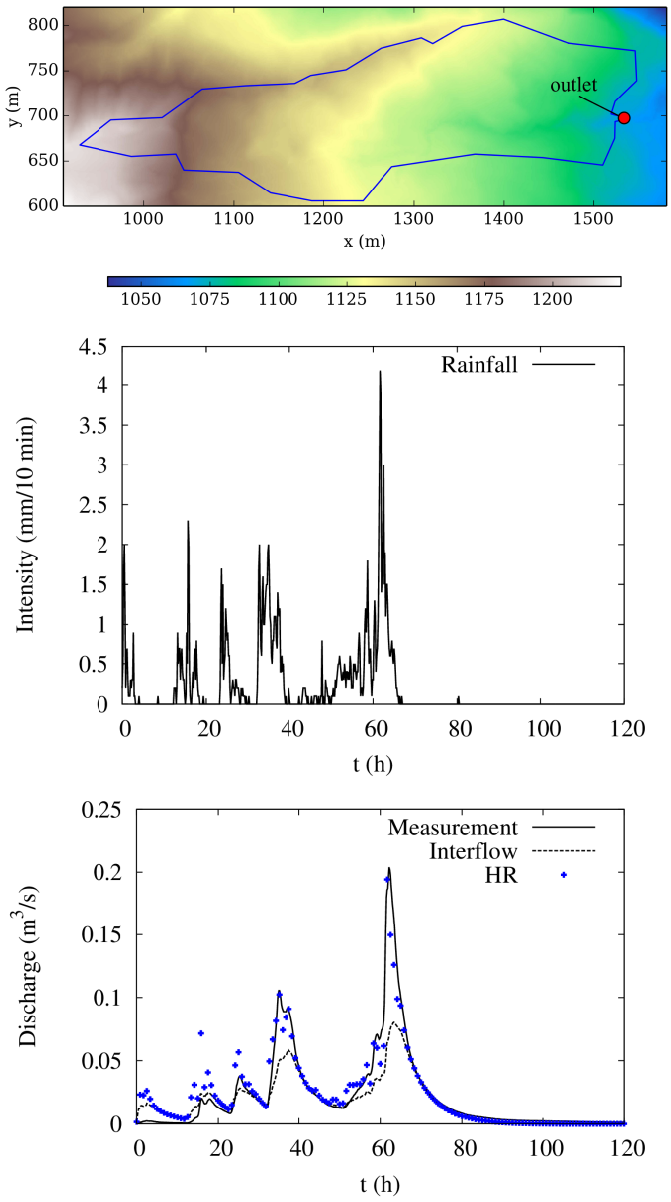

Figure 2.7: Rainfall-runoff in a small alpine catchment: Bottom elevation, watershed (blue) and location of the outlet (top); intensity of the rainfall event plotted over time (middle); HR model results with parameters from [128] (bottom)

Table 2.8: Rainfall-runoff in a small alpine catchment: Simulation parameters, initial and boundary conditions.

Parameter	Meaning	Value
σ	Standard deviation	$0.19\text{m} - 0.21\text{m}$
I	Slope	locally varying
n	Manning's coefficient (HR)	$0.067\,\text{sm}^{-1/3}$
i	Rainfall intensity	time series
T	Simulation time	120 h
BC	Boundary condition	open boundary
h_0	Initial water depth	0

details in the topography. It also can be seen that the discretization with a cell size of 10 m (Figure 2.8 (middle)) still represents an acceptable amount of local heterogeneities and even the discretization with a cell size of 20 m (Figure 2.8 (bottom)) is able to capture the main topologic characteristics of the catchment. However, in the latter case the watershed boundaries start to blur and the location of the measurement weir is captured in a single cell. Small scale preferential flow paths in the domain as observed in [128] can not be represented by the coarse resolution. Additionally, numerical diffusion increases due to the mesh resolution effects [160]. All these effects have to be captured to some extent by the roughness formulations.

In order to calculate its standard deviation, the microtopography is isolated by calculating the deviations of each DEM point in a cell from the bottom elevation of the cell. The standard deviation of the microtopography is then calculated as $\sigma = 0.19\,\text{m}$ for a grid cell size of 5 m and $\sigma = 0.21\,\text{m}$ for a grid cell size of 10 m and 20 m.

Table 2.8 shows the simulation parameters, initial and boundary conditions for this simulation.

The proposed roughness formulation (RM) and three other roughness approaches are compared in this test case: calibrated constant Manning's coefficient (CM), variable Manning's coefficient (VM) and the model of Lawrence (LAW). Model discharges at the outlet are superposed with the interflow computed by the linear reservoir (cf. Equations 2.27 and 2.28) and are compared with measurement data.

Upscaling with roughness formulations

Models are calibrated for a quadratic grid with a cell size of 10 m. Table 2.9 shows the calibrated model parameters and the corresponding RMSD

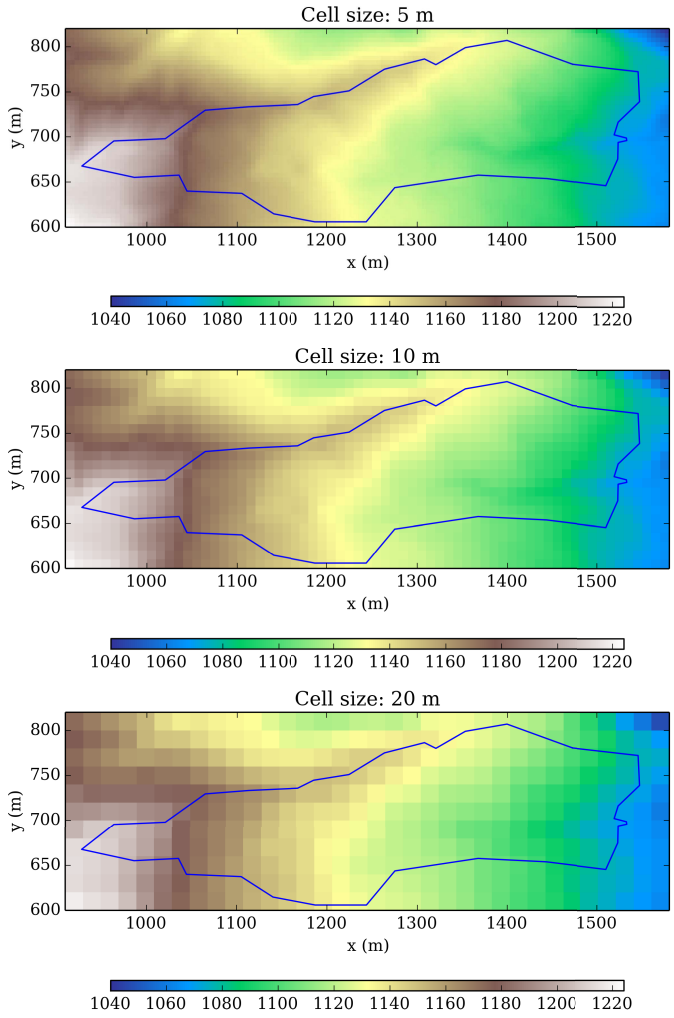

Figure 2.8: Rainfall-runoff in a small alpine catchment: Bottom elevation discretization in dependency of mesh resolution

with regard to measurement data for each model. All models have almost the same RMSD, however the RM model and the CM model give the lowest RMSD. The HR model results in a similar RMSD as the coarse models. The reason is that due to computational restraints, the HR model was calibrated manually with fewer trials than an optimization algorithm would require [128]. The usage of numerical optimization algorithms to calibrate the HR model would demand unfeasibly high computational effort. The hydrograph calculated by the HR model is compared with measurement data in Figure 2.7 (bottom). In the early stages of the rainfall event, specifically for $t < 20\,\mathrm{h}$, the interflow is overestimated by the linear reservoir model and thus, the HR model results overshoot the measured data significantly. Reason for this deviation might be previous hydrological events in the catchment, which can not be taken into account. This can be seen in Figure 2.7 (bottom), where at the beginning of the simulation the interflow overshoots the measured time series. Most likely, in the real event the rainfall infiltrated into the groundwater instead of becoming part of the interflow. Better results might be obtained by using a more sophisticated approach than a constant runoff coefficient to estimate the effective rainfall. At around $t = 20\,\mathrm{h}$ the deviation between model and measurement begins to decrease. After $t = 30\,\mathrm{h}$, the hydrograph is captured quite accurately by the models. The hydrographs of the CM, VM, LAW and RM model are plotted in Figure 2.9 (blue triangles). As the HR model, these models also overshoot the measurement data for $t < 20\,\mathrm{h}$. The CM model shows good agreement for the calibrated cell size. Both peaks are captured well. The VM model captures both occuring peaks (at about $t = 35\,\mathrm{h}$ and $t = 65\,\mathrm{h}$) the best. The LAW model and the RM model tend to undershoot both peaks. However, the RM model captures the tails of both curves more accurately.

Application to different cell size

In order to investigate the transferability of calibrated parameters to different resolutions, cell size is varied to 5 m and 20 m. Table 2.10 shows the RMSD for each model in dependency of cell size. In Figure 2.9, the hydrographs for a cell edge length of 5 m (red circle) and a cell edge length of 20 m (black square) are plotted. For the CM model, varying the cell size decreases both peaks and decreases the arrival time of the first wave. In Table 2.10 it can be seen that the RMSD increases with varying cell size. For the VM model, increasing or decreasing the cell size lowers both peaks (Figure 2.9). For the LAW model, mesh refinement leads to an overall increase in discharge and increasing the cell size leads to an overall decrease

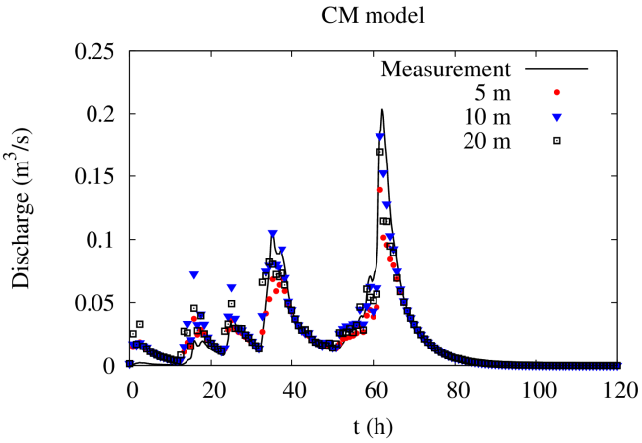
CM model
Measurement
5 m
10 m
20 m
Discharge (m3/s)
t (h)
0.25
0.2
0.15
0.1
0.05
0
0
20
40
60
80
100
120

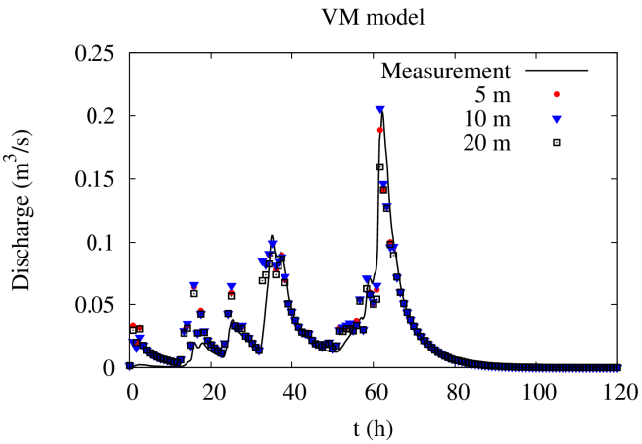
VM model
Measurement
5 m
10 m
20 m
Discharge (m3/s)
t (h)
0.25
0.2
0.15
0.1
0.05
0
0
20
40
60
80
100
120

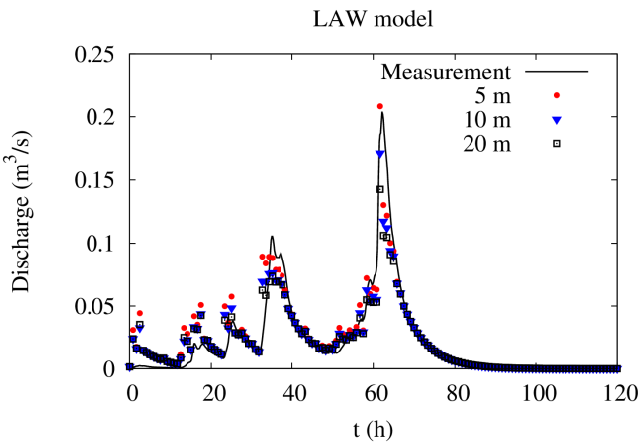
LAW model
Measurement
5 m
10 m
20 m
Discharge (m3/s)
t (h)
0.25
0.2
0.15
0.1
0.05
0
0
20
40
60
80
100
120

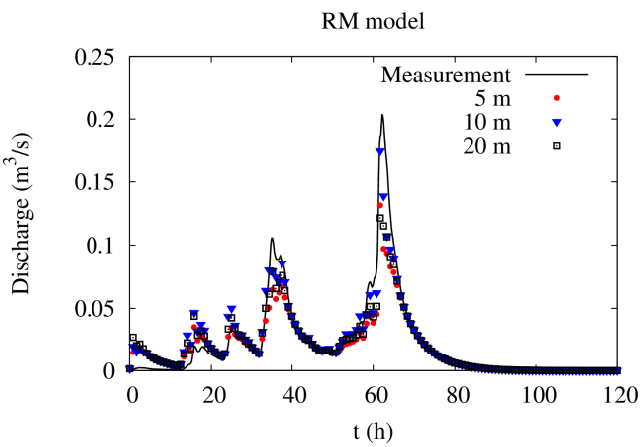
RM model
Measurement
5 m
10 m
20 m
Discharge (m3/s)
t (h)
0.25
0.2
0.15
0.1
0.05
0
0
20
40
60
80
100
120

Table 2.9: Rainfall-runoff in a small alpine catchment, 10 m grid size: Calibrated parameter values and corresponding RMSD for each model (HR: High-resolution, CM: Constant Manning, VM: Variable Manning, LAW: Lawrence, RM: proposed approach).

Model	Calibrated parameter(s)	RMSD
HR	$n = 0.067\,\mathrm{sm}^{-1/3}$	0.011
CM	$n = 0.115\,\mathrm{sm}^{-1/3}$	0.010
VM	$n_0 = 0.01\mathrm{sm}^{-1/3}$;$h_0 = 0.058\mathrm{m}$;$\epsilon = 0.11$	0.012
LAW	$\phi = 10\,\%$; $k = 0.21\,\mathrm{m}$	0.012
RM	$n = 0.035\mathrm{sm}^{-1/3}$;$\alpha_0 = 0.3$;$\alpha_1 = 0.87$	0.010

in the discharge. Varying the cell size for the RM model leads to a significant decrease in both peaks. The arrival time of both waves is captured accurately in all cases. In Table 2.10 it can be seen that the VM model shows good transferability, while the calibration of the CM, LAW and RM model results show higher RMSDs if the cell size is changed.

A manual calibration of the RM model was carried out to further investigate this models parameters transferability. It was found out that the transferability of the parameters of the RM model can be increased if accuracy is sacrificed. For the parameter combination $n = 0.07\,\mathrm{sm}^{-1/3}$, $\alpha_0 = 0.51$ and $\alpha_1 = 0.54$, which result in a RMSD = 0.012, the RM model showed good transferability of its parameters across the investigated cell sizes.

The speedup, as calculated according to Equation 2.24, in dependency of grid cell size is shown in Table 2.11. As expected, increasing the cell size reduces the cell number and thus the computational effort significantly. The speedup of the different roughness models is about the same. Of course the computational time depends on the hardware and the numerical code, however the speedup certainly can be transferred with little variance to different hardware and codes.

2.6 Discussion

The speedup in the presented examples varied in a wide range between 20 to 2520 (cf. Tables 2.6, 2.11). The width of the range can be explained with the way the cell size influences the speedup. In fact, the two major influences on the speedup are the number of cells and the Courant-Friedrichs-Lewy stability criterion (CFL), which limits the time step size [77]. Both the

Table 2.10: Rainfall-runoff in a small alpine catchment: RMSD for each model in dependency of cell size (CM: Constant Manning, VM: Variable Manning, LAW: Lawrence, RM: proposed approach).

Model	5 m	10 m	20 m
CM	0.015	0.010	0.013
VM	0.012	0.012	0.012
LAW	0.013	0.012	0.014
RM	0.016	0.010	0.013

Table 2.11: Rainfall-runoff in a small alpine catchment: Computational benefit for different grid sizes Δx (HR: high-resolution, other: all upscaled roughness models).

Model	Δx	cell number	SPEEDUP
HR	1 m	147400	1
other	5 m	5896	56
other	10 m	1474	336
other	20 m	374	2520

number of cells and the CFL criterion are dependent on the cell size. In [77], these effects have been taken into account to express a relationship between computational cost C with cell size Δx as

$$C \sim k\Delta x^{-3}, \tag{2.29}$$

where k is a factor which depends on the computational scheme. The additional operations performed for the calculation of the source terms have been found insignificant, which is the reason why all models get the same speedup for the same cell size, i.e. same number of cells. However, in Table 2.6 the coarse grid has 400 times less cells than the high-resolution grid causing a speedup of 70. In contrast, the coarse grid of Table 2.11 has roughly the same factor of decrease in cell numbers with respect to its high-resolution grid, however the speedup is 2520. The variation in the speedup might be related to the total duration of the simulation. As the decrease in cell numbers decreases the number of floating point operations per time step, the longer the simulation runs the higher the deviation between the walltime durations of both models becomes.

Another issue to be discussed is the calibration effort. While in general it can be assumed that the calibration effort increases with increasing

number of calibration parameters, the calibration effort is very dependent on the initial guess. The authors have shown in [113], that due to this dependency, sometimes models with three calibration parameters require less calibration steps than models with two parameters. However, in this work, the calibration of the constant Manning model with one parameter required significantly less calibration steps. This is also related to the optimization methods, because scalar functions can be optimized very efficiently while functions of higher dimension require more sophisticated and computationally demanding optimization methods. In the authors' opinion, the additional accuracy of the variable Manning or the proposed roughness approach outweighs the higher calibration effort. It should also be mentioned, that even if the calibration step is taken into account, the coarse grid simulations are faster than the high-resolution simulation in the investigated cases. Further, as seen in the last example, the high-resolution simulation itself needs to be calibrated for real case applications.

2.7 Conclusions

A novel conceptual roughness formulation for shallow water simulations on coarse grids was developed. The formulation is dependent on the inundation ratio, which is calculated using the standard deviation of the microtopography with regard to its mean value. A physical interpretation of the free parameters was given: the parameter C_0 is an increased Chézy coefficient, α_0 is an additional dimensionless roughness coefficient accounting for the microtopography and α_1 is a geometric conveyance parameter. The presented roughness formulation was then compared to several existing roughness formulations from literature. It was demonstrated in three computational examples, that high-resolution results can be approximated with satisfactory accuracy by calibrating the roughness formulation parameters. The exact values of the calibration parameters may vary in dependency of the numerical methods used to solve the equations, hence the optimized parameters reported in this study should be taken with caution.

The first example studied one-dimensional rainfall-runoff over a sine-wave shaped microtopography. The presented roughness approach returned the lowest root mean square deviation from the high-resolution model results. In the second example, calibrated parameters were transferred to different hydraulic conditions with some success. Varying the slope or the initial inundation increased the error for all models. The presented roughness formulation, together with the variable Manning's coefficient, resulted in the lowest root mean square deviations. It was shown that the proposed

roughness formulation can be calibrated more accurately than the variable Manning's coefficient formulation, however the latter showed a better calibration stability. In the last example, the proposed roughness approach was tested for a real case application. Here, again the presented roughness formulation and the variable Manning's coefficient approach were shown to be good trade-offs between accuracy and computational efficiency. It was shown that it is possible to upscale shallow water models using suitable roughness formulations. Due to mesh resolution effects [58, 160], the coarse grid models are not able to reproduce the high-resolution solutions exactly. In general, it can be concluded that accuracy increases with the number of free calibration parameters. However, as the number of parameters increases, the calibration process becomes more difficult. Using coarser grids resulted in a speedup between 20 and 2520. The reasons for the wide range of the speedup have been discussed. Overall, the proposed roughness approach is superior when compared to the other roughness approaches with respect to accuracy.

2.8 Acknowledgements

The authors thank the Alexander von Humboldt-Foundation for the Humboldt Research Fellowship granted to Dr. Dongfang Liang. Parts of the numerical simulations were computed on the supercomputers of Norddeutscher Verbund für Hoch- und Höchstleistungsrechnen in Berlin. The authors are grateful to Ulrich Razafison from Université de Franche-Comté, France for the correspondence on his shallow water model.

Chapter 3

Porosity-based coarse grid approach: mathematical model

Published as:
[110] Özgen, I., Liang, D., and Hinkelmann, R. (2016) Shallow water equations with depth-dependent anisotropic porosity for subgrid-scale topography. *Applied Mathematical Modelling* 40, pp. 7447–7473.
doi: 10.1016/j.apm.2015.12.012

This is the postprint version of the publication. The final publication is available at ScienceDirect via `https://doi.org/10.1016/j.apm.2015.12.012`.

3.1 Abstract

This paper derives a novel formulation of the depth-averaged shallow water equations with anisotropic porosity for computational efficiency reasons. The aim is to run simulations on coarser grids while maintaining an acceptable accuracy through the introduction of porosity terms, which account for subgrid-scale effects. The porosity is divided into volumetric and areal porosities, which are assigned to the cell volume and the cell edges, respectively. The former represents the volume in the cell available to flow and the latter represents the area available to flow over an edge, hence introducing anisotropy. The porosity terms are variable in time in dependence of the water elevation in the cell and the cumulative distribution function

of the unresolved bottom elevation. The main novelty of the equations is the formulation of the porosities which enables full inundation of the cell. The applicability of the equations is verified in five computational examples, dealing with dam break and rainfall-runoff simulations. Overall, good agreement between the model results and a high-resolution reference simulation has been achieved. The computational time decreased significantly: on average three orders of magnitude.

3.2 Introduction

Shallow water models are applied in a broad range of areas such as river hydraulics [111, 74, 82, 118], dam break simulations [165, 94], urban flooding [88, 90, 91, 119] and recently also for overland flow in natural catchments [26, 102, 23, 128, 154, 114] and urban runoff [16, 89], among many others (cf. e.g. [63]). In overland flow simulations, usually there is a large difference between the scales of the features significantly influencing the flow and the scale of the simulation domain. For example, in a natural catchment with a scale around a square kilometer, local depressions and microtopograpy with horizontal scales smaller than a square meter influence the flow field significantly [32, 6, 141]. Similar observations are made for urban flood models where the scale of buildings is exceeded by the scale of the city in several orders of magnitude, e.g. a building has a scale of around $100\,\mathrm{m}^2$ while the city may span up to $100\,\mathrm{km}^2$. Recent developments in survey technology such as light detection and ranging (LIDAR) and laser scanning are able to provide high accuracy high-resolution elevation data sets at relatively low cost [46]. However, the integration of these data into numerical models is often challenging because of finite computer resources [31, 97]. In order to capture the impact of the smallest relevant scale on the flow, the microtopography has to be explicitly discretized. This leads to meshes with small cell size and therefore high cell number which in return leads to an increased computational effort. Despite developments in CPU power, high-resolution simulations across large catchments are in practice often unfeasible without supercomputers [129].

Instead of explicitly discretizing the small-scale topography, its influence on the flow can be conceptually accounted for on coarser meshes to reduce the computational effort [33]. One such approach introduces a porosity term into the shallow water equations, which refers to the fraction of a computational cell available for flow and is a concept borrowed from groundwater flow modeling. The porosity then conceptually accounts for subgrid-scale topography. In literature, the extended shallow water equations incorporat-

ing this porosity are called shallow water equations with porosity or porous shallow water equations. The initial porous shallow water equations have been derived by Defina [26] to account for microtopography in overland flow. Later, the concept has been applied in urban flood modeling as a building treatment method [55, 51, 132, 18, 19, 20, 126]. These porous urban flood models use a single isotropic porosity to account for the buildings in the cell, assuming isotropic behaviour. The reason for this assumption is that the shallow water equations with single porosity are derived from the differential form of the classical shallow water equations using a representative elementary volume (REV) similar to the derivation of the Darcy flow equation in groundwater flow modeling, e.g. [3]. The REV is by definition isotropic and therefore only a single isotropic porosity can be derived for each cell (cf. [51]), which leads to the loss of directionality and hence may falsify the preferential flow paths. To the authors' knowledge, two approaches have been developed to overcome the loss of directionality and both have been developed for building treatment in urban flood models. The first approach has been developed by Guinot [48] and introduces multiple porosities in each cell, which account for different directions and storages. These porosities can be derived from the differential form of the shallow water equations without violating the continuum model and REV assumption. The second approach has been introduced by Sanders et al. [125]. This approach additionally assigns so-called areal or conveyance porosities to the cell edges, which introduce directionality to the equations. If the differential form of shallow water equations is used, these areal porosities can not be introduced without violating the REV assumption. Therefore, the integral form of the shallow water equations is used, as it does not require the assumption of an REV for the derivation. Yet, using the integral form of the shallow water equations means that only a finite volume method can be utilized for the numerical solution [48, 125]. Because these types of models are not isotropic anymore, they are referred to as anisotropic porosity shallow water models.

While there is ongoing research at the University of Liege to incorporate depth-dependent porosities into an urban flood model [10], the porous shallow water models for building treatment generally do not allow full inundation of the buildings. This is a valid assumption for urban flood modeling, however a porous shallow water model for generalized flow requires partial as well as full inundation of unresolved topography. Therefore, this paper examines the possibility of extending the equations derived in [125] to enable full inundation of the subgrid-scale unresolved topography to apply it to general surface flow modeling. This leads to a novel formulation of the porosities and the interfacial pressure terms and a mutual dependency between water elevation and porosity.

Finally, it should be noted that the shallow water equations with porosity can not reproduce a high-resolution solution exactly, because they can not resolve local details of the flow. However, the anisotropic porosity model has been found to be able to reproduce overall flow characteristics with satisfactory accuracy.

This paper is organized as follows: first the integral shallow water equations with anisotropic porosity are presented; then the numerical methods are discussed briefly; five computational examples are shown to demonstrate model capabilities; finally conclusions are given. In the following, the unresolved subgrid-scale topography features such as microtopography in overland flow modelling or buildings in urban flood modelling are referred to as unresolved solid structures or unresolved topography.

3.3 Governing equations

In this section, the integral shallow water equations with anisotropic porosity are derived for an arbitrary control volume. As aforementioned, the numerical solution of the shallow water equations in integral form is only possible with the finite volume method.

Anisotropic porosities

For the derivation of porosity, the phase function i inside a given control volume is introduced as

$$i\left(x,y\right)=\begin{cases}1, & \text{if } \eta\left(x,y\right)>z_b\left(x,y\right)\\ 0, & \text{else}\end{cases} \tag{3.1}$$

where η is the water elevation, z_b is the bottom elevation and x, y are the horizontal Cartesian coordinates. Figure 3.1 illustrates the water elevation η and bottom elevation in a vertical section through a control volume. For illustration purposes, i is evaluated in two points. If the bottom elevation exceeds the water elevation, i.e. dry case, the phase function is 0. If the water elevation exceeds the bottom elevation, i.e. wet case, the phase function equals 1. Therefore, the phase function indicates whether a certain point (x,y) in the control volume is wet or dry. Porosity is defined as the ratio of volume or area of fluid to the whole volume or area of the control volume. Then, the volumetric porosity ϕ is defined as

$$\phi=\frac{\int_\Omega i\left(\eta-z_b\right)d\Omega}{\int_\Omega\left(\eta-z_0\right)d\Omega} \tag{3.2}$$

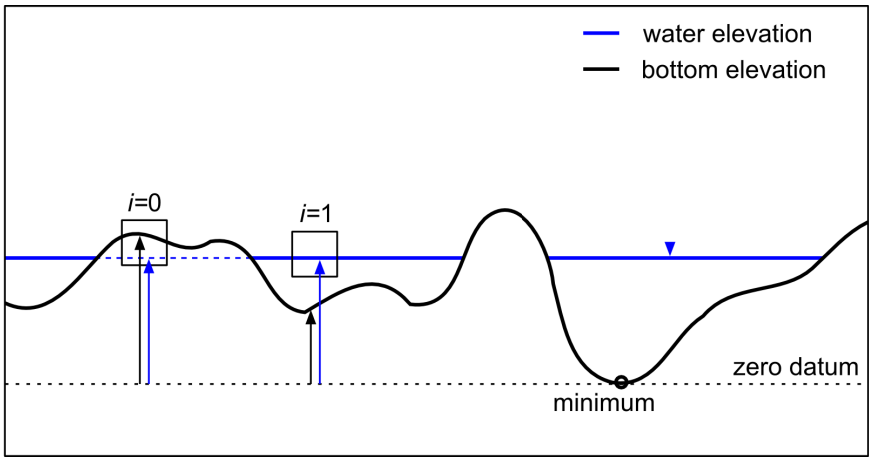

Figure 3.1: Definition of phase function i, water elevation η (blue), bottom elevation z_b (black) and zero datum z_0 (dashed) in a vertical section through a control volume

and the areal porosity ψ of the boundary of the control volume is defined as

$$\psi = \frac{\oint_{\partial\Omega} i\,(\eta - z_b)\,dr}{\oint_{\partial\Omega} (\eta - z_0)\,dr} \tag{3.3}$$

where Ω stands for the area of the control volume, $\partial\Omega$ stands for the boundary of the control volume, z_0 is the zero datum of the control volume (cf. Figure 3.1, dashed line) and r is the path along the boundary $\partial\Omega$. The values of the porosities depend on the zero datum z_0. Here, the lowest bed elevation inside the control volume (denoted as minimum in Figure 3.1) is chosen as the zero datum. This means, that in the finite-volume method the zero datum will vary for each cell.

Figure 3.2 shows an exemplary control volume with the definition of Ω and $\partial\Omega$. Figure 3.2 (left) shows a three-dimensional view of a partially inundated control volume, where blue colour indicates the water column and grey colour indicates bottom topography. Figure 3.2 (right) shows the top view of the control volume (top) and a vertical section through the boundary of the control volume denoted with (A-A') (bottom). Here, darker shades of grey indicate higher bottom elevation. Again, in each point where the water inundates the bottom topography the phase function $i = 1$ and at the points where the bottom topography elevation exceeds the water elevation $i = 0$. Both elevations are calculated with the minimum bottom elevation inside the control volume as the zero datum, which is marked in Figure 3.2 (left). The volumetric porosity ϕ is calculated with Equation

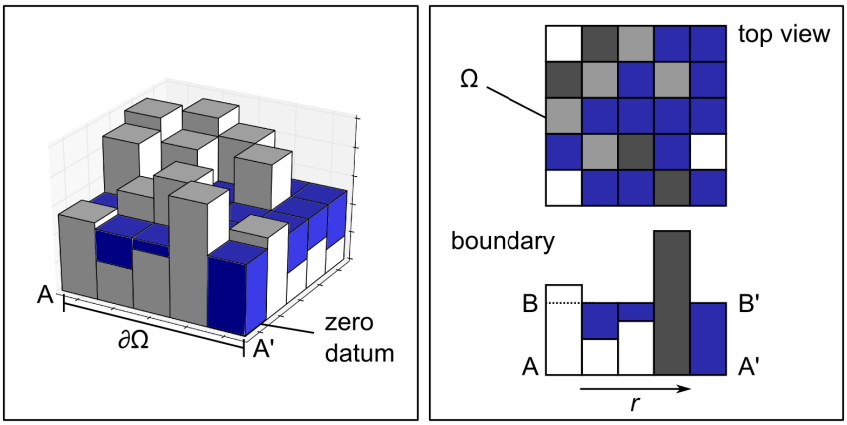

Figure 3.2: Definition of control volume area Ω, control volume boundary $\partial\Omega$ and path r in three dimensional view (left) top view and vertical section through the cell edge marked with A-A' (right)

3.2, and is the ratio of the volume of the fluid (blue columns) to the volume of the control volume. The volume of the control volume is calculated by multiplying the elevation of the water column, i.e. the distance (A'-B') in Figure 3.2 (right, bottom) with the total horizontal area of the cell Ω, shown in Figure 3.2 (right, top). For example, in the case illustrated in Figure 3.2, $\Omega = (\text{A-A'})^2$. Similarly, the areal porosity ψ is calculated as the ratio of the vertical area of the fluid at the boundary edge (coloured blue in Figure 3.2 (right, bottom)) to the vertical area of the boundary, described by the path (A-A'-B'-B) in Figure 3.2 (right, bottom).

It can be shown that the constant porosities derived in [125] can be obtained by simplifying Equations 3.2 and 3.3 (cf. 3.7). In contrast to these constant porosities, the porosities derived in this work are variable in time.

Integral-differential form of the shallow water equations with anisotropic porosity

The integral formulation of the shallow water equations can be obtained by applying the balance equation for mass and momentum to a fixed Eulerian control volume under the assumption of hydrostatic pressure distribution [56] (pp. 47 ff.). Prior to the integration, the conserved variables h, q_x and q_y are multiplied with the phase function i (Equation 3.1) to account for the unresolved topography. Then, the temporal change of the vector of

conserved variables $\mathbf{q}$ can be expressed as:

$$\frac{\partial}{\partial t}\int_{\Omega} i\mathbf{q}d\Omega + \oint_{\partial\Omega} i\mathbf{F}\mathbf{n}dr = \int_{\Omega} \mathbf{s}d\Omega + \oint_{\partial\Omega^*} \mathbf{s}^* dr \tag{3.4}$$

Here, t is the time and $\mathbf{s}$ is the source vector. $\mathbf{q}$ and $\mathbf{s}$ are usually expressed as:

$$\mathbf{q} = \begin{bmatrix} h \\ q_x \\ q_y \end{bmatrix}, \qquad \mathbf{s} = \begin{bmatrix} i_r \\ s_{b,x} + s_{f,x} \\ s_{b,y} + s_{f,y} \end{bmatrix} \tag{3.5}$$

where $h = \eta - z_b$ stands for water depth. q_x and q_y are the unit discharges in x- and y-direction, respectively. i_r is a mass source term, e.g. rainfall intensity; $s_{b,x}$, $s_{b,y}$, $s_{f,x}$, $s_{f,y}$ are the bed slope and the friction source terms in x- and y-direction, respectively, and are calculated as:

$$s_{b,x} = -gh\frac{\partial z_b}{\partial x}, \qquad s_{b,y} = -gh\frac{\partial z_b}{\partial y} \tag{3.6}$$

$$s_{f,x} = -c_f q_x \frac{\sqrt{q_x^2 + q_y^2}}{h^2}, \qquad s_{f,y} = -c_f q_y \frac{\sqrt{q_x^2 + q_y^2}}{h^2} \tag{3.7}$$

The slope source terms account for variations in bottom and the friction source terms account for the bottom roughness. c_f stands for the friction coefficient. $\mathbf{F}$ is the flux vector and can be expressed via $\mathbf{f}$ and $\mathbf{g}$ as

$$\mathbf{F}\mathbf{n} = \mathbf{f}n_x + \mathbf{g}n_y \tag{3.8}$$

where $\mathbf{n}$ is the unit normal vector to the boundary; n_x and n_y are its components and $\mathbf{f}$ and $\mathbf{g}$ are the flux vectors in x- and y-direction defined as

$$\mathbf{f} = \begin{bmatrix} q_x \\ uq_x + 0.5gh^2 \\ uq_y \end{bmatrix}, \qquad \mathbf{g} = \begin{bmatrix} q_y \\ vq_x \\ vq_y + 0.5gh^2 \end{bmatrix}. \tag{3.9}$$

Here, u and v are the depth-averaged velocity in x- and y-direction, respectively. g is the gravitational acceleration. $\mathbf{s}^*$ is the source vector accounting for fluid pressure along the interface between the fluid and solid $\partial\Omega^*$. It results from the macroscopic description, which does not differentiate between fluid and solid (cf. [5], pp. 200-201).

In the limit of no structures to account for, the phase function i returns 1, the integral along $\partial\Omega^*$ vanishes and therefore Equation 3.4 converges to the classical two-dimensional shallow water equations, which can be found in, e.g. [56] (p. 47). In [26], while properties of the differential form of the equations are discussed, it is argued that the equations may fail

to give a good approximation for very shallow flow, because some of the assumptions made for the derivation, e.g. a smooth free surface, do not hold. Although the assumptions made in deriving the integral form are not violated during very shallow flow, other statements made in [26] still apply and may lead to an inaccurate approximation. Namely, very shallow flow with partially dry area is dominated by the effects of bottom irregularities which direct most of water laterally which increases the flow path and the amount of dissipated energy [26]. If these bottom irregularities are only conceptually taken into account by using the porosity and the interfacial pressure terms, the model will not be able to reproduce the correct flow paths and may underestimate the dissipated energy. Unresolved topography which lies inside the computational cell can only be accounted for with the volumetric porosity. This is a limitation of the model, because directionality is introduced in the model in form of the areal porosities, to which the unresolved topography inside the cell can not contribute. Hence, structures which would have influenced the flow direction, e.g. roads and curbs, but lie completely inside the cell, will not effect the flow direction. As a result, their impact on the flow may be underestimated by the model.

Storage and flux terms

The porosity terms in Equation 3.2 and 3.3 are used to express discrete forms of the integral terms containing the phase function i.

The evaluation of the integral of $i\mathbf{q}$ in Equation 3.4 is considered. In the following, volume-averaged variables will be used to find a suitable approximation for this integral. The volume-averaged water elevation is calculated as:

$$\bar{\eta} = \frac{\int_\Omega i\eta d\Omega}{\int_\Omega i d\Omega} \tag{3.10}$$

The volume-averaged velocity is calculated as:

$$\bar{\mathbf{v}} = \frac{\int_\Omega ih\mathbf{v} d\Omega}{\int_\Omega ih d\Omega} \tag{3.11}$$

The volume-averaged variables are constant within the control volume Ω. Applying Equation 3.10 to Equation 3.2 and using $\eta - z_b = h$ leads to:

$$\phi = \frac{\int_\Omega i\,(\eta - z_b)\,d\Omega}{\int_\Omega (\eta - z_0)\,d\Omega} = \frac{\int_\Omega ih d\Omega}{\int_\Omega (\bar{\eta} - z_0)\,d\Omega} \tag{3.12}$$

As established above, $\bar{\eta}$ is constant inside the control volume. Hence, the expression $(\bar{\eta} - z_0)$ is also constant inside the control volume and can be

taken outside of the integration:

$$\phi = \frac{\int_\Omega i h d\Omega}{(\bar{\eta} - z_0) \int_\Omega d\Omega} = \frac{\int_\Omega i h d\Omega}{(\bar{\eta} - z_0)\,\Omega} \tag{3.13}$$

Then, Equation 3.13 can be rearranged to

$$\int_\Omega i h d\Omega = \phi\,(\bar{\eta} - z_0)\,\Omega, \tag{3.14}$$

which corresponds to the evaluation of the integral of the mass storage (first entry of $\mathbf{q}$) in Equation 3.4. The momentum storage in x-direction (second entry of $\mathbf{q}$) can be written by using $q_x = uh$ as:

$$\int_\Omega i q_x d\Omega = \int_\Omega i u h d\Omega \tag{3.15}$$

If the velocity u is approximated by the volume-averaged velocity, the equation becomes:

$$\int_\Omega i u h d\Omega \approx \int_\Omega i \bar{u} h d\Omega = \bar{u} \int_\Omega i h d\Omega \tag{3.16}$$

Then, Equation 3.13 can be used to write:

$$\bar{u} \int_\Omega i h d\Omega = \phi \bar{u}\,(\bar{\eta} - z_0)\,\Omega \tag{3.17}$$

The same derivation can be applied in y-direction (third entry of $\mathbf{q}$ in Equation 3.4) to get:

$$\int_\Omega i q_y d\Omega = \int_\Omega i v h d\Omega \approx \int_\Omega i \bar{v} h d\Omega = \bar{v} \int_\Omega i h d\Omega = \phi \bar{v}\,(\bar{\eta} - z_0)\,\Omega \tag{3.18}$$

The integral of $\mathbf{q}$ in Equation 3.4 can be replaced using Equations 3.13, 3.17 and 3.18 to write

$$\frac{\partial}{\partial t} \phi \Omega \bar{\mathbf{q}} + \oint_{\partial\Omega} i \mathbf{F} \mathbf{n} dr = \int_\Omega \mathbf{s} d\Omega + \oint_{\partial\Omega^*} \mathbf{s}^* dr, \tag{3.19}$$

where $\bar{\mathbf{q}}$ is the vector of volume-averaged variables:

$$\bar{\mathbf{q}} = \begin{bmatrix} (\bar{\eta} - z_0) \\ \bar{u}\,(\bar{\eta} - z_0) \\ \bar{v}\,(\bar{\eta} - z_0) \end{bmatrix} \tag{3.20}$$

The integral of $i\mathbf{Fn}$ in Equation 3.4 can be evaluated by defining the area-averaged variables. Here, the area under consideration ($\partial\Omega$) is the

boundary of the control volume. The closed curve integral of an arbitrary variable q can be splitted into integrals along n segments:

$$\oint_{\partial\Omega} q dr = \int_{j}^{j+1} q dr + \int_{j+1}^{j+2} q dr + ... + \int_{j+n}^{j} q dr \tag{3.21}$$

This is illustrated in Figure 3.3, where the black line denotes $\partial\Omega$ and the blue line denotes a piecewise linear approximation of it. The approximation is intentionally crude for a better illustration. In theory, the integration can be carried out on the splitted parts of $\partial\Omega$ (Figure 3.3, black line), however in a finite volume method context the integration is carried out on piecewise linear approximations of the boundary (Figure 3.3, blue line). The area-averaged variables are calculated as:

$$\hat{h} = \frac{\int_r ihdr}{\int_r idr} \tag{3.22}$$

$$\hat{\eta} = \frac{\int_r i\eta dr}{\int_r idr} \tag{3.23}$$

$$\hat{\mathbf{v}} = \frac{\int_r ih\mathbf{v}dr}{\int_r ihdr} \tag{3.24}$$

r is the path between two points on $\partial\Omega$, measured counter clockwise around $\partial\Omega$, e.g. the path between point j and $j+1$ in Figure 3.3 (marked with the index $k+1$). The relationship between $\partial\Omega$ and r is that $\partial\Omega$ is the sum of all paths r. $\hat{h}$ is the area-averaged water depth, $\hat{\eta}$ is the area-averaged water elevation and $\hat{\mathbf{v}} = (\hat{u}, \hat{v})$ is the area-averaged velocity vector. In a finite volume method, variables would be averaged per cell edge, thus the area would be the edge under consideration. Therefore, the term edge-averaged value is used interchangeably. To differentiate the area-averaged values from the volume-averaged values, the area-averaged values are denoted with a circumflex (hat), e.g. $\hat{h}$, and the volume averaged values are denoted with a bar, e.g. $\bar{h}$.

The flux term **Fn** in Equation 3.4 is:

$$\mathbf{Fn} = \begin{bmatrix} q_x n_x + q_y n_y \\ \left(uq_x + 0.5gh^2\right) n_x + vq_x n_y \\ uq_y n_x + \left(vq_y + 0.5gh^2\right) n_y \end{bmatrix} \tag{3.25}$$

Equation 3.3 can be rearranged to:

$$\int_r i\left(\eta - z_b\right) dr = \psi \int_r \left(\eta - z_0\right) dr \tag{3.26}$$

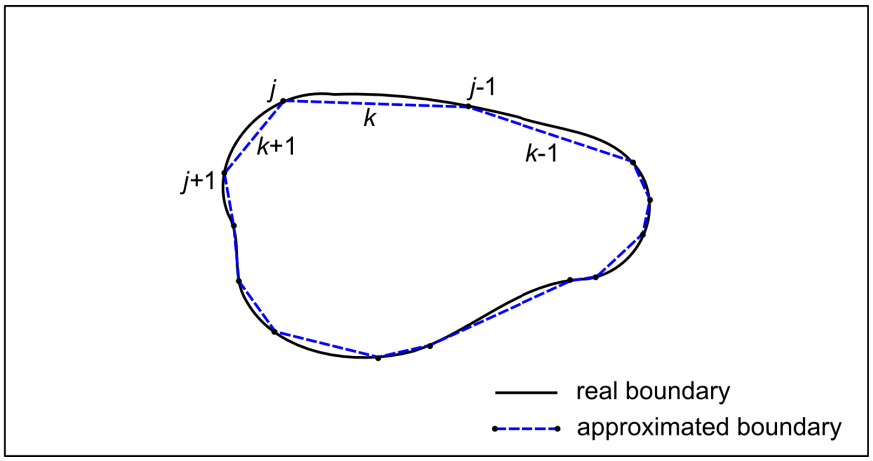

Figure 3.3: Definition of path index k and vertex index j: top view of an arbitrary control volume; black color indicates the exact boundary, blue color indicates the approximated boundary

Further, applying the relation $h = \eta - z_b$ and Equation 3.23 leads to:

$$\int_r ihdr = \psi \int_r (\hat{\eta} - z_0)\, dr = \psi\, (\hat{\eta} - z_0)\, r \tag{3.27}$$

Equation 3.24 in combination with Equation 3.27 can be rearranged to:

$$\int_\Omega ih\mathbf{v}dr = \hat{\mathbf{v}} \int_\Omega ihdr = \psi\hat{\mathbf{v}}\, (\hat{\eta} - z_0)\, r \tag{3.28}$$

This can be written in x- and y-direction as

$$\int_r ihudr = \psi\hat{u}\, (\hat{\eta} - z_0)\, r \tag{3.29}$$

and

$$\int_r ihvdr = \psi\hat{v}\, (\hat{\eta} - z_0)\, r, \tag{3.30}$$

respectively. Using $q_x = hu$ and $q_y = hv$, the integral of the mass flux (first entry of $\mathbf{Fn}$) is approximated as:

$$\int_r (q_x n_x + q_y n_y)\, dr = \psi\hat{u}\, (\hat{\eta} - z_0)\, r n_x + \psi\hat{v}\, (\hat{\eta} - z_0)\, r n_y \tag{3.31}$$

The momentum fluxes (second and third entries of $\mathbf{Fn}$) are approximated by using the area-averaged values $\hat{h}$, $\hat{u}$ and $\hat{v}$. In x-direction this results in:

$$\int_r \left(ih\hat{u}\hat{u}n_x + 0.5igh^2 n_x + ih\hat{v}\hat{u}n_y\right) dr \tag{3.32}$$

The area-averaged values are taken outside of the integral:

$$\hat{u}\hat{u}n_x \int_r ihdr + \int_r 0.5ig\hat{h}hn_x dr + \hat{v}\hat{u}n_y \int_r ihdr \tag{3.33}$$

Equation 3.27 can be used to rewrite Equation 3.32:

$$\hat{u}\hat{u}n_x\psi\left(\hat{\eta}-z_0\right)r + 0.5g\hat{h}n_x\psi\left(\hat{\eta}-z_0\right)r + \hat{v}\hat{u}n_y\psi\left(\hat{\eta}-z_0\right)r \tag{3.34}$$

The approximation of the momentum flux in y-direction is straight forward. Using Equation 3.21 to replace the closed curve integral, Equation 3.19 is rewritten as

$$\frac{\partial}{\partial t}\phi\Omega\bar{\mathbf{q}} + \sum_k \psi_k r_k \hat{\mathbf{F}}_k \mathbf{n}_k = \int_\Omega \mathbf{s}d\Omega + \oint_{\partial\Omega^*} \mathbf{s}^* dr, \tag{3.35}$$

where k is the index of the path integral. The vector $\hat{\mathbf{F}}\mathbf{n}$ is written as:

$$\hat{\mathbf{F}}\mathbf{n} = \begin{bmatrix} \hat{u}\left(\hat{\eta}-z_0\right)n_x + \hat{v}\left(\hat{\eta}-z_0\right)n_y \\ \hat{u}\hat{u}\left(\hat{\eta}-z_0\right)n_x + 0.5g\hat{h}\left(\hat{\eta}-z_0\right)n_x + \hat{u}\hat{v}\left(\hat{\eta}-z_0\right)n_y \\ \hat{v}\hat{u}\left(\hat{\eta}-z_0\right)n_x + \hat{v}\hat{v}\left(\hat{\eta}-z_0\right)n_y + 0.5g\hat{h}\left(\hat{\eta}-z_0\right)n_y \end{bmatrix} \tag{3.36}$$

Solid-fluid interfacial pressure source term

$\partial\Omega^*$ is the interface between fluid and solid, denoted with blue lines in Figure 3.4, where the top view of a square-shaped control volume is given. The dashed black line shows the boundary of the control volume ($\partial\Omega$) and the grey blocks represent single elements of simplified structures, e.g. buildings. Representing the unresolved fluid pressure at the interface $\partial\Omega^*$, $\mathbf{s}^*$ consists of two components; the stationary component $\mathbf{s}^*_{st}$ which can be calculated if hydrostatic pressure distribution at the interface is assumed and the non-stationary component $\mathbf{s}^*_{ns}$ which accounts for drag effects of the unresolved structures [125]:

$$\oint_{\partial\Omega^*} \mathbf{s}^* dr = \oint_{\partial\Omega^*} \mathbf{s}^*_{st} dr + \int_\Omega \mathbf{s}^*_{ns} d\Omega \tag{3.37}$$

While the stationary component $\mathbf{s}^*_{st}$ acts along the interface $\partial\Omega^*$, the non-stationary component acts on the whole control volume Ω.

In theory, the calculation of the stationary component $\mathbf{s}^*_{st}$ is straightforward. Figure 3.5 shows a vertical section through a control volume and the two possible cases of submergence: partially submerged (left) and fully submerged (right). If these cases are considered separately and hydrostatic

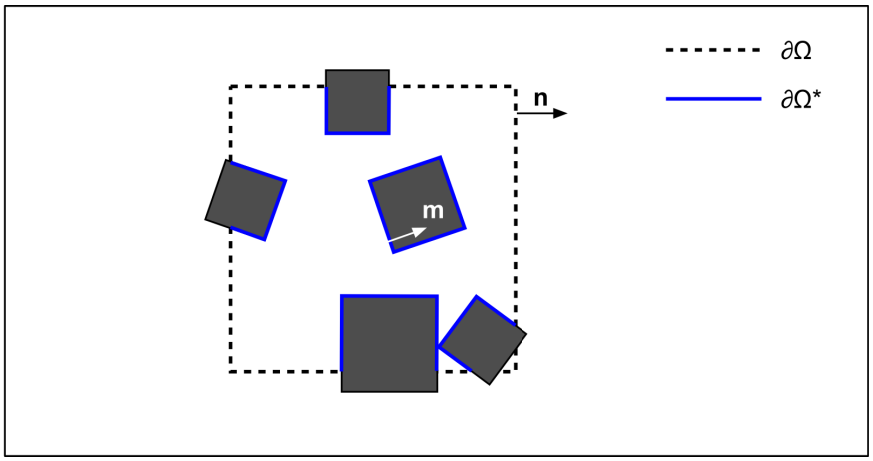

Figure 3.4: Definition of the interface $\partial\Omega^*$ (blue); grey blocks represent elements of microtopography

pressure is assumed, the pressure of the fluid on the solid p^* can be written as

$$p^*(x,y) = \begin{cases} 0.5\,g\,(\eta - z_b)^2 & \text{if } \eta(x,y) \leq z_b^* \\ 0.5\,g\,((\eta - z_b^*) + (\eta - z_b))\,(z_b^* - z_b) & \text{else} \end{cases} \tag{3.38}$$

where z_b^* is the bottom elevation of the microtopgraphy that the fluid pressure is acting on (cf. Figure 3.5). If $\mathbf{m} = (m_x, m_y)$ is the unit normal vector along $\partial\Omega^*$, which points inside the solid structure as illustrated in Figure 3.4, the stationary component of the interfacial pressure source term can be written as:

$$\mathbf{s}_{st}^* = \begin{bmatrix} 0 \\ p^* m_x \\ p^* m_y \end{bmatrix} \tag{3.39}$$

The difficulty in the calculation of $\mathbf{s}_{st}^*$ is that the interface between solid and fluid $\partial\Omega^*$ is unknown because it is not resolved. Therefore, the stationary term can not be solved exactly and has to be approximated. One approach to estimate $\mathbf{s}_{st}^*$ can be found in [125].

The non-stationary component of Equation 3.37 essentially accounts for drag which occurs during the flow through the unresolved structures, e.g. buildings or microtopography, as the fluid moves between the single elements of the structure. Because it occurs at unresolved scales, the drag force can not be calculated. In [125], a generalized drag law is suggested to

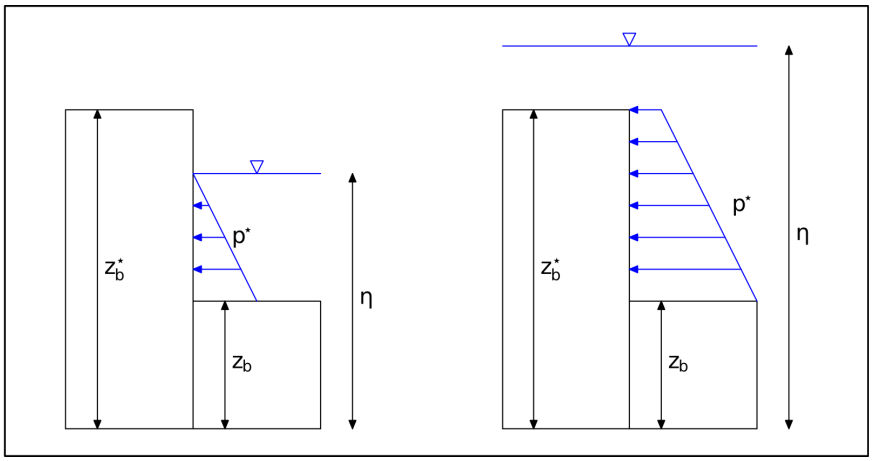

Figure 3.5: Definition of p^* and z_b^*; partially submerged control volume (left), fully submerged control volume (right): blue color indicates the water column

approximate this term as:

$$\mathbf{s}_{ns}^* = \begin{bmatrix} 0 \\ c_D u|\mathbf{v}| \\ c_D v|\mathbf{v}| \end{bmatrix} \tag{3.40}$$

Here, $|\mathbf{v}|$ is the Euclidian norm of the vector of velocities $\mathbf{v} = (u, v)$ and c_D is a dimensionless drag coefficient. The determination of c_D is challenging, often requires a calibration process and has not been fully understood yet. Several approaches have been suggested to overcome this difficulty. In [125], it is acknowledged that the drag effect may be estimated by an increased roughness coefficient as demonstrated in [88]. In [26], momentum correction terms are calculated which depend on the volumetric porosity and a so-called effective water depth, which is the water volume per unit area. Also, different methods with varying complexity for estimating c_D have been presented in [55, 51, 132, 125]. In [125], a vegetative resistance model as proposed in [107] is used to estimate c_D. In this study, the drag force approach is used, because it is commonly used and studied in literature, e.g. [55, 51, 132, 125]. Here, the drag force approach of [107] is slightly modified to allow the full submergence of the control volume. Then, c_D is calculated as:

$$c_D = 0.5\, c_D^0\, a \cdot \min\left(h, z_b^* - z_b\right) \tag{3.41}$$

Here, a is the horizontally projected area of the elements of the solid structure per unit volume in one cell and c_D^0 is a bulk drag coefficient accounting

for the whole solid structure (cf. [107]) and min is the minimum function. A similar approach is given in [55] to account for inundated subgrid-scale structures. Both a and c_D^0 are not fully understood yet [125], they depend on the configuration of the solid structures as well as the shape of single elements, flow direction and several other factors which have yet to be identified. Therefore, in this work the model is calibrated with the product $c_D^0 \cdot a$ as a whole. Hence, both a and c_D^0 lose their strict physical interpretations and become calibration parameters.

3.4 Numerical method and computational examples

The numerical solution of Equation 3.35 can only be achieved with the finite volume method, as the equation does not contain spatial differential expressions. Numerical studies of the authors have shown that a second order reconstruction of the bottom elevation is necessary to obtain accurate results, especially in sloped domains (cf. [128]). Further, a second-order accurate scheme allows to compensate to some degree the loss of accuracy in the approximation due to coarse cells in the anisotropic porosity model. Thus, for the following computational examples, the presented equations are solved with a second-order monotonic upstream-centered scheme for conservation laws (MUSCL) presented in [60] being used for both the anisotropic porosity model and the high-resolution model. It is acknowledged that the high-resolution model is suffering more from the additional calculations per cell associated with the second order reconstruction process in comparison to the anisotropic porosity model. A two-step explicit Runge-Kutta method is used to advance in time [99]. The numerical scheme is implemented in the Hydroinformatics Modeling System (hms), an in-house scientific programming framework [128].

Calculation of porosities

Similar to [26], it is suggested to calculate the porosities ϕ and ψ with statistical properties of the unresolved subgrid-scale features of the topography.

In a preprocessing step, the bottom elevation in each computational cell is sampled on a finer scale such that the discrete cummulative distribution function (CDF) can be calculated individually in each cell. The CDF can then be used at the beginning of each time step to evaluate how many of the samples are submerged by the water depth inside the cell. Basically, the

CDF is used as a structure to store the different bottom elevations mapped to the number of their occurences.

For example, let the computational cell have a CDF based on 25 samples of bottom elevation inside the cell. It is assumed that each sample corresponds to an equal area inside the cell. For sake of simplicity, let 10 of the samples have a bottom elevation of 0, let 10 of the samples have a bottom elevation of 0.2 m and let 5 of the samples have a bottom elevation of 0.4 m. Then, the zero datum in the cell is defined as 0 and the water depth h in the cell corresponds to the water elevation η as $h = \eta - 0 = \eta$. Further, assume the water depth is $h = 0.1\,\mathrm{m}$. The volume of the water inside the cell corresponds to $V_w = 10 \cdot 0.1 \cdot c$, where c is the area of one sample. The total volume is $V_t = 25 \cdot 0.1 \cdot c$. Then, the volumetric porosity is calculated as $\phi(h = 0.1) = V_w/V_t = 10/25$.

If the water depth rises to $h = 0.3\,\mathrm{m}$, the volume of water becomes $V_w = 10{\cdot}0.3{\cdot}c{+}10{\cdot}(0.3{-}0.2){\cdot}c$, and the total volume becomes $V_t = 25{\cdot}0.3{\cdot}c$. Hence, the volumetric porosity is calculated as $\phi(h = 0.2) = V_w/V_t = 40/75$.

The same approach is applied to calculate areal porosities.

Error and speedup calculation

In the following, computational examples are presented to evaluate the capability of the equations. To the authors' knowledge, no analytical solutions for the shallow water equations with anisotropic porosity have been reported in literature. The shallow water equations with isotropic porosity in [26] are compared with large-scale real case applications. The analytical and semi-analytical solutions presented in [51] are valid for isotropic porosity only. In [125], the anisotropic porosity model results are compared with measurement data.

Therefore, in this work four examples are presented where the high-resolution shallow water model (HR) results are considered to be the reference solution. In a final example, the anisotropic porosity model (AP) results are compared with measurement data. The resolution of the HR model is always chosen such that further refinement does not change the result. Turbulence and fluid viscosity are neglected in all test cases.

In order to assess the quality of the model results, the L_1-norm, defined as

$$L_1 = \frac{1}{N} \sum_{i}^{N} |x_i - \dot{x}_i| \tag{3.42}$$

is used, where N stands for the total number of solutions, x_i is the reference solution, $\dot{x}_i$ is the model solution and i is the sample index.

The computational benefit of the anisotropic porosity model is quantified using the speedup, defined as

$$\zeta = \frac{t_{\mathrm{HR}}}{t_{\mathrm{AP}}} \tag{3.43}$$

whereby t_{HR} and t_{AP} are the wall-times of the HR model and the AP model, respectively.

One-dimensional dam break on dry bed with sine-wave shaped microtopography

In this computational example, a one-dimensional dambreak on dry bed is simulated. The domain is 6 m long, 0.5 m wide and the initial water elevation is defined as:

$$\eta(x) = \begin{cases} \eta_0, & x \leq 3\,\mathrm{m} \\ z_b(x), & x > 3\,\mathrm{m} \end{cases} \tag{3.44}$$

η_0 stands for the initial water elevation and is varied from 0.025 m to 0.06 m for different simulation runs. The bottom elevation of the domain is described with a sine-wave as:

$$z_b(x) = A \sin\left(\frac{2\pi}{\lambda}x + \frac{\pi}{2}\right) + 0.01 \tag{3.45}$$

Here, λ is the wavelength and A is the amplitude of the sine-wave. In this example they are set to $\lambda = 0.05\,\mathrm{m}$ and $A = 0.01\,\mathrm{m}$. Figure 3.6 (left) shows the initial conditions for $\eta_0 = 0.03\,\mathrm{m}$. Only the section from $2.5\,\mathrm{m} < x < 3.5\,\mathrm{m}$ is plotted because the small wavelength of the sine-wave makes it difficult to illustrate the bottom elevation over the whole domain. At the outlet of the domain at $x = 6\,\mathrm{m}$, an open boundary forcing the water elevation gradient to zero is set. All other boundaries are closed boundaries. Bottom roughness is accounted for with a Manning's coefficient of $n = 0.016\,\mathrm{sm}^{-1/3}$.

The reference solution is obtained by using a classical shallow water model with an element size of $\Delta x = 0.01\,\mathrm{m}$ (HR model). As shown in Figure 3.6 (right), this resolution is sufficient to explicitly discretize the bottom elevation (Equation 3.45). In contrast, the model with anisotropic porosities (AP model) uses a mesh with element size of $\Delta x = 0.1\,\mathrm{m}$. Figure 3.6 (right) shows exactly one computational cell of the AP model and the bottom topography inside it. The resolution of the AP model's mesh is not sufficient to explicitly discretize the sine-wave, therefore the bottom

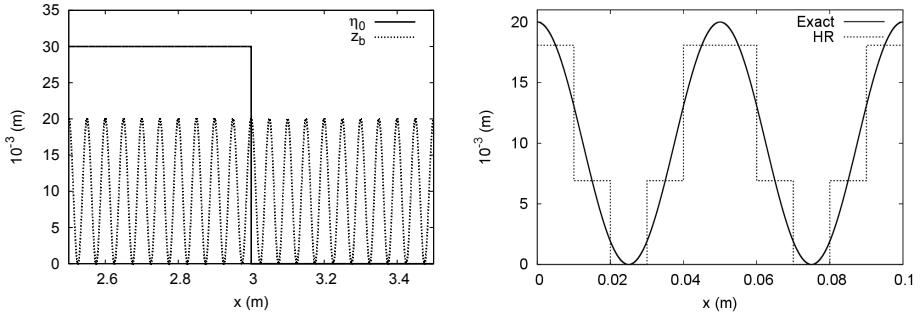

Figure 3.6: Dam break on dry bed with sine-wave shaped microtopography: Initial conditions for $\eta_0 = 0.03\,\mathrm{m}$ (left); bottom elevation distribution inside one AP model cell and the HR model discretization (dashed lines) (right)

elevation is described by $z_b(x) = 0\,\mathrm{m}$. A classical shallow water model (SWE model) with the same resolution as the AP model is used to illustrate the effect of the AP model. Good agreement between the HR model and the AP model is achieved for $c_D^0 \cdot a = 10\,\mathrm{m}^2$ as shown in Figure 3.7 and 3.8. In [125], $c_D^0 = 2$ is recommended but values up to $c_D^0 = 6$ have been reported (M. Bruwer, personal communication, 24 March 2015) which shows that this value has an uncertainty. The results for water elevation, velocity and unit discharge are plotted on the left side in Figure 3.7 (top, middle and bottom, respectively). The fluctuations in the HR model solution are due to the sine-wave shaped microtopography as the water accelerates when flowing down the sine-wave and decelerates when climbing up the crests of the sine-wave. The SWE model shows poor agreement in all cases. The AP model captures the advance of the front correctly and the obstructive effects of the microtopography could be reproduced well (Figure 3.7 (top left)). The velocity is underestimated between $0 < x < 1\,\mathrm{m}$ and slightly overestimated between $1\,\mathrm{m} < x < 4\,\mathrm{m}$ (Figure 3.7 (middle left)). The unit discharge behaves similar as the velocity (Figure 3.7 (bottom left)). Water elevation, velocity and unit discharge are all captured well. On the right side in Figure 3.7, the sensitivity of $c_D^0 \cdot a$ is illustrated. The product $c_D^0 \cdot a$ is varied from 0 to $500\,\mathrm{m}^2$. As $c_D^0 \cdot a$ increases, the roughness of the model increases. The AP model is sensitive with regard to $c_D^0 \cdot a$ until a critical value of about $c_D^0 \cdot a = 500\,\mathrm{m}^2$ is reached. It was observed that for $c_D^0 \cdot a > 500\,\mathrm{m}^2$ this parameter is not very sensitive. This is because after reaching a certain value, friction is artificially limited in the numerical scheme to avoid velocities to change direction. For details on this friction treatment, the reader is referred to [93].

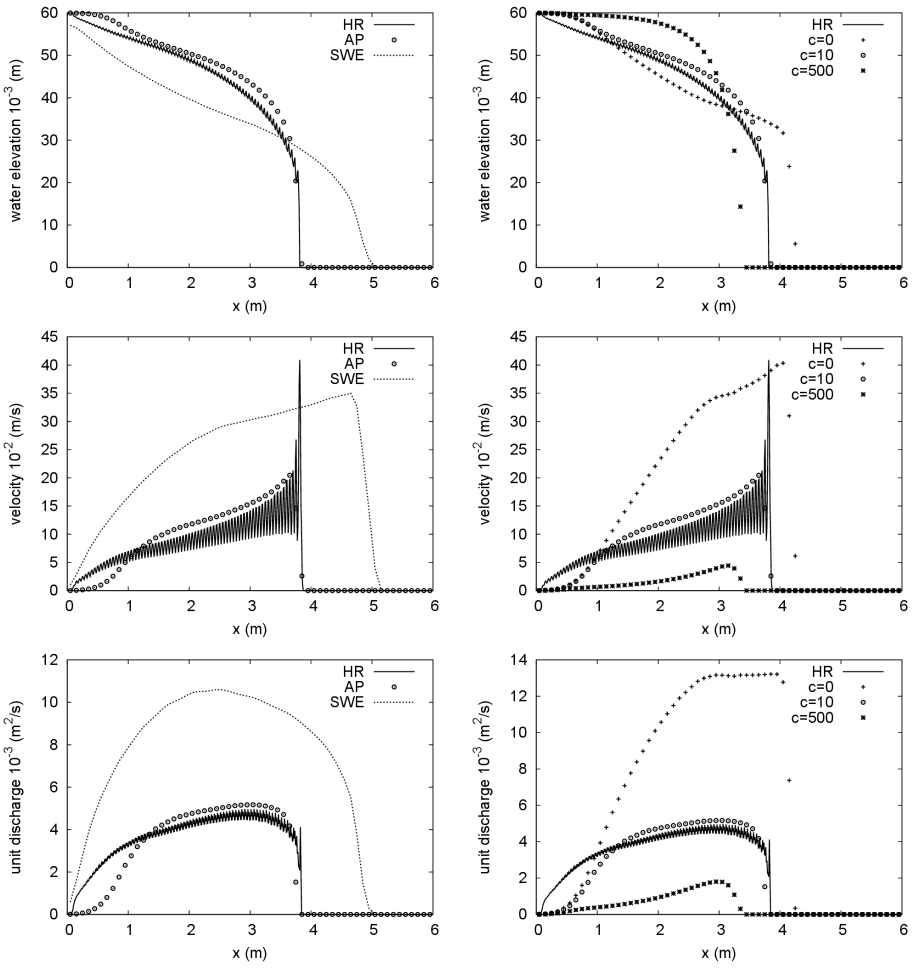

Figure 3.7: Dam break on dry bed with sine-wave shaped microtopography: Comparison of model results at $t = 4\,\mathrm{s}$ with $\eta_0 = 0.06\,\mathrm{m}$ (the anisotropic porosity model (AP), the high-resolution reference solution (HR) and a coarse grid classical shallow water model (SWE)) (left), sensitivity study of $c_D^0 \cdot a$ (denoted as c) (right)

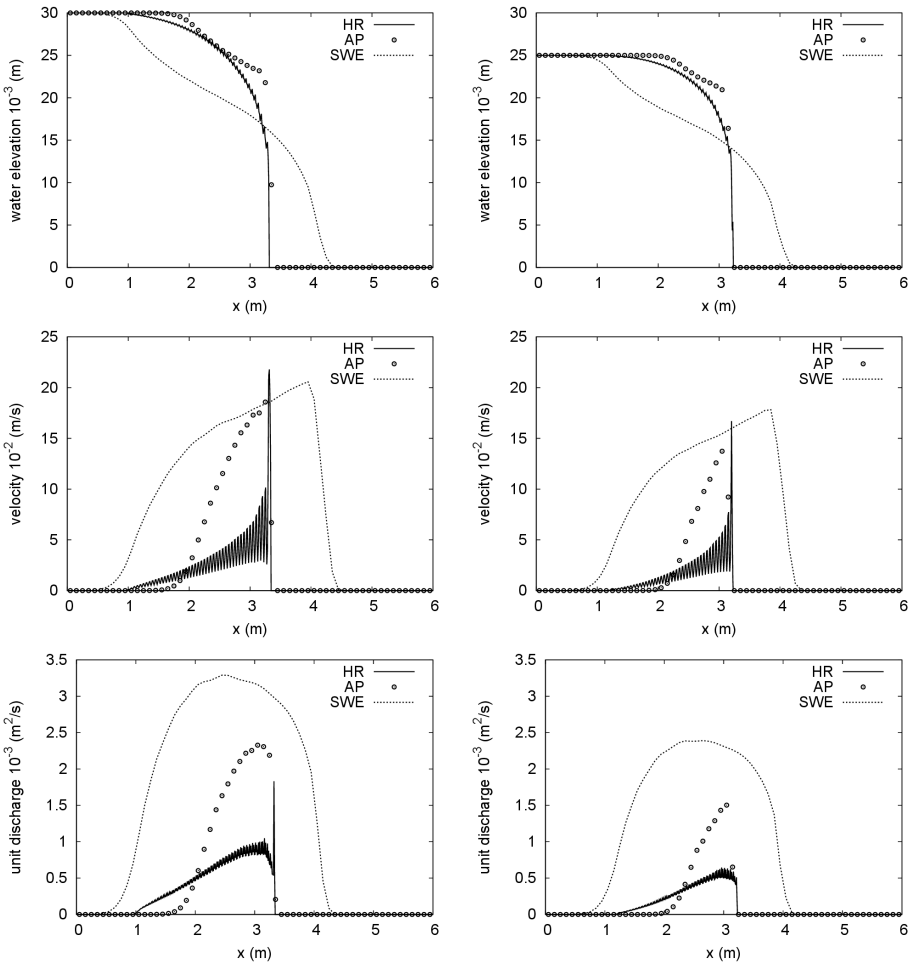

Figure 3.8: Dam break on dry bed with sine-wave shaped microtopography: Comparison of model results at $t = 4\,\mathrm{s}$ with $\eta_0 = 0.03\,\mathrm{m}$ (left) and $\eta_0 = 0.025\,\mathrm{m}$ (right) (the anisotropic porosity model (AP), the high-resolution reference solution (HR) and a coarse grid classical shallow water model (SWE))

$\eta\,(\mathrm{m})$	$L_{1,AP}(\eta)\,(\mathrm{m})$	$L_{1,SWE}(\eta)\,(\mathrm{m})$
0.025	$3.8 \cdot 10^{-4}$	$28 \cdot 10^{-4}$
0.03	$6.4 \cdot 10^{-4}$	$34 \cdot 10^{-4}$
0.06	$15 \cdot 10^{-4}$	$76 \cdot 10^{-4}$

Table 3.1: Dam break on dry bed with sine-wave shaped microtopography: L_1-error for water elevation as calculated by the anisotropic porosity model (AP) and the coarse shallow water model (SWE)

$\eta\,(\mathrm{m})$	$L_{1,AP}(v)\,(\mathrm{m/s})$	$L_{1,SWE}(v)\,(\mathrm{m/s})$
0.025	$0.8 \cdot 10^{-2}$	$5.7 \cdot 10^{-2}$
0.03	$1.6 \cdot 10^{-2}$	$7 \cdot 10^{-2}$
0.06	$1.2 \cdot 10^{-2}$	$13.8 \cdot 10^{-2}$

Table 3.2: Dam break on dry bed with sine-wave shaped microtopography: L_1-error for velocity as calculated by the anisotropic porosity model (AP) and the coarse shallow water model (SWE)

$\eta\,(\mathrm{m})$	$L_{1,AP}(q)\,(\mathrm{m^2/s})$	$L_{1,SWE}(q)\,(\mathrm{m^2/s})$
0.025	$1.0 \cdot 10^{-4}$	$8.6 \cdot 10^{-4}$
0.03	$2.6 \cdot 10^{-4}$	$12 \cdot 10^{-4}$
0.06	$4.9 \cdot 10^{-4}$	$44 \cdot 10^{-4}$

Table 3.3: Dam break on dry bed with sine-wave shaped microtopography: L_1-error for unit discharge as calculated by the anisotropic porosity model (AP) and the coarse shallow water model (SWE)

The initial water elevation η_0 is varied to 0.025 m and 0.03 m to study the influence of the water elevation. Figure 3.8 (left) and Figure 3.8 (right) show that the solution is enhanced by the AP model for different initial water elevations. In both cases, the overestimation of the velocity and the discharge is higher than for $\eta_0 = 0.06\,\mathrm{m}$. It is noted, that the drag coefficient $c_D^0 \cdot a = 10\,\mathrm{m}^2$ is kept constant for these simulations. Case specific calibration might further enhance the solution. The L_1-error for the presented cases is summarised in Table 3.1, 3.2 and 3.3 for water elevation, velocity and discharge. For all variables, the L_1-error of the SWE model is about one order of magnitude higher than the AP model error. The computation with the AP model was carried out approximately 1000 times faster than with the HR model.

Two-dimensional dam break across a porosity discontinuity

The following example simulates a two-dimensional dam break across a porosity discontinuity on a 100 m × 10 m domain. This example was initially introduced in [51] as a one-dimensional benchmark for the shallow water model with isotropic porosity and a quasi-analytical solution for the one-dimensional case was derived. This solution is not valid for the two-dimensional case, therefore the results of the anisotropic porosity model (AP) is compared with a high-resolution shallow water model (HR). The computational domain is illustrated in Figure 3.9 (left). The discontinuity of the porosity as well as the discontinuity of the water elevation is located at $x = 50\,\mathrm{m}$:

$$\eta_0(x,y) = \begin{cases} 2\,\mathrm{m}, & x \leq 50\,\mathrm{m} \\ 1\,\mathrm{m}, & x > 50\,\mathrm{m} \end{cases} \qquad \phi_0(x,y) = \begin{cases} 1, & x \leq 50\,\mathrm{m} \\ 0.8, & x > 50\,\mathrm{m} \end{cases} \tag{3.46}$$

At the outlet $x = 100\,\mathrm{m}$, an open boundary forcing the water elevation gradient to zero is set. All other boundaries are closed wall boundary conditions. The porosity jump is constructed via randomly generated obstacles which are explicitly discretized in the HR model and are taken into account by the porosities in the AP model. All obstacles are square shaped with an edge length of 0.1 m and with infinitive vertical height and are spatially distributed according to a random uniform distribution such that each cell of the AP model has a volumetric porosity of $\phi = 0.8$ for $x > 50\,\mathrm{m}$ as illustrated in Figure 3.9 (right) for one exemplary cell. During the whole simulation, the obstacles are never fully inundated, which means that the volumetric porosity stays constant in each cell. The simulation is run for $t = 4\,\mathrm{s}$. The HR model is calculated on a grid with square-shaped elements with an edge length of 0.02 m. The AP model uses a computational grid with square-shaped elements with an edge length of 0.5 m. $c_D^0 \cdot a = 10\,\mathrm{m}^2$ is chosen for the AP model. Bottom roughness in both models is taken into account by a Manning's coefficient of $n = 0.016\,\mathrm{sm}^{-1/3}$.

Results for water elevation and unit discharge at different longitudinal sections at $t = 4\,\mathrm{s}$ are plotted in Figure 3.10 (left) and Figure 3.10 (right), respectively. L_1-errors for water elevation and unit discharge at the sections are given in Table 3.4. The AP model results show good agreement with the reference solution calculated by the HR model. After the dam break at $x = 50\,\mathrm{m}$, the rarefaction wave traveling in upstream direction as well as the shock wave travelling in flow direction are captured well, although at about $x = 30\,\mathrm{m}$ the water elevation is underestimated in all sections. The fluctuation of the water elevation, which results from the superposition

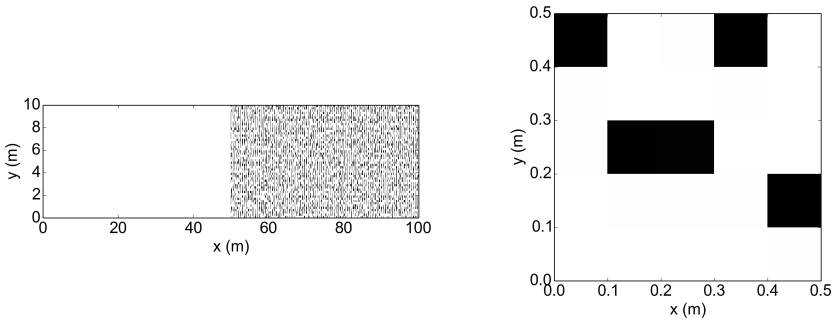

Figure 3.9: Dam break across a porosity discontinuity: Top view on the computational domain (left); top view on an exemplary computational cell of the AP model (right), black color indicates the location of obstacles

y (m)	$L_1(\eta)$ (m)	$L_1(q)$ (m^2/s)
0.525	$8.1 \cdot 10^{-3}$	$5.3 \cdot 10^{-2}$
1.455	$7 \cdot 10^{-3}$	$3.9 \cdot 10^{-2}$
2.25	$7.4 \cdot 10^{-3}$	$5.3 \cdot 10^{-2}$

Table 3.4: Dam break on dry bed across a porosity discontinuity: L_1-error for water elevation and unit discharge

of waves due to the obstacles, calculated by the HR model can not be reproduced by the AP model. The unit discharge is captured very well by the AP model (Figure 3.10 (right)). The discretized obstacles in the HR model narrow the cross section available to flow and lead to a high localized flow velocity and therefore a high unit discharge. This can not be reproduced by the AP model. As pointed out in [51], this is not a failure of the AP model, but is a consequence of the macroscopic modeling using the porosity concept. The AP model results were computed roughly 3000 times faster than the HR model results.

Two-dimensional dam break on dry bed with random microtopography

This example considers a two-dimensional dam break on dry bed with random microtopography. The domain spans 6 m in x-direction and 3 m in

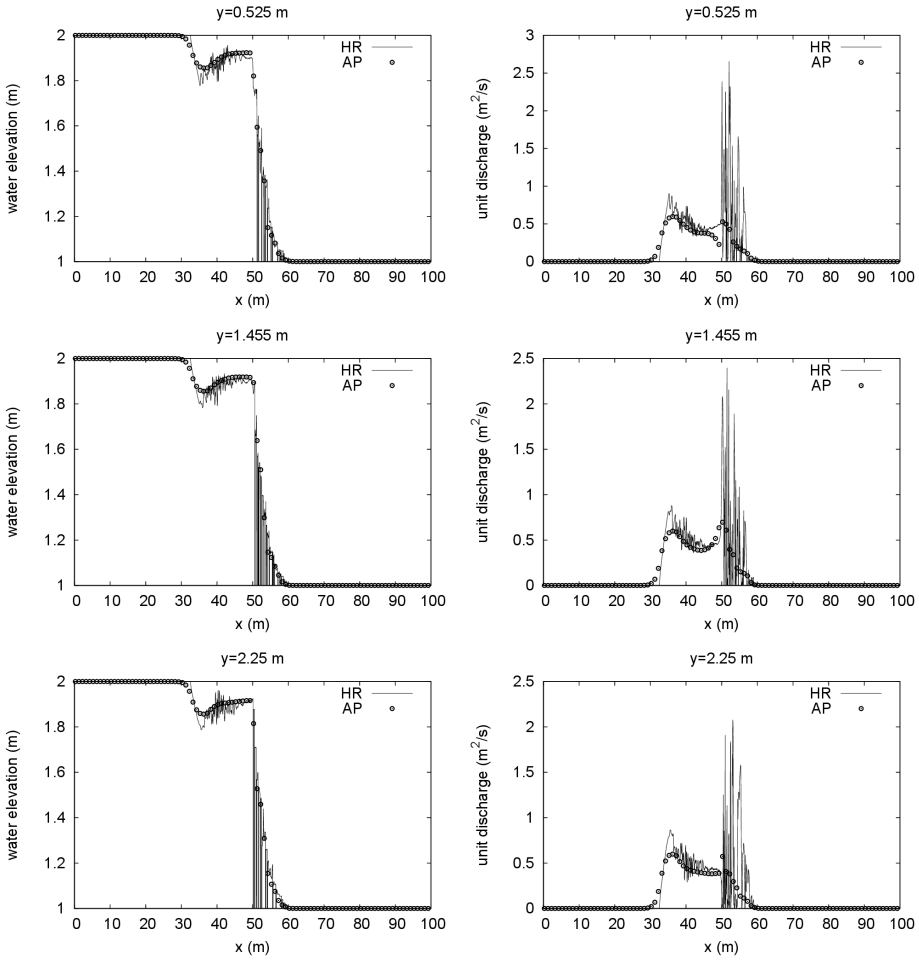

Figure 3.10: Dam break across a porosity discontinuity: Water elevation (left) and unit discharge (right) at $t = 4\,\mathrm{s}$ for different longitudinal sections for the anisotropic porosity model (AP) and the high-resolution reference solution (HR)

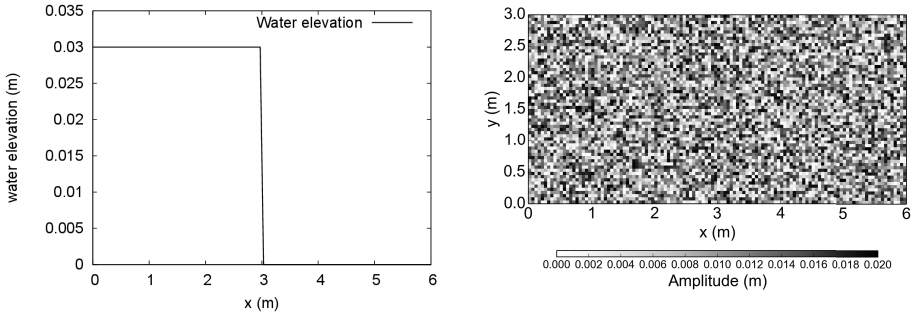

Figure 3.11: Dam break on bed with random microtopography: Initial conditions (left); microtopography in the domain (right)

y-direction. The water elevation is defined as:

$$\eta(x) = \begin{cases} 0.03\,\mathrm{m}, & x \leq 3\,\mathrm{m} \\ z_b(x,y), & x > 3\,\mathrm{m} \end{cases} \tag{3.47}$$

The microtopography is generated as square-shaped deviations with an edge length of 0.05 m, and their amplitudes $z_{b,mic}$ are distributed between 0 and 0.02 m according to a Gaußian distribution function as illustrated in Figure 3.11 (right). All boundaries are closed except at the right side of the domain ($x = 6\,\mathrm{m}$), where an open boundary condition as in previous the example is applied. A reference solution is computed with a shallow water model on a $0.01\,\mathrm{m} \times 0.01\,\mathrm{m}$ grid (HR). The anisotropic porosity model uses square grid cells with an edge length of 0.1 m (AP). The bottom friction is expressed via a Manning coefficient $n = 0.016\,\mathrm{sm}^{-1/3}$. The drag force of the AP model is estimated with the product $c_D^0 \cdot a = 10\,\mathrm{m}^2$. The simulation runs for $t = 2\,\mathrm{s}$.

Results for water depth at different sections through different y-values are plotted in Figure 3.12. Here, dry cells are not plotted for the HR model. The L_1-errors for water elevation and velocity at different times are given in Table 3.5 and 3.6. The AP model shows very good agreement with the HR model. The shock is captured with satisfactory accuracy at all times, however local details of the water elevation variation such as small scale fluctuations due to the microtopography can not be captured.

Velocity profiles through the same sections as in Figure 3.12 are plotted in Figure 3.13. Although the maximum values of the velocity profiles are not reproduced by the AP model, overall good agreement between the HR model and the AP model is observed.

Figure 3.14 shows a topview on the water elevation distribution in the domain at the same time steps as in Figure 3.12 for the HR model (left)

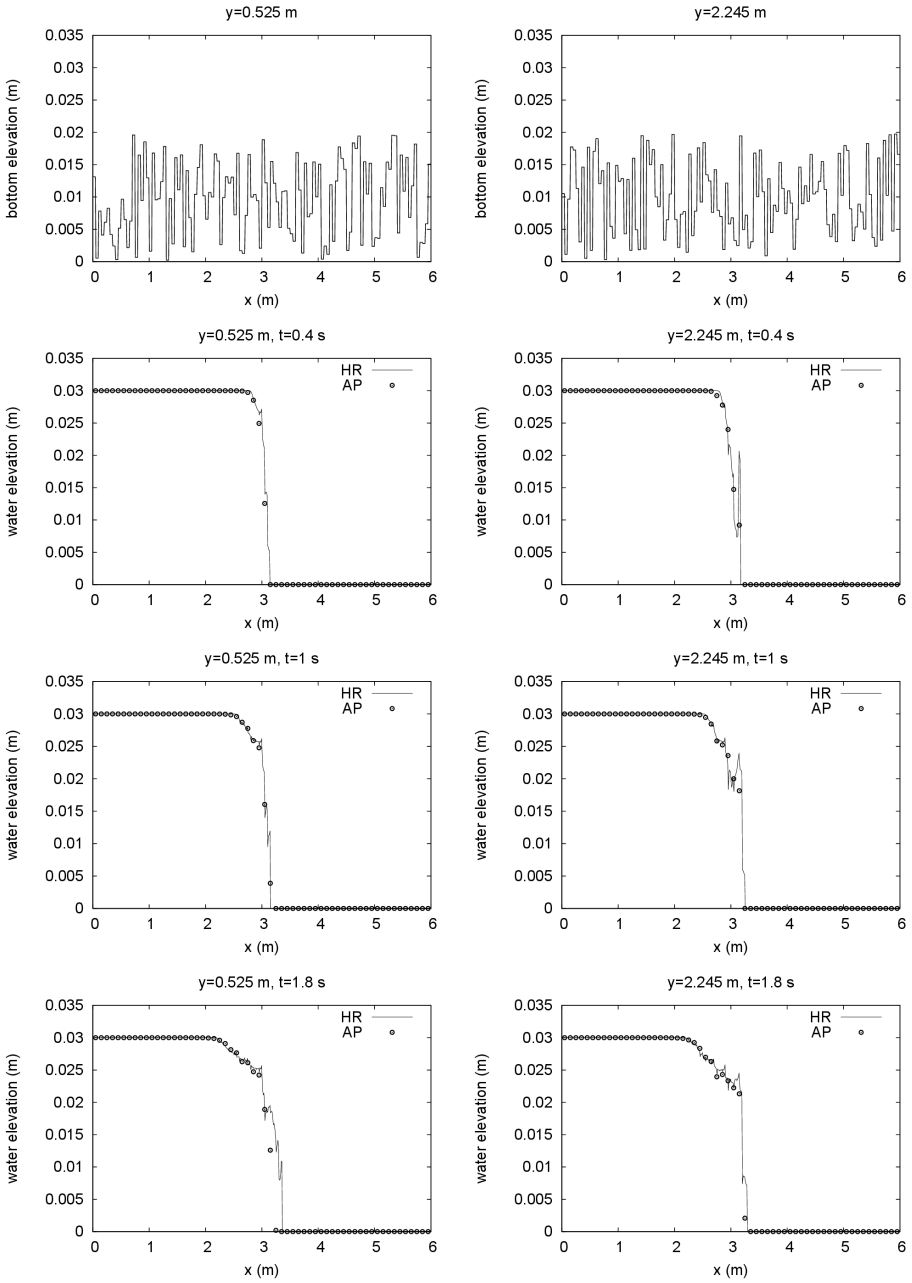

Figure 3.12: Dam break on bed with random microtopography: Water elevations at $y = 0.525\,\mathrm{m}$ (left) and $y = 2.245\,\mathrm{m}$ (right) at different times for the anisotropic porosity model (AP) and the high-resolution reference solution (HR); the high-resolution bottom topography is plotted at the very top of each column for illustration purposes

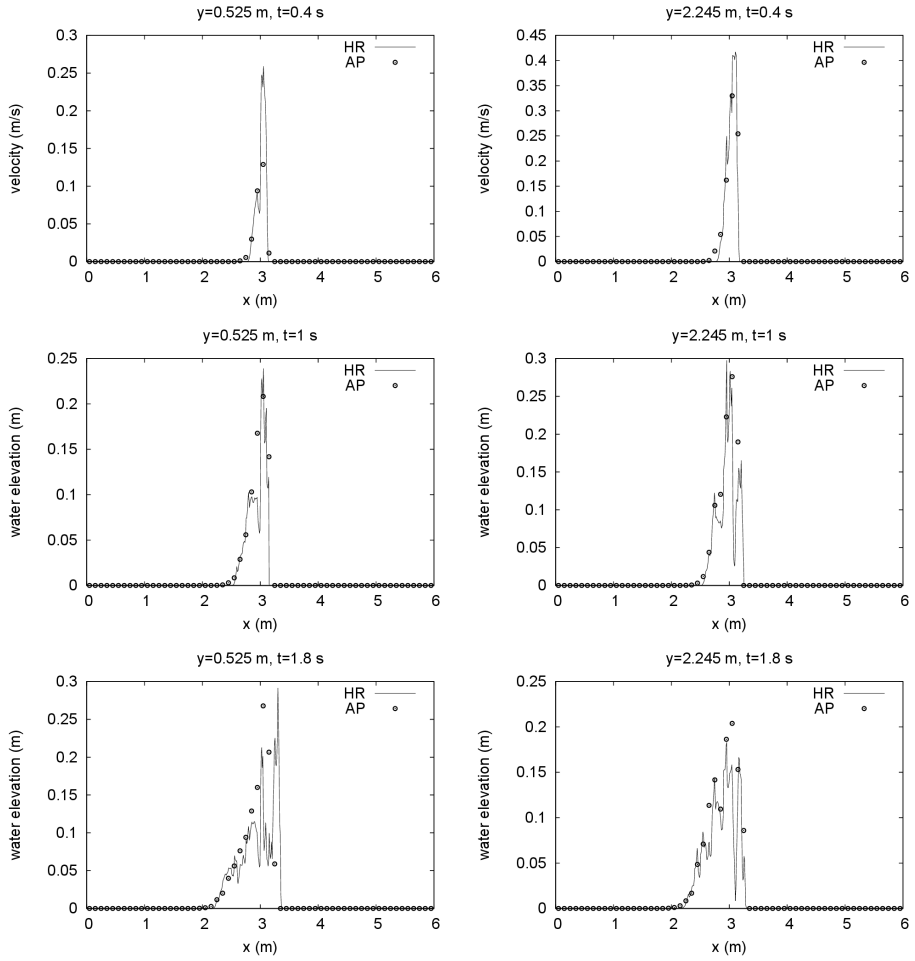

Figure 3.13: Dam break on bed with random microtopography: Flow velocities at $y = 0.525\,\mathrm{m}$ (left) and $y = 2.245\,\mathrm{m}$ (right) at different times for the anisotropic porosity model (AP) and the high-resolution reference solution (HR)

$t\,(\mathrm{s})$	$L_1(\eta)\,(\mathrm{m})$	$L_1(v)\,(\mathrm{m/s})$
0.4	$1.8 \cdot 10^{-4}$	$2 \cdot 10^{-3}$
1	$2.5 \cdot 10^{-4}$	$3.6 \cdot 10^{-3}$
1.8	$6 \cdot 10^{-4}$	$9.1 \cdot 10^{-3}$

Table 3.5: Dam break with random microtopography: L_1-error for water elevation and velocity for $y = 0.525\,\mathrm{m}$

$t\,(\mathrm{s})$	$L_1(\eta)\,(\mathrm{m})$	$L_1(v)\,(\mathrm{m/s})$
0.4	$2.7 \cdot 10^{-4}$	$4 \cdot 10^{-3}$
1	$2.5 \cdot 10^{-4}$	$5 \cdot 10^{-3}$
1.8	$2 \cdot 10^{-4}$	$6 \cdot 10^{-3}$

Table 3.6: Dam break with random microtopography: L_1-error for water elevation and velocity for $y = 0.525\,\mathrm{m}$

and the AP model (right). The HR model resolves the microtopography explicitly and as the water elevation is calculated as $\eta = h + z_b$, in the dry part of the domain, the water elevation equals the bottom elevation. It is observed that the overall characteristics of the advancing front and the rarefaction wave moving upstream are captured well by the AP model. However, the spatial distribution of the AP model results have low accuracy, as they suffer from numerical diffusion due to coarse grids as well as the lack of information on small scale bottom elevation variations. The results of the AP model are calculated approximately 1000 times faster than the HR model.

Rainfall-runoff on an inclined plane with random microtopography

Rainfall-runoff is heavily influenced by the microtopography of the domain [162]. In this example, the surface runoff on a $6\,\mathrm{m} \times 3\,\mathrm{m}$ inclined plane with a slope of 0.02 and a Manning's coefficient of $n = 0.016\,\mathrm{sm}^{-1/3}$ is simulated. The bottom elevation for the high-resolution model (HR) is calculated as:

$$z_b\,(x, y) = 1 - 0.02 \cdot x + z_{b,mic}\,(x, y) \tag{3.48}$$

Here, $z_{b,mic}$ is the amplitude of the microtopography, which is generated as square blocks with an edge length of $0.02\,\mathrm{m}$ and a vertical amplitude varying between 0 and $0.003\,\mathrm{m}$ according to a Gaußian distribution function. The

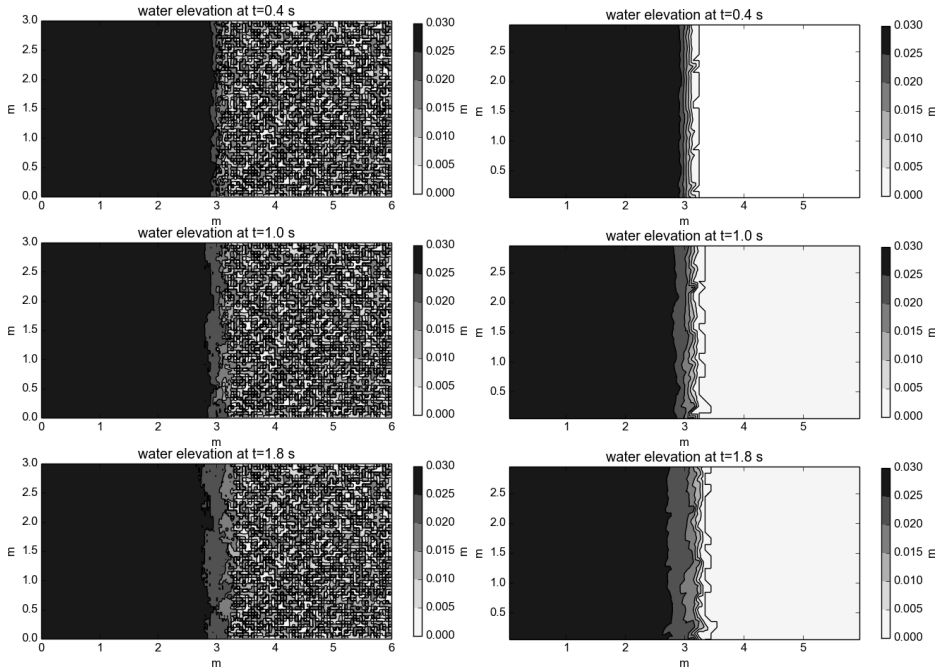

Figure 3.14: Dam break on bed with random microtopography: Water elevations at different time steps for the high-resolution reference solution (HR) (left) and the anisotropic porosity model (AP) (right)

microtopography is applied only inside a rectangular area spanning from $(2.25\,\mathrm{m}, 0.75\,\mathrm{m})$ to $(3.75\,\mathrm{m}, 2.25\,\mathrm{m})$ whereby the first pair of coordinates denotes the bottom left corner and the latter pair denotes the top right corner of the rectangle as illustrated in Figure 3.15 (right top). For the anisotropic porosity model (AP), the microtopography is not explicitly discretized and the bottom elevation is calculated as:

$$z_b\left(x, y\right) = 1 - 0.02 \cdot x \tag{3.49}$$

The domain without microtopography is illustrated in Figure 3.15 (left). Rainfall is imposed for 100 s with the intensity being varied from $i_r = 1 \cdot 10^{-5}\,\mathrm{m/s}$ to $i_r = 1 \cdot 10^{-3}\,\mathrm{m/s}$ for different simulation runs. The boundary at the outlet is an open boundary, all other boundaries are closed. The HR model uses a square grid with an element size $\Delta x = 0.02\,\mathrm{m}$, the AP model uses a square grid with an element size of $\Delta x = 0.1\,\mathrm{m}$. A calibration resulted in $c_D^0 \cdot a = 0$, i.e. no drag force influence.

The normalised discharges at the outlet of the domain ($x = 6\,\mathrm{m}$) are compared for the different rainfall intensities in Figure 3.16. The normalized

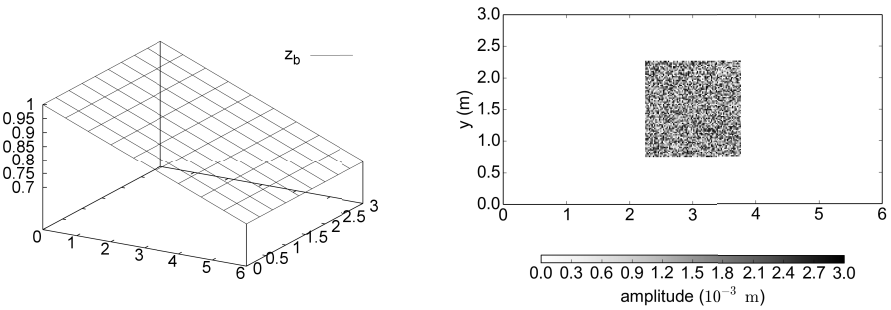

Figure 3.15: Rainfall-runoff on an inclined plane with random microtopography: Side view of the computational domain without microtopography (left); top view of the position and spatial distribution of microtopography (right top); top view of the positions of evaluation points (right bottom)

discharge is calculated as the ratio of the model discharge (Q_{model}) to the rainfall discharge, whereby the rainfall discharge for a $l \times w$ rectangular domain is calculated as [123]:

$$Q_{\text{rain}} = l \cdot w \cdot i_r \tag{3.50}$$

The comparison shows that the influence of the microtopography is overestimated by the AP model. In the early time of the simulation, both hydrographs agree well but when the wave which is influenced by the microtopography reaches the outlet the hydrographs start to deviate.

For $i_r = 1 \cdot 10^{-5}\,\text{m/s}$ the AP model does not reach its concentration time in 100 s. The agreement at the late stages of the simulation (after $t = 80\,\text{s}$) is less good. This suggests that in the AP model, the influence of the microtopography is overestimated in these test cases and thus the water is artificially held back and does not reach the outlet. This argument is supported by the fact that the agreement gets better for increasing rainfall intensity, cf. e.g. the hydrograph of $i_r = 1 \cdot 10^{-3}\,\text{m/s}$. As the intensity increases, the influence of the microtopography on the flow decreases. For $i_r = 1 \cdot 10^{-4}\,\text{m/s}$ the hydrograph of the AP model rises a little bit too slow and for $i_r = 1 \cdot 10^{-3}\,\text{m/s}$ both hydrographs agree well. The water depths behave similarly. The results of the AP model are on average computed 550 times faster than the reference solution.

The L_1-errors for different intensities are given in Table 3.7. Here, the L_1-error is divided by the corresponding intensity for better comparison of the cases.

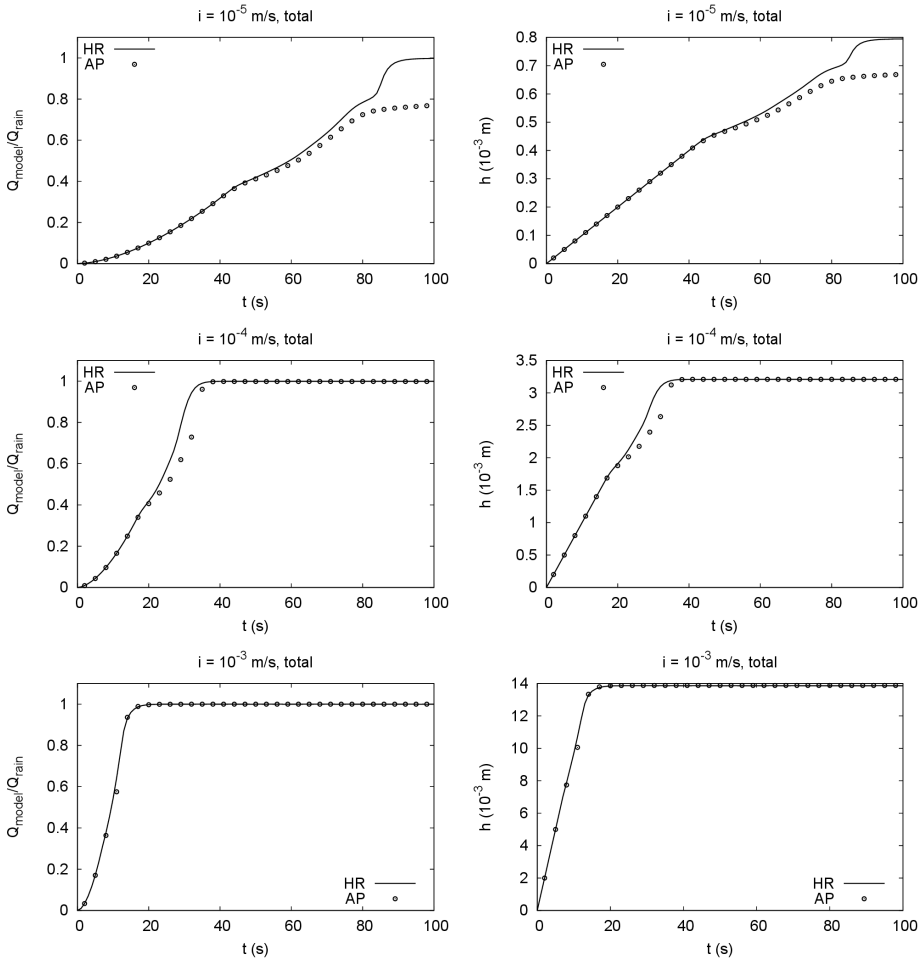

Figure 3.16: Rainfall-runoff on an inclined plane with random microtopography: Comparison of normalized discharges (left) and water depths (right) at the outlet computed by the HR model and the AP model for different rainfall intensities

$i\,(\mathrm{m/s})$	$L_1(q)\,((\mathrm{m}^2/\mathrm{s})/(\mathrm{m/s}))$	$L_1(h)\,(\mathrm{m}/(\mathrm{m/s}))$
10^{-3}	$1.4 \cdot 10^{-2}$	$3.8 \cdot 10^{-2}$
10^{-4}	$10 \cdot 10^{-2}$	$40 \cdot 10^{-2}$
10^{-5}	$28 \cdot 10^{-2}$	$280 \cdot 10^{-2}$

Table 3.7: Rainfall-runoff on an inclined plane with random microtopography: scaled L_1-error for unit discharge and water elevation at the outlet, errors are scaled by division by the corresponding rainfall intensity

point	$L_1(q)$ $((\mathrm{m}^2/\mathrm{s})/(\mathrm{m}/\mathrm{s}))$
1	$2 \cdot 10^{-1}$
2	$1.6 \cdot 10^{-1}$
3	$10 \cdot 10^{-1}$
4	$3.1 \cdot 10^{-1}$
5	$0.13 \cdot 10^{-1}$

Table 3.8: Rainfall-runoff on an inclined plane with random microtopography: scaled L_1-error for unit discharge at the gauges for $i = 10^{-4}\,\mathrm{m/s}$, errors are scaled by division by the rainfall intensity

For $i_r = 1 \cdot 10^{-4}\,\mathrm{m/s}$, model results at different points are compared (cf. Figure 3.17, right bottom). Figure 3.17 also shows a comparison of normalized discharges at these evaluation points. Good agreement between the discharges is observed at the points 1, 2 and 5. However, especially at points 1 and 2 is a temporal delay in the hydrograph of the AP model which again comes from the overestimation of the influence of microtopography. Point 3, which is located inside the area with microtopography, shows the worst agreement which might result from the aforementioned overestimation as well as the macroscopic approach of the AP model which is not expected to reproduce local flow processes. At point 4 the discharge is overshot by the AP model.

Model results for the same points are compared in Figure 3.18 for $i_r = 1 \cdot 10^{-5}\,\mathrm{m/s}$. Here, it is seen that the agreement at the points where the flow is influenced by the microtopography, namely points 2, 3 and 4, gets worse for lower intensities. Especially at point 3, which is located inside the area with microtopography, the AP model returns a discharge which is 3 times higher than the HR model discharge and is temporally delayed.

The L_1-errors at the different points are given in Table 3.8 and 3.9 for $i = 10^{-4}\,\mathrm{m/s}$ and $i = 10^{-3}\,\mathrm{m/s}$, respectively. Again, the L_1-errors are divided by the corresponding intensity.

Figure 3.19 shows temporal snapshots of the discharge distribution in the domain at $t = 15\,\mathrm{s}$, $t = 20\,\mathrm{s}$ and $t = 50\,\mathrm{s}$ for both the HR model (left) and the AP model (right). The resolution of the AP model is much coarser than the HR model and therefore local details can not be resolved as good as in the HR model but general properties of the flow field are reproduced. At $t = 20\,\mathrm{s}$ the overestimation of microtopography can be seen very clearly, as the flow calculated by the HR model (Figure 3.19, left middle) has already reached the right border of the microtopography area while the flow calculated by the AP model (Figure 3.19, right middle) has

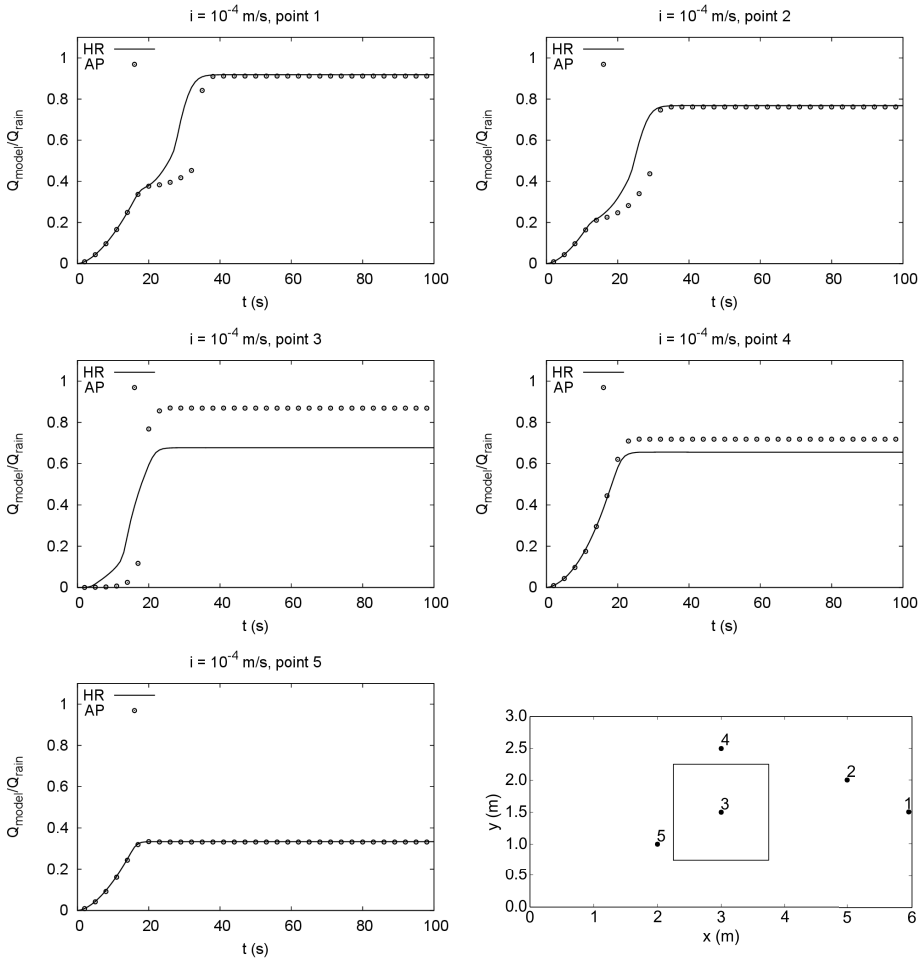

Figure 3.17: Rainfall-runoff on an inclined plane with random microtopography: Comparison of normalized discharges computed by the HR model and the AP model for $i_r = 1{\cdot}10^{-4}$ m/s at different evaluation points (plotted in the right bottom)

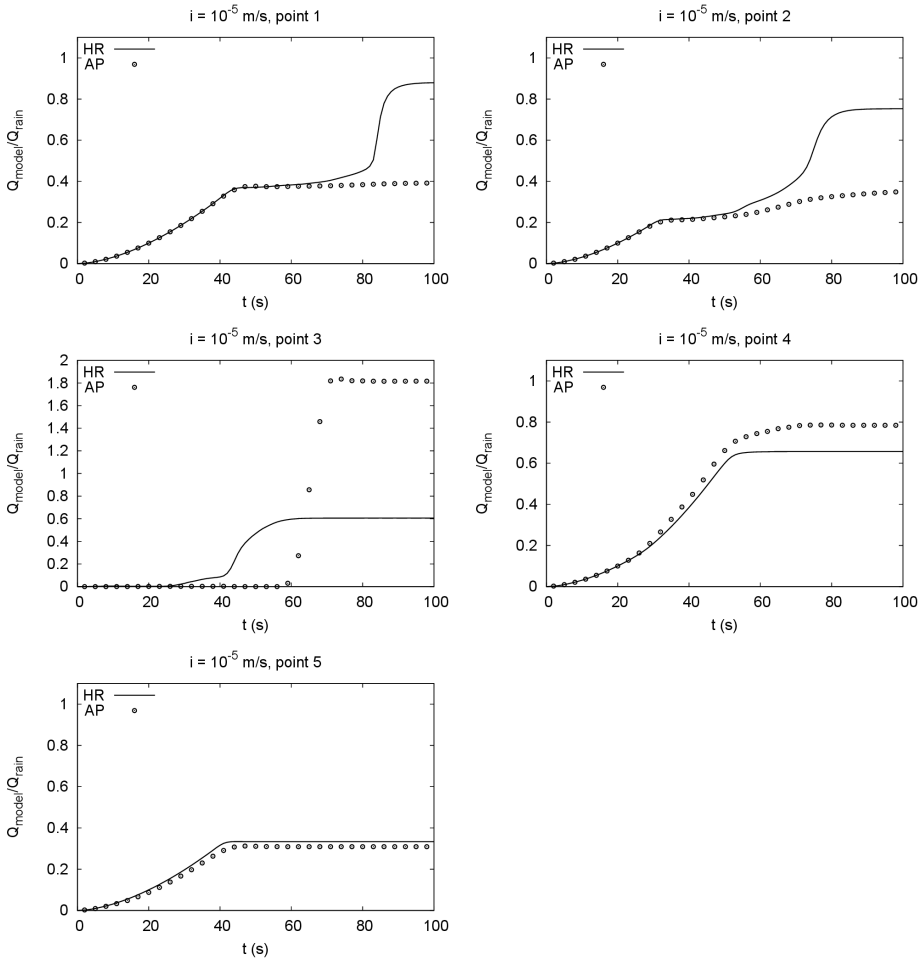

Figure 3.18: Rainfall-runoff on an inclined plane with random microtopography: Comparison of normalized discharges computed by the HR model and the AP model for $i_r = 1{\cdot}10^{-5}$ m/s at different evaluation points (plotted in the right bottom of Figure 3.17)

point	$L_1(q)$ $((\mathrm{m}^2/\mathrm{s})/(\mathrm{m}/\mathrm{s}))$
1	$5.1 \cdot 10^{-1}$
2	$7.2 \cdot 10^{-1}$
3	$30 \cdot 10^{-1}$
4	$4 \cdot 10^{-1}$
5	$1.2 \cdot 10^{-1}$

Table 3.9: Rainfall-runoff on an inclined plane with random microtopography: scaled L_1-error for unit discharge at the gauges for $i = 10^{-5}\,\mathrm{m/s}$, errors are scaled by division by the rainfall intensity

only reached the middle of the microtopography area. The discharge of the AP model is higher than of the HR model, however the porosity slows down the front of the AP model flow. This can also be observed in Figure 3.17 (left middle), where the discharge at point 3 is delayed and overestimated by the AP model. At $t = 50\,\mathrm{s}$ the flow fields reasonably resemble (Figure 3.19, bottom).

Dam-break flow through an idealised city

In this computational example, results of a dam-break experiment conducted at the Université catholique de Louvain, Belgium, [133] are numerically reproduced.

Domain description, initial and boundary conditions

The domain is a 35.8 m long and 3.6 m wide channel with horizontal bed. The idealised city consists of 5×5 buildings, each of them being a square block with an edge length of 0.30 m. The distance between the blocks is 0.10 m. The dam-break is constructed by opening a 1 m wide gate, which initially seperates part of the channel with water ponding at 0.40 m from the rest of the channel (reservoir), where a very thin layer of 0.011 m water due to imperfect tightness of the gate is reported. For further details on the experimental setup and employed measurement techniques, the reader is referred to [133]. The domain is illustrated in Figure 3.20, where the reservoir is coloured in grey.

For the numerical model, only the reservoir and the first 16 m of the channel is discretised for computational efficiency. In preliminary studies it had been observed that for the duration of the simulations, $t = 15.5\,\mathrm{s}$, the shock wave does not travel further than this length. The downstream

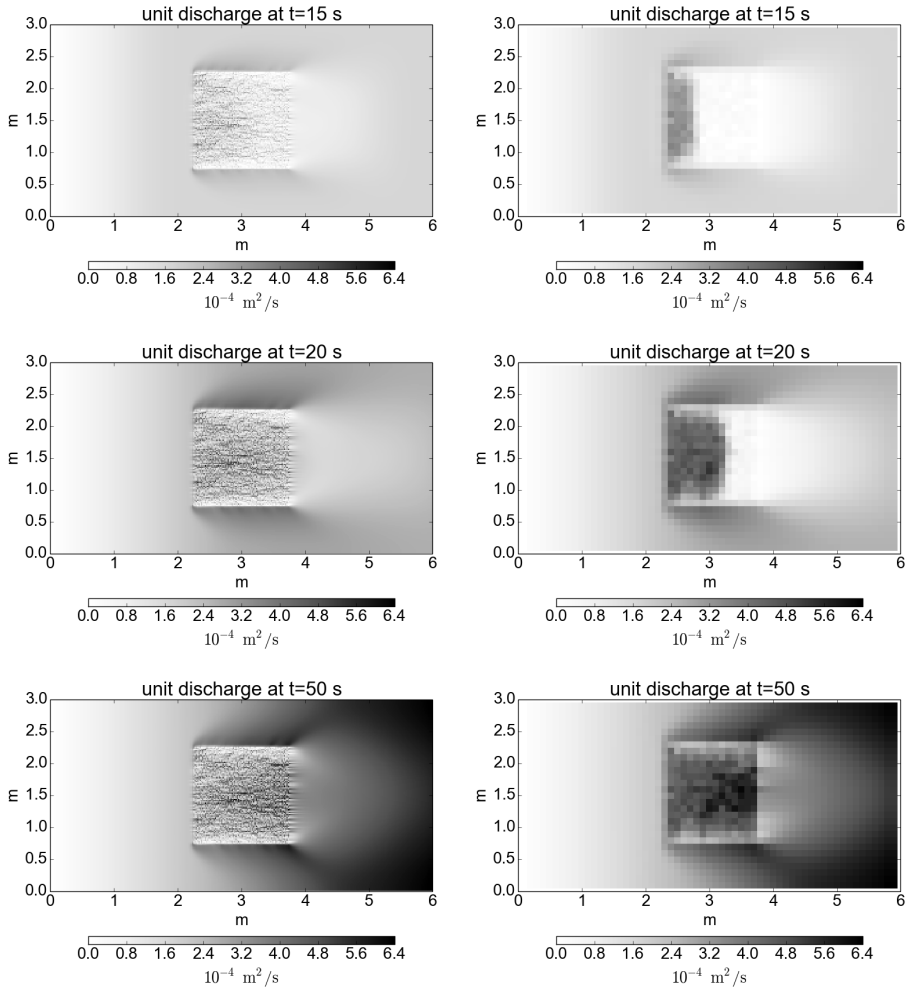

Figure 3.19: Rainfall-runoff on an inclined plane with random microtopography: Comparison of snap shots of unit discharges computed by the HR model (left) and the AP model (right) at different time steps

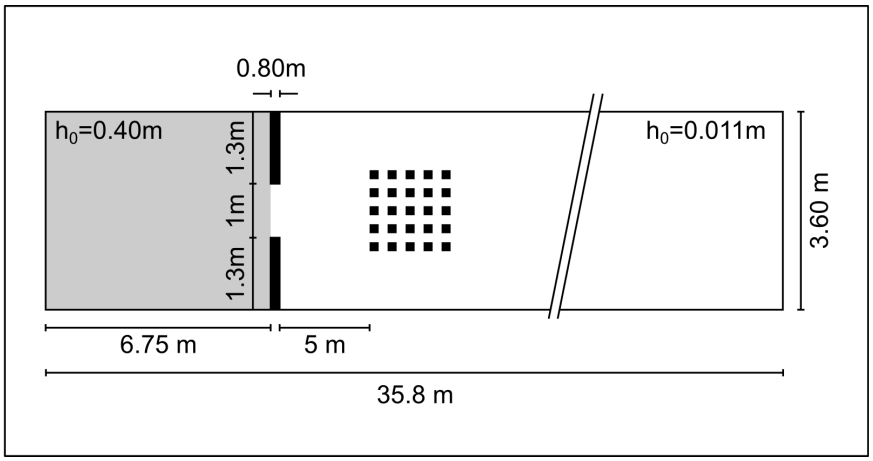

Figure 3.20: Dam break flow through an idealised city: Computational domain and initial conditions

boundary is an open boundary and all other boundaries are closed boundaries.

The HR model uses a triangular mesh with three different cell sizes: the inside of the reservoir is discretised with cells with a characteristic length of $l_{c,1} = 0.3\,\mathrm{m}$. The area inside the channel which is sufficiently far away from the building blocks is discretised with a characteristic length of $l_{c,2} = 0.1\,\mathrm{m}$. The space between the buildings is discretised with a characteristic length of $l_{c,3} = 0.01\,\mathrm{m}$. The buildings are represented as holes in the mesh, which is a method commonly used in urban flood modeling [127]. With the value chosen for $l_{c,3}$, the space between two buildings is discretised with about 10 cells and the total cell number is 95975. The AP model uses square-shaped cells with an edge length of 0.25 m in the whole domain, which results in 1272 cells in total.

Experimental data is available at 64 measurement gauges distributed inside the channel [133]. The positions of these gauges are given in Figure 3.21. Errors are calculated for all gauges. In the discussion, results are plotted only for 4 gauges, namely gauges 1, 18, 44 and 55, to avoid too many figures. These gauges are pointed out in Figure 3.21.

The roughness of the channel has been estimated in [133] with a Manning's coefficient of $n = 0.01\,\mathrm{sm}^{1/3}$. This value is used for both the HR and the AP model.

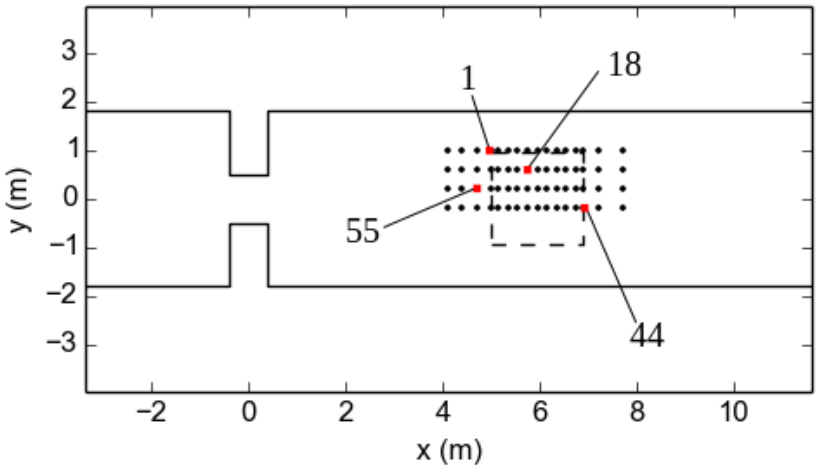

Figure 3.21: Dam break flow through an idealised city: Location of the gauges, area of building array is marked with dashed line

Model calibration and run time

The AP model is calibrated with the value $a \cdot c_D^0$. The best results in this specific case were obtained by completely neglecting the drag force, i.e. $a \cdot c_D^0 = 0$. No calibration is carried out for the HR model. The HR model simulation takes about 3000 s wall-clock time to finish. The AP model requires about 4 s wall-clock time. Consequently, the speedup is calculated as 750 (cf. 3.10).

Discussion

The HR model makes overall a good prediction of the water depth at the evaluated gauges. In Figure 3.22, the water depth calculated by the HR model at the aforementioned gauges is plotted together with the measured water depth. Overall, the numerical results approximate the experimental results very well. The arrival time of the wave is predicted correctly at all gauges. Larger deviations between the results occur at the later stages of the simulation. At gauge 18, which is located between the buildings, the wave reflections from the walls of the buildings superpose and create several peaks between $t = 3.5$ s and $t = 6.5$ s in the HR model results which were not observed during the experiment. Further, at gauge 1, which is at the upper right corner of the building block, the water depth is underestimated by the HR model. This might be because of the hydraulic jump observed

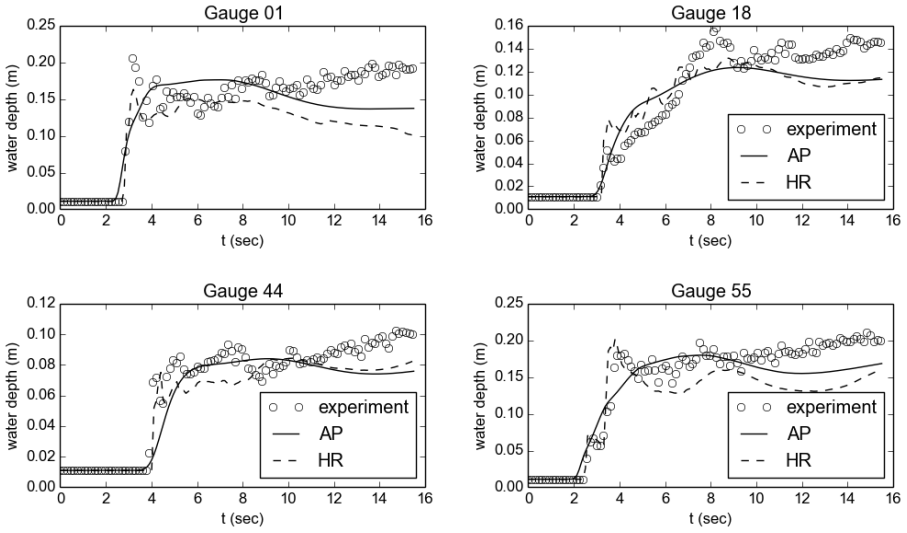

Figure 3.22: Dam break flow through an idealised city: Discharges calculated by the anisotropic porosity model (AP), high-resolution model (HR) and the measurement data at gauges 1, 18, 44 and 55

at the impact section which leads to increased local water levels which are not reproduced by the HR model. These points might raise the question, whether a turbulence model should be used, however Soares-Frazão and Zech [133] report that adding turbulence to the numerical model leads to a worse agreement between numerical and experimental results.

The anisotropic porosity model (AP) shows good agreement with the HR model results, although the results of the AP model are smoother and more diffused than the HR model results. In Figure 3.22, AP model results for water depth are plotted for the four gauges as well. Gauge 1 and gauge 18 show very good agreement, while the arrival time of the wave at gauge 44 is delayed. Gauge 55, located in the front of the building block, shows the worst agreement of the four. Here, the AP model overshoots the HR model. The peak at around $t = 4$s is not reproduced. Overall, the general properties of the AP model results, i.e. the lack of local and spatial fluctutations, agree with the observations in [76]. In general, the AP model error manifests itself in excessive damping of the results.

L_1-errors of both models in regard to the experimental data are calculated as the average L_1-error of all 64 gauges. The HR model has a L_1-error of 0.02 m, the AP model has a L_1-error of 0.07 m.

3.5 Conclusions

An integral formulation of the two-dimensional shallow water equations with anisotropic porosity for flow over partially and fully inundated topography was derived. A novel formulation for the porosities was proposed and an approximation for the storage and flux terms was presented. The porosities are dependant on the water elevation in the cell. This relationship can be approximated by calculating a cummulative distribution function for the unresolved bottom elevation and evaluating it at the water elevation. Due to the macroscopic point of view, additional terms appear in the governing equations. Suitable approximations for these terms have been referred to. The non-stationary term was approximated with a drag force approach. The integral formulation of the equations can only be solved by the finite volume method. A second order MUSCL scheme was used to solve the equations with a two-step explicit Runge-Kutta method for time stepping.

Five computational examples, ranging from simple academic benchmarks to nearly 'real case' laboratory experiments were shown to demonstrate the capabilities and limitations of the new approach. Due to the lack of analytical solutions a high-resolution shallow water model was used to calculate reference solutions. In the last test case, experimental data was used for model evaluation. The shallow water model with porosity showed overall good agreement with the reference solutions. The aforementioned drag term was used to calibrate the model and a sensitivity study regarding this term was carried out. Except in the last test case, good results are obtained with $c_D^0 \cdot a = 10$. However, further studies to investigate the drag force coefficient values and the possibility to represent the drag effect with increased friction are required.

As bottom slope increases, the accuracy of the anisotropic shallow water model decreases. Experimental studies show that a large bed slope reduces the effect of microtopography [136] and the presented model seems to underestimate the reduction.

A challenge in practical applications is the isolation of the part of topography modeled as porosity from the global topography. Usually, the global topography is defined as the roughness of the surface of the earth and represented by the cell value. The unresolved topography is thought about as subgrid-scale deviations from this value which creates heterogeneity inside the cell. The issue of identifying these deviations has been researched in the context of isolating microtopography and different methods have been proposed in the literature, e.g. [120]. However, finding suitable methods to correctly isolate the part of topography to be modeled as porosity remains an open issue, which seems to be the main limitation of applying the

Case	Δx_{HR}	n_{HR}	Δx_{AP}	n_{HR}	$n_{\mathrm{HR}}/n_{\mathrm{AP}}$	speedup
3.3	0.01 m	30000	0.1 m	300	100	1000
3.4	0.02 m	2500000	0.5 m	4000	625	3000
3.5	0.01 m	180000	0.1 m	1800	100	1000
3.6	0.02 m	45000	0.1 m	1800	25	550
3.7	$0.01 - 0.3$ m	95975	0.25 m	1272	75.4	750

Table 3.10: Summary of speedups obtained in all simulations, n: Number of cells, Δx: edge length, HR: high-resolution model, AP: anisotropic porosity model

proposed model to 'real world cases'.

Local details of the flow could not be exactly reproduced by the anisotropic porosity model, because the concept of porosity as a statistical property of the topography is not expected to reproduce processes at this scale [51].

The novel anisotropic porosity was found to be a good balance between computational time and accuracy. Table 3.10 gives an overview of the speedups in the simulations in dependency of cell size Δx and cell number n. The ratio of cell numbers ($n_{\mathrm{HR}}/n_{\mathrm{AP}}$) is identified as the main factor of the speedup. In the presented computational examples, the anisotropic porosity model provided a computational benefit around three orders of magnitude, depending on the ratio of the cell numbers, i.e. the difference in cell size.

3.6 Acknowledgement

The authors thank Prof. Andrea Defina, Università degli Studi di Padova, Italy, for the insightful personal communication, and the Local Organizing Committee of the Advances in Numerical Modelling of Hydrodynamics Workshop, Sheffield, UK, guest editor Dr. Daniel Caviedes-Voullième and the anonymous reviewers for their valuable comments.

3.7 Appendix: Derivation of porosities by Sanders *et al.* [125]

It can be shown that the definitions of porosity in [125] can be considered as a special case of Equations 3.2 and 3.3, where submergence of microtopog-

raphy is not allowed. If microtopography is not allowed to be submerged, the wet fraction of the control volume will remain constant. Further, if the wet fraction of the control volume is considered to have the same constant bed elevation $z_b = z_0$, Equation 3.2 can be simplified to

$$\phi = \frac{\int_\Omega i\,(\eta - z_0)\,d\Omega}{\int_\Omega (\eta - z_0)\,d\Omega} = \frac{(\eta - z_0)\int_\Omega i d\Omega}{(\eta - z_0)\int_\Omega d\Omega} = \frac{1}{\Omega}\int_\Omega i d\Omega. \tag{3.51}$$

If the same assumptions are made for the boundary of the control volume, Equation 3.3 simplifies to

$$\psi = \frac{\oint_{\partial\Omega} i\,(\eta - z_0)\,dr}{\oint_{\partial\Omega} (\eta - z_0)\,dr} = \frac{1}{\partial\Omega}\oint_{\partial\Omega} i dr. \tag{3.52}$$

Equations 3.51 and 3.52 are the porosities introduced in [125] for building treatment. The assumptions made are valid for describing the effects of buildings, which are unlikely to become submerged by the flood wave. If the porosities are used to describe the effects of microtopography, Equations 3.2 and 3.3 have to be used. A significant difference between Equations 3.2 and 3.3 (with inundation) and Equations 3.51 and 3.52 (without inundation) is that the porosities that allow inundation are dependent on the water elevation η, which is variable in time. If the water elevation increases, the porosities increase. Therefore, the porosities are functions of time if the terrain variation within a control volume is considered and inundation is allowed, while without inundation the wet fraction of the control volume remains constant and thus, the porosities are constant in time.

Chapter 4

Porosity-based coarse grid approach: numerical model

Published as:
[116] Özgen, I., Zhao, J., Liang, D., and Hinkelmann, R. (2016) Urban flood modeling using shallow water equations with depth-dependent anisotropic porosity. *Journal of Hydrology* 541, pp. 1165–1184.
doi: 10.1016/j.hydrol.2016.08.025

This is the postprint version of the publication. The final publication is available at ScienceDirect via `https://doi.org/10.1016/j.hydrol.2016.08.025`.

4.1 Abstract

The shallow water model with anisotropic porosity conceptually takes into account the unresolved subgrid-scale features, e.g. microtopography or buildings. This enables computationally efficient simulations that can be run on coarser grids, whereas reasonable accuracy is maintained via the introduction of porosity. This article presents a novel numerical model for the depth-averaged equations with anisotropic porosity. The porosity is calculated using the probability mass function of the subgrid-scale features in each cell and updated in each time step. The model is tested in a one-dimensional theoretical benchmark before being evaluated against measurements and high-resolution predictions in three case studies: a dam-

break over a triangular bottom sill, a dam-break through an idealized city and a rainfall-runoff event in an idealized urban catchment. The physical processes could be approximated relatively well with the anisotropic porosity shallow water model. The computational resolution influences the porosities calculated at the cell edges and therefore has a large influence on the quality of the solution. The computational time decreased significantly, on average three orders of magnitude, in comparison to the classical high-resolution shallow water model simulation.

4.2 Introduction

In shallow water modeling of river hydraulics [111, 74], urban flooding [91, 98], urban runoff [16, 88, 89] and rainfall-runoff on natural environments [102, 113, 128, 154], the topographical features have a large influence on the numerical results. The availability of digital elevation data has increased significantly due to recent improvements in surveying technology, notably laser scanning and light detection and ranging (LIDAR) technologies, which provide high-resolution data sets at relatively low cost [41, 46]. However, mainly due to computational constraints, incorporating these data sets into shallow water models is challenging [97, 31]. The difficulty arises from multiple scales in the physical processes. For example, in a small natural catchment with a scale of around a square kilometer, local depressions and microtopography with horizontal scales less than a square meter influence the flow field significantly [6, 32, 141]. Similarly, in urban flood models the city may spread up to several hundred square kilometers but the flood flow can be diverted, slowed down or completely blocked by man-made structures, e.g. buildings, bridges or walls, whose characteristic scale are in meters. In order to accurately capture the effect of microtopography or buildings, they have to be included in the discretization. Due to the co-existence of multiple scales, this leads to extremely large computational mesh, which requires large data storage, large number of operations per time step, small time step size and thus large computational effort. In fact, the computational cost is inversely proportional to the third power of the cell size [77]. Therefore, practical applications have to compromise between spatial accuracy and computational efficiency [80] and are often carried out on super-computers [129].

For super-computers, high-performance parallel computation methods on shared or distributed memory have been developed in literature [56] and very recently graphic processing units have been exploited for scientific computation, e.g. [80, 81, 129].

A different approach to speed up simulations is to conceptually account for small scale ground variations without explicitly discretizing them [97]. This allows to run the simulations on coarser meshes. In this context, the shallow water equations with porosity have been initially developed by Defina [27, 26] to account for microtopography in partially inundated cells. Here, a single porosity is assigned to each cell, which represents the fraction of the cell that contributes to the flow. The porosity is calculated by a distribution function, which returns the porosity depending on the water depth in the cell. The distribution function is defined for the whole domain. In [154], Defina's porous shallow water equations are applied to coupled simulations of surface and subsurface flows in natural catchments.

The porosity concept was also applied to urban flood modeling by Hervouet [55] to account for buildings. Significant contribution to the porosity concept in the context of urban flood modeling was made by Guinot and Soares-Frazão [51, 132, 48]. Because the buildings in urban flood models are usually not fully submerged during the flood event, the area available for the flow stays constant during the simulation. Consequently, most porous urban flood models assign a constant porosity to each cell which only depends on the fraction of the cell occupied by buildings. An exception is the urban flood model presented in [53], wherein the authors calculate the inundated area of each cell according to the water elevation and use it in the mass balance. Although the authors do not explicitly use porosity terms, the model in [53] is essentially equivalent to a single porosity model with a depth-dependent porosity. The same strategy for porosity calculation is followed in this work. Further studies regarding the shallow water equations with single porosity in the context of urban flooding were carried out in [18, 39, 100, 132, 152]. Single porosity shallow water models can not differentiate between spatial directions. The flow in all directions is governed by the same porosity. However, buildings in urban flood models usually have a directionality which leads to preferential flow paths of the water. Therefore, Sanders et al. [125] introduced the anisotropic porosity shallow water model, wherein a volumetric porosity inside the cell is defined to account for the fraction of the cell available for water. In addition an areal porosity is assigned to each cell edge which describes the conveyance there (Sanders' model). The equations were derived using the integral form of the shallow water equations, thus these equations can be solved only by a finite volume method. Sanders' model was further investigated in [19, 77, 126]. In [114] a modified version of Sanders' model that allows full submergence of unresolved topographic features by introducing a mutual dependency between water depth and porosity is derived.

This article presents a numerical model to solve the equations derived in

[114] on Cartesian grids. The main difference from Sanders' model is that submergence of unresolved topography leads to a different formulation of the porosities depending on the water depth in the cell. The main contribution of this work is the discussion on discretizing the porosity terms in the cell and at the edge and the illustration of the model's behaviour via detailed case studies. In the present model, each cell and each edge are automatically assigned an individual porosity that depends on the water depth and the underlying topography. Thus, the model is automatically adjusted based on the computational mesh. The model performance is investigated in a theoretical test case. Then, case studies of laboratory experiments are presented to further investigate the model's behaviour.

4.3 Governing equations

The two-dimensional shallow water equations with anisotropic porosity can be written in integral-differential form as:

$$\frac{\partial}{\partial t}\int_{\Omega} i\mathbf{q}d\Omega + \oint_{\partial\Omega} i\mathbf{F}\mathbf{n}dr = \int_{\Omega} i\mathbf{s}d\Omega + \oint_{\partial\Omega^*} \mathbf{s}^* dr^* \tag{4.1}$$

Here, Ω is the total base area of the control volume, $\partial\Omega$ is the boundary of the control volume, r is the path along the boundary $\partial\Omega$, $\partial\Omega^*$ is the boundary between the fluid and the solid inside the control volume and r^* is the path along this boundary (cf. [125, 113]). i is the so-called phase function, defined as:

$$i\left(x,y\right) = \begin{cases} 1, & \eta\left(x,y\right) > z_b\left(x,y\right) \\ 0, & \text{else} \end{cases} \tag{4.2}$$

η is the water elevation, z_b is the bottom elevation, $\mathbf{q}$ is the vector of conserved variables, $\mathbf{s}$ is the source term vector, $\mathbf{F}$ is the flux vector and $\mathbf{n} = \left[n_x, n_y\right]^T$ is the normal vector of the boundary, with n_x and n_y are the components of the normal vector in x- and y-directions of the Cartesian coordinate system, respectively. Figure 4.1 illustrates the phase function, η and z_b. The vectors $\mathbf{q}$ and $\mathbf{s}$ are expressed as:

$$\mathbf{q} = \begin{bmatrix} h \\ q_x \\ q_y \end{bmatrix}, \qquad \mathbf{s} = \begin{bmatrix} i_r \\ s_{b,x} + s_{f,x} \\ s_{b,y} + s_{f,y} \end{bmatrix} \tag{4.3}$$

Here, $h = \eta - z_b$ stands for water depth, q_x and q_y are the unit discharges in x- and y-directions, respectively. i_r is the mass source term, e.g. rainfall

intensity; $s_{b,x}$, $s_{b,y}$ are the bed slope source terms in x- and y-directions, respectively which account for variations in bottom, $s_{f,x}$, $s_{f,y}$ are the friction source terms in x- and y-directions, respectively:

$$s_{b,x} = -gh\frac{\partial z_b}{\partial x}, \quad s_{b,y} = -gh\frac{\partial z_b}{\partial y}, \tag{4.4}$$

$$s_{f,x} = -c_f q_x \frac{\sqrt{q_x^2 + q_y^2}}{h^2}, \quad s_{f,y} = -c_f q_y \frac{\sqrt{q_x^2 + q_y^2}}{h^2} \tag{4.5}$$

c_f is the Chézy roughness coefficient, which can be expressed via Manning's law:

$$c_f = gn^2 h^{-1/3} \tag{4.6}$$

n is Manning's roughness coefficient and g is the gravitational acceleration. The flux vector is often split into its x- and y-component:

$$\mathbf{Fn} = \mathbf{f}n_x + \mathbf{g}n_y \tag{4.7}$$

$\mathbf{f}$ and $\mathbf{g}$ are defined as:

$$\mathbf{f} = \begin{bmatrix} q_x \\ uq_x + 0.5gh^2 \\ uq_y \end{bmatrix}, \quad \mathbf{g} = \begin{bmatrix} q_y \\ vq_x \\ vq_y + 0.5gh^2 \end{bmatrix} \tag{4.8}$$

Here, u and v are the velocities in x- and y-directions, respectively. Finally, $\mathbf{s}^*$ is the source vector accounting for fluid pressure along the interface $\partial\Omega^*$. The calculation of $\mathbf{s}^*$ is non-trivial and will be addressed in the next section.

4.4 Numerical model

Finite volume formulation of the equations

The integral-differential form of the shallow water equations can be solved with the finite volume method. However, the phase function i can not be evaluated explicitly in the finite volume cell, because the bottom elevation inside the cell is not resolved. Therefore, the integral terms on the left hand side of Equation 4.1 have to be calculated with the concept of porosity.

In [110], the volumetric porosity is defined as:

$$\phi = \frac{\int_\Omega i\,(\eta - z_b)\,d\Omega}{\int_\Omega (\eta - z_0)\,d\Omega} \tag{4.9}$$

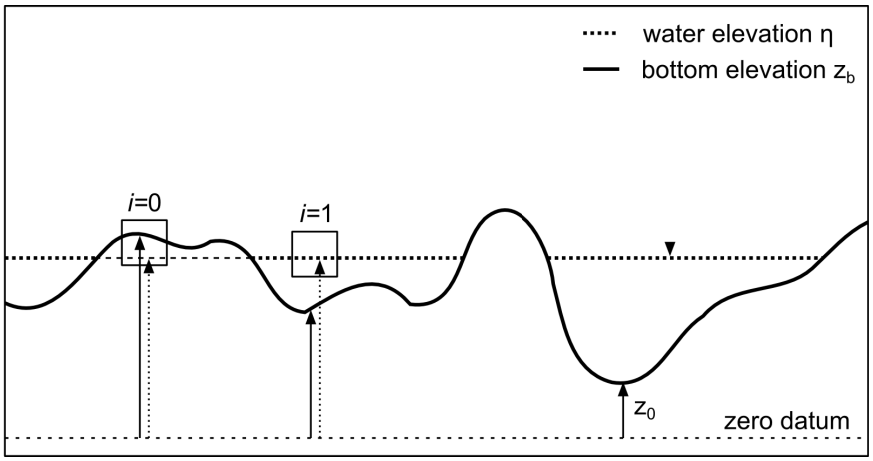

Figure 4.1: Definition of phase function i, water elevation η (dashed), bottom elevation z_b (black) and zero datum z_0 in a vertical section through a control volume

The areal porosity is calculated as:

$$\psi = \frac{\oint_{\partial\Omega} i\,(\eta - z_b)\,dr}{\oint_{\partial\Omega} (\eta - z_0)\,dr} \tag{4.10}$$

Here, z_0 is the elevation of the lowest point inside the control volume with regard to a datum. Both are illustrated in Figure 4.1. Evaluating the integral terms leads to modified flux and storage vectors [110]. Rewriting the line integral as a sum over the finite volume edges transforms Equation 4.1 to:

$$\frac{\partial}{\partial t}\left(\phi\Omega\bar{\mathbf{q}}\right) + \sum_k \psi_k r_k \hat{\mathbf{F}}_k \mathbf{n}_k = \int_\Omega i\mathbf{s}d\Omega + \oint_{\partial\Omega^*} \mathbf{s}^* dr \tag{4.11}$$

k is the index of the path integral and r_k is the length of the integration path. The storage vector $\mathbf{q}$ in Equation 4.3 is rewritten as:

$$\bar{\mathbf{q}} = \begin{bmatrix} (\bar{\eta} - z_0) \\ \bar{u}\,(\bar{\eta} - z_0) \\ \bar{v}\,(\bar{\eta} - z_0) \end{bmatrix} \tag{4.12}$$

The bar over a variable indicates volume-averaged variables which are constant within the cell:

$$\bar{\eta} = \frac{\int_\Omega i\eta d\Omega}{\int_\Omega i d\Omega}, \quad \bar{\mathbf{v}} = \frac{\int_\Omega ih\mathbf{v}d\Omega}{\int_\Omega ihd\Omega} \tag{4.13}$$

If $i = 0$ over the whole control volume, the averaging is not carried out and the volume-averaged variables are taken to be $\bar{\eta} = 0$ and $\bar{\mathrm{v}} = 0$. The flux vector in Equation 4.3 is rewritten as:

$$\hat{\mathbf{F}}\mathbf{n} = \begin{bmatrix} \hat{u}\left(\hat{\eta} - z_0\right) n_x + \hat{v}\left(\hat{\eta} - z_0\right) n_y \\ \hat{u}\hat{u}\left(\hat{\eta} - z_0\right) n_x + 0.5g\left(\hat{\eta} - z_0\right)^2 n_x + \hat{u}\hat{v}\left(\hat{\eta} - z_0\right) n_y \\ \hat{v}\hat{u}\left(\hat{\eta} - z_0\right) n_x + \hat{v}\hat{v}\left(\hat{\eta} - z_0\right) n_y + 0.5g\left(\hat{\eta} - z_0\right)^2 n_y \end{bmatrix} \tag{4.14}$$

The circumflex over a variable indicates area-averaged variables at the edge:

$$\hat{h} = \frac{\int_r ihdr}{\int_r idr}, \quad \hat{\eta} = \frac{\int_r i\eta dr}{\int_r idr}, \quad \hat{\mathbf{v}} = \frac{\int_r ih\mathbf{v}dr}{\int_r ihdr} \tag{4.15}$$

As before, if $i = 0$ over the whole edge the averaging is not carried out and all variables are taken to be nil. Then, Equation 4.11 can be solved with a suitable time integration method.

Porosity computation

In order to calculate the porosities, the Probability Mass Function (PMF) of the unresolved bottom elevation inside the cell is calculated in the pre-processing step. The PMF is defined as the probability density function with discrete variables and can be computed by sampling the bottom elevation at a resolution much higher than the computational mesh. This assumes that the bottom elevation data is resolved at the finer resolution than the computational mesh resolution. The PMF is calculated for each cell and each edge seperately. In the context of this work, the PMF value of a certain elevation corresponds to the fraction of area below this elevation over the total area of the cell or the fraction of length of the edge below the specified elevation over the total length. Then, for any given water elevation $\bar{\eta}$, the volumetric porosity ϕ can be calculated as:

$$\phi\left(\bar{\eta}\right) = \frac{1}{\bar{\eta}\Omega} \sum_{i}^{N} \min\left(0, \bar{\eta} - z_{b,i}\right) \mathrm{PMF}\left(z_{b,i}\right) \Omega_i \tag{4.16}$$

Here, i is the index of bottom elevation $z_{b,i}$. $\mathrm{PMF}\left(z_{b,i}\right)$ is the value of the PMF evaluated at $z_{b,i}$. In the present numerical model, the class index increases as the bottom elevation increases, i.e. the lowest bottom elevation corresponds to the smallest class index and the highest bottom elevation corresponds to the largest class index. N denotes the total number of classes. Similarly, the areal porosity ψ at one edge is computed as:

$$\psi\left(\hat{\eta}\right) = \frac{1}{\hat{\eta}\Delta k} \sum_{i}^{N} \min\left(0, \hat{\eta} - z_{b,i}\right) \mathrm{PMF}\left(z_{b,i}\right) \Delta k_i \tag{4.17}$$

Δk is the length of the edge. The PMF for the edge is sampled from the subgrid cells adjacent to the edge under consideration. Because the adjacent neighbour cell also contributes to the porosity of the edge. The samples at the edges are modified as:

$$\begin{cases} z_{b,i}^{L} = z_{b,i}^{R}, & \text{if } z_{b,i}^{L} < z_{b,i}^{R} \\ z_{b,i}^{R} = z_{b,i}^{L}, & \text{if } z_{b,i}^{L} > z_{b,i}^{R} \end{cases} \tag{4.18}$$

Here, the superscripts L and R denote the left and right sides of the edge, respectively. The idea is to take clustering effects and cell blockage which have been reported in [160, 161] into account. The PMF is computed for each cell and edge once in the pre-processing step and is stored. Once the PMF is obtained, the mesh used for sampling is discarded and therefore the information of the high-resolution bottom elevation is not available anymore. The bottom elevation of each computational cell is set at the lowest value found from the high-resolution mesh. Additionally, the elevation at each edge is stored and used in the subsequent computation. The porosities are updated at the beginning of each time step according to Equations 4.16 and 4.17. It is noted that in Equation 4.16 and 4.17 each sample is weighted equally. This assumes that each sample represents an equal amount of area. This is easy to assume for either square-shaped or rectangular-shaped grid cells if the subgrid-scale elevations are evenly distributed. For a triangular cell, evenly distributed subgrid-scale bottom elevations would not represent equal areas and the equations must be further modified to account for this. One approach would be to perform a Voronoi-tessellation in each cell to calculate weights for each sample. In this study, only structured grids with square-shaped cells are used.

Choice of water elevation for areal porosity calculation

The areal porosity at the edge is calculated according to the water elevation at the edge. Because the edge is an interface between two neighbouring cells, a choice between two water elevations has to be made to calculate the areal porosity, namely the water elevation at the left $\hat{\eta}_L$ and the water elevation at the right $\hat{\eta}_R$ of the edge. In this work, the upstream water elevation is chosen for porosity calculation. For example, if the case illustrated in Figure 4.2 is considered, the areal porosity ψ will be computed according to the water elevation on the left side of the edge $\hat{\eta}_L$. In Figure 4.2, $\hat{z}_b$ is the bottom elevation at the edge. The calculation of $\hat{z}_b$ is discussed in the next section (Section 4.4).

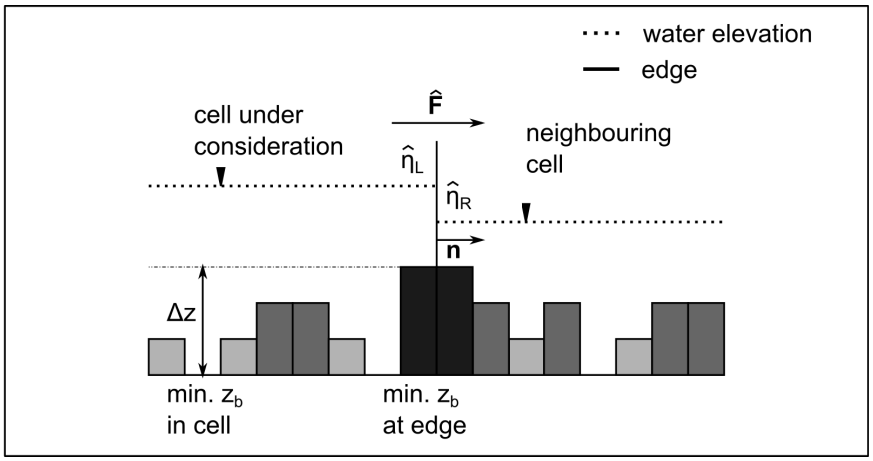

Figure 4.2: Side view of two neighbouring cells for the choice of the water elevation to calculate ψ, the cell under consideration is on the left side, water elevation is dashed line, definitions of Δz, $\mathbf{n}$, $\hat{\eta}_L$ and $\hat{\eta}_R$

Flux computation

The numerical scheme is a Godunov-type explicit finite volume scheme with second order MUSCL reconstruction [150]. Values at cell center are linearly extrapolated to the edges, whereby the slope of the extrapolation function is limited by a min-mod slope limiter [64]. The reconstructed values are used to calculate the numerical fluxes over the cell edge by solving the Riemann problem at the edge using a Harten, Lax and van Leer approximate Riemann solver with the contact wave restored (HLLC) [143]. As suggested in [2], only $\hat{\eta}$, $\hat{\mathbf{q}}$ and $\hat{h}$ are extrapolated. At wet-dry interfaces, the MUSCL reconstruction is omitted to ensure numerical stability [91, 60, 92].

The reconstruction of the bottom elevation at the edge differs slightly from most reconstructions, e.g. [2, 60]. In a first step, the bottom elevation at the edge $z_{b,i}^{rec}$ is calculated as

$$z_{b,i}^{rec} = \hat{\eta}_i - \hat{h}_i. \tag{4.19}$$

In an additional second step the difference between the lowest bed elevation at the edge and the bottom elevation of the cell is calculated:

$$\Delta z_i = z_b^{\text{edge}} - z_{b,i}^{\text{cell}} \tag{4.20}$$

z_b^{edge} refers to the lowest elevation at the edge and $z_{b,i}^{\text{cell}}$ refers to the bottom elevation of the cell on the left or right side of the edge (cf. Figure 4.2).

Then, Δz_i is added to $z_{b,i}^{rec}$:

$$\hat{z}_{b,i} = z_{b,i}^{rec} + \Delta z_i \tag{4.21}$$

The reconstruction carried out for the left and right side of the edge gives $\hat{\eta}_L$, $\hat{\mathbf{q}}_L$, $\hat{h}_L$, $\hat{z}_{b,L}$, $\hat{\eta}_R$, $\hat{\mathbf{q}}_R$, $\hat{h}_R$, $\hat{z}_{b,R}$. Hereinafter, the cell on the left side of the edge is assumed to be the cell under consideration. Then, the non-negative water depth reconstruction [2] is carried out as follows: The bottom elevation at the edge is defined as:

$$\hat{z}_b = \max\left(\hat{z}_{b,L}, \hat{z}_{b,R}\right) \tag{4.22}$$

Water elevation on the left side of the edge and the bottom elevation at the edge are compared and the lower value is set as the new bottom elevation.

$$\hat{z}_b = \min\left(\hat{z}_b, \hat{\eta}_L\right) \tag{4.23}$$

Water depths are reconstructed as:

$$\hat{h}_R = \max\left(0, \hat{\eta}_R - \hat{z}_b\right) - \max\left(0, \hat{z}_{b,R} - \hat{z}_b\right), \quad \hat{h}_L = \hat{\eta}_L - \hat{z}_b \tag{4.24}$$

The vector of velocities at the left and right sides of the edge ($\hat{\mathbf{v}}_i = [\hat{u}_i, \hat{v}_i]^T$) are calculated as:

$$\hat{\mathbf{v}}_i = \begin{cases} 0, & \hat{h}_i < \epsilon \\ \hat{\mathbf{q}}_i / \hat{h}_i, & \hat{h}_i \geq \epsilon \end{cases} \tag{4.25}$$

ϵ is a threshold to avoid division by 0 and further indicates whether a cell is considered wet or dry. In this work it is chosen $\epsilon = 10^{-6}$ m. Finally, $\hat{h}_L$, $\hat{\mathbf{v}}_L$, $\hat{h}_R$ and $\hat{\mathbf{v}}_R$ are used by the HLLC Riemann solver to compute the flux over the edge.

Source term computation

Bed slope and friction source term computation

In Equation 4.1, three source terms have to be numerically solved: the bed slope source term, the friction source term and the solid-fluid interfacial pressure source term. The first two source terms occur as a result of depth-averaging and can be found also in the classical two-dimensional shallow water equations. The last term results from the ground unevenness not resolved by the computational mesh and is discussed in [125, 110].

The bed slope source term can be written as

$$\mathbf{s}_b = \begin{bmatrix} 0 \\ s_{b,x} \\ s_{b,y} \end{bmatrix} \tag{4.26}$$

where the definitions of the terms are given in Equation 4.4. In [148], the divergence form for bed slope is presented, which transforms the bed slope source term within the cell into a flux term over its edges:

$$\int_{\Omega} i\mathbf{s}_b d\Omega = \oint_{\partial\Omega} i\mathbf{F}_b \mathbf{n} dr \tag{4.27}$$

The integral is evaluated and the line integral is approximated by the algebraic expression:

$$\oint_{\partial\Omega} i\mathbf{F}_b \mathbf{n} dr = \sum_k \psi_k r_k \hat{\mathbf{F}}_b \mathbf{n}_k \tag{4.28}$$

Hou et al. [60] propose an extension of this approach to higher order accuracy by dividing the integral over the cell into integrals over subcells. This allows non-linear variations of bed elevation, which is suitable for the model presented in this work because separate bottom elevations are defined at the cell edges. The vector of bed slope flux at edge k is written as:

$$\mathbf{F}_{b,k}\mathbf{n}_k = \begin{bmatrix} 0 \\ -0.5 n_x g \left(h_k + \bar{h}\right) \left(\hat{z}_{b,k} - \bar{z}_b\right) \\ -0.5 n_y g \left(h_k + \bar{h}\right) \left(\hat{z}_{b,k} - \bar{z}_b\right) \end{bmatrix} \tag{4.29}$$

Using Equation 4.10, the evaluation of the integral in Equation 4.28 over edge k in x-direction gives:

$$\begin{aligned} &\int_{\partial\Omega_k} -0.5 i n_x g \left(h_k + \bar{h}\right) \left(\hat{z}_{b,k} - \bar{z}_b\right) dr \\ &= -0.5 g \left(\hat{z}_{b,k} - \bar{z}_b\right) \int_{\partial\Omega_k} g \left(i h_k + i\bar{h}\right) dr \\ &= -0.5 g \left(\hat{z}_{b,k} - \bar{z}_b\right) \left(\psi_k \left(\hat{\eta}_k - z_0\right) r_k + \int_{\partial\Omega_k} i\bar{h} dr \right) \end{aligned} \tag{4.30}$$

The latter integral in Equation 4.30 is approximated with:

$$\int_{\partial\Omega_k} i\bar{h} dr \approx \psi_k \bar{h} r_k \tag{4.31}$$

The evaluation of the integral in y-direction is similar. Then, the evaluated bottom slope flux vector $\hat{\mathbf{F}}_{b,k}\mathbf{n}_k$ over the edge k can be written as:

$$\hat{\mathbf{F}}_{b,k}\mathbf{n}_k = \begin{bmatrix} 0 \\ -0.5 n_x g \left(\hat{\eta}_k - z_0 + \bar{h}\right) \left(\hat{z}_{b,k} - \bar{z}_b\right) \\ -0.5 n_y g \left(\hat{\eta}_k - z_0 + \bar{h}\right) \left(\hat{z}_{b,k} - \bar{z}_b\right) \end{bmatrix} \tag{4.32}$$

For the friction source term, the standard expression of the friction source vector as introduced in Equation 4.5 is used. The term is discretized in a point implicit way as shown in [128].

Solid-fluid interfacial pressure source term computation

The solid-fluid interfacial pressure source term treatment follows the modeling concept in [125]. The term is split into a stationary and non-stationary part:

$$\oint_{\partial\Omega^*} \mathbf{s}^* dr = \oint_{\partial\Omega^*} \mathbf{s}^*_{st} dr + \int_{\Omega} i\mathbf{s}^*_{ns} d\Omega \tag{4.33}$$

The stationary part balances the pressure and flux terms as the flow converges to a stationary state and the non-stationary part results from the water elevation fluctuation inside the computational cell that can not be resolved [125]. The non-stationary term $\mathbf{s}^*_{ns}$ is integrated over the cell. In [125, 113], this term follows a generalized drag law proposed in [107]:

$$\mathbf{s}^*_{ns} = \begin{bmatrix} 0 \\ c_D \bar{u}\sqrt{\bar{u}^2 + \bar{v}^2} \\ c_D \bar{u}\sqrt{\bar{u}^2 + \bar{v}^2} \end{bmatrix} \tag{4.34}$$

c_D is the dimensionless drag coefficient, which is calculated with:

$$c_D = 0.5\, c_D^0 a \cdot \min\left(h, z_b^{\max} - z_b^{\min}\right) \tag{4.35}$$

The parameter a represents the projected width of the obstruction facing the flow per unit planform area and depends on the angle of attack and width of the obstacle [125]. c_D^0 is a reference drag coefficient obtained by calibration, and a is a modification coefficient. In theory, it is possible to determine a exactly from the geometry data and calibrate only c_D^0, yet this is not done in this work. Instead, the model is calibrated using the product $c_D^0 \cdot a$. The reason for this is that calculating the angle of attack for the value of a during the simulation is not trivial. In addition, the value of c_D^0 depends on the Reynolds number and the shape of the obstacle. In [107, 125], it is suggested that the value of a should be estimated in a predictor step and then updated in a corrector step based on the flow values of the predictor step. This approach is not followed in this work, because it requires extra knowledge of the subgrid-scale obstacles beyond the porosity function, i.e. information about the shape and the directionality of the obstacles have to be stored. An additional challenge is that the values of a and c_D^0 depend on the water depth in the cell, as the geometry of the obstacles might vary in the vertical direction. The full assessment of the present approach requires additional research. Additionally, the value $c_D^0 \cdot a$ is assumed constant over the whole domain, because the cases investigated are relatively simple. However, each cell could also be assigned a separate $c_D^0 \cdot a$. This would allow a better representation of the heterogeneity in

the domain, but the drawback is that the model calibration becomes very complicated and requires large quantities of data. This further suggests that a more precise definition of both a and c_D^0 is required. Overall, the calculation of the non-stationary term needs further research.

The stationary part of the interfacial pressure source term is essential, as it well-balances the scheme. Here, the vector of the stationary interfacial pressure source term is derived by evaluating the C-property of the scheme. This leads to the same formulation as in [125]:

$$\oint_{\partial\Omega^*} \mathbf{s}_{st}^* dr = \sum_k \psi_k \hat{\mathbf{F}}_{*,k} \mathbf{n}_k r_k, \tag{4.36}$$

with:

$$\hat{\mathbf{F}}_{*,k} = \begin{bmatrix} 0 \\ 0.5\bar{h}^2 n_{k,x} \\ 0.5\bar{h}^2 n_{k,y} \end{bmatrix} \tag{4.37}$$

The proof of C-property is trivial and omitted for sake of brevity.

Time integration

A two-step total variation diminishing Runge-Kutta method [45] is used. The values at next time step $n+1$ are calculated in two stages. The first stage is

$$\tilde{\phi}^{n+1}\tilde{\mathbf{q}}^{n+1} = \phi^n \mathbf{q}^n - \Delta t \sum_k \psi_k^n \hat{\mathbf{F}}_{tot,k}^n r_k \mathbf{n}_k + \Delta t \phi^n (\mathbf{s}^n + \mathbf{s}_{ns}^{*,n})\Omega, \tag{4.38}$$

and the final value is then calculated as

$$\begin{aligned} &\phi^{n+1}\mathbf{q}^{n+1} = \\ &\frac{1}{2}(\phi^n \mathbf{q}^n + \tilde{\phi}^{n+1}\tilde{\mathbf{q}}^{n+1} \\ &- \Delta t \sum_k \psi_k^n \tilde{\hat{\mathbf{F}}}_{tot,k}^{n+1} r_k \mathbf{n}_k + \Delta t \tilde{\phi}^{n+1}(\tilde{\mathbf{s}}^{n+1} + \mathbf{s}_{ns}^{*,n+1})\Omega). \end{aligned} \tag{4.39}$$

Here, $\hat{\mathbf{F}}_{tot,k} = \hat{\mathbf{F}}_k - \hat{\mathbf{F}}_{b,k} - \hat{\mathbf{F}}_{*,k}$. The first term of the vector $\phi^{n+1}\mathbf{q}^{n+1}$, i.e. $\phi^{n+1}\left(\bar{\eta} - z_0\right)^{n+1}$ expresses the volume of water inside the cell. In order to determine the individual value of ϕ^{n+1} and $\bar{\mathbf{q}}^{n+1}$, a corresponding water depth has to be calculated. In literature, tabulated values are used to map water volume to a certain water elevation [117]. In this work, the exact values of ϕ^{n+1} and $(\bar{\eta} - z_0)^{n+1}$ are calculated from the water volume in an iterative way. Once $\left(\bar{\eta} - z_0\right)^{n+1}$ is calculated, ϕ^{n+1}, q_x and q_y can be determined. Using an iterative solution significantly increases the computational

cost. In the current model implementation, the evaluation of porosities, i.e. Equations 4.16 and 4.17, turns out to be the most expensive part of the code, taking up to 15% of the total CPU time. It is important to note that this is not the one-off evaluation of porosity, but all evaluations summed up. The reason for the high cost is that, due to their dependency on water depth, the porosity values have to be evaluated several times for different water depths during one time step. Equation 4.16 is solved at the beginning of the time step in each cell. During MUSCL reconstruction Equation 4.17 is solved at each edge. Then, Equation 4.16 is solved repeatedly during the iterative procedure to determine the new water depth and porosity in the next time step. For a two-stage Runge-Kutta method all these calculations have to be carried out twice in each time step.

A more efficient, approximate solution for this problem is presented in [161]. However, in our opinion the calculation of the water depth should have very high accuracy, so the mass conservation is strictly satisfied.

The presented scheme is of explicit nature and therefore its stability is restricted by the Courant-Friedrichs-Lewy criterion (CFL), although the theoretical analyses of the stability constraint are very complicated for the present equations. The CFL criteria given in [125] is

$$Cr = \psi\lambda\Delta r\frac{\Delta t}{\phi\Omega} \leq 1, \tag{4.40}$$

where $\lambda = |un_x + vn_y| + \sqrt{gh}$ is the largest wavespeed at the cell edge. Numerical experiments show that Equation 4.40 degenerates the time step in cases with small porosity such that in the worst case the simulation comes to a halt.

In this work, the CFL number is heuristically calculated as

$$Cr = \frac{\left(|\mathbf{v}| + \sqrt{gh}\right)\Delta t}{\Delta x}. \tag{4.41}$$

For the presented cases, $Cr < 0.3$ gives satisfactory results.

Boundary conditions

Boundary conditions are imposed on the boundary edge of the cell according to the theory of characteristics proposed in [135]. State variables at the boundary edge can be computed using Riemann invariants. The porosities are mirrored from the cell inside the domain.

4.5 Computational examples

Kim *et al.* [76] noted three types of errors of the porous shallow water model: (1) structural model errors, (2) scale errors and (3) porosity model errors. Errors of type 1 refer to the limitations of the mathematical model concept of the shallow water equations and are defined by the difference between measurement and high-resolution model (HR) results. Errors of type 2 are associated with the lack of sufficient grid resolution. In [76] it is suggested to study the difference between HR model results and the HR model results which have been averaged over each porosity model grid cell (CR, standing for coarse-resolution). Errors of type 3 are the errors introduced by the porosity concept and are defined as the difference between the porosity model results (AP, standing for anisotropic porosity) and the CR model results.

Following the studies presented in [76], the errors are computed using an L_1-norm:

$$L_1 = \frac{1}{N} \sum_{j=1}^{N} |w_{1,j} - w_{2,j}| \tag{4.42}$$

Here, N is the number of points compared, w stands for a variable, e.g. h or q, $w_{1,j}$ and $w_{2,j}$ are results of two different models and j is the point index. The AP model is first calibrated by minimizing the L_1-norm in a manual calibration process. In a second step the fine calibration is automated using the SciPy library [72]. In the following examples, the errors of type 1, 2 and 3 as well as the differences between HR model and AP model, and AP model and measurement data are presented.

The classical shallow water model used for obtaining the reference results is the model presented in [128]. All simulations are run in parallel with 8 threads of an Intel® Core™ i7-2600 CPU (3.40 GHz).

All triangular meshes are generated using the mesh generator Gmsh [42].

Idealized test case: Dam-break flow through artificial street network

The first test case is a test case which is initially proposed in [48]. The HR model is used to generate the reference solution. The aim of this test case is to assess the sensitivity of the porosities ϕ and ψ to the mesh. Thus, different meshing strategies for the AP model are compared against each other. A second objective is to test the sensitivity of the model to the proposed drag coefficient $a \cdot c_D^0$. For this purpose, the drag coefficient is varied and the results are compared.

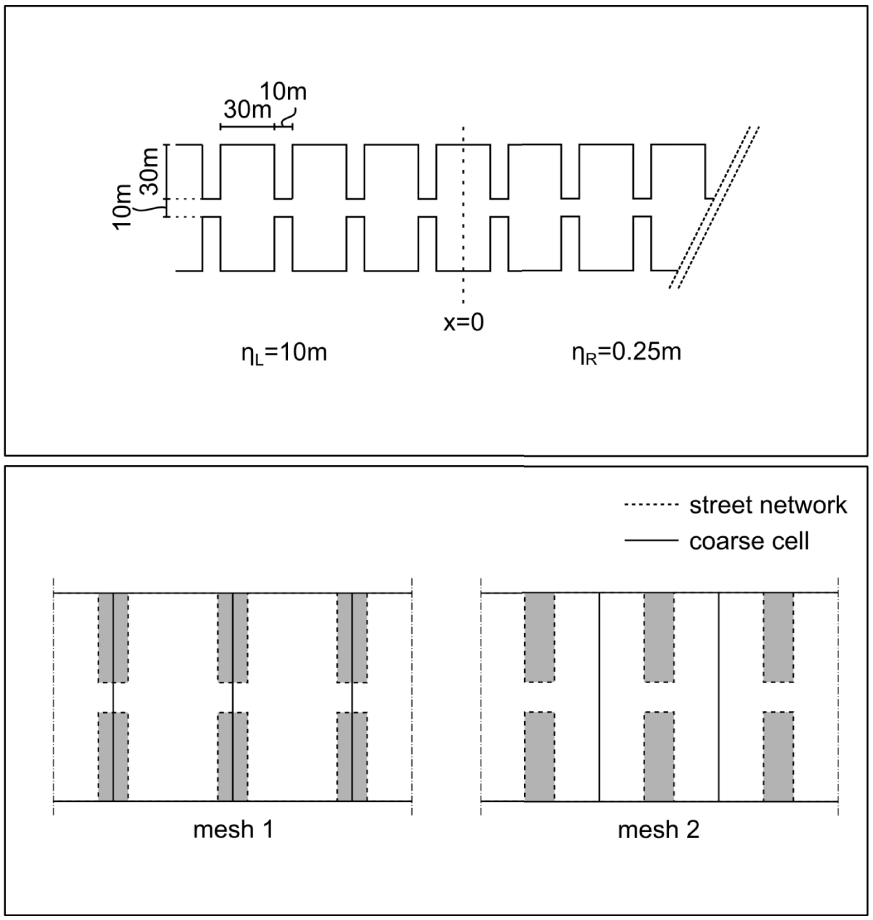

Figure 4.3: Idealized test case: Dam-break flow through periodic structures: Top view on domain (not correctly scaled) [48] (top), meshing strategies (bottom)

Domain description, initial and boundary conditions

The computational domain is an infinitely long, frictionless street with periodical structures as shown in Figure 4.3. The initial water elevation on the left is $\eta_L = 10\,\mathrm{m}$ and on the right side $\eta_R = 0.25\,\mathrm{m}$. The discontinuity of water elevation located at $x = 0$, which is the middle of the domain.

The HR model is two-dimensional and uses triangular cells with a characteristic length of 1 m. The AP model is one-dimensional with a cell length of 40 m.

Influence of different meshes and areal porosity

The AP model is expected to be sensitive to the mesh, because the areal porosity ψ depends on the position of the cell edge. Two configurations are investigated: (1) the cell edge is located at the narrow section of the street network (cf. Figure 4.3 (bottom left)), i.e. $\psi = 1/7$, (2) the cell edge is located in the wider section of the street network (cf. Figure 4.3 (bottom right)), i.e. $\psi = 1$. The volumetric porosity in both cases is the same and is calculated to be $\phi = 11/14$. Thus, the difference in results can be directly related to the different areal porosities.

Comparison of model results at $t = 50\,\mathrm{s}$ are plotted in Figure 4.4 (top). The AP model with $\psi = 1/7$ (mesh 1) produces the blockade effects of the structure better than the AP model with $\psi = 1$ (mesh 2). Because both models do not resolve the street network explicitly, they can not reproduce the local fluctuations in the water elevation. In both models, the right-traveling shock wave as well as the left-traveling rarefaction wave are not captured accurately. If the edge is placed at the narrow section of the street network (mesh 1), introduces correct amount of resistance to the flow. In upstream direction, the water depth is slightly underpredicted. While the agreement is not perfect, the AP model results resemble the HR model solution. If the edge is placed at the wide section, the model is equivalent to the isotropic porosity shallow water model of [51, 132]. Here, the shock and rarefaction waves advance too quickly, and the AP model results are completely different from the HR model results.

The CR model is compared with the AP model with $\psi = 1/7$ in Figure 4.4 (middle left) and with the AP model with $\psi = 1$ in Figure 4.4 (middle right). The CR model is more diffusive than the HR model. Local water depth fluctuations are averaged out. The AP model with $\psi = 1/7$ shows better agreement with the CR model results than the AP model with $\psi = 1$.

This shows that the AP model results are very sensitive to the areal porosity ψ and therefore are very sensitive to the mesh. Results indicate that the mesh should be constructed in such way that the cell edges are located on the blocking structures to capture their influence. If a structure is located completely inside a cell, its influence on the flow is only modeled by the volumetric porosity which can not model its obstruction to the flow sufficiently.

The right traveling shock wave in the AP model advances too slow. The reason for this might be that the local acceleration at narrow sections can not be taken into account by the AP model, which leads to an underestimation of the mass and momentum fluxes.

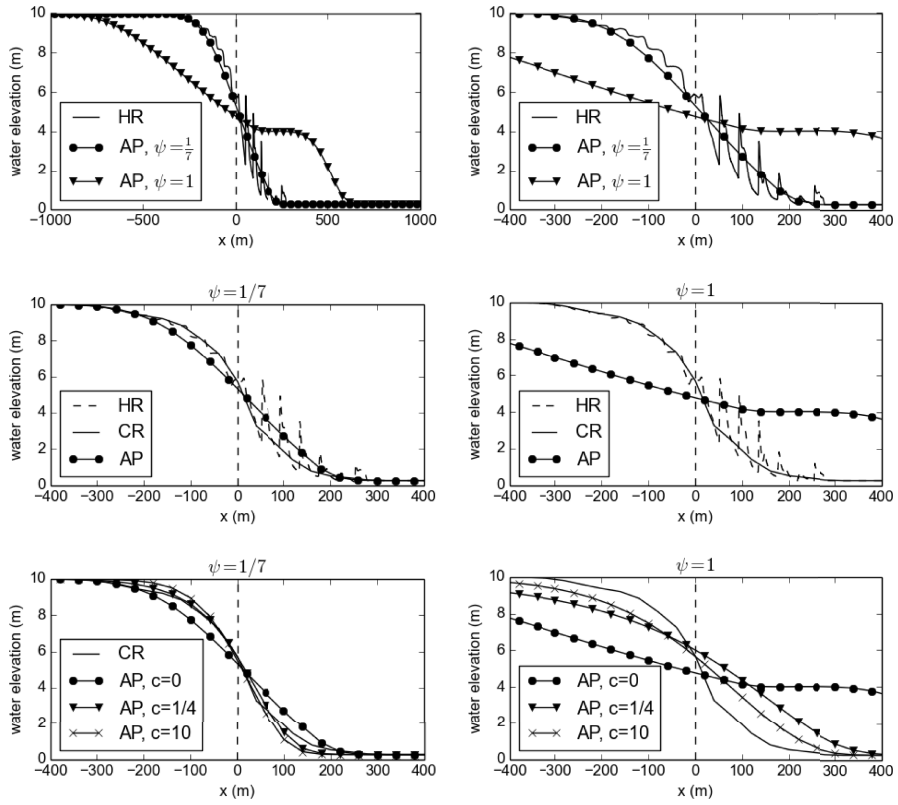

Figure 4.4: Idealized test case: Dam-break flow through periodic structures: Results for $a \cdot c_D^0 = 0$ at $t = 50\,\mathrm{s}$ in the whole domain (top left), detail of the results for $x = [-400, 400]$ (top right), CR model results for water depth compared with HR model results and AP model with $\psi = 1/7$ (middle left), and AP model with $\psi = 1$ (middle right), CR model results for water depth compared with AP model results for different values of $c = a \cdot c_D^0$ at $t = 50\,\mathrm{s}$ for $\psi = 1/7$ (bottom left), for $\psi = 1$ (bottom right)

Influence of drag coefficient

The value $a \cdot c_D^0$ is now varied to study its influence on the AP model. Beginning from $a \cdot c_D^0 = 0$, the value is increased with a step size of $0.25\,\mathrm{m}^{-1}$ until $a \cdot c_D^0 = 10\,\mathrm{m}^{-1}$. Figure 4.4 (bottom left) shows the AP model with $\psi = 1/7$, while Figure 4.4 (bottom right) shows the AP model results with $\psi = 1$. In both cases, increasing the drag coefficient improves the agreement until a critical value $a \cdot c_D^0 > 1$ is exceeded. After that, the drag coefficient does not change the result anymore. For the AP model with $\psi = 1/7$, the value $a \cdot c_D^0 = 0.25$ gives the best agreement. For the AP model with $\psi = 1$ the agreement improves for $a \cdot c_D^0 > 1$ but stays overall poor.

Figure 4.5 compares the sensitivity of both models to the drag coefficient. For this purpose, Δ is calculated as

$$\Delta_i = L_1 \left(AP((ac_D^0)_i), AP((ac_D^0)_{i+1}) \right) \tag{4.43}$$

where $(ac_D^0)_0 = 0$, $(ac_D^0)_1 = 0.25$, $(ac_D^0)_2 = 0.5$, and so on, and $AP(x)$ is the result of the AP model for the drag coefficient x. For a meaningful comparison, Figure 4.5 shows a normalized value obtained by dividing each Δ_i by the maximum Δ_i, i.e.

$$\Delta_{n,i} = \frac{\Delta_i}{\max \Delta_i}. \tag{4.44}$$

Figure 4.5 shows, that the AP model with $\psi = 1/7$ is less sensitive to the drag coefficient than the AP model with $\psi = 1$. This implies that the areal porosity effect dominates the flow such that the influence of the drag force on the momentum is less significant. For values $ac_D^0 > 1$, the influence of the increasing drag coefficient is negligible. This is because the numerical scheme limits the drag force source term in such way that the flow direction is not reversed.

If the areal porosities are large, the numerical flux is not limited as strictly and blocking effects of the obstructions are not reproduced as well as for smaller areal porosities. In this case, increasing the drag coefficient has larger influence on model results. The drag force depends only on the volumetric porosity, which is the same for both cases. Increasing the drag coefficient has a similar effect as increasing the friction coefficient and the results are similar to the findings by Liang *et al.* [88] who capture the effect of buildings to some extent using an increased roughness coefficient. If the areal porosities are small, the flow is blocked more severely at the edges and the flow velocity is not as high as in the unobstructed flow. Therefore, changing the value of $a \cdot c_D^0$ does not effect the results as much.

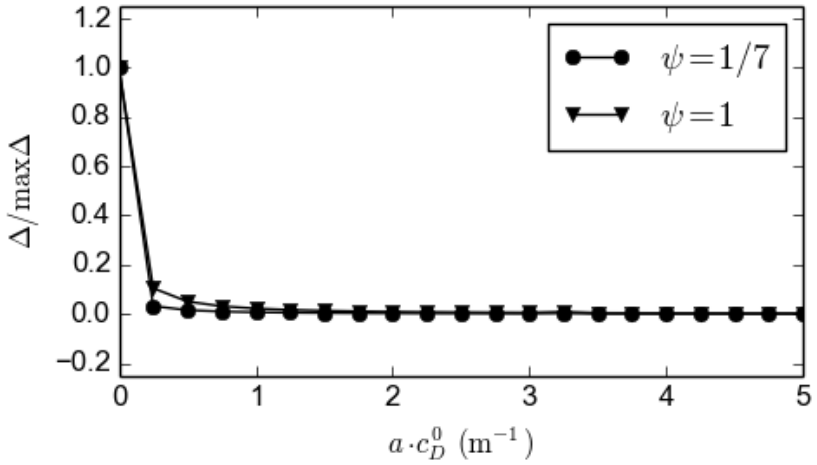

Figure 4.5: Idealized test case: Dam-break flow through periodic structures: Sensitivity of the AP model results for different values of $a \cdot c_D^0$ at $t = 50\,\mathrm{s}$ with $\Delta_i = L_1[AP(ac_D^0)_i - AP(ac_D^0)_{i+1}]$

Dam-break flow over a triangular bottom sill

Herein, the depth-dependent porosity is demonstrated by replicating a laboratory experiment conducted at the Université catholique de Louvain, Belgium, [134].

Domain description, initial and boundary conditions

The experiment was carried out in a 5.6 m long and 0.5 m width channel. The peak of the triangular bottom sill is located at $x = 4.45\,\mathrm{m}$ and is 0.065 m high. The sill is symmetrical and has a base length of 0.9 m. The initial conditions and the geometry is given in Figure 4.6. An initial water elevation of $\eta_{res} = 0.111\,\mathrm{m}$ is ponding in the reservoir before the gate is opened. The gate is located at $x = 2.39\,\mathrm{m}$. On the downstream side of the sill, water is at rest with an initial water elevation of $\eta = 0.02\,\mathrm{m}$.

The HR model uses square shaped cells with a side length of 0.01 m. It is noted that this test case is essentially one-dimensional. However, the domain was discretized in two dimensions, resulting in a mesh with 28000 cells. The AP model uses square shaped cells with side length of 0.4 m, which gives a mesh with 56 cells. The bottom of the AP model is completely flat and the sill is accounted for only by the porosity terms. Figure 4.7

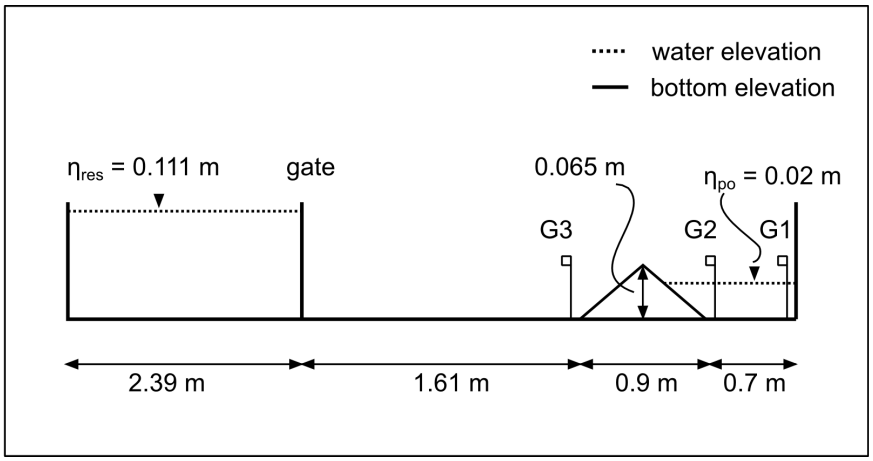

Figure 4.6: Dam-break over triangular bottom sill: Side view on domain (not correctly scaled) [134]

(bottom right) shows a sideview of the AP model mesh with the HR model bed elevation plotted for reference.

Measured water depth over time is available at 3 measurement gauges, located at $x = 5.575\,\mathrm{m}$ (G1), $x = 4.925\,\mathrm{m}$ (G2) and $x = 3.935\,\mathrm{m}$ (G3). The locations of the gauges are given in Figure 4.6.

The roughness of the channel is quantified in [134] with a Manning's coefficient of $n = 0.011\,\mathrm{sm}^{-1/3}$. This value is used both in the HR and the AP model.

Model calibration and run time

The AP model is calibrated by changing the value $a \cdot c_D^0$ in Equation 4.35. Calibration is carried out manually using the CR model as reference. Good agreement has been achieved with $a{\cdot}c_D^0 = 5\,\mathrm{m}^{-1}$. The HR model takes about 4000 s to finish, while the AP model takes only 3.5 s. This corresponds to a speedup of about 1140.

Error analysis

Structural model errors This test case features an obstruction that is unsubmerged at the beginning of the simulation, completely submerged by the dam-break wave in the middle of the simulation, partially submerged towards the end of the simulation. In Figure 4.7, snapshots of the HR model results at various times are shown. The HR model shows excellent

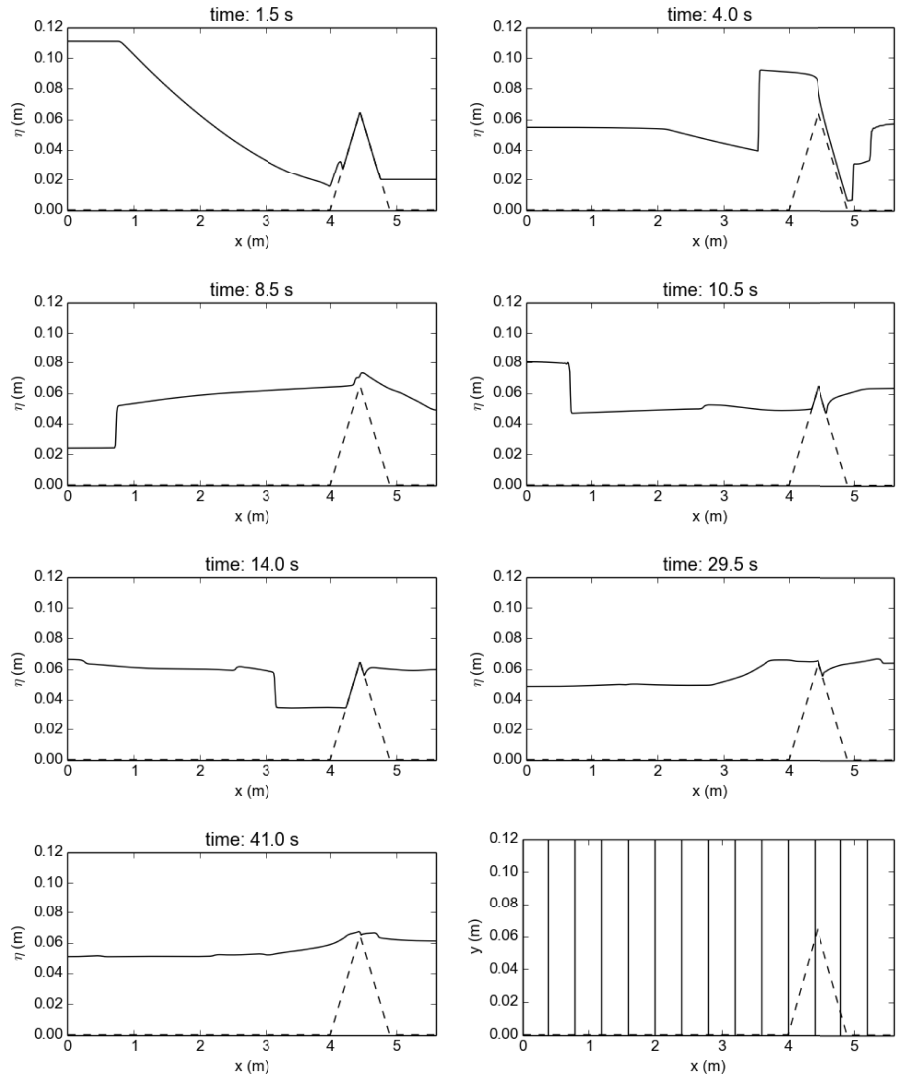

Figure 4.7: Dam-break over triangular bottom sill: Snapshots at different time steps of HR model results for water elevation and AP model mesh plotted over HR model bed elevation (bottom right)

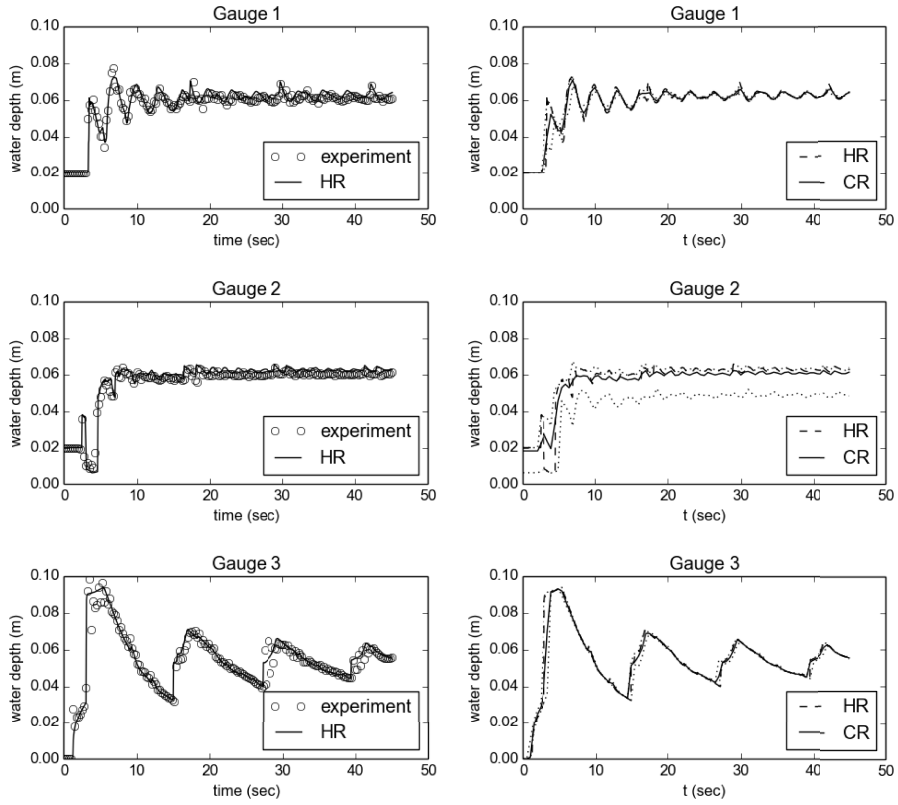

Figure 4.8: Dam-break over triangular bottom sill: HR model results for water depth compared with experimental data [134] (left), CR model results for water depth compared with HR model results, dotted lines denote the minimum and maximum values inside the coarse cell (right)

agreement with the experimental results, as seen in Figure 4.8 (left), especially at gauge 2 and gauge 3. The larger discrepancy at gauge 1 might be explained by the splashing of water in the experiment which can not be reproduced by the shallow water equations.

Scale errors Scale errors are calculated by mapping the HR model results to a coarser grid, which in this study is the grid of the AP model. The value at a low resolution cell is determined by arithmetic averaging the values over all the high-resolution cells lying inside the low resolution cell. The CR model results show very good agreement with the HR model results, as seen in Figure 4.8 (right), where the comparison at the three gauges is shown. The dotted lines show the maximum and minimum water depths

sampled inside the coarse grid. It can be seen that at gauge 1 and gauge 3, the difference between the minimum and the maximum water depth is low. At gauge 2, which is located just behind the sill, the deviation is high. Owing to the reflected waves, the flow at gauge 2 is more complex than at the other gauges. Consequently, here the agreement between CR model and HR model is not as close as at the other gauges. It is observed that the CR model introduces some diffusion to the results and the curves are smoother than the HR model results.

Porosity model errors The porosity model errors are assessed by comparing AP model results to CR model results, as shown in Figure 4.9 (left). The AP model shows good agreement with the CR model at all gauges. At gauge 1, which is located furthest away from the gate the predicted wave arrives a bit late. However, after 5 s the arrival time of the second peak is captured despite the slightly undershot peak water level. The third peak is captured accurately. After that, the AP model does not predict as much fluctuation as the CR model but the average water elevation does not differ much. The agreement at gauge 2 and gauge 3 is much better. Especially at gauge 3 all waves are captured with good agreement. At gauge 2, the rise of the curve starts correctly but the AP model overshoots the CR model at about 8 s. A comparison between AP model result with experimental data is shown in Figure 4.9 (right). The AP model reproduces the experimental data well.

Summary The L_1-errors are listed in Table 4.1 and 4.2. In both tables, the errors are calculated as the arithmetic mean of the errors at the 3 gauges. Table 4.1 shows a summary of the cell sizes and L_1-errors for HR model, CR model and AP model. Here, the errors are calculated using the experimental data as a reference. Overall, the errors are two orders of magnitude smaller than the initial water elevation in the reservoir ($\eta_{res} = 0.111\,\mathrm{m}$). The L_1-errors for structural, scale and porosity model errors are summarised in Table 4.2. All errors are in the same order of magnitude, which is one order of magnitude smaller than the maximum measured water depth. The porosity model (E_3) error is the largest, followed by the structural model error (E_1). The scale error (E_2) is the smallest error. It is concluded that in this example, the error introduced by the coarse grid is the smallest. The mathematical model limitation of the shallow water equations introduces larger errors than the grid coarsening, but the largest error is introduced by not resolving the sill explicitly.

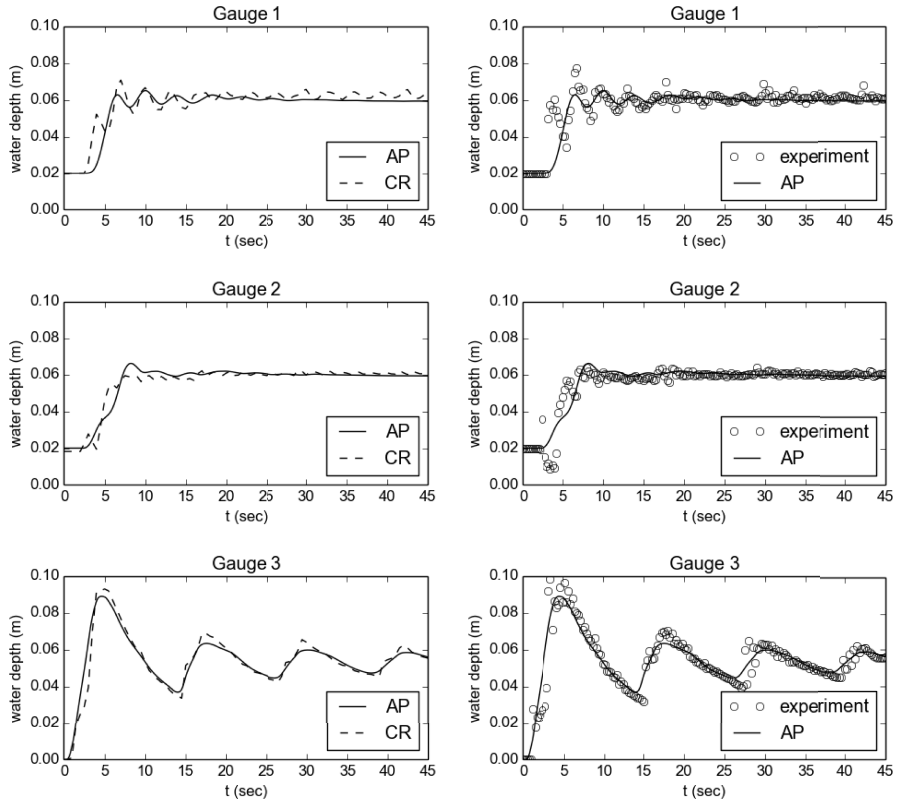

Figure 4.9: Dam-break over triangular bottom sill: AP model results for water depth compared with CR model results (left), AP model results for water depth compared with experimental data [134] (right)

Model	Mesh	Resol. (m)	Cell nr.	Time (s)	L_1 (m)
HR	Square	0.01	28000	4000	0.0024
CR	Square	0.01	28000	4000	0.0031
AP	Square	0.4	56	3.5	0.0035

Table 4.1: Dam-break over triangular bottom sill: Summary of shallow water model formulations and corresponding meshes (HR: High-resolution, CR: averaged HR model, AP: anisotropic porosity); L_1-norm is calculated with regard to the experimental results

Type	L_1 (m)
E_1	0.0024
E_2	0.0016
E_3	0.0038

Table 4.2: Dam-break over triangular sill: Model error (E_1), scale error (E_2) and porosity error (E_3)

Dam-break flow through an idealized city

In this computational example, results of a dam-break experiment conducted at the Université catholique de Louvain, Belgium, [133] are numerically reproduced.

Domain description, initial and boundary conditions

The domain is a 35.8 m long and 3.6 m wide channel with horizontal bed. The idealized city consists of 5×5 buildings, each of them being a square block with a side length of 0.30 m. The distance between the blocks is 0.10 m. The center of the building block is placed 5.95 m away from the gate and rotated 22.5° in counter-clockwise direction around its center. The dam-break is constructed by opening a 1 m gate, which initially seperates the reservoir, where water is ponding at 0.40 m, from the rest of the channel, where a very thin layer of 0.011 m water is reported. For further details on the experimental setup and employed measurement techniques, the reader is referred to [133]. The domain is illustrated in Figure 4.10 (top left), where the reservoir is coloured in grey.

The computational domain only includes the reservoir and the first 16 m of the channel. For the duration of the simulations, $t = 15.5$ s, the shock wave does not travel further than this length. The downstream boundary is an open boundary and all other boundaries are closed boundaries.

The HR model uses a triangular mesh with variable cell sizes: the reservoir is discretized with cells with a characteristic length of $l_{c,1} = 0.3$ m. The area inside the channel which is sufficiently far away from the building blocks is discretized with a characteristic length of $l_{c,2} = 0.1$ m. The space between the buildings is discretized with a characteristic length of $l_{c,3} = 0.01$ m. The buildings are represented as holes in the mesh, which is a method commonly used in urban flood modeling [127]. Hence, the gap between two buildings is discretized with about 10 cells and the total cell number is 96339. The AP model uses square-shaped cells with side length 0.25 m, whereby the volumetric porosity is calculated using 125 subgrid

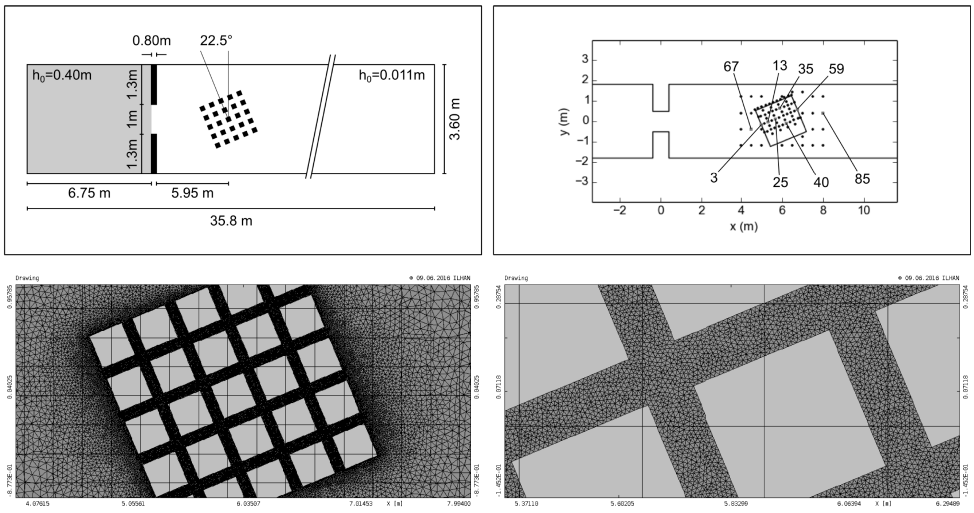

Figure 4.10: Dam-break through idealized city: Top view on domain (not correctly scaled) [133] (top left), position of all 87 gauges (black), results are plotted for 8 gauges (indicated by their numbers), the boundary of the building block is plotted for reference (top right), comparison of HR model mesh (triangular) and CR and AP model mesh (square), meshing of the building block (bottom left), mesh detail between houses (bottom right)

cells, resulting in a mesh with 1272 cells. The HR mesh is compared to the AP model mesh in Figure 4.10 (bottom). Both meshes in the region of the building block is shown in Figure 4.10 (bottom left), while in Figure 4.10 (bottom right) a close-up view is shown. A building is in general contained in 4 AP model cells. The buildings do not align with the cell edges. As discussed in Section 4.5, the blocking effect of buildings is not captured accurately if the building is positioned inside the cell instead of at the edge, but this is inevitable for some fron-row houses (cf. Figure 4.10 (bottom)).

Experimental data are available at 87 measurement gauges distributed inside the channel [133]. The positions of these gauges are given in Figure 4.10 (top right). In the discussion, results are plotted for 8 gauges, namely gauges 3, 13, 25, 35, 40, 59, 67 and 85.

The roughness of the channel has been estimated in [133] with a Manning's coefficient of $n = 0.01\,\mathrm{sm}^{1/3}$. This value is used for both the HR and the AP model.

Model calibration and run time

The AP model is calibrated with the value $a \cdot c_D^0$ in the drag law, given in Equation 4.35. Calibration is carried out with regard to the CR model results using Brent's algorithm for minimisation [7]. Brent's search returns $a \cdot c_D^0 = 1.9\,\mathrm{m}^{-1}$ with a corresponding L_1-error of 0.025 m. The HR model simulation takes about 3000 s to finish. The AP model requires about 4 s. Consequently, the speedup is calculated as 750.

Error analysis

Structural model errors The HR model makes overall an acceptable prediction of the water depth at the evaluated gauges. In Figure 4.11, the water depth calculated by the HR model at the aforementioned gauges is plotted together with the measured water depth. The arrival time of the wave is predicted correctly at all gauges, although the HR model predicts a slightly later arrival. Larger deviations between the results occur at the later stages of the simulation, where the HR model results undershoot the experimental data. For this test case, Soares-Frazão and Zech [133] report lower computed water depths as well. The deviations might partly be caused by the frictionless wall-boundaries imposed at the buildings and the wave reflections that can not be modeled by the shallow water equations. The model overestimates the the flow velocities, leading to overall lower water depths. As time passes, this effect becomes more significant. Gauge 67 is located in front of the houses. Overall, the characteristics of the experimental data set are captured by the HR model, i.e. the small peak at around $t = 2\,\mathrm{s}$ and the rise at around $t = 4\,\mathrm{s}$, however the first peak is delayed and the second rise at $t = 4\,\mathrm{s}$ is too early. In general, the HR model appears to overpredict the steepness of the water level variations. This is especially distinct at the sharp rise of the HR model curve at $t = 4\,\mathrm{s}$ in comparison to the smoother rise of the experimental curve. As in [133], this indicates that the entrance contraction can not be reproduced by the mathematical model. This is also indicated by the discrepancies at gauge 3, which is located at the entrance of the building block. The rise of the water level is again delayed. The drop in water depth at around $t = 6\,\mathrm{s}$ is not observed in the experiment. Gauge 13, located slightly behind gauge 3, shows good agreement. Here, the front of the wave is captured accurately in time. The agreement at gauges 25, 35 and 59, which are all located between the buildings, is very well.

Gauge 40, which is also located between the buildings, shows worse agreement than the aforementioned gauges. As at gauge 3, the general

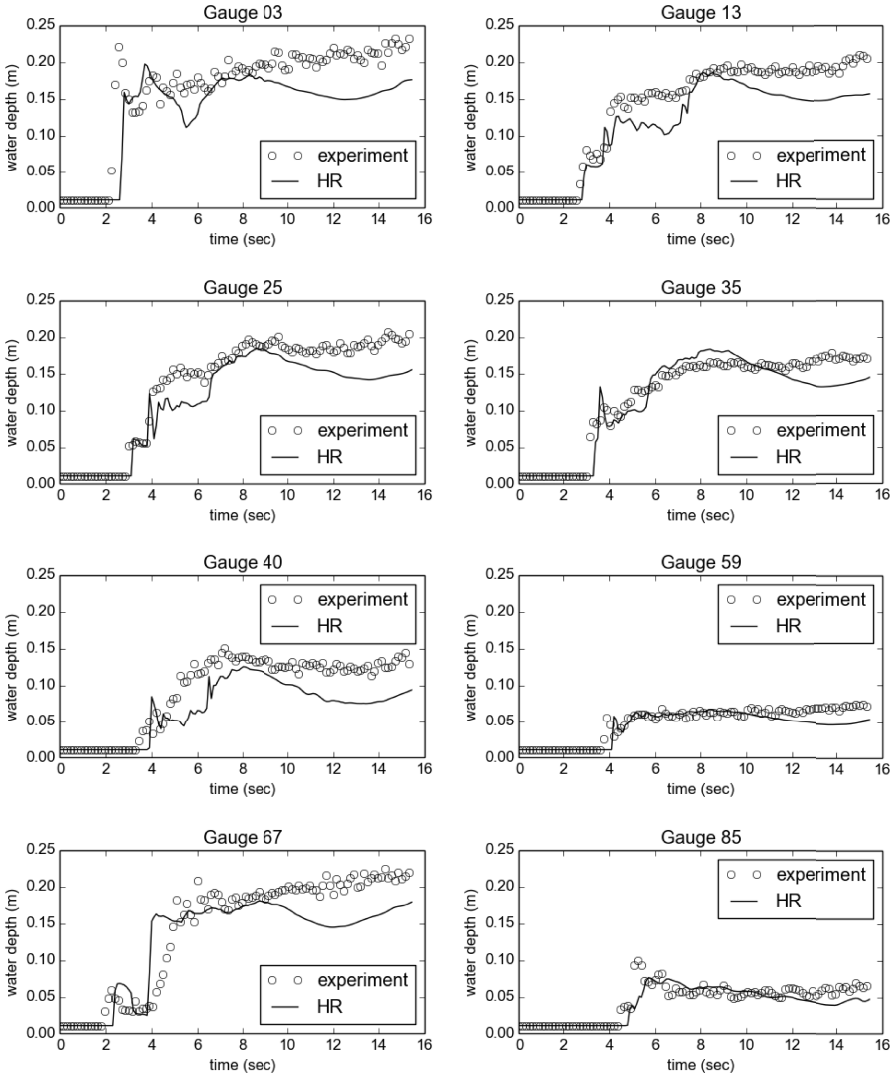

Figure 4.11: Dam-break through idealized city: HR model results for water depth compared with experimental data of [133]

shape of the experimental data is reproduced. Finally, at gauge 85, which is outside of the building block, good agreement is achieved.

Overall, this is a challenging test case for the mathematical model. The angled position of the buildings that are not aligned with the flow direction coupled with the hydraulic jump at the entrance of the building block increases the difficulty. In addition, wave reflections and turbulent eddies are not accounted for in the model. Consequently, the structural model error is relatively high.

Scale errors In Figure 4.12, the averaged water depth is plotted against the HR model water depth at the four gauges. The measured water depth is omitted to avoid cluttering the figure. Maximum and minimum values of the high-resolution cells lying inside the low-resolution cell are plotted as well. Overall, the averaging process smooths out the HR model results. Local fluctuations are not captured by the CR model. It is noted that a large difference between the minimum and the maximum in a coarse cell indicates complex flows. As expected, the location of the gauge can be related to the complexity of the flow. Gauges 67 and 85 are located outside of the building block and the minimum and maximum of the values at these gauges do not differ much. Conversely for the other gauges located between the buildings, the local fluctuation is high. In general, the difference between the minimum and maximum gives a good indication for the difference between HR and CR model. If the flow in a coarse cell is complex, there exist high differences between minimum and maximum water levels inside the cell. This complex flow can not be resolved on the scale of the CR model, thus it introduces an error due to scale to the CR model result. Consequently, the difference between HR and CR model is high at, e.g. Gauge 3, positioned at the front of the building block where the flow is complex, and at Gauge 40, located at a crossroad. In contrast, if the flow inside a coarse cell is relatively smooth, the loss of information due to low resolution is not that severe. This is seen, e.g. at Gauge 85, located outside of the building block.

Porosity model errors The AP model shows acceptable agreement with the CR model, although some gauges observe less good agreement, e.g. gauge 85 the agreement is poor. In general, the results of the AP model are smoother and more "smeared" than the CR model results. In Figure 4.13, AP and CR model results are plotted for eight gauges. The AP model water depth at gauge 3 shows similarities to the maximum value at this gauge. Gauges 13, 25 and 67 show good agreement. At gauge 35, the shape of the curve is reproduced but the AP model underestimates the

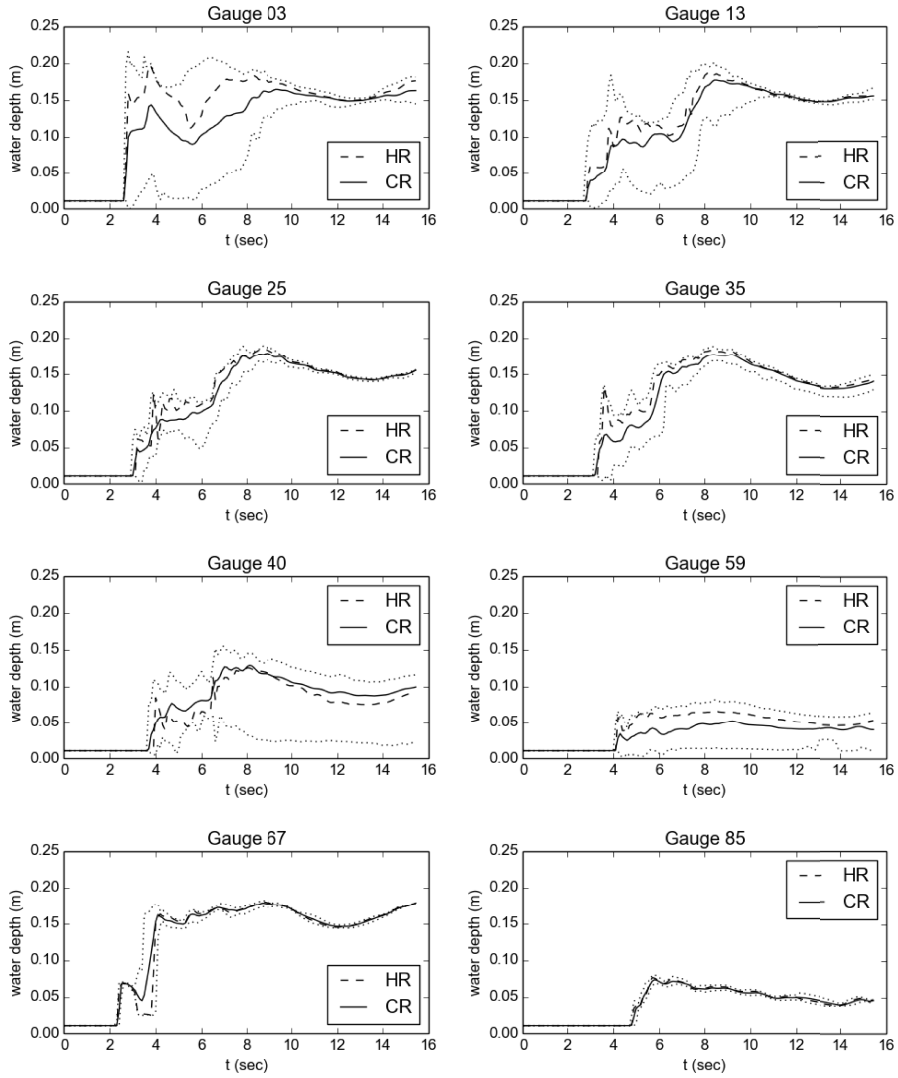

Figure 4.12: Dam-break through idealized city: CR model results for water depth compared with HR model results, dotted lines denote the minimum and maximum values inside the coarse cell

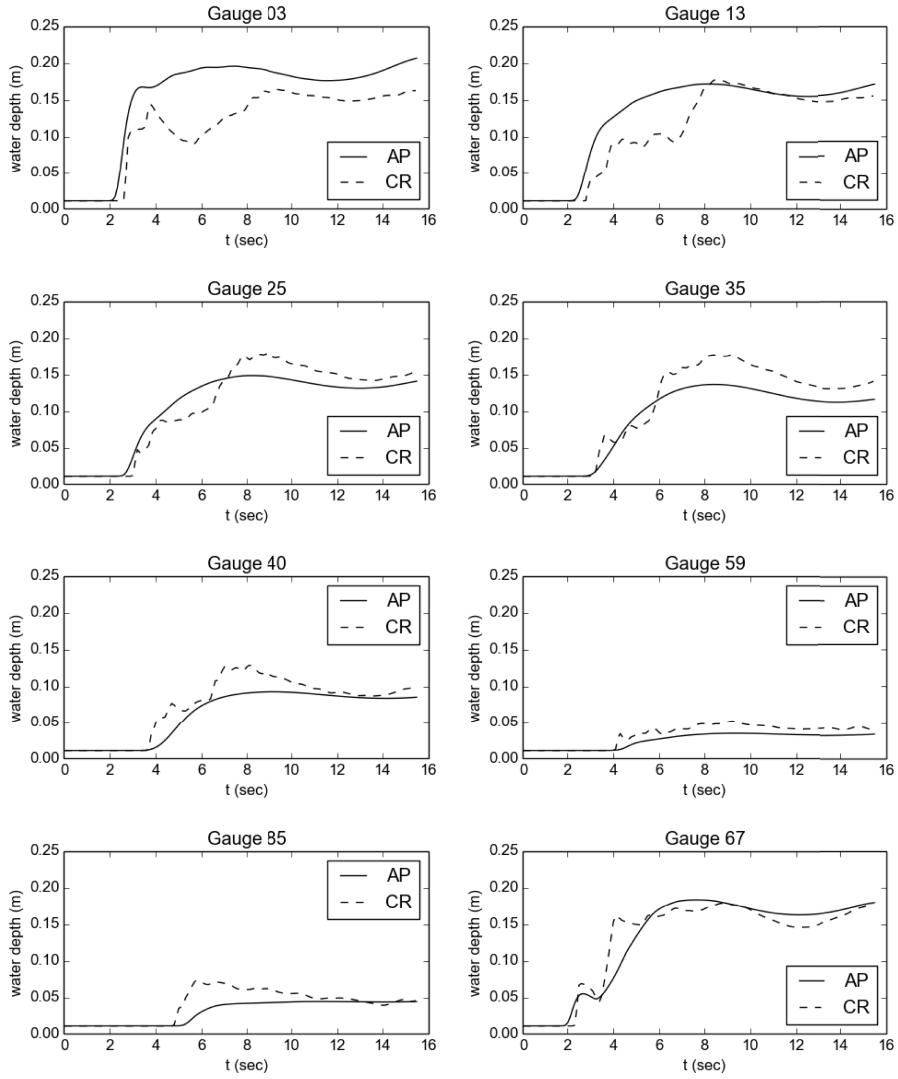

Figure 4.13: Dam-break through idealized city: AP model results for water depth compared with CR model results

water depth. Gauge 85, which is located behind the building block, shows the worst agreement among the eight presented gauges. The AP model is unable to reproduce the CR model result, with underestimated peak water level and delayed arrival time. Overall, the general properties of the AP model results, i.e. the lack of local and spatial fluctutations, are consistent with the findings in [76].

Model	Mesh	Resol. (m)	Cell nr.	Time (s)	L_1 (m)
HR	Triangle	0.01 - 0.3	95975	3000	0.020
CR	Triangle	0.01 - 0.3	95975	3000	0.021
AP	Square	0.25	1272	4	0.026

Table 4.3: Dam-break through idealized city: Summary of shallow water model formulations and corresponding meshes (HR: High-resolution, CR: averaged HR model, AP: anisotropic porosity); L_1-norm is calculated with regard to the experimental results

Type	L_1 (m)
E_1	0.020
E_2	0.018
E_3	0.025

Table 4.4: Dam-break through idealized city: Model error (E_1), scale error (E_2) and porosity error (E_3)

Summary An overview of the results of this computational study is given in Table 4.3 and 4.4. The L_1-errors in Table 4.3 are calculated by taking the measured data by averaging the L_1-errors of all 87 gauges. Moreover, the AP model results are plotted against the measurement data in Figure 4.14. The errors are as expected: the HR model has the lowest error, the CR model comes second and the AP model shows the largest error. However, the errors have the same order of magnitude and are one order of magnitude smaller than the initial water depth in the reservoir ($h_0 = 0.4\,\mathrm{m}$). Table 4.4 shows the structural, scale and porosity errors E_1, E_2 and E_3, respectively. The values are again averaged over 87 gauges. In this example, the error due to coarser cells is smaller than the structural and porosity errors. Indeed, the CR model results show good agreement with the HR model (cf. Figure 4.12), while the difference between CR model and AP model is larger.

Rainfall-runoff in an idealized urban catchment

A series of experiments regarding pluvial flooding in urban catchments were carried out at the Universidad de A Coruna, Spain [16]. One of these experiments is studied in this computational example.

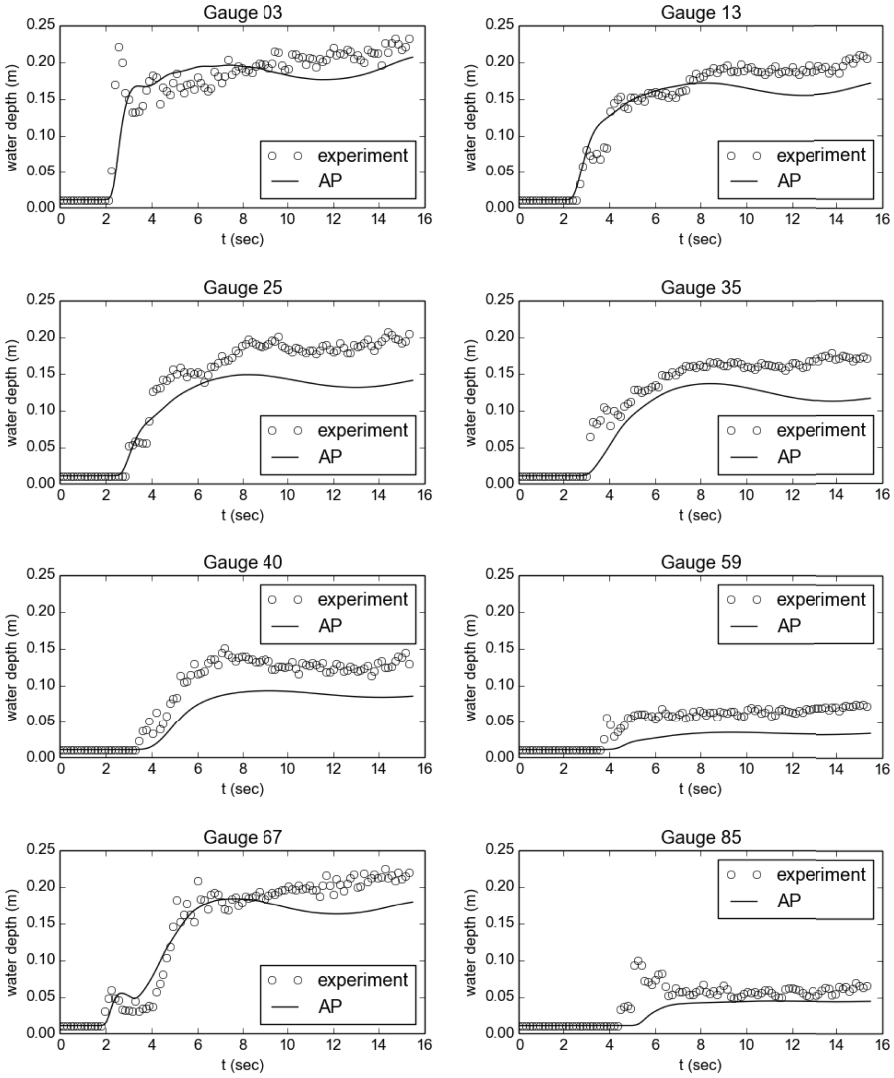

Figure 4.14: Dam-break through idealized city: AP model results for water depth compared with experimental data of [133]

Domain description, initial and boundary conditions

Constant rainfall with an intensity of $i = 300\,\mathrm{mm/h}$ is applied for 20 s to a 2.5 m long and 2 m wide rectangular inclined domain with a slope of 0.05. Inside of the domain, a simplified urban district is built using $0.30\,\mathrm{m} \times 0.20\,\mathrm{m}$ wooden blocks as houses. The configuration of the houses is plotted in Figure 4.15 (top). The domain is initially dry. Further details regarding the experimental setup and more building configurations can be found in [16]. In the numerical models, the outlet of the domain is an open boundary and all other boundaries are closed. The simulation runs for 150 s.

The HR model discretises the domain with a triangular mesh with varying cell size, starting at $l_{c,1} = 0.05\,\mathrm{m}$ at the boundary of the domain to $l_{c,2} = 0.01\,\mathrm{m}$ between the buildings, which are again represented as holes in the mesh. The resulting mesh has 62058 cells. The AP model uses square shaped cells with a side length of 0.125 m, which results in a mesh with 320 cells. The two meshes are compared in Figure 4.15. The whole domain is plotted in Figure 4.15 (middle) with the houses marked out as reference and in Figure 4.15 (bottom) the region between houses. One building can be contained in approximately 6 AP model cells. Again, the alignment of the buildings does not match the AP model mesh cells.

In contrast to the previous examples, no measurement data inside the domain is available, Cea *et al.* [16] measured the total discharge at the outlet of the domain.

Model calibration and run time

The roughness of the domain is reported in [16] in form of a Manning's coefficient of $0.016\,\mathrm{sm}^{-1/3}$. The results of the HR model agree well with the experimental data, thus no further calibration is required. The HR simulation takes about 5340 s. The AP model uses the same roughness coefficient ($0.016\,\mathrm{sm}^{-1/3}$) and a drag force with $a \cdot c_D^0 = 0.5\,\mathrm{m}^{-1}$ (determined with Brent's method). In each cell, 400 subgrid-cells are used to calculate the porosity. The AP model simulation runs for about 43 s, which is a speedup of about 124. The lower speedup in comparison to the first test case is because the stability criterion has to be set to $Cr = 0.1$ in this example. The numerical simulation of rainfall is prone to instabilities because of small water depths and the presence of the mass source [105].

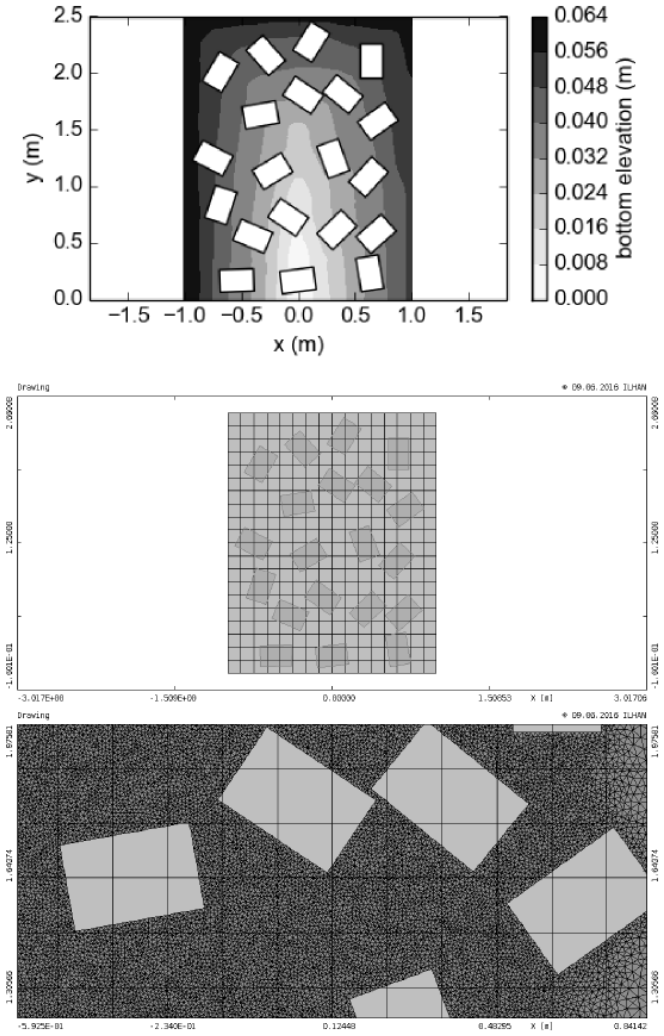

Figure 4.15: Rainfall-runoff in an idealized urban catchment: Bottom elevation in the domain and configuration of houses (top), CR and AP model mesh of the whole domain (middle), comparison of HR model mesh (triangular) and CR and AP model mesh (square) between houses (bottom)

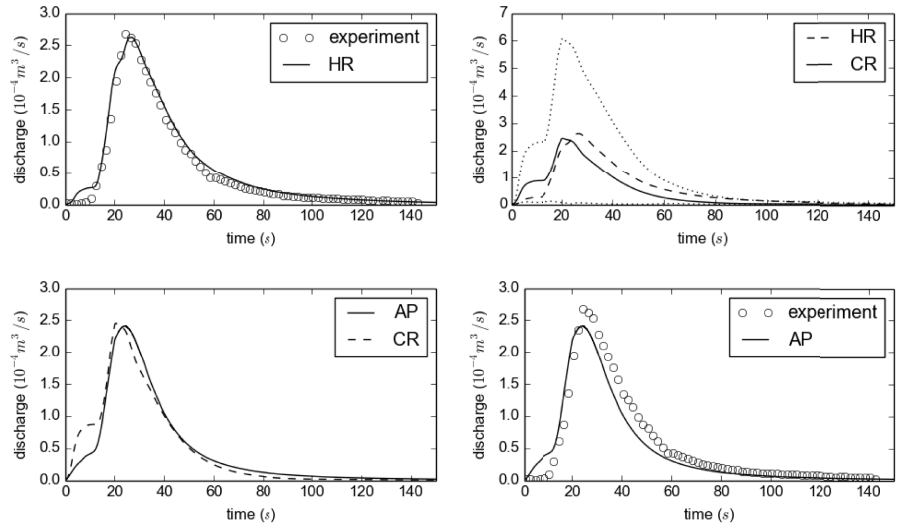

Figure 4.16: Rainfall-runoff in an idealized urban catchment: HR model results for discharge at the outlet of the domain compared with experimental data [16] (top left), CR model results for discharge at the outlet compared with HR model results, dotted lines denote the minimum and maximum values inside the coarse cell (top right), AP model results for discharge at the outlet compared with CR model results (bottom left), AP model results for discharge at the outlet compared with experimental data [16] (bottom right)

Error analysis

Structural model errors The HR model shows good agreement with the experimental data. The discharge at the outlet of the domain as calculated by the HR model is plotted against the measured discharge in Figure 4.16 (top left). In the first 10 s of the simulation, the model discharge overshoots the measured discharge. This has been also observed in [16], and is most likely because at the beginning of the experiment the shear stress on the thin water film in the domain is holding the water back. This can not be reproduced by the shallow water model. After the first 10 s, both hydrographs show very good agreement.

Scale errors The CR model agrees with the HR model, yet the agreement is not as good as in the first test case, especially at the beginning of the simulation. In Figure 4.16 (top right), the maximum and minimum values of the subgrid-cells are also plotted. It is seen that the peak of the curve

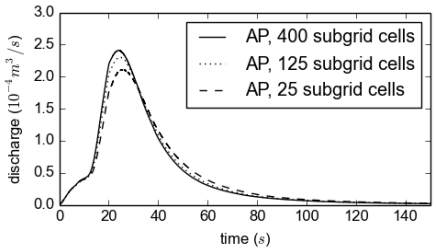

Figure 4.17: Rainfall-runoff in an idealized urban catchment: Sensitivity of the subgrid-cell number on the AP model results

of maximum values is about 3 times larger than the peak of the CR model while the curve of minimum values is close to zero. Generally, it can be concluded that the scale error underestimates the retention effect of the domain.

Porosity model errors The AP model results are plotted against the CR model results in Figure 4.16 (bottom left) and against the experimental results in Figure 4.16 (bottom right). The AP model results show a similar evolution as the CR model results. The major difference between both curves is at the beginning of the simulation. The AP model undershoots the CR model results. Yet, as can be seen in Figure 4.16 (bottom right), it better matches the measured discharge at the end of the domain. Figure 4.17 shows a sensitivity analysis with regard to the subgrid-cell number, from which it is concluded that the model is sensitive to the subgrid-cell number. Apparently, a grid convergence test should be carried out for the subgrid-cell number for each simulation. The subgrid-cell number required to reach subgrid convergence increases if the subgrid-scale obstacles are not aligned with the edges. Yet, even with a small number of subgrid-cells, reasonable results can be obtained (cf. Figure 4.17).

Model validation In order to show that the calibrated model is valid for different hydraulic conditions, the rainfall intensity is decreased to $i = 180\,\mathrm{mm/h}$ and its duration is increased to 40 s. The same mesh and model parameters are used.

Results are plotted in Figure 4.18. The HR model results are compared with the experimental data in Figure 4.18 (top left). The hydrograph of the HR model is very similar to the previous simulation with $i = 300\mathrm{mm/h}$, as it overshoots the experimental data in the beginning but shows good

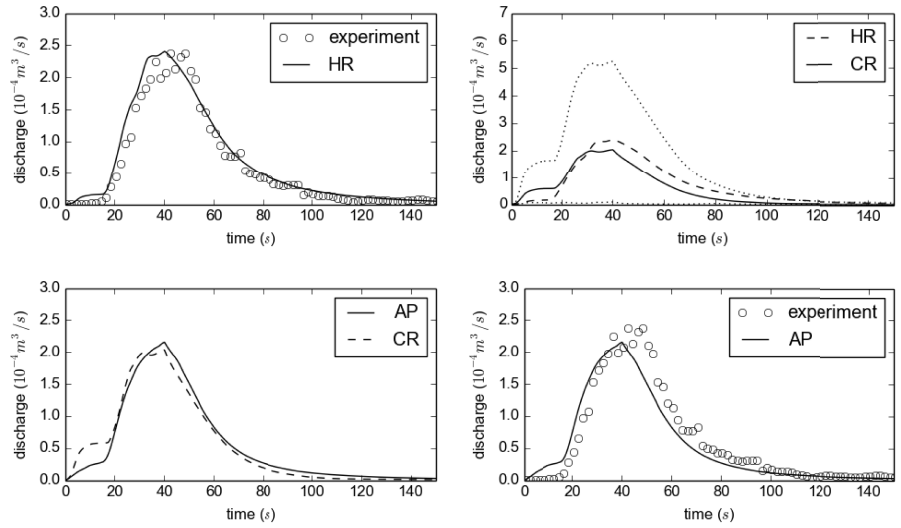

Figure 4.18: Rainfall-runoff in an idealized urban catchment: Model validation with rainfall intensity $i = 180\,\text{mm/h}$, HR model results for discharge at the outlet of the domain compared with experimental data [16] (top left), CR model results for discharge at the outlet compared with HR model results, dotted lines denote the minimum and maximum values inside the coarse cell (top right), AP model results for discharge at the outlet compared with CR model results (bottom left), AP model results for discharge at the outlet compared with experimental data [16] (bottom right)

agreement during the later stage of the simulation. Similarly, the CR model results overshoot the HR model at the beginning and undershoot it at later times (Figure 4.18 (top right). The AP model results, plotted in Figure 4.18 (bottom left) shows good agreement with the CR model, only the first 20 s show significant discrepancy. In Figure 4.18 (bottom right), the AP model is compared to the experimental data. The agreement between the AP model and the experimental data is good. Comparing Figure 4.18 to Figure 4.16 shows that the AP model behaviour is consistent for varying hydraulic conditions.

The errors, summarised in Table 4.5 and Table 4.6, support that the model results are consistent with the first simulation. The structural error is the smallest, the second smallest error is the scale error and the largest error is the porosity error (cf. Table 4.6). However, if model results are compared to experimental results (Table 4.5), the AP model error is less than the CR model error.

Model	Mesh	Resol. (m)	Cell nr.	Time (s)	L_1 (m^3/s)
HR	Triangle	0.01 - 0.05	62058	5340	$1.3 \cdot 10^{-5}$
CR	Triangle	0.01 - 0.05	62058	5340	$2.6 \cdot 10^{-5}$
AP	Square	0.125	320	43	$1.7 \cdot 10^{-5}$

Table 4.5: Rainfall-runoff in an idealized urban catchment: Validation: Summary of shallow water model formulations and corresponding meshes (HR: High-resolution, CR: averaged HR model, AP: anisotropic porosity); L_1-norm is calculated with regard to the experimental results

Type	L_1 (m^3/s)
E_1	$1.3 \cdot 10^{-5}$
E_2	$2.0 \cdot 10^{-5}$
E_3	$5.5 \cdot 10^{-5}$

Table 4.6: Rainfall-runoff in an idealized urban catchment: Validation: Model error (E_1), scale error (E_2) and porosity error (E_3)

Summary A summary is listed in Table 4.7. The total rainfall discharge is calculated by multiplying rainfall intensity with the area of the domain, which gives $Q_{rain} = 4.2 \cdot 10^{-4}\,\mathrm{m}^3/\mathrm{s}$. The HR model error is two orders of magnitude smaller than Q_{rain}, but the CR and AP model errors are only one order of magnitude smaller. The errors of type 1, 2 and 3 are given in Table 4.8. The structural error (E_1) is about two orders of magnitude smaller than the experimental results and both scale (E_2) and porosity (E_3) errors are about one order of magnitude smaller than the experimental results. Although E_3 is greater than E_2, in this test case the scale error seems to be the most significant error and the porous model somehow negates the scale errors. Simulation runs with larger cells, e.g. $\Delta x = 0.25\,\mathrm{m}$, which are not shown here, fail to calculate good results. The main reason is that blockage effects, which have a big influence on the flow field, are underestimated for too large cells. If the coarse cell is too large such that the building lies completely inside the cell, it is not taken into account for the edge porosity and thus, its blockage effects can not be reproduced. This model limitation might give a good upper bound for the size of the coarse cell: it should be possible to capture the significant blockage effects via the edge porosities. If the coarse cell length is chosen too large, the subgrid obstacles can not occupy a significant portion of the edge and their influence on the flow will be underestimated. The authors suggest to use an edge length of about the obstacle size if the obstacles are not arranged densely. For dense building

Model	Mesh	Resol. (m)	Cell nr.	Time (s)	L_1 (m^3/s)
HR	Triangle	0.01 - 0.05	62058	5340	$6.0 \cdot 10^{-6}$
CR	Triangle	0.01 - 0.05	62058	5340	$2.4 \cdot 10^{-5}$
AP	Square	0.125	320	43	$2.0 \cdot 10^{-5}$

Table 4.7: Rainfall-runoff in an idealized urban catchment: Summary of shallow water model formulations and corresponding meshes (HR: High-resolution, CR: averaged HR model, AP: anisotropic porosity); L_1-norm is calculated with regard to the experimental results

Type	L_1 (m^3/s)
E_1	$6.0 \cdot 10^{-6}$
E_2	$2.2 \cdot 10^{-5}$
E_3	$2.4 \cdot 10^{-5}$

Table 4.8: Rainfall-runoff in an idealized urban catchment: Model error (E_1), scale error (E_2) and porosity error (E_3)

arrays, such as the first example, larger cells might be chosen. It is noted that in [19], a method to represent this type of building blockage effects is shown which does not depend on edge porosities. This method requires additional pre-processing and is not used in this work.

4.6 Conclusions

A two-dimensional shallow water model with depth-dependent anisotropic porosity is tested in four test cases. The main novelty of the proposed model is the calculation of the porosities that depends on the water depth.

The formulation of the porosities suggests that the model is sensitive to the computational mesh. The model is tested in a theoretical test case to assess the sensitivity of the model to different meshes and the drag coefficient $a \cdot c_D^0$. The computational mesh determines the values of the volumetric and the areal porosities. The areal porosities are the terms that introduce anisotropy to the model. It is found that the mesh has to be constructed such that the main obstructions are located at the cell edges. Otherwise, their influence on the flow diminishes significantly. The sensitivity of the drag coefficient is related to the areal porosities. If the flow is mainly influenced by obstructions that block and divert the flow, the head loss due to drag is not as significant. This means that in cases where the areal

porosities affect the flow significantly, the model is less sensitive to the drag coefficient. However, if the obstructions are located mainly inside the cells, the drag coefficient becomes a more influential parameter. In all cases, the model needs to be calibrated to determine the value $a \cdot c_D^0$.

In three case-studies, where measured data are available, three types of errors are presented in L_1-norm, as shown in [76]. In all cases, the porosity model error has the same order of magnitude as the scale error. The results are in agreement with the case study conducted in [76]. Good agreement has been achieved between the porosity model and the reference solution.

The model was calibrated using the drag coefficient $a \cdot c_D^0$. Based on the research in [125, 113] and the current results, a value up to $10\,\mathrm{m}^{-1}$ seems reasonable. After this value, the drag coefficient does not change the simulation results anymore. In the investigated cases, especially the range between 0 and $1\,\mathrm{m}^{-1}$ is found to alter the results significantly. It is noted that this claim is based solely on the authors' experience.

Using the porosity model concept allows to run simulations on significantly coarser grids. The speedup in all investigated cases is significant, the anisotropic porosity model is about three orders of magnitude faster than the high-resolution model. The main reason behind the speedup is of course the reduced cell number.

Limitations of the presented porosity model are its mesh dependency, which means that different results may be obtained for the same case if different meshes are used and the ambiguity of the drag coefficient approximation. Further systematic research that addresses these issues would certainly improve these type of models' accuracy and reliability.

4.7 Acknowledgement

The scholarship granted to Jiaheng Zhao by the Chinese Scholarship Council is gratefully acknowledged. The authors thank Prof. Sandra Soares–Frazão from Université catholique de Louvain, Belgium, for the experimental data of the second example. The authors thank Martin Bruwier from Université de Liège, Belgium, for the insightful conversation about stability constraints of the water depth-dependent anisotropic porosity model. Finally, gratitude is expressed to the three anonymous reviewers who helped to significantly improve the article.

Chapter 5

Porosity-based coarse grid approach: stability and flux correction

Submitted as:
[115] Özgen, I., Zhao, J., Kim, B., Liang, D., and Hinkelmann, R. (nd) An anisotropic-porosity shallow water model with novel monotonicity treatment and subgrid-scale drag estimation. *International Journal for Numerical methods in Fluids*.

This is the preprint version of the publication.

5.1 Abstract

Porous shallow water models are a promising approach to reduce computational cost in urban flood simulations. In this type of models, buildings and other obstacles are not explicitly discretized but rather accounted for by means of porosity. The porosity terms are normally related to the fraction of the cell that is available to fluid flow. In the anisotropic-porosity shallow water model, an additional porosity term is defined at each cell edge that describes the conveyance. Models with only one porosity value at a cell edge have limited capability to capture porosity discontinuities at the cell edge. This paper proposes a simple flux correction that is described using two conveyance porosities (defined at the left and right side of the edge) to

improve the model accuracy at porosity discontinuities. A novel approach to estimate the head-loss due to subgrid-scale building-fluid interaction in an anisotropic way is presented. A well-balanced first order Godunov-type scheme using an HLL solver is used to solve the governing equations on unstructured meshes. A novel way to maintain the monotonicity during the variable reconstruction is presented. The model is tested in two academic examples and a laboratory experiment. The proposed flux correction improves the results especially in cases with a large porosity discontinuity. The proposed monotonicity treatment prevents spurious oscillations of flow velocities, but decreases the model accuracy if applied too strictly. The presented head-loss estimation is shown to improve the model results compared to an isotropic head-loss estimation, especially for cases with unsymmetric building configurations.

5.2 Introduction

Shallow water models with porosity are consist of a set of equations to model large scale flood events in urban areas. The porosity accounts for the presence of buildings and other obstacles that block the water flow. The advantage of using the porous shallow water formulation is that buildings do not have to be discretized explicitly with mesh refinement and simulations can be carried out with a coarser resolution.

The benefit of using coarser cells is illustrated by the estimation of computational cost for explicit models in [76] as

$$C \sim k\frac{1}{\Delta x^3}, \tag{5.1}$$

where k is a parameter that depends on the implementation of the numerical scheme. As the cell size increases, the computational cost decreases with order 3. This results in simulations that run two [125] up to three orders of magnitude [110] faster than the classical high-resolution shallow water model.

In the pioneering work of [51, 132] a single porosity shallow water model is proposed. The cell is considered a representative elementary area (REA) and the buildings are accounted for by a porosity term. Flux terms are limited by the same porosity that describes the volume available in the cell. Then, a lateralized Godunov-type finite volume scheme is proposed to solve the equations. In [151], the numerical scheme is further developed. A different numerical scheme to solve the equations that is based on a modified Rusanov method can be found in [100].

In [125], the porous shallow water equations were derived without an REA assumption which enabled the use of different porosities to represent the conveyance of the edge. The flux terms are limited by the conveyance porosities, while the space inside the cell is described by a volume porosity. These equations are referred to as anisotropic porosity shallow water equations. In [125], the equations are solved with a Godunov-type finite volume scheme and the same numerical scheme is applied and discussed extensively in [77, 76]. A modified version of the equations has been presented in [110, 116, 10].

This paper presents a well-balanced first order Godunov-type finite-volume scheme to solve the anisotropic-porosity shallow water equations on unstructured grids. The scheme is a simplification of the model presented in [116], where the main difference is a modified reconstruction of the interface variables and additional treatment to prevent spurious oscillations. A simple Harten, Lax and van Leer (HLL) approximate Riemann solver is used that is motivated by the solver shown in [51]. A limitation of the conventional anisotropic shallow water model is that a porosity discontinuity across the edge can not be represented accurately if the edge conveyance is described with a single porosity. In order to improve the accuracy of the model in this case, this study proposes a simple flux correction based on an empirical equation for head loss due to a rapid narrowing. In addition, a novel way to estimate the drag force in an anisotropic way is presented.

The proposed scheme is applied to two analytical examples, where it is shown that the prediction of the present model agrees well with the reference solution. Then, the model is applied to replicate a laboratory experiment [139], to study its limitations. In the last section, conclusions are drawn.

5.3 Governing equations

The anisotropic-porosity shallow water equations derived in [125] are written in integral vector form as

$$\frac{\partial}{\partial t}\int_{\Omega} i\mathbf{q}d\Omega + \oint_{\Gamma} i\left(\mathbf{F}\cdot\mathbf{n} - \mathbf{F}^{*}\right)d\Gamma = \oint_{\Gamma^{*}} i\mathbf{H}\cdot\mathbf{m}d\Gamma + \int i\mathbf{s}d\Omega, \qquad (5.2)$$

cf. [76], with t being time, x and y being the Cartesian coordinates, i being a binary function that returns 1 if the evaluation point is available to flow and 0 if the evaluation point coincides with an obstruction, Ω being the control volume area, Γ being the path along the boundary of the control volume and Γ^{*} being the path along the unresolved obstruction-fluid interface inside the control volume. $\mathbf{n}$ is the unit outward normal vector along Γ and $\mathbf{m}$ is

the unit outward normal vector along Γ^*. For a more detailed discussion see [125]. $\mathbf{F}^*$ is a flux correction term that is based on a head-loss due to geometric contractions and is discussed in Sec. 5.4. The other vectors are defined as

$$\mathbf{q} = \begin{bmatrix} h \\ q_x \\ q_y \end{bmatrix}, \quad \mathbf{F} = \begin{bmatrix} q_x & q_y \\ q_x^2/h + \frac{1}{2}gh^2 & q_x q_y/h \\ q_x q_y/h & q_y^2/h + \frac{1}{2}gh^2 \end{bmatrix}, \tag{5.3}$$

$$\mathbf{H} = \begin{bmatrix} 0 & 0 \\ \frac{1}{2}gh|_{\eta_0}^2 & 0 \\ 0 & \frac{1}{2}gh|_{\eta_0}^2 \end{bmatrix}, \quad \mathbf{s} = \begin{bmatrix} s_m \\ -s_{b,x} - \left(c_D^f + c_D^b\right) q_x |\mathbf{q}|/h^2 \\ -s_{b,y} - \left(c_D^f + c_D^b\right) q_y |\mathbf{q}|/h^2 \end{bmatrix}. \tag{5.4}$$

h is the water depth, q_x and q_y are unit discharges in x- and y-direction, respectively, $|\mathbf{q}|$ is the norm of the vector of unit discharges, i.e. $\mathbf{q} = [q_x, q_y]^T$, g is the gravitational constant, s_m is the mass source term, $s_{b,x}$ and $s_{b,y}$ are the bed slope source terms in x- and y-direction, respectively, c_D^f and c_D^b are the drag coefficients for bed friction and subgrid-scale obstructions, respectively. The terms in the matrix $\mathbf{H}$ result from the macroscopic modeling point of view [125] with $h|_{\eta_0}$ being the water depth corresponding to a constant water surface elevation η_0, and represent the pressure force acting at the obstruction-fluid interface, similar to the geometry source term that arises in the cross-section-averaged shallow water equations, cf. e.g., [118].

5.4 Numerical scheme

Finite-volume scheme

In each finite-volume cell j and cell edge k, porosities are defined as follows:

$$\phi_j = \frac{1}{\Omega_j} \int_{\Omega_j} i d\Omega, \; \psi_k = \frac{1}{\Delta r_k} \int_{\Gamma_k} i dr_k \tag{5.5}$$

Here, ϕ_j is the volumetric porosity, representing the fraction of the cell available to flow and ψ_k is the conveyance porosity, representing the fraction of the edge available to flow. A similar modeling concept can be found in [19], where flux terms are limited by a so-called conveyance reduction factor and storage terms are multiplied with a building coverage ratio.

This study adopts a dual conveyance porosity approach, i.e. the conveyance porosity is calculated at infinitesimally small distances left and right to the edge and the edge itself is considered a porosity discontinuity.

Discretizing Eq. 5.2 with an explicit finite-volume method that uses a forward Euler time discretization gives

$$(\phi_j \mathbf{q}_j)^{n+1} = (\phi_j \mathbf{q}_j)^n + \frac{\Delta t}{\Omega}\left[\int_\Omega i\mathbf{s}^n d\Omega - \sum_{k=1}^{n_b} \psi_k \mathbf{F}_k^n \cdot \mathbf{n}_k \Delta r_k\right]. \tag{5.6}$$

Here, n_b is the number of edges and Δr_k is the length of the edge k. As shown below, due to the way the vectors in Eq. 5.3 and 5.4 are discretized, $\mathbf{H}$ does not appear in Eq. 5.6.

Reconstruction of face variables

At the interface between two cells, the bed elevation is set to a single value as shown in [2] as

$$z_k = \max(z_L, z_R), \tag{5.7}$$

where L and R denote the left and right cell of the edge k. For the reconstruction from cell j to edge k, the water depth is calculated in a positivity preserving way as

$$h_k = \max(0, \eta_j - z_k). \tag{5.8}$$

Following the simplified hydrostatic reconstruction in [60], the bed elevation of the edge is then modified only according to the water elevation of the cell under consideration as

$$z_k = \min(\eta_j, z_k) \tag{5.9}$$

to preserve C-property at wet/dry interfaces.

Velocities are reconstructed as suggested in [125]:

$$u_k = \frac{(\phi q_x)_j}{(\psi h)_k} \qquad v_k = \frac{(\phi q_y)_j}{(\psi h)_k} \tag{5.10}$$

The reconstruction is carried out twice at each edge, once for each adjacent cell. Conveyance porosities ψ_L and ψ_R at the left and right side of each edge, respectively, are determined in the preprocessing step and thus, the value of ψ changes depending on whether the cell is located at the left or right side of the edge.

If the product $(\psi h)_k$ is very small, unphysically high velocities may be calculated. The same issue emerges during a second-order reconstruction of interface variables. As discussed in [61], in order to avoid numerical instablity, the monotonicity conditions

$$\max(u_j, u_i) \geq u_k \geq \min(u_j, u_i), \tag{5.11}$$

$$\max(v_j, v_i) \geq v_k \geq \min(v_j, v_i), \tag{5.12}$$

have to be satisfied, where j and i denote indices of two adjacent cells connected by the edge k. The issue is also addressed to certain extend in [125], where the reconstruction is reverted ("to avoid division by zero") to $u_k = u_j$, $v_k = v_j$, if $(\psi h)_k$ is smaller than a threshold value. Here, a similar treatment is proposed. As spurious velocities with high local extreme values induce numerical instability, these critical velocities should be limited as

$$\begin{aligned} &\text{if } u_k > \max(u_j, u_i) \text{ then } u_k = \max(u_j, u_i); \\ &\text{or if } u_k < \min(u_j, u_i) \text{ then } u_k = \min(u_j, u_i), \end{aligned} \tag{5.13}$$

$$\begin{aligned} &\text{if } v_k > \max(v_j, v_i) \text{ then } v_k = \max(v_j, v_i); \\ &\text{or if } v_k < \min(v_j, v_i) \text{ then } v_k = \min(v_j, v_i). \end{aligned} \tag{5.14}$$

A suggestion for the correct identification of critical velocities is given here, which is similar to the treatment in [61]. Unphysically high velocities may occur during the reconstruction of velocities (Eq. 5.10) for large values of the ratio

$$\frac{\psi h_k}{\phi h_j}, \tag{5.15}$$

which results in the first criterion

$$\frac{h_k}{h_j} \leq \frac{\phi\gamma}{\psi}, \tag{5.16}$$

where γ is a prescribed threshold that is lower than 1. Another critical case is that after the hydrostatic reconstruction, the water depth at edge k is smaller than the difference between bottom elevations in cell j and at edge k. Thus, the second criterion is

$$h_k \leq |z_k - z_j|. \tag{5.17}$$

The type of reconstruction of velocities can be deduced directly by the reconstructed water depth. If the condition

$$h_k \leq \min(|z_k - z_j|, \frac{\phi\gamma}{\psi} h_j) \tag{5.18}$$

is satisfied, the velocities are limited according to Eq. 5.13 and 5.14, else Eq. 5.10 is used.

Numerical flux computation

The reconstructed values from Eq. 5.10 at the left and right side of the edge are used as the states of a Riemann problem. The HLL approximate Riemann solver derived in this work uses the simplified wave speed estimates in [25] to calculate the left and right wave speeds, S_L and S_R, respectively, as

$$S_L = \min\left(u_L - c_L, u_R - c_R, 0\right), \tag{5.19}$$

$$S_R = \max\left(u_L + c_L, u_R + c_R, 0\right), \tag{5.20}$$

with $c_L = \sqrt{gh_L}$ and $c_R = \sqrt{gh_R}$. Components of the numerical flux ($\mathbf{F}_*$) can then be calculated as mass flux, normal momentum flux and tangential momentum flux.

Motivated by [51], the conveyance porosity of the edge is calculated as

$$\bar{\psi} = \min(\psi_L, \psi_R) \tag{5.21}$$

The HLL mass flux can be calculated as

$$(\psi hu)_* = \bar{\psi}\frac{S_R(hu)_L - S_L(hu)_R + S_L S_R(h_L - h_R)}{S_R - S_L}, \tag{5.22}$$

which is the classical HLL flux formulation for mass balance multiplied by the conveyance porosity. Similarly momentum flux normal to the edge is calculated with the HLL flux formula as

$$\begin{aligned}\left(\psi hu^2 + \frac{g}{2}\psi h^2\right)_* = \frac{\bar{\psi}}{S_R - S_L}\Big(S_R\left(hu^2 + \frac{g}{2}h^2\right)_L \\ - S_L\left(hu^2 + \frac{g}{2}h^2\right)_R + S_L S_R\left((hu)_R - (hu)_L\right)\Big).\end{aligned} \tag{5.23}$$

The tangential momentum flux is calculated using an upwind formulation based on $(\psi hu)_*$ as

$$(\psi huv)_* = \begin{cases}(\psi hu)_* v_R, & (\psi hu)_* < 0, \\ (\psi hu)_* v_L, & (\psi hu)_* \geq 0.\end{cases} \tag{5.24}$$

Preservation of C-property

The interfacial pressure term in $\mathbf{H}$ and the bed slope source term in $\mathbf{s}$ in Eq. 5.4 are discretized in a similar manner to that in [116] using the divergence

form of source terms [148] as

$$\oint_{\Gamma^*} i\frac{1}{2}gh|^2_{\eta_0}\mathbf{m}d\Gamma + \int_{\Omega}\mathbf{s}_b d\Omega = \sum_k \bar{\psi}_k \frac{1}{2}g\left[(z_k - z_j)(h_k + h_j) + h_j^2\right]\mathbf{n}_k \Delta r_k. \tag{5.25}$$

Here, $\bar{\psi}_k$ represents a conveyance porosity that represents both the left and the right side of the edge, calculated using Eq. 5.21. Evaluating the numerical flux for a quiescent steady state ($u = v = 0$ and $\eta_L = \eta_R$), cf. [61], shows that the proposed discretization preserves the quiescent steady state as it exactly balances out the pressure force terms.

Head loss term calculation

Head loss term at the finite volume edge

The head-loss term at the edge k, i.e. $\mathbf{F}^*$ in Eq. 5.2, is only calculated across sudden geometric discontinuities, i.e. $\psi_L \neq \psi_R$. Here, it is suggested to use the head-loss ΔH according to a slightly modified version of [13, 21] cited in [132] as

$$\Delta H_{k,j} = \left[\left(\frac{1}{m} - 1\right)^2 + \frac{1}{9}\right]\frac{\psi^2_{k,L}}{\psi^2_{k,R}}\frac{|\mathbf{v}|}{2g}n_{k,j}, \qquad j = x, y. \tag{5.26}$$

m is the contraction coefficient and a value of $m = 0.62$ is recommended in [13, 21]. The head-loss is applied as a momentum flux correction at each edge and the correction term $\mathbf{F}^*$ in Eq. 5.2 is

$$\mathbf{F}^* = \begin{bmatrix} 0 \\ \Delta H_{k,x} \\ \Delta H_{k,y} \end{bmatrix} \tag{5.27}$$

Head loss term inside the finite volume cell

As shown in Eq. 5.4, head-loss due to building drag is accounted for by the drag formulation in [107]:

$$s_{d,j} = c_D^b h^{-2} q_j |\mathbf{q}|, \; j = x, y, \tag{5.28}$$

where

$$c_D^b = \frac{1}{2}cw_p h, \tag{5.29}$$

with w_p being the projected width of the obstruction and c being the drag coefficient. In previous studies [125, 76, 110, 116], the difficulty of finding a suitable expression of the projected width w_p has been pointed out. The main difficulty is that w_p depends on the angle of attack and therefore on the flow itself. [125] suggest that w_p could be determined in a preprocessing step using the geometric data set. This would require storing different values of w_p at different angles of attack for each cell. Furthermore, as pointed out in [125] the drag force is then solved iteratively by firstly calculating a velocity based on an estimated w_p and then updating w_p based on the new velocity to solve for c_D. In [110], it is acknowledged that both c and w_p contain great uncertainty and the product cw_p is used as calibration parameter. This neglects the direction of the flow and might not be suitable for complex 'real world' applications.

Herein, following the discussion in [151] where a fourth-order tensor with two up to four free calibration parameters is derived, it is suggested to use a tensor of second-order to describe the drag force. Firstly, the areal porosities are used to estimate the parameter w_p in cell i as

$$w_{p,j} = (1 - \dot{\psi}_j)\Delta k, \; j = x, y, \tag{5.30}$$

whereby Δk is the characteristic length of the cell and $\dot{\psi}$ denotes an estimated areal porosity inside the cell that is herein calculated as

$$\dot{\psi}_j = \frac{1}{2}(\bar{\psi}_k + \bar{\psi}_m), \; j = x, y. \tag{5.31}$$

In other words, the arithmetic average of both areal porosities at the two edges k and m that intersect a line drawn through the cell center in j-direction. Hereby, $\bar{\psi}_k$ and $\bar{\psi}_m$ are calculated using Eq. 5.21. The variables for the case $j = x$ and $j = y$ are sketched in Fig. 5.1. Based on preliminary studies, the characteristic length Δk is set equal to the circumference.

Then, the drag force is calculated as

$$\begin{aligned} \mathbf{s}_d = &\begin{bmatrix} c^b_{D,x} & 0 \\ 0 & c^b_{D,y} \end{bmatrix} \begin{bmatrix} q_x \\ q_y \end{bmatrix} h^{-2}|\mathbf{q}| = \\ &\begin{bmatrix} \frac{1}{2}cw_{p,x}h & 0 \\ 0 & \frac{1}{2}cw_{p,y}h \end{bmatrix} \begin{bmatrix} q_x \\ q_y \end{bmatrix} h^{-2}|\mathbf{q}|, \end{aligned} \tag{5.32}$$

where the only calibration parameter is c in Eq. 5.29.

This formulation should be seen as an approximation to the real projected length w_p. It contains more information about flow direction, rather than simply calibrating with the isotropic product cw_p as in [110]. It may be less accurate than the method with extensive preprocessing suggested in

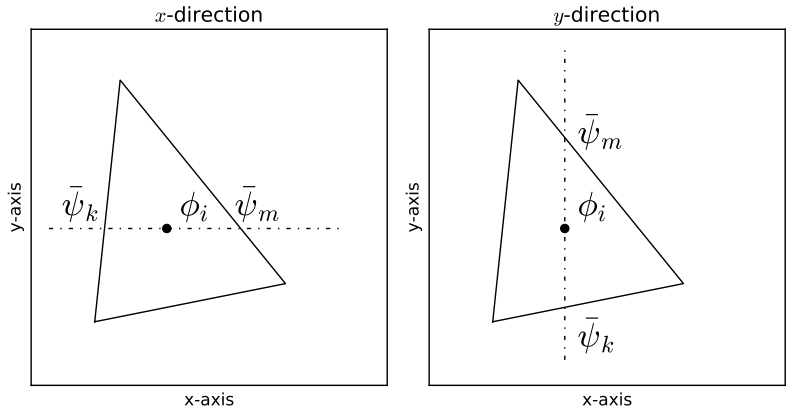

Figure 5.1: Definition for $\bar{\psi}_k$, $\bar{\psi}_m$ and ϕ_i in x-direction (left) and y-direction (right)

[125], but it requires less computational effort. Compared to the anisotropic tensor in [151], it has fewer calibration parameters.

In addition, the calculation of the drag force now depends on the areal porosities, which implies that the model results depend on the computational mesh. However, in practice this drawback is not very relevant, as the anisotropic-porosity model is expected to be mesh dependent [48, 49].

Splitting point-implicit friction and drag force source term computation

As in [125], the friction and drag force source terms are calculated using the splitting point-implicit discretization introduced in [11]. As this is not elaborated in detail in [125], a short overview is given here.

The vectors $\bar{\mathbf{q}}$, $\mathbf{f}$, $\mathbf{s}_f$ and $\mathbf{s}_d$ are defined as follows:

$$\bar{\mathbf{q}} = \begin{bmatrix} q_x \\ q_y \end{bmatrix}, \mathbf{f} = \begin{bmatrix} q_x^2/h + \frac{1}{2}gh^2 & q_x q_y/h \\ q_x q_y/h & q_y^2/h + \frac{1}{2}gh^2 \end{bmatrix},$$
$$\mathbf{s}_f = \begin{bmatrix} -\phi c_D^f q_x |\bar{\mathbf{q}}|/h^2 \\ -\phi c_D^f q_y |\bar{\mathbf{q}}|/h^2 \end{bmatrix}, \mathbf{s}_d = \begin{bmatrix} -c_D^b q_x |\bar{\mathbf{q}}|/h^2 \\ -c_D^b q_y |\bar{\mathbf{q}}|/h^2 \end{bmatrix}. \tag{5.33}$$

If bed friction is calculated using Manning's law and the vector s_{tot} can defined as

$$s^n_{tot,j} = s^n_{f,j} + s^n_{d,j} = -\left(\phi g N^2 h^{-7/3} + c^b_D h^{-2}\right) q_j |\mathbf{q}|, \tag{5.34}$$

where n denotes the time level, N is Manning's coefficient and $j = x, y$. Then, $\mathbf{s}^{n+1}_{tot}$ can be written as a Taylor series expansion around the nth time level as

$$\mathbf{s}^{n+1}_{tot} = \mathbf{s}^n_{tot} + \mathbf{J}^n \Delta\bar{\mathbf{q}} + O\left(\Delta\mathbf{q}^2\right), \; \mathbf{J}^n = \left(\frac{\partial \mathbf{I}_{tot}}{\partial \bar{\mathbf{q}}}\right)^n, \tag{5.35}$$

with $\mathbf{s}_{tot} = [s_{tot,x}, s_{tot,y}]$, $\Delta\bar{\mathbf{q}} = \bar{\mathbf{q}}^{n+1} - \bar{\mathbf{q}}^n$ and $\mathbf{J}$ is the Jacobian matrix of $\mathbf{s}_{tot}$,

$$\mathbf{J} = \begin{bmatrix} \frac{\xi q_x^2}{|\bar{\mathbf{q}}|} + \xi|\bar{\mathbf{q}}| & \frac{\xi q_x q_y}{|\bar{\mathbf{q}}|} \\ \frac{\xi q_x q_y}{|\bar{\mathbf{q}}|} & \frac{\xi q_y^2}{|\bar{\mathbf{q}}|} + \xi|\bar{\mathbf{q}}| \end{bmatrix}, \; \xi = -\left(g N^2 h^{-7/3} + c_D h^{-2}\right). \tag{5.36}$$

For computational efficiency, the non-diagonal entries of $\mathbf{J}$ are dropped, as suggested in [11].

The final solution for the momentum equations is

$$(\phi\bar{\mathbf{q}})^{n+1} = (\phi\bar{\mathbf{q}})^n + \frac{1}{\mathbf{I} - \mathbf{J}^n}\left(-\frac{1}{\Omega}\sum_k (\mathbf{f}_k \mathbf{n}_k)^n + \Delta t \left(\phi \mathbf{s}_{tot}\right)^n\right), \tag{5.37}$$

where $\mathbf{I}$ is the identity matrix.

Wetting/drying treatment and zero porosity treatment

The proposed reconstruction of interface variables, cf. Sec. 5.4, is sufficient to keep the scheme stable at wet/dry fronts [2, 60]. A cell is considered dry if the water depth is smaller than a threshold, ϵ, and in this case all velocities and discharges are forced to zero. The threshold here is set to $\xi = 10^{-6}\,\mathrm{m}$.

Another case to be considered is when $\psi = 0$, which implies that the edge is essentially a solid wall. Then, the scheme automatically calculates a zero flux.

Stability

Similar to the numerical scheme reported in [125], the stability of the proposed scheme is limited by the Courant-Friedrichs-Lewy condition

$$\max(\psi_k S_k \Delta r_k)\frac{\Delta t}{\phi_j \Omega_j} \leq 1, \tag{5.38}$$

which is evaluated for each edge k of each cell j in the computational domain, with ψ_k standing for the lower conveyance porosity at the edge and S_k standing for the maximum wave speed at the edge.

5.5 Computational examples

The model is first verified in two simple benchmarks that are proposed in literature. Then, a case study at the laboratory scale is presented. The quality of results is quantified in terms of the absolute value of the difference between model result and reference solution, calculated as

$$\epsilon_{1,i} = |q_{m,i} - q_{r,i}| \tag{5.39}$$

at point i with $q_{m,i}$ and $q_{r,i}$ standing for model result and reference solution at point i, respectively. The sum of this error over all points in the domain is referred to as the L_1-norm of the error:

$$L_1 = \sum_{k=1}^{n} \epsilon_{1,i} \tag{5.40}$$

If the domain is in space, the points refer to the cell centers. If the domain is in time, then the points refer to discrete time steps.

Stationary flow in a channel with rapid porosity transition

This test case studies stationary flow in a frictionless channel with rapid porosity transition. The case is proposed in [125], where it is discussed that a reference solution can be obtained by solving an analogous stationary flow problem in a channel with variable width using the conservation of energy at each point (Bernoulli's equation). The porosity is dependent upon the x-coordinate such that $\phi = 1$ for $x < 400$ and $x > 600$ m, $\phi = 0.75$ for $x > 410$ and $x < 590$ m, ϕ decreases linearly from 1.0 to 0.75 between $x = 400$ and 410 m and increases linearly from 0.75 to 1.0 between 590 to 600 m. Drag force and friction are neglected. Initial conditions and model parameters are given in Tab. 5.1.

Comparisons of model results with the reference solution for water depth and velocity are plotted in Fig. 5.2. The error calculated according to Eq. 5.39 is plotted in Fig. 5.3. The error plot agrees with the results reported in [125], where localized errors due to the porosity discontinuity are reported. The error in front of the section with reduced porosity is higher than that

Symbol	Meaning	Value
$q_{0,L}$	Unit discharge at left boundary	$2\ \mathrm{m^2 s^{-1}}$
$h_{0,R}$	Water depth at right boundary	2 m
L	Length of the domain	1000 m
Δx	Cell size	0.25 m
m	Contraction coefficient	0.62
γ	Threshold to limit velocity	10^{-3}
N	Manning's coefficient	neglected
c	Drag coefficient	neglected
$\phi(x)$	Porosity function	described in text

Table 5.1: Parameters of the stationary flow in a channel with rapid porosity transition

behind the section. This is because the downstream boundary regulates the water depth, while the upstream boundary is an inflow boundary where the water depth regulates itself. Thus, the numerical model converges to the exact water depth downstream but overestimates the water depth slightly at the inflow boundary. The $L_{1,v}$-norm is calculated as 0.2 m/s for velocity and $L_{1,h}$-norm is calculated as 0.2 m for water depth. This corresponds to an average L_1-norm of $5 \cdot 10^{-5}$ m/s for velocity and $5 \cdot 10^{-5}$ m for water depth.

Dam-break flow across a porosity discontinuity

This example studies a one-dimensional dam-break with different porosity values on the left and right sides of the dam. It is initially introduced in [51] for the single porosity shallow water model. The reference solution can be obtained by iteratively solving the corresponding Riemann problem across a porosity discontinuity using a Newton-Raphson procedure.

The computational parameters for the benchmark are given in Tab. 5.2. Results are plotted in Fig. 5.4–5.6 for different porosity configurations. The L_1-errors for the investigated configurations are summarized in Tab. 5.3. It is seen that the proposed head-loss correction of momentum flux improves the model accuracy compared to the discretization that depends solely on the areal porosity ψ as in [125, 110, 10] (ψ-AP model), however the two models become identical as the ratio ψ_L/ψ_R goes to 1. For $\psi_L/\psi_R = 1.0/0.5$, the two model results are almost the same. Although the accuracy is improved, the results still do not completely agree with the reference solution. Specifically the front of the shock wave is not fully accurately captured.

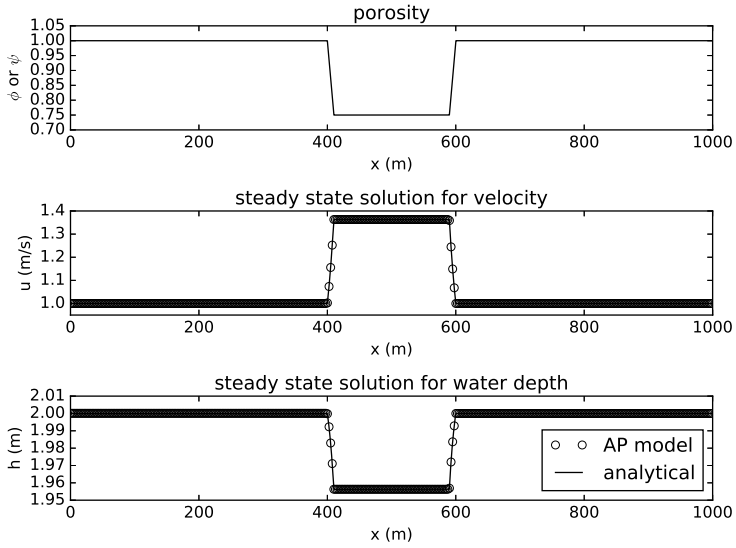

Figure 5.2: Stationary flow in a channel with rapid porosity transition: Reference and numerical solutions at steady state

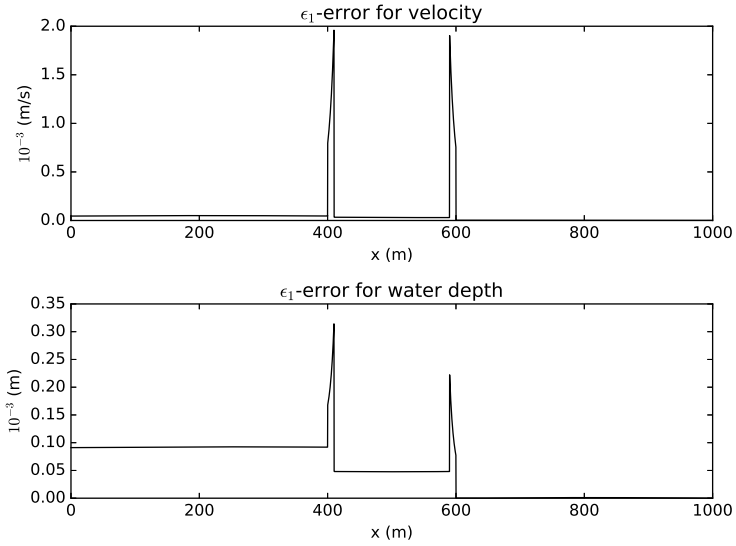

Figure 5.3: Stationary flow in a channel with rapid porosity transition: Errors at steady state

Symbol	Meaning	Value
$h_{0,L}$	Initial water depth on the left side	10 m
$h_{0,R}$	Initial water depth on the right side	1 m
L	Length of the domain	100 m
x_0	Location of the dam	50 m
Δx	Cell size	0.1 m
m	Contraction coefficient	0.62
γ	Threshold to limit velocity	10^{-3}
N	Manning's coefficient	neglected
c	Drag coefficient	neglected
ϕ_L	Porosity, left-hand side of the dam	1.0
ϕ_R	Porosity, right-hand side of the dam	$0.1, 0.2, 0.5$

Table 5.2: Parameters of the dam-break test case with porosity discontinuity

This is because the water depth downstream of the discontinuity is either overestimated or underestimated, which leads to an over- or underestimation of the gradient in water depth at the front. Hence, the shock wave travels with a different speed than the reference solution.

It is noted that the single porosity models in [51, 132] are able to correctly replicate the reference solution in this benchmark. This is because the single porosity shallow water model comprises a momentum source term that accounts for the gradient in the porosity. In these models, the flow is accelerated in the direction of the porosity gradient and slowed down if the flow is opposite to the porosity gradient. The conventional anisotropic-porosity model lacks this source term, because it vanishes during the integration process [125] and therefore can not describe the influence of a porosity gradient on the flow. This explains the deviation between model results and reference solution and why it decreases for smaller porosity gradients. By correcting the momentum flux based on the head-loss due to a sudden narrowing, the proposed anisotropic porosity model introduces the influence of a porosity gradient and is able to replicate flow at a porosity discontinuity more accurately while keeping the advantage of additional subgrid-scale information at the edges.

Flash flood in Toce River Valley

This test case replicates the laboratory experiment in [139], which has been used commonly in the porous shallow water model literature, cf. [51, 132,

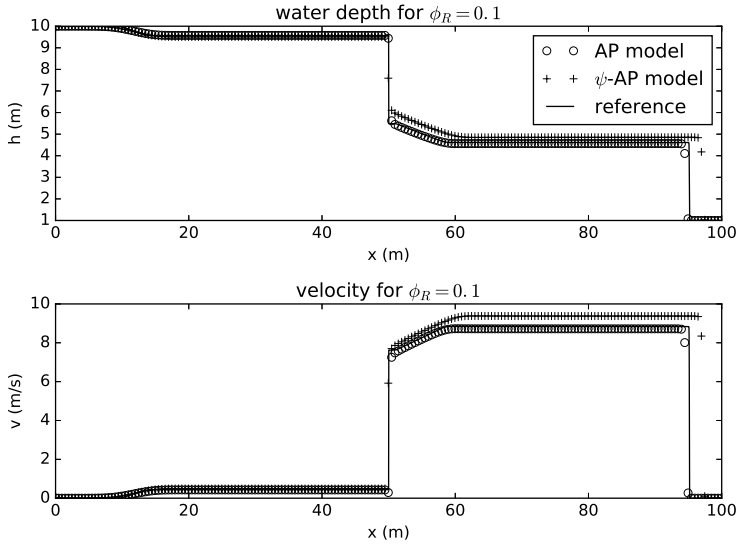

Figure 5.4: Dam-break flow across a porosity discontinuity: Reference and numerical solution for case with $\phi_R = 0.1$

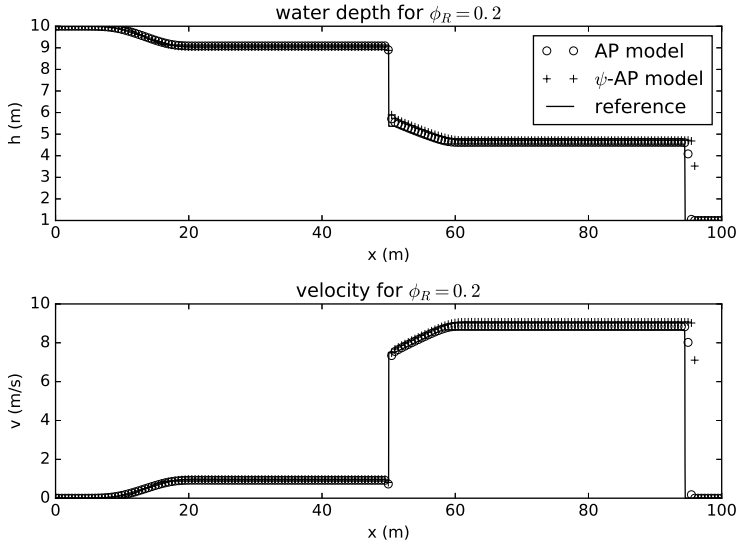

Figure 5.5: Dam-break flow across a porosity discontinuity: Reference and numerical solution for case with $\phi_R = 0.2$

ϕ_L	ϕ_R	c. $L_{1,h}$	uc. $L_{1,h}$	c. $L_{1,q}$	uc. $L_{1,q}$
1.0	0.1	53.5 m	233.1 m	104.3 m^2/s	439.5 m^2/s
1.0	0.2	66.1 m	186.1 m	111.1 m^2/s	338.1 m^2/s
1.0	0.5	75.3 m	81.7 m	120.3 m^2/s	131.7 m^2/s

Table 5.3: L_1-error for the simulation runs (c. $L_{1,h}$: with flux correction, uc. $L_{1,h}$: without flux correction)

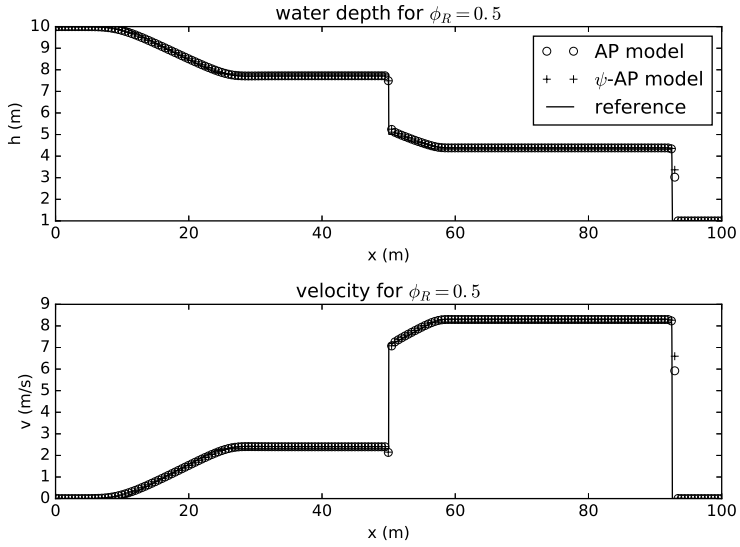

Figure 5.6: Dam-break flow across a porosity discontinuity: Reference and numerical solution for case with $\phi_R = 0.5$

125, 49, 77].

The domain is a 1 : 100 scaled physical model of the Toce River Valley, Italy. The topography data are available with a resolution of 5 cm. Bed friction is accounted via a Manning coefficient that is reported in [139] as $N = 0.0162$ $sm^{-1/3}$. The model city consists of twenty houses which are square-shaped blocks with an edge length of 0.15 m.

The mesh is generated using the mesh generator Gmsh [42] with an element size of 0.5 m as shown in Fig. 5.7. The resolution corresponds to the mesh size reported in [125] and results in a total of 462 triangular mesh cells. The inflow boundary conditions with measured time series of discharge and water depth are imposed [139] because the flow condition is critical. The computational parameters for the test case are summarized in

Symbol	Meaning	Value
h_0	Initial water depth	0 m
$\mathbf{v}_0$	Initial velocity	0 m/s
Δx	Cell size	0.5 m
ϕ, ψ	Porosity	Acc. to buildings
m	Contraction coefficient	0.62
γ	Threshold to limit velocity	10^{-5}, 10^{-3}
N	Manning coefficient	$0.0162\ \mathrm{sm}^{-1/3}$
c	Drag force coefficient	0, 5, $10\,\mathrm{m}^{-2}$
$q_b(t)$	Boundary condition at inflow	Time series

Table 5.4: Parameters of the Toce Valley test case

γ	$L_{1,2}$	$L_{1,3}$	$L_{1,4}$	$L_{1,5}$	$L_{1,6}$	$L_{1,7}$	$L_{1,8}$	$L_{1,9}$	$L_{1,10}$
10^{-3}	0.81	2.49	4.41	1.32	1.10	0.81	3.98	1.19	1.70
10^{-4}	0.81	2.45	4.33	1.32	1.01	0.80	3.98	1.19	1.70
10^{-5}	0.79	2.32	4.17	1.34	0.99	0.80	3.98	1.18	1.70

Table 5.5: Flash flood in Toce River Valley – aligned case: L_1-error (m) for different gauges for different γ-values

Tab. 5.4.

Influence of γ-value

In the first two simulation runs drag force is neglected and only the γ-value in Eq. 5.16 is varied to study its influence. For $\gamma = 10^{-5}$, spurious oscillations in velocity occur at the wet/dry interfaces. If the threshold is increased to $\gamma = 1.0^{-3}$, the spurious oscillations are avoided. Results for these test cases are compared in Fig. 5.8 with measurement data. It is seen that especially at gauge 4 and gauge 5 the influence of γ is high. Here, increasing the threshold γ introduces numerical diffusion, as also reported in [60]. The results do not differ significantly between $\gamma = 10^{-4}$ (slightly less diffusive) and $\gamma = 10^{-3}$, thus the results for $\gamma = 10^{-4}$ have been omitted to avoid cluttering. Tab. 5.5 summarizes the L_1-errors for each gauge.

The present results are in agreement with results reported in [125, 77] in terms of over- and underprediction at different gauges. Only gauge 4 is captured more accurately by the model in [125]. Comparison with results of the single porosity model in [132] shows that the over- and underpredictions

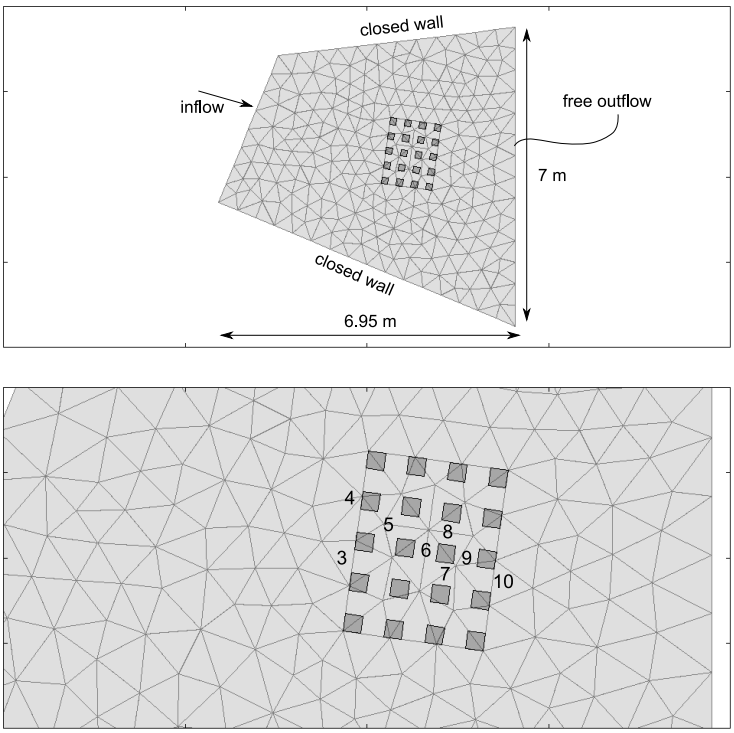

Figure 5.7: Flash flood in Toce River Valley – aligned case: top view of mesh whole domain (top); mesh detail showing the buildings and the gauges located between the buildings (buildings are plotted for illustration purposes only) (bottom)

at different gauges are reproduced, although the present results are more diffusive. This is because the model in [132] uses a mesh with higher resolution than the present model. In addition, the model results reported in [132] benefit from calibration of model parameters [125]. The test case has also been modeled in [128] using a high-resolution second-order accurate classical shallow water model. Comparison of the two model predictions shows that the presented model behaves very similar to the classical shallow water model, although the results presented here are much more diffusive. Furthermore, as the over- and underpredictions are in agreement between the two models, it can be assumed that these are systematic model errors resulting from the limitations of the shallow water assumptions, cf. [76].

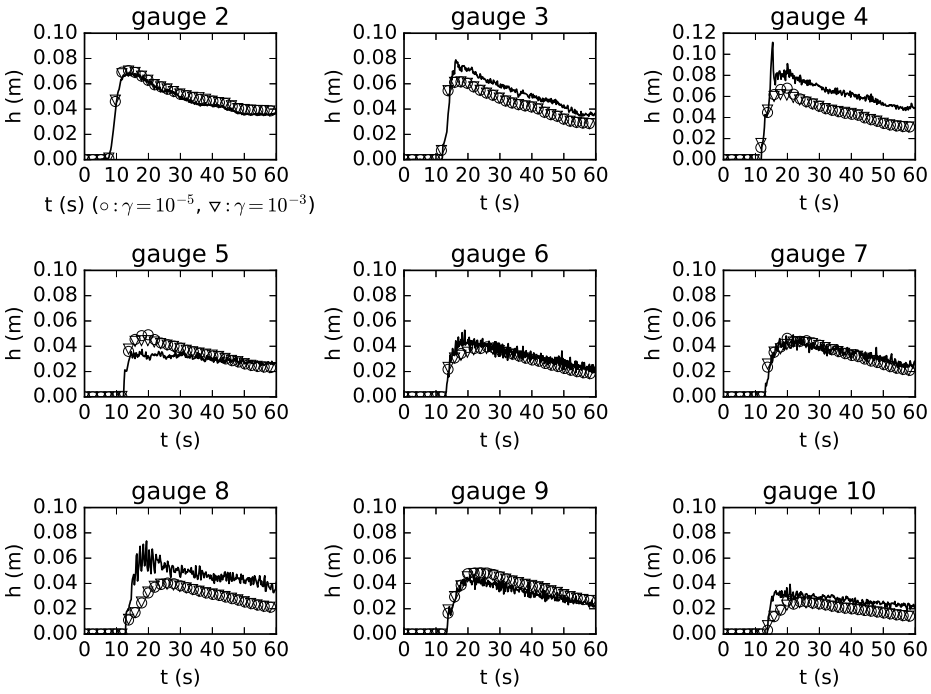

Figure 5.8: Flash flood in Toce River Valley – aligned case: Model predictions and measurements of water depth for $c = 0$ and $\gamma = 10^{-5}$ and $\gamma = 10^{-3}$

Influence of drag coefficient

The sensitivity of the drag force coefficient is studied. The threshold for the velocity limitation is set to $\gamma = 10^{-3}$ and the drag coefficient c is set to $c = 2$ and $c = 5\,\mathrm{m}^{-2}$, separately. Results are plotted in Fig. 5.9 and L_1-errors between predictions and measurements are summarized in Tab. 5.6. The prediction accuracy at gauges 6, 7 and 8 is improved by the increased drag coefficient. These are the gauges that are positioned between the buildings and therefore are most affected by drag force. The model does not behave as sensitively to the drag coefficient as the model in [125], where $c \approx 2\,\mathrm{m}^{-2}$ causes significant change in the model prediction. However, it is observed that the influence of the drag force on the results follows the same trend. In both [125] and the present model, the water depths at all gauges rise with increasing drag coefficient. The difference in the sensitivity between models is most likely due to the difference in the projected width estimation.

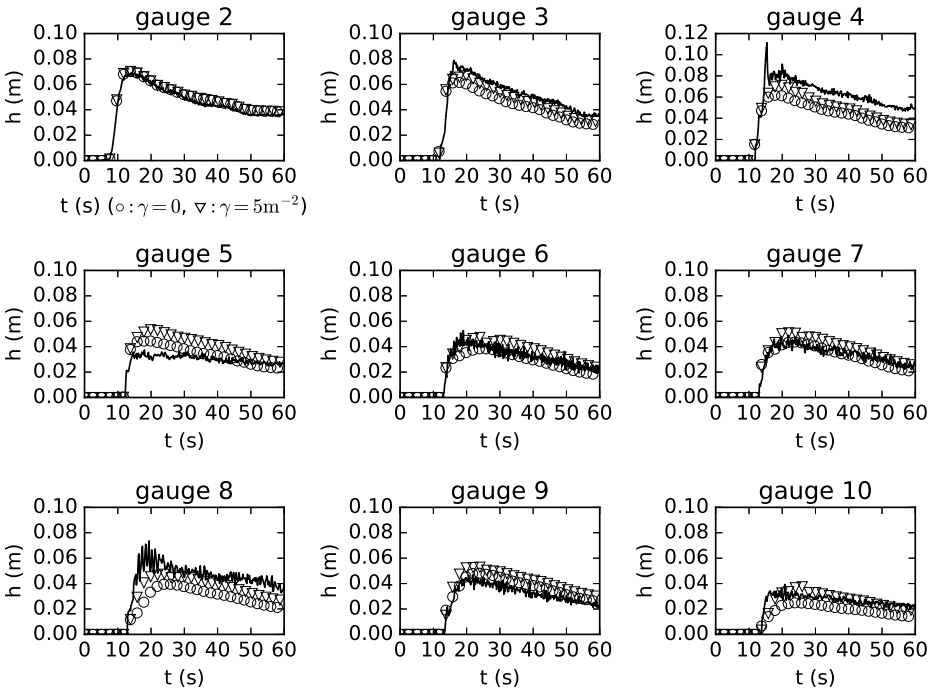

Figure 5.9: Flash flood in Toce River Valley – aligned case: Model predictions and measurements of water depth for $\gamma = 10^{-3}$ and $c = 0$ and $c = 5\,\mathrm{m}^{-2}$

c	$L_{1,2}$	$L_{1,3}$	$L_{1,4}$	$L_{1,5}$	$L_{1,6}$	$L_{1,7}$	$L_{1,8}$	$L_{1,9}$	$L_{1,10}$
0	0.81	2.49	4.41	1.32	1.10	0.81	3.98	1.19	1.70
$2\mathrm{m}^{-2}$	0.80	2.00	4.12	1.68	1.13	1.02	3.35	1.59	1.31
$5\mathrm{m}^{-2}$	0.79	1.48	3.18	2.55	1.15	1.19	2.16	2.13	0.74

Table 5.6: Flash flood in Toce River Valley – aligned case: L_1-error (m) for different gauges for different c-values

drag	$L_{1,2}$	$L_{1,3}$	$L_{1,4}$	$L_{1,5}$	$L_{1,6}$	$L_{1,7}$	$L_{1,8}$	$L_{1,9}$	$L_{1,10}$
isotr.	0.80	2.21	4.08	1.64	0.72	0.78	3.16	1.48	1.47
novel	0.79	1.48	3.18	2.55	1.15	1.19	2.16	2.13	0.74

Table 5.7: Flash flood in Toce River Valley – aligned case: L_1-error (m) at different gauges for drag formulations

drag	$L_{1,2}$	$L_{1,3}$	$L_{1,4}$	$L_{1,5}$	$L_{1,6}$	$L_{1,7}$	$L_{1,8}$	$L_{1,9}$	$L_{1,10}$
isotr.	0.92	2.23	4.17	6.09	5.29	0.97	5.76	0.80	1.29
novel	0.93	1.70	3.50	4.70	4.40	0.88	4.31	1.40	2.03

Table 5.8: Flash flood in Toce River Valley – staggered case: L_1-error (m) at different gauges for drag formulations

Comparison of novel drag formulation with isotropic drag formulation in [110]

In this section, results obtained with the novel drag formulation are compared with results obtained with the isotropic drag formulation in [110], where the drag coefficient c_D^b in Eq. 5.28 is calculated as

$$c_D^b = \frac{1}{2} C h. \tag{5.41}$$

Here, C accounts for both the projected width w_p and c in Eq. 5.29 and is a model calibration parameter. For the simulation here, a value of $C = 2\ \mathrm{m}^{-1}$ is chosen by trial and error. For the proposed drag formulation, $c = 5\,\mathrm{m}^{-2}$.

Results are compared in Fig. 5.10 and L_1-errors are presented in Tab. 5.7. It is observed that both drag formulations yield similar results. This is most likely due to the regularity and alignment of the building block.

The argument is supported by an additional simulation run that investigates the same domain with a different building configuration, the so-called "staggered" case. The computational mesh is the same as before, but the buildings are rearranged as shown in Fig. 5.11 (top). All model parameters are kept the same.

The results in the staggered case are improved by the proposed drag force formulation, as seen in Fig. 5.12. The summary of L_1-errors is given in Tab. 5.8. It can be seen that the model accuracy is enhanced at gauges 6, 7, 8 and 9.

Finally, results can be significantly improved by adopting a special computation mesh as shown in Fig. 5.11 (bottom). This can be regarded as

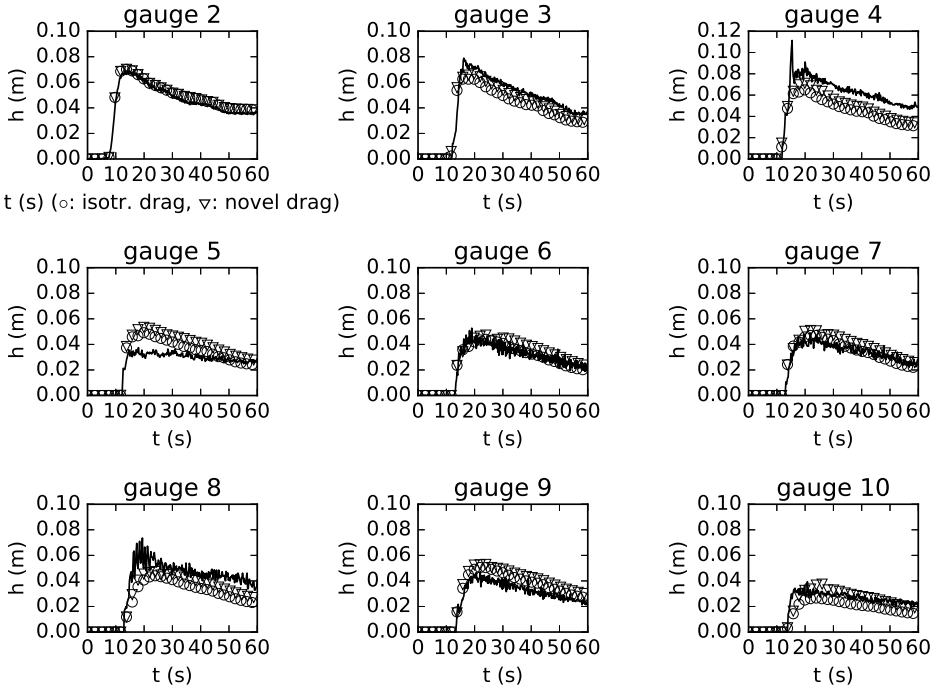

Figure 5.10: Flash flood in Toce River Valley – aligned case: Model predictions and measurements of water depth for novel drag formulation and isotropic drag formulation from [110]

a variation of the "gap-conforming" meshes in [125], where the edges align with the gap between the buildings. It is noted that in [125], in the gap-conforming meshes cell vertices are located at the center of the buildings. Because the essence of both meshes is the same (conforming to the gap between buildings), the name "gap-conforming" is used hereinafter as well. As before, the mesh is created using an edge length of 0.5 m. Results using this mesh are shown in Figure 5.13 and the L_1-errors are summarized in Tab. 5.9. Again, the present drag formulation also improves results at every gauge. The improvement is not as significant as in the case with the non-conforming mesh. Comparison with results reported in [125] show that the present model behaves similarly to the model in [125] for the staggered case in terms of the over- and undershooting. However, it does not reproduce the results as accurately as the model in [125] which uses an almost exact projected length.

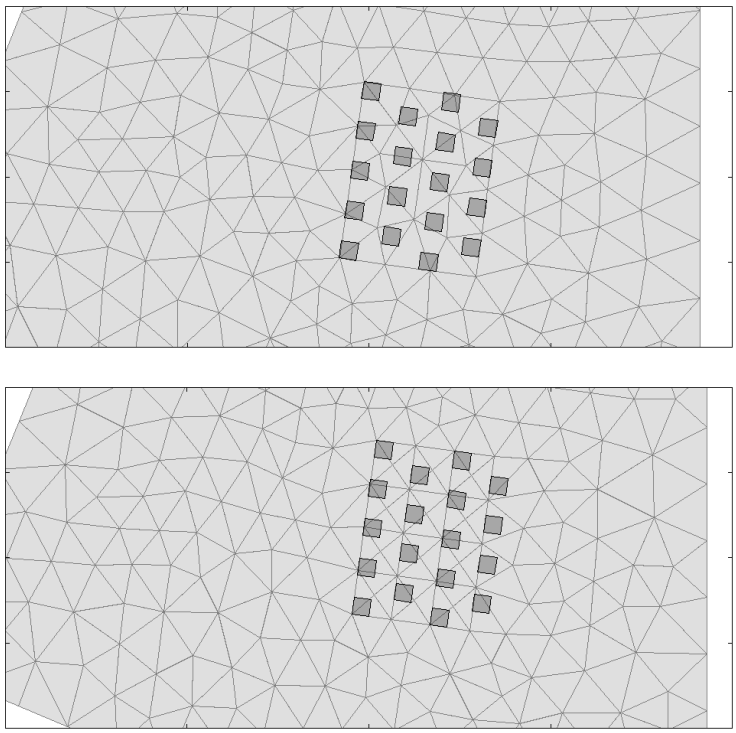

Figure 5.11: Flash flood in Toce River Valley – staggered case: top view of mesh detail showing the buildings (buildings are plotted for illustration purposes only) with old mesh (top) and gap-conforming mesh (bottom)

drag	$L_{1,2}$	$L_{1,3}$	$L_{1,4}$	$L_{1,5}$	$L_{1,6}$	$L_{1,7}$	$L_{1,8}$	$L_{1,9}$	$L_{1,10}$
isotr.	0.92	1.82	4.14	3.04	4.96	0.91	2.32	1.28	1.54
novel	0.92	1.25	3.37	2.52	4.29	0.67	2.95	0.67	2.18

Table 5.9: Flash flood in Toce River Valley – staggered case: L_1-error (m) at different gauges for drag formulations for the gap-conforming mesh

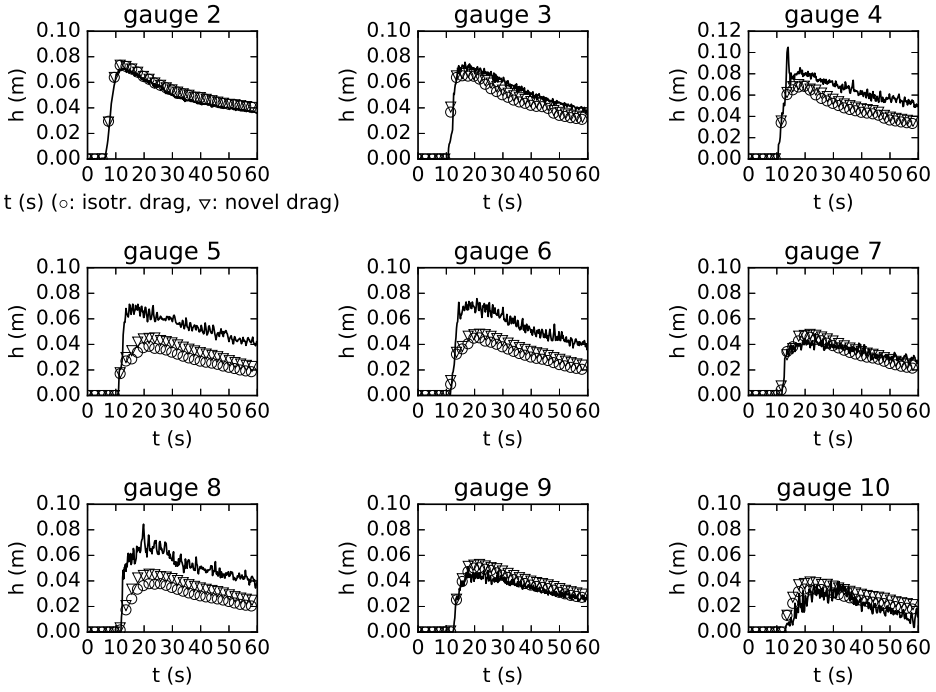

Figure 5.12: Flash flood in Toce River Valley – staggered case: Model predictions and measurements of water depth for novel drag formulation and isotropic drag formulation from [110]

5.6 Conclusions

A simple and efficient scheme was proposed to solve the anisotropic-porosity shallow water equations on unstructured meshes. The scheme is well-balanced and able to maintain stationary flow states. The computational cost is reduced as reported in [125, 110, 116] two-orders up to three-orders of magnitude compared to conventional high-resolution simulations.

In order to avoid spurious oscillations due to the reconstruction of the velocity terms at the edge, a novel criterion to limit the velocities is proposed. The criterion requires the specification of one numerical parameter (γ) that enables to control how strict the monotonicity criterion is applied. The stricter the limitation is applied, the more diffusive the model results become. Consequently, avoiding spurious velocities relaxes the time step and the simulation runs faster. In the presented test case in Sec. 5.5 with complex topography and wetting and drying, a value of $\gamma = 10^{-3}$ was found

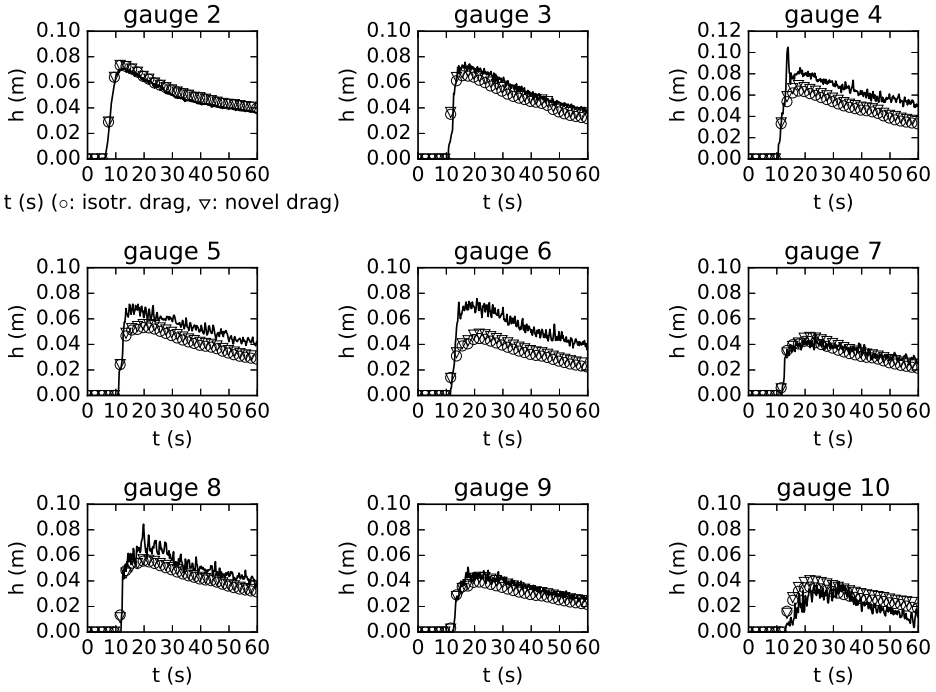

Figure 5.13: Flash flood in Toce River Valley – staggered case: Model predictions and measurements of water depth for novel drag formulation and isotropic drag formulation from [110] for the gap-conforming mesh

to be a good balance between accuracy and robustness.

The traditional anisotropic-porosity shallow water model describes the conveyance of the edge using a single areal porosity. Thus, a large discontinuity across the edge cannot be represented accurately. Using a simple head-loss term to correct the numerical flux improves the model accuracy at large discontinuities significantly. The proposed head-loss term does not introduce any calibration parameters to the model, as the proposed value for the contraction coefficent $m = 0.62$ yields good results in the investigated cases.

A simple method to estimate the projected width in the drag force calculation is proposed that does not require extensive preprocessing. The projected width is calculated separately in the x-direction and y-direction, thus the drag force is calculated in an "anisotropic" way. The proposed drag coefficient calculation enhances the accuracy of the results, especially if the building configuration is staggered. The choice of the characteristic

length in the proposed drag formulation influences the results significantly. In this work, the circumference of the cell was found to yield satisfactory results for both aligned and staggered building configurations.

The model is mesh dependent and in order to get accurate results special care has to be taken concerning the computational mesh. The mesh-dependency of the anisotropic-porosity model is well-known and has been reported in [125, 116]. Meshes that partially align with building geometry, especially gap-conforming meshes [125], provide more accurate results. If gap-conforming meshes are used, the influence of the drag formulation on the model results is not significant. Thus, if the mesh is appropriate, a simple estimation for the drag force head-loss may be sufficient.

In recent years, some effort has been devoted to reduce the mesh-dependency of the anisotropic-porosity model (M. Bruwier, private communication). As discussed in [48, 49], the mesh-dependency of the model can not be removed completely, as it is inherent in the model derivation. Thus, in the authors' opinion, another approach that would enhance the model accuracy would be to develop unstructured meshing techniques to automatically generate gap-conforming meshes.

5.7 Acknowledgement

The authors are grateful to the scholarship granted to Jiaheng Zhao by the Chinese Scholarship Council.

Chapter 6

Coupling of coarse grid approaches

Published as:
[109] Özgen, I. (2017) A coarse grid approach-based model chain for fast rainfall-runoff predictions in natural and urban areas. In: Proceedings of the 37th IAHR World Congress 2017, Kuala Lumpur, Malaysia.

6.1 Abstract

Flood events in urbanized areas are usually caused by localized rainfall events with very high intensity that occur in catchments located at the upstream of the city. The typical model chain for forecasting this type of event is a hydrological model that generates input for a two-dimensional hydraulic model. However, in recent years, the depth-averaged two-dimensional shallow water equations are applied to compute rainfall-runoff in natural catchments as well as inundation areas in city environment. The application is limited by computational constraints, that result from the high mesh resolution required to account for microtopography in natural and buildings in urban catchments. In this context, coarse grid approaches aim to reduce computational cost by enabling simulations on coarser meshes and introducing subgrid treatments to recover some of the information at subgrid-

scale. This contribution presents a novel model chain that comprises two coarse grid approaches with specialized application domains: (1) friction law-based coarse grid approach and (2) anisotropic porosity-based coarse grid approach. The hydrological model that is usually used for these type of predictions is replaced by a shallow water model with a specialized friction law to account for microtopography. The urban flood inundation model is sped up by introducing anisotropic porosity terms to account for buildings. The model chain is applied to predict rainfall-runoff in an idealized city, based on a real rainfall event in a real natural catchment. An averaged behavior of a high-resolution model chain can be obtained with significantly lower computational cost such that the simulations run on average about 100 times faster than the high-resolution counterpart.

6.2 Introduction

In most forecasting systems, a model chain that consists of a hydrological model and a two-dimensional hydraulic model is used to predict inundated areas for a rainfall event. Here, the hydrological model calculates a discharge at the outlet of the natural catchment that is then down-scaled and used as a boundary condition to drive the hydraulic model that computes inundation areas in city environment.

Using a hydraulic model instead of the hydrological model is currently hardly feasible due to high computational cost. In addition, the computational cost of conventional hydraulic finite-element and finite-volume codes typically prevents model discretization at a resolution that is achievable with airborne LIDAR technology [97]. The computational constraint on the discretization scale can be illustrated by the fact that the computational cost of an explicit finite-volume code is quantified by [76] as inversely proportional to the third power of the cell size. Codes that operate on the high-resolution data set scale to simulate flooding of large urban catchments are usually utilizing high-performance computing technology on supercomputers to achieve feasible computation time, e.g. [56, 129, 80, 1].

Besides from high-performance computing, the issue can be approached in two ways, either by simplifying the mathematical model [97, 19, 20, 69], or by reducing the cell number by means of a subgrid parameterization of the building or microtopography effects on the flow. Fig. 6.1 shows an overview of the motivation for using coarse grid approaches in hydro- and environmental system modeling.

A very straight-forward subgrid approach is artificially increasing the roughness parameter in the shallow water model to account for head loss

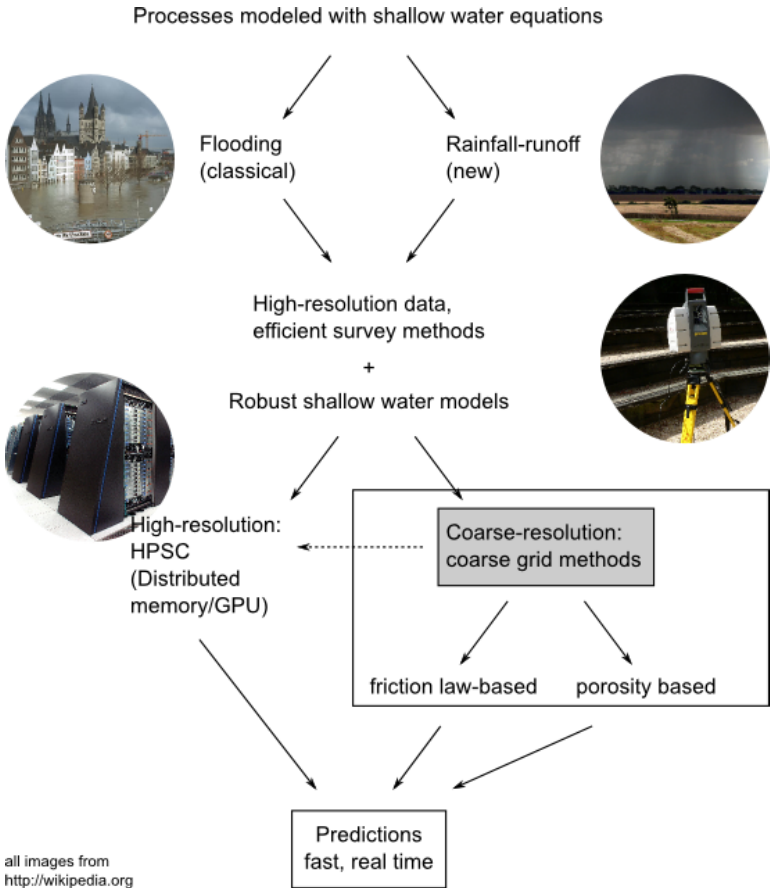

Figure 6.1: Motivation for using coarse grid methods

due to unresolved obstacles. This approach has been investigated for urban flood modeling in [106], wherein it is noted that this approach may lead to errors in the modeled flow routes and in [88], wherein it is reported that finding suitable values for the roughness parameters is rather non-intuitive. For applications in natural catchments, [123] derive a friction approach to account for ridges and furrows and [70] present a friction approach that accounts for vegetation. In this study, we use the friction law derived in [114] to account for unresolved microtopography to enable an efficient shallow water equations-based computation of rainfall-runoff in natural catchments that replaces the hydrological model in the aforementioned model chain.

Another coarse grid approach is based on a porosity term. Essentially, in this approach the computational cell with unresolved buildings inside of it, is treated as a porous medium. Thus, a porosity term is introduced into the shallow water equations. Following the pioneering work by Defina [26]

and Hervouet *et al.* [55], Guinot & Soares-Frazão [51] and Soares-Frazão *et al.* [132] presented the so-called isotropic porosity shallow water equations and provided a Godunov-type finite-volume method to solve them. The isotropic porosity shallow water equations are derived using a representative elementary area (REA) assumption. Guinot [48] notes that the existence of an REA in urbanized areas is debatable. Assuming that a REA exists, [48] then shows that the scale of the assumed REA exceeds the mesh resolution for several orders of magnitudes, but points out that from a numerical point of view, it is safe to choose a mesh resolution below the REA scale, as the numerical convergence requires the cell size to become infinitely small. We note that from an application point of view, the discussion about the REA scale is unimportant as satisfying results are obtained by using the isotropic porosity model [51, 132].

The anisotropic porosity shallow water equations have been derived in [125], to overcome a limitation of the isotropic porosity shallow water model, that is, the impossibility for the isotropic porosity shallow water model to account for directional effects induced by local anisotropic structures. Sanders *et al.* [125] derive the equations in integral form to remove the constraint of isotropy imposed by the REA assumption. In the anisotropic porosity model by [125], directionality is accounted for by means of additional porosity terms at the edges of the computational cell. A similar approach was later adopted in [20], where edge conveyance coefficients are defined at each edge. As pointed out by many researchers, e.g. [125, 48, 110], the integral approach results in porosity terms that are heavily mesh-dependent. Currently, there is no treatment available to overcome the mesh-dependency of the anisotropic porosity shallow water model, although research in this direction is currently carried out at the University of Liege (M. Bruwier, private communication). In this work, the anisotropic porosity shallow water equations, solved by the numerical model presented in [116], are used to predict inundation heights in urban environment.

In this study, the anisotropic porosity shallow water model for urban environment is coupled with the friction-based coarse grid approach for natural catchments to obtain a novel model chain that can be applied for the fast prediction of urban runoff.

6.3 Governing equations

In this section, we give an overview of the mathematical model concepts that are used. For sake of brevity, we omit the derivation of the equations. The reader is referred to [114] and [110] for a detailed discussion of the friction

law-based coarse grid approach and the anisotropic porosity shallow water equations, respectively. We further note that in the following, turbulence and molecular viscosity as well as other momentum diffusion terms are neglected. This has the advantage that the governing equations become hyperbolic instead of being of mixed type. The physical justification is that in very shallow flows such as rainfall-runoff, turbulence is mainly produced by bed friction [17].

Classical shallow water equations with specialized friction law

The classical shallow water equations are written in differential form as

$$\frac{\partial \mathbf{q}}{\partial t} + \frac{\partial \mathbf{f}}{\partial x} + \frac{\partial \mathbf{g}}{\partial y} = \mathbf{s} \tag{6.1}$$

where t is time, x and y denote the axes of the Cartesian coordinate system, $\mathbf{q}$ is the vector of conserved variables, $\mathbf{f}$ and $\mathbf{g}$ are the flux vectors in x- and y-direction, respectively, and s is the source term vector. The flux and storage vectors in Eq. 6.1 are defined as

$$\mathbf{q} = \begin{bmatrix} h \\ hu \\ hv \end{bmatrix}, \ \mathbf{f} = \begin{bmatrix} hu \\ hu^2 + gh^2/2 \\ huv \end{bmatrix}, \ \mathbf{g} = \begin{bmatrix} hv \\ hvu \\ hv^2 + gh^2/2 \end{bmatrix}, \tag{6.2}$$

with h standing for water depth, u and v standing for velocity in x- and y-direction, respectively, and g standing for the gravitational acceleration, usually set to $9.81\,\mathrm{m/s^2}$. The source term vector is defined as

$$\mathbf{s} = \begin{bmatrix} i \\ -gh\partial z/\partial x - f_x \\ -gh\partial z/\partial y - f_y \end{bmatrix}. \tag{6.3}$$

Here, i is the rainfall intensity, z is the bed elevation and f_x and f_y are the friction source terms in x- and y-direction, respectively. The definition of the friction source terms is according to the friction law in [114]:

$$f_x = -\left(ngh^{-\frac{1}{3}} + K\right)||\mathbf{v}||u, \tag{6.4}$$

where $\mathbf{v} = [u, v]^T$ is the vector of velocity and $||\mathbf{v}||$ denotes the Euclidian norm of the vector, n is Mannings roughness coefficient and K is a geometrical parameter defined as

$$K = \alpha_0 \exp\left(\alpha_1 \left(\Lambda - 1\right)\right), \tag{6.5}$$

with α_0 and α_1 being calibration parameters and Λ being the so-called inundation ratio [83]:

$$\Lambda = \frac{h}{(1 - s_0)\, k} \tag{6.6}$$

Here, s_0 is the bottom slope and k is the characteristic roughness height, which is set equal to the standard deviation of the subgrid-scale structure. While in [114], a spatially uniform distribution of the roughness height is used, [112] examined, whether calculating the roughness height individually in each cell improves the model accuracy and report no significant improvement in natural catchments.

Anisotropic porosity-based shallow water equations

The anisotropic porosity shallow water equations are written in an integral-differential form as

$$\int_\Omega i \frac{\partial \mathbf{q}}{\partial t} d\Omega + \oint_{\partial\Omega} i\mathbf{F}\mathbf{n} dr = \int_\Omega i\mathbf{s} d\Omega, \tag{6.7}$$

where $i(x, y)$ is a so-called phase function that returns 1 if (x, y) corresponds to a void or 0 if (x, y) corresponds to an obstruction. We note that $\mathbf{Fn} = \mathbf{f}n_x + \mathbf{g}n_y$, and that the flux and storage vectors correspond to Eq. 6.2, and the source term vector contains an additional source term that models the fluid-building interaction at subgrid scale. This reads

$$\int_\Omega i\mathbf{s} d\Omega = \int_\Omega i\mathbf{p} d\Omega + \oint_{\partial\Omega^*} g\frac{h^2|_{\eta_0}}{2}\mathbf{m} dr + \int_\Omega c\mathbf{v}||\mathbf{v}|| d\Omega, \tag{6.8}$$

where the term with p now corresponds to the source term of Eq. 6.3 and the second term on the right-hand side is the additional source term, calculated by a path integral along the fluid-building interface with $\mathbf{m}$ being the unit normal vector pointing outside of the fluid phase. The third term is a head loss term calculated via a drag force formulation with c being the drag force coefficient. A finite-volume type discretization of the equation then yields:

$$\left(1 + \kappa^{n^*}\right)(\phi\mathbf{q})^n - \Delta t \sum_k \left(\psi_k \mathbf{F}_k \mathbf{n}_k\right)^{n^*} \Delta r_k, \tag{6.9}$$

where κ represents an implicit treatment of friction and drag source terms [11], ϕ is the cell porosity, ψ is the edge porosity, n stands for the time level and the choice of n^* determines the time-stepping method. If $n^* = n$, the method corresponds to an explicit forward Euler time-stepping, if $n^* = n + 1/2$ the method corresponds to a two-step Runge-Kutta scheme.

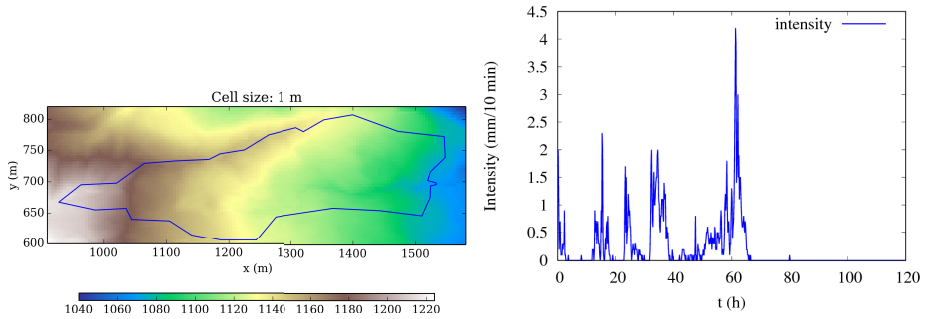

Figure 6.2: Catchment topography (left); intensity of the rainfall event (right)

6.4 Numerical method

The governing equations are solved in integral-differential form (Eq. 6.7) with a Godunov-type finite-volume method. Second order accuracy is achieved by means of a linear MUSCL reconstruction. Time is discretized by a second order accurate two-step TVD Runge-Kutta scheme, cf. Eq. 6.9. More details about the numerical method can be found in [116].

6.5 Computational example

The two presented coarse grid approaches are coupled to obtain a model chain that is applied to model runoff in an urbanized environment caused by a heavy rainfall event in a natural catchment located at the upstream of the city. We consider an idealized city that is located at the outlet of the subcatchment and impose the discharge of the subcatchment as an inflow boundary condition of the model of the city. While there is measurement data available for the discharge of the subcatchment, no measurement data is available for the city.

Friction law-based coarse grid approach for rainfall-runoff in natural catchment

Initial and boundary conditions

The natural catchment is a real world subcatchment of the Heumöser slope in Vorarlberg, Austria, that spans about 100000 m^2. Bottom elevation is provided in 1 m by 1 m resolution by the Austrian Torrent and Avalanche

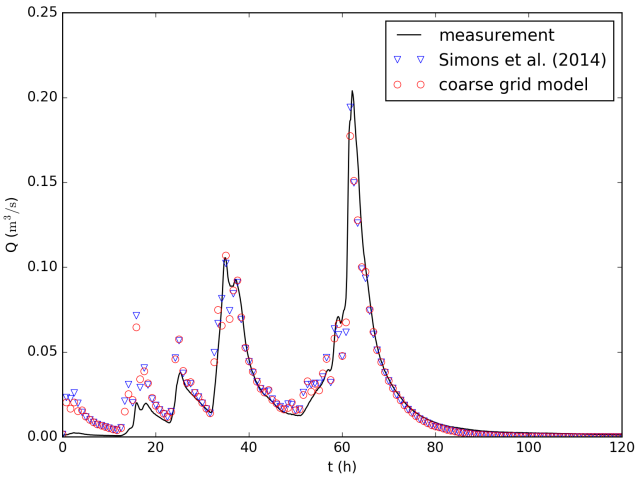

Figure 6.3: Comparison of coarse grid model results with measurement data and a high-resolution simulation by [128]

Control department, cf. Fig. 6.2 (left). The whole domain is initially dry. Discharge is generated by a spatially uniform rainfall according to a time series measured in July 2008 with a temporal resolution of 10 min, cf. Fig. 6.2 (right). Here, the rainfall intensity is multiplied with the runoff coefficient $\psi = 0.3$ to account for infiltration [128]. In addition, following [128], the interflow component is modeled by means of a linear storage model, with a storage coefficient of $K = 6\,\mathrm{h}$, and added to the overland flow to obtain the total discharge at the outlet. All boundaries are open boundaries. The domain is discretized with a quadratic grid with cell size of 10 m. The model is calibrated as reported in [114] with $n = 0.035\,\mathrm{sm}^{-1/3}$, $\alpha_0 = 0.3$ and $\alpha_1 = 0.87$. The simulation runs for 120 h, i.e. 5 days.

Results

Model results for the discharge at the outlet of the domain are compared with field measurement data and a high-resolution simulation (mesh resolution 1 m) by [128] in Fig. 6.3.

Both the high-resolution model and the coarse grid model overshoot the measurement data at the beginning of the simulation. As discussed in [16], this might be due to shear effects on the thin water film in the real world that cannot be reproduced with the mathematical model of the shallow water equations. After $t = 20\,\mathrm{h}$, the deviation between the models and the measurement data diminishes. The third and fourth peaks at about

$t = 40\,\mathrm{h}$ and $t = 60\,\mathrm{h}$, respectively, are captured fairly accurately.

The friction-law based coarse grid approach reduces the computational cost such that the simulation results are obtained 350 times faster than the high-resolution simulation of [128].

Anisotropic porosity shallow water model for urban environment

We define an idealized city geometry to complete the model chain. We assume that the city, that represents the real city of Ebnit, Austria, in a very simplified way, is directly located at the outlet of the natural catchment, such that we can apply the model result obtained in the simulation above as an inflow boundary condition to drive the anisotropic urban flood model. In a second simulation run, we artificially increase the discharge at the boundary to produce a more hazardous flood event.

Initial and boundary conditions

The domain is a 500 m by 300 m large urban basin with flat bed, wherein the only topographical features are the buildings inside the domain, cf. Fig. 6.4 (top). We construct a building block with elements that are rectangles with dimensions 20 m by 30 m. Outside of the block, we position a C-shaped building that represents an important building with a high damage potential, e.g. school or university. We are interested in the arrival time of the flood wave and the resulting water depth at this location. Thus, a gauge is positioned at the front of this building. The domain is initially dry, the discharge calculated by the previous model run is imposed at a 25 m wide inlet at the west boundary of the domain that shall represent a breach in the dam that protects the city. All other boundaries are open boundaries.

In Fig. 6.4 (bottom), the coarse mesh used by the anisotropic porosity model is shown. Buildings are plotted only for illustration purposes and are actually accounted for by means of the porosity terms. We note that the mesh is constructed such that the outline of the building block aligns with cell edges. This discretization significantly enhances the quality of the results.

The high-resolution mesh consists of 8222 triangular cells with element size ranging between 10 m and 5 m, and the coarse-resolution mesh consists of 698 triangular cells with cell size of 25 m.

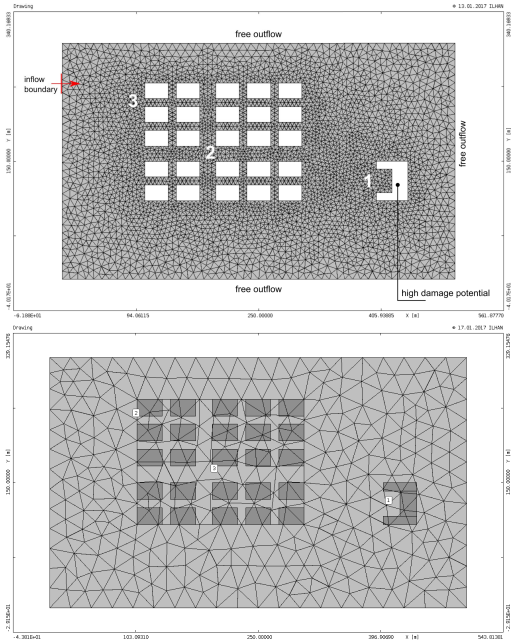

Figure 6.4: High-resolution mesh, building configuration and position of gauges and the inlet (left); coarse resolution mesh for the anisotropic porosity model with buildings plotted for illustration purposes (right)

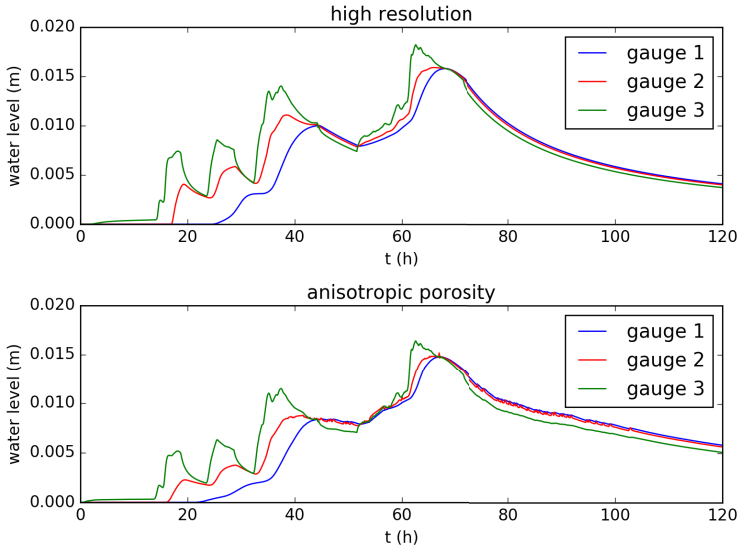

Figure 6.5: Model results for the high-resolution simulation (top) and the anisotropic porosity approach (bottom)

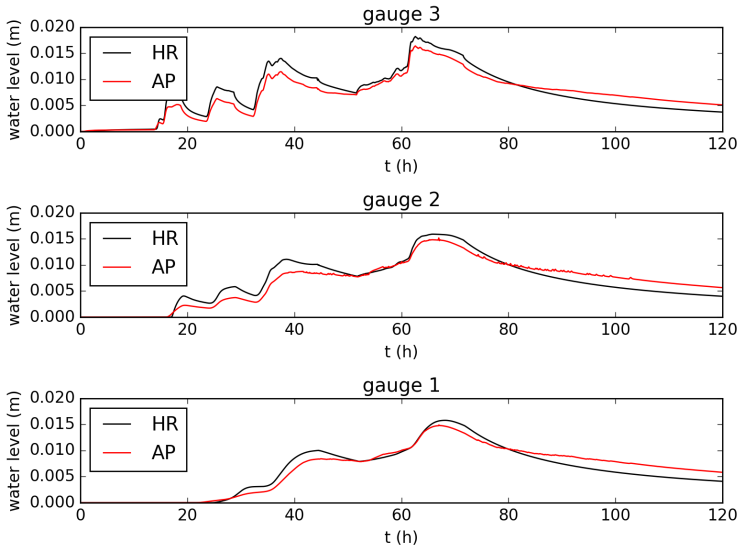

Figure 6.6: Comparison of high-resolution model results (HR) with anisotropic porosity model results (AP) at gauges 3 (top), 2 (center) and 1 (bottom)

Results

Model results for both the high resolution simulation and the anisotropic porosity approach are shown in Fig. 6.5. The overall dynamics of the flood wave is captured well by the anisotropic porosity model. The hydrograph consists of four peaks that correspond to the peaks in the inflow (cf. Fig. 6.3). For both models, the runoff arrives at gauge 1 (highest damage potential) at about $t = 20\,\mathrm{h}$, while gauge 2 at city center is inundated at about $t = 15\,\mathrm{h}$. We observe that gauge 3 is influenced more by fluctuations in the inflow than gauge 2 and gauge 3. The maximum water depth is measured at gauge 3 at about 62 h, which corresponds to the maximum peak in the inflow data. In comparison to the inflow hydrograph, the results at the gauges are damped and temporally delayed. This behavior is captured by both models, although we see that the maximum water depth in the anisotropic porosity approach results (about 1.6 cm) is smaller than in the high resolution results (about 1.8 cm).

The results of both model runs are compared in Fig. 6.6. In the beginning, the results of the anisotropic porosity approach overall undershoot the hydrograph produced by the high resolution model. In the late stage of the simulation, when the inflow begins to decline ($t = 80\,\mathrm{h}$), the anisotropic

porosity model results overshoot the high resolution hydrograph. We report an average deviation of about 3 mm in water depth at all gauges but an exact prediction of the arrival times of the runoff waves in all cases.

The forecast of this model chain predicts that fortunately the rainfall event in the natural catchment is not heavy enough to cause substantial damage in the city. The maximum water depth we observed is about 2 cm and located at the city border. The model chain is able to reproduce an averaged behavior of the high resolution simulation and is about 100 times faster than its high-resolution counterpart.

For illustration purposes, we artificially increase the discharge at the inlet boundary by factor 100. Results for the increased discharge are shown in Fig. 6.7. We observe that the water level at all gauges increases significantly and the arrival time of the flood wave is significantly shorter. At gauge 3, a maximum water level of about 1.6 m at $t = 60$ h is predicted by the high-resolution model (Fig. 6.7 (top)) which is accurately captured by the anisotropic porosity shallow water model as well (Fig. 6.7 (bottom)). As the flood wave propagates through the city environment, the amplitude of the water level is damped such that at gauge 2, the maximum water level calculated by the high-resolution model is about 0.8 m at about $t = 60$ h. Here, the anisotropic porosity model underestimates the water level and yields a maximum value of about 0.75 m. Finally, at gauge1, that is located in the area with high damage potential, the porosity model overestimates the maximum water level slightly.

Overall, the dynamic of the flood is reproduced accurately by the anisotropic porosity model. Fig. 6.8 shows a comparison of the model results per gauge where the aforementioned discussions can be observed as well. Fig. 6.9 shows water levels plotted at different time steps and good agreement between both models is observed. In both cases, the simulation with the anisotropic porosity model runs about 100 times faster.

6.6 Conclusions

We presented and coupled two coarse-grid approaches, i.e. modified friction-law approach and anisotropic porosity approach, for application in urban runoff and urban flood modeling. The novelty of the presented approach is that the model chain contains two hydraulic models instead of the more common model chain hydrological model coupled with hydraulic model.

As a proof of concept, we simulated runoff and inundation in an idealized city using the suggested model chain. Model results are promising and indicate that this approach might indeed be used to forecast flood arrival

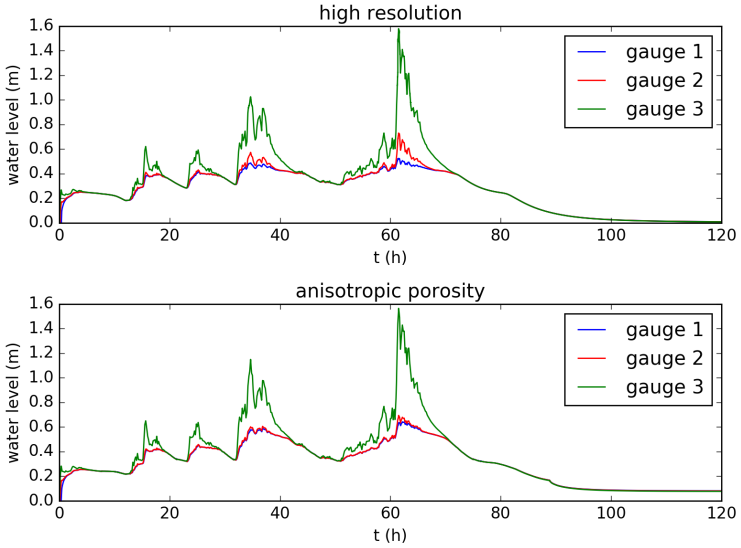

Figure 6.7: Model results for case with artificially increased discharge for the high-resolution simulation (top) and the anisotropic porosity approach (bottom)

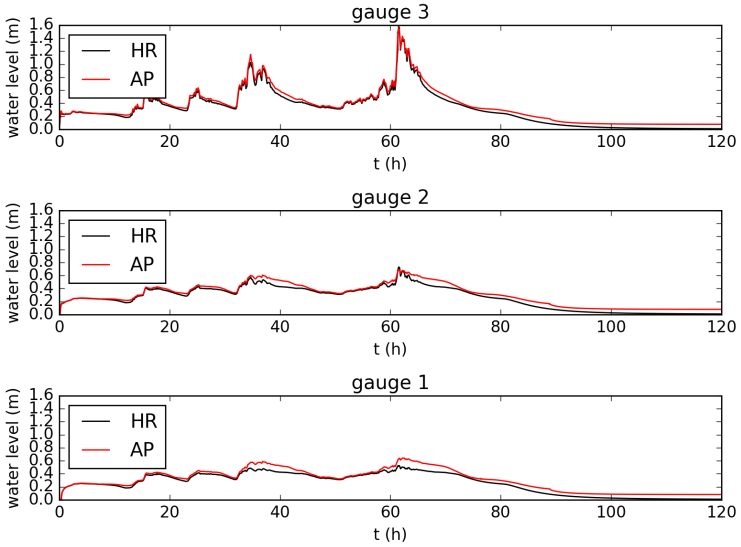

Figure 6.8: Comparison of high-resolution model results (HR) with anisotropic porosity model results (AP) at gauges 3 (top), 2 (centers) and 1 (bottom) for case with artificially increased discharge

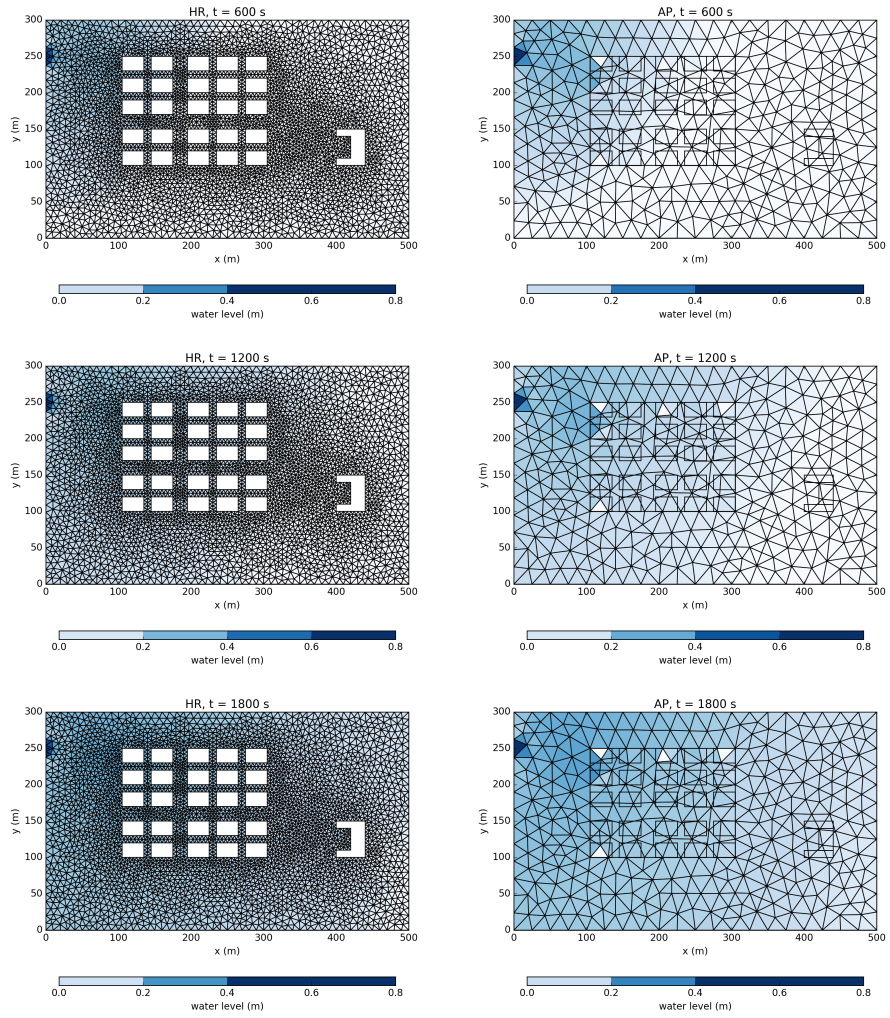

Figure 6.9: Water level plotted at different time steps for the artificially increased discharge for high-resolution model (left) and anisotropic porosity model (right)

times and flood inundation areas. The decrease in computational cost enables to obtain model results in feasible time spans on a personal computer. On average, the models run about two orders of magnitude faster than their high-resolution counterparts.

Future research may focus on studying the presented model approaches at even larger scales, e.g. large natural catchments and cities.

6.7 Acknowledgements

This work was supported by the DFG Research Training Group Urban Water Interfaces (DFG-GRK2032). Guidance and supervision by Prof. R. Hinkelmann, Technische Universitt Berlin, Germany, and Dr. D. Liang, University of Cambridge, UK, is gratefully acknowledged.

Chapter 7

Supplementary work

This chapter summarizes supplementary work carried out during my time as a PhD student at Technische Universität Berlin during the years from 2014 to 2017.

7.1 Effect of buildings on the S-curve of urban catchments

Published as:

[89] Liang, D., Özgen, I., Hinkelmann, R., Xiao, Y., and Chen, J.M. (2015) Shallow water simulation of overland flows in idealised catchments. *Environmental Earth Sciences* 74, pp. 7307–7318.
doi: 10.1007/s12665-015-4744-5

This is the postprint version of the publication. The final publication is available at Springer via `https://doi.org/10.1007/s12665-015-4744-5`.

Abstract

This paper investigates the relationship between the rainfall and runoff in idealised catchments, either with or without obstacle arrays, using an extensively-validated fully-dynamic shallow water model. This two-dimensional hydrodynamic model allows a direct transformation of the spatially distributed rainfall into the flow hydrograph at the catchment outlet. The model was first verified by reproducing the analytical and experimental

results in both one-dimensional and two-dimensional situations. Then, dimensional analyses were exploited in deriving the dimensionless S-curve, which is able to generically depict the relationship between the rainfall and runoff. For a frictionless plane catchment, with or without an obstacle array, the dimensionless S-curve seems to be insensitive to the rainfall intensity, catchment area and slope, especially in the early steep-rising section of the curve. Finally, the model was used to study the hydrological response of an idealised catchment covered with buildings, which were represented as an obstacle array. The influences of the building array size and layout on the catchment response were presented in terms of the dimensionless time at which the catchment outflow reaches 50% of the equilibrium value.

7.2 Numerical treatment of wet/dry fronts

Published as:

[37] Fišer, M., Özgen, I., Hinkelmann, R. and Vimmr, J. (2016) A mass conservative well-balanced reconstruction at wet/ dry interfaces for the Godunov-type shallow water model. *International Journal for Numerical Methods in Fluids* 82, pp. 893–908.
doi: 10.1002/fld.4246

This is the postprint version of the publication. The final publication is available at Wiley via `https://doi.org/10.1002/fld.4246`.

Abstract

This paper presents a novel mass conservative, positivity preserving wetting and drying treatment for Godunov-type shallow water models with second-order bed elevation discretization. The novel method allows to compute water depths equal to machine accuracy without any restrictions on the time step or any threshold that defines whether the finite volume cell is considered to be wet or dry. The resulting scheme is second-order accurate in space and keeps the C-property condition at fully flooded area and also at the wet/dry interface. For the time integration, a second-order accurate RungeKutta method is used. The method is tested in two well-known computational benchmarks for which an analytical solution can be derived, a C-property benchmark and in an additional example where the experimental results are reproduced. Overall, the presented scheme shows very good agreement with the reference solutions. The method can also be used in the discontinuous Galerkin method.

7.3 Diffusive wave model

Published as:

[69] Jahanbazi, M., Özgen, I., Aleixo, R. and Hinkelmann, R. (2017) Development of a diffusive wave shallow water model with a novel stability condition and other new features. *Journal of Hydroinformatics*, 19, pp. 405–425.
doi: 10.2166/hydro.2017.108

This is the postprint version of the publication. The final publication is available at IWA Publishing via `https://doi.org/10.2166/hydro.2017.108`.

Abstract

One of the approaches to flood modelling is numerical simulation of the diffusive wave approximation of the shallow water equations. Improving these models in various aspects is still an open area of research. In this study, a new diffusive wave model with explicit time integration was developed which includes some novel features: (1) time steps are determined using a novel stability criterion which resulted in more dynamic time steps (i.e., broader range) compared to the conventional Courant-Friedrichs-Lewy stability condition; (2) stability constraints are reduced, considering the flow processes within surface ponds; (3) besides Manning's formula, which is the common equation for computing velocities in diffusive wave models, the free fall velocity and a new equation for wave-front velocity are employed; and (4) the influence of upstream surface ponds on downstream flow is considered. This paper introduces the enhanced diffusive wave model, the so-called overland flow simulator cellular automata (OFS-CA), and its results for five test cases. Available analytical solutions and an experimental study were used for verification. Two other shallow water models were used for comparison and benchmarking. Overall, good agreements were observed and OFS-CA was computationally less expensive compared to the other two shallow water models.

Chapter 8

Synthesis

8.1 Conclusions

Surface water systems are multiscale systems, wherein small scale features may have significant influence on the large scale flow field. Explicitly discretizing these small features in large domains leads to meshes with high cell number. Due to finite computer resources, the simulation on these meshes is often only feasible on supercomputers. Coarse grid approaches can be used to decrease the cell number of the mesh while conceptually accounting for the subgrid-scale features to perform computationally efficient simulations.

The main outcome of this work are the two coarse grid approaches that have been developed, namely the friction law-based coarse grid approach [114] (Chapter 2), and the porosity-based coarse grid approach, i.e. the anisotropic porosity shallow water model [110, 116, 115] (Chapters 3-5). Both model concepts have been studied in several test cases, ranging from very idealized academic benchmarks to laboratory scale experiments and "real world" applications.

As a proof of concept, a model chain that comprises both coarse grid approaches was applied to forecast a hypothetical flood event in an idealized city that results from rainfall concentration in a natural catchment (Chapter 6). The modeling results are promising, the inundation heights and the flood arrival time could be reproduced by the coarse grid approach-based model chain accurately enough for forecasting and early warning purposes.

A short overview of supplementary work that is related to the research

topic was given (Chapter 7).

General conclusions

Before drawing more detailed conclusions for each model approach, the following general conclusions can be drawn:

- It is possible to coarsen the computational mesh and to some extent recover subgrid-scale information by means of conceptual model approaches.
- These conceptual model approaches are based on sampling the topography information on a much finer scale than the computational grid and finding a suitable way to incorporate this information into the coarse grid shallow water model.
- The sampling of the subgrid-scale information may require more preprocessing than conventional shallow water models.
- The sampled subgrid-scale information is usually assigned individually to each computational cell which introduces mesh-dependency to the models. This mesh-dependency cannot be overcome completely.
- The coarse grid approaches cannot fully restore the model accuracy to equal a conventional high-resolution shallow water model, but reproduce an averaged behaviour of it.
- On average, the coarse grid approach reduces the simulation wall-time between two and three orders of magnitude, compared to a conventional high-resolution shallow water model. The magnitude of the speedup depends on the factor of grid coarsening and the specific problem that is investigated. The coarser the resolution is chosen, the higher the speedup becomes. For cases that are numerically challenging, e.g. rainfall-runoff over rough terrain, the speedup decreases because the time step size of the coarse grid model degenerates significantly.
- Overall, the approaches yield accurate results for the water depths and integral discharges at the outlet but less accurate results for the velocities and the unit discharges inside the domain. Localized flow processes at subgrid-scale cannot be resolved.
- Obtaining accurate results using the coarse grid approaches requires more user experience than the conventional shallow water model.

Friction law-based coarse grid approach

In Chapter 2, a novel friction law-based coarse grid approach, which uses three free calibration parameters and a water depth-dependent inundation ratio to calculate flow resistance in dependency of the water depth is developed. The inundation ratio depends on the roughness height, which is chosen to be the standard deviation of the subgrid-scale microtopography. The standard deviation can be calculated globally for the whole domain or locally in each cell.

Following conclusions are drawn for friction law-based coarse grid approaches:

- Implementing the friction-law based approach into an existing software framework is straight-forward, which is the main advantage of this approach.
- The approach is applicable to both structured and unstructured grids, using triangular, quadrilateral or mixed type elements.
- The approach yields stable results for rainfall-runoff simulations, because the numerical treatment of a friction source term is well understood in the state of the art of shallow water modeling, e.g. point-implicit discretization [11] or wave Riemann description [104].
- The calibration of three parameters is challenging for the modeler and is currently addressed by means of automatic calibration using numerical optimization methods for multidimensional functions. Based on personal experience, the Limited-memory Broyden, Fletcher, Goldfarb and Shanno algorithm (L-BFGS-B) [164] is recommended [114]. If an optimum set of parameters cannot be obtained with the L-BFGS-B algorithm, a brute force approach is recommended.
- Using automated calibration, good agreement between the coarse grid model and reference solutions or field measurements is obtained. The calibration effort is found reasonable, compared to the speedup that is obtained. Once the model is properly calibrated, the error introduced by applying it to different hydraulic conditions is found to be small. However, the modeler should be aware that there is a risk of overfitting the model.
- If calibrated correctly, the proposed friction approach outperforms many friction laws from literature in terms of accuracy.

- Applying the calibrated model to different hydraulic conditions or using a different mesh resolution decreases the accuracy of the results. Then, the model is required to be calibrated again for the specific hydraulic condition or mesh resolution.

Porosity-based coarse grid approach

In Chapters 3-4, a novel extension of the anisotropic porosity shallow water equations initially derived in [125] is presented. The extension derives a novel water depth-dependent formulation of the porosity terms that enables full inundation of subgrid-scale obstacles, which was not considered in the conventional anisotropic porosity shallow water model. A second-order Godunov-type finite-volume method to solve the modified equations on structured grids is presented.

In Chapter 5, the conventional anisotropic porosity shallow water model is studied and a Godunov-type finite-volume scheme is proposed for the solution of the equations on unstructured meshes. A novel monotonicity condition is derived which improves the robustness of the model. Improved calculation of the numerical flux and source term calculation are presented.

The porous shallow water model uses porosity terms to account for subgrid-scale topography information. The fraction of the cell that is available to flow, i.e. not blocked by buildings, is expressed by the volumetric porosity. In addition, in anisotropic porosity shallow water models, an additional edge porosity term, which represents the fraction of the edge available for flow, is assigned to each edge. The porosity terms are directly linked to the high-resolution topography data set, which needs to be sampled at a finer resolution than the computational mesh.

For the porosity-based coarse grid approaches, the following conclusions are drawn:

- In urban flood modeling the buildings usually are not inundated by the flood wave and thus, the porosity terms are constant model parameters. However, the porosity terms can be calculated in dependency of the water depth to account for inundation of the subgrid-scale features. Promising results are obtained using this novel formulation, which indicates that the porous shallow water model might be applied to a broader range of hydraulic and environmental problems such as rainfall-runoff modeling in natural catchments.

- Implementing the porosity-based approach into an existing software framework is more complicated than the friction law-based coarse

grid approaches. Here, porosity values have to be stored in each cell and each edge. In addition, additional source terms appear in the equations which have to be treated numerically. Thus, a large section of the existing code has to be completely rewritten.

- As the high-resolution data needed to calculate the porosities is usually provided in form of equidistant points, the porosity calculation is easy on structured grids, but becomes more complicated on unstructured triangular meshes.

- The porosity calculation that directly depends on the underlying topography results in a mesh-dependent model. In addition, the value of the edge porosity term changes depending on the location of the edge which means that even if the cell centroid remains at the same point and the cell is rotated, the values of the edge porosities may change. Hence, the anisotropic porosity model is mesh-dependent.

- The mesh-dependency was investigated in several cases, and it was found that a poor meshing strategy significantly reduces the accuracy of the model.

- If structured grids are used, aligning cell edges with building edges enhances the model accuracy.

- If unstructured triangular meshes are used, gap-conforming meshing, i.e. cell vertices are located at building centroids, is found to be the best meshing strategy. This is in agreement with current research reported in [125, 77, 76, 50].

- In this work, results obtained with unstructured triangular meshes are in general more accurate than the results obtained with structured grids. This is because unstructured triangular meshes are more flexible than structured grids and can better be fit to the building geometry. In addition, structured grids cause more numerical diffusion [14].

- As obstacles are not explicitly discretized, head loss terms due to obstacle-fluid interaction appear in the equations. Most commonly, these interactions are splitted in two parts: (1) the dynamic part and (2) the stationary part. As these processes are not resolved by the model, closure terms have to be derived (as in turbulence modeling). Usually, the stationary part is discretized as a geometric pressure term that is used to well-balance the model and the dynamic part is

described using a drag law. The optimal closure for these terms has not yet been found.

- The ambiguity of the drag law-based head loss formula reduces the model accuracy. Hence, a simple drag law-based head loss estimation that takes into account anisotropic features was presented. This approach increases the model accuracy to some extent.

- The reconstruction of the interface variables in the presence of edge porosities was identified as a source of instability. If the ratio between edge porosity and volumetric porosity is very small (investigations point to values smaller than 0.1 or 0.01, depending on the problem), spurious velocities may appear.

- A monotonicity treatment was proposed to suppress unphysically high velocities during the reconstruction process.

- In the presence of a porosity discontinuity across the edge, the anisotropic porosity model overestimates the momentum flux. Because a single edge porosity is assigned to each edge, the model cannot represent a porosity discontinuity across the edge. This is also recently addressed in [50], where it is shown that the eigenvalues of the anisotropic porosity shallow water model are different from the isotropic porosity model that is able to represent these type of discontinuities.

- In this work, the porosity discontinuity issue is addressed by adopting a double edge porosity approach. Defining a porosity at the left and right side of the edge allows to calculate an empirical head loss formula-based flux correction term. The head loss formula accounts for the momentum loss at sudden contractions, which is an analogical problem to the porosity discontinuity. This correction enhances the model accuracy significantly for large porosity jumps.

Final notes

Depending on the particular problem, one coarse grid approach has been found more advantageous than the other. While the friction law-based approach has been found to yield better results for rainfall-runoff simulations in natural catchments, the porosity-based approach yields better results for urban flood simulations.

8.2 Open issues and future research

The following open issues are identified which could be addressed in future research:

- The application of the friction law-based approach could be improved by a systematic study of the calibration parameters. Default values for common material and roughness heights, similar to the tables for Manning's coefficient available in literature would guide the modeler in the calibration process. An additional challenge here is that the calibration also depends on the mesh resolution, which needs to be addressed as well. This would require laboratory studies and extensive numerical simulations.

- The calculation of the roughness height in the friction law-based approach is not completely analysed. In [114], the roughness height was calculated globally for the whole domain and in [112], the roughness height was calculated individually in each cell. In an application to a natural catchment (Heumös slope, Austria), no significant improvement was observed. However, this could be related to the specific study site and the sensitivity of the roughness height calculation should be investigated in different case studies to draw final conclusions.

- In [115], it is reported that the anisotropic porosity shallow water model is not able to correctly calculate the flux in the presence of a porosity discontinuity and an empirical flux correction is proposed. This is not entirely satisfactory, and future research should focus on deriving a physically-based mechanism to account for the porosity discontinuity.

- Another interesting research area is the development of augmented Riemann solutions to the equations. A major limitation here is that the system of equations is only available in integral differential form. However, following the eigenvalue analysis in [50], one could derive augmented Riemann solutions for these equations that would stabilize the solution.

- The mesh-dependency of the anisotropic porosity shallow water model cannot be entirely removed. Thus, in order to enhance model accuracy, research should focus on an automatic gap-conforming mesh generation for anisotropic porosity shallow water models. A possible

way would be to extract the building boundaries as individual polygons using image analysis tools and then forcing a constraint Delaunay triangulation with the centroids of these polygons as fixed points.

- Given the benefit of the unstructured meshes, the anisotropic porosity model with depth-dependent porosity terms should be extended to unstructured triangular meshes. A possible way to calculate the porosity functions is to carry out a Voronoi tessellation in each cell and weighting each sampled topography data with its corresponding Voronoi area.

- Except of the work in [50], where levee failure in a small neighborhood is investigated, the anisotropic porosity shallow water model has not been applied to a "real world" case yet. An important step for future research would be to apply the anisotropic porosity model to a large scale "real world" urban catchment, possibly at city scale, but at least at the scale of several districts to identify possible undetected limitations of the model.

- Here, an interesting approach that would further decrease the computational cost would be applying high-performance scientific computing techniques to the coarse grid methods. Here, a distributed memory parallelization could significantly reduce the computational time. Using GPU-based parallelization is also possible.

- Another interesting line of work would be the coupling of coarse grid methods and adaptive methods. Possible combinations are a simple mesh adjusting coarse grid model, where cells are refined based on an error estimator, or a model-adaptivity where model concepts and cell sizes are adjusted according to the state of the solution, e.g. conventional high-resolution shallow water model to resolve the shock wave and porosity model on coarser resolution in smooth regions.

- Finally, the coarse grid approaches could be coupled with different processes such as contaminant and heat transport and morphodynamics. The extension to contaminant and heat transport is straightforward but modeling morphodynamics is expected to be challenging. The major challenge is the coarse resolution of the computational mesh that averages bed elevation inside the cell. Smaller topographic features are accounted for conceptually. However, these small topographic features are expected to erode. In the friction law-based approach this would change the roughness height, and in the porosity-based approach this would change not only the value of the porosity

terms but the porosity function itself. In addition, the calculation of sediment and bedload fluxes in the presence of porosity is ambiguous. Nevertheless, a coarse grid model for morphodynamics would be very interesting for long-term simulations. Another possible application area of the coarse grid approaches would be to account for vegetation in rivers and reservoirs.

Bibliography

[1] M. Abily, N. Bertrand, O. Delestre, P. Gourbesville, and C.-M. Duluc. Spatial global sensitivity analysis of high resolution classified topographic data use in 2d urban flood modelling. *Environmental Modelling & Software*, 77:183–195, 2016.

[2] E. Audusse, F. Bouchut, M.-O. Bristeau, R. Klein, and B. Perthame. A Fast and Stable Well-Balanced Scheme with Hydrostatic Reconstruction for Shallow Water Flows. *SIAM Journal on Scientific Computing*, 25(6):2050–2065, Jan. 2004.

[3] J. Bear and Y. Bachmat. *Introduction to Modeling of Transport Phenomena in Porous Media*. Kluwer Academic Publishers, Dordrecht, Boston, London, 1990.

[4] G. Bidur, A. Chen, D. Djordjević, and D. Savić. Application of cellular automata approach for fast flood simulation. In *Urban Water Management – Challenges and Opportunities*, Exeter, UK, 2011.

[5] B. R. Bird, W. E. Stewart, and E. N. Lightfood. *Transport Phenomena*. John Wiley & Sons, New York, USA, 2 edition, 2007.

[6] G. Blöschl and M. Sivapalan. Scale issues in hydrological modelling: a review. *Hydrological Processes*, 9:251–290, 1995.

[7] R. P. Brent. *Algorithms for Minimization without Derivatives*. Prentice-Hall, Englewood Cliffs, New Jersey, 1973.

[8] A. Bronstert, A. Agarwai, B. Boessenkool, M. Fischer, L. Köhn, J. Laudan, T. Moran, U. Öztürk, V. Rözer, T. Sieg, K. Vogel, and

D. Wendi. Stellungnahme zu den Sturzflutereignissen Ende Mai / Anfang Juni in Süddeutschland am Beispiel der Sturzflut in Braunsbach. Technical report, Universität Potsdam, 2016.

[9] A. Bronstert, H. Bormann, G. Bürger, U. Haberlandt, F. Hattermann, M. Heistermann, S. Huang, V. Kolokotronis, Z. Kundzewicz, L. Menzel, G. Meon, B. Merz, A. Meuser, E. Paton, and T. Petrow. Hochwasser und Sturzfluten an Flüssen in Deutschland. In *Klimawandel in Deutschland*, chapter 10, pages 87–101. Springer-Verlag, Berlin Heidelberg, 2016.

[10] M. Bruwier, P. Archambeau, S. S. Erpicum, M. Pirotton, and B. Dewals. A shallow-water model with depth-dependent porosity for urban flood modeling. In *E-proceedings of the 36th IAHR World Congress*, The Hague, the Netherlands, 2015.

[11] T. R. A. Bussing and E. M. Murman. Finite-volume method for the calculation of compressible chemically reacting flows. *AIAA Journal*, 26(9):1070–1078, 1988.

[12] R. H. Byrd, P. Lu, and J. Nocedal. A Limited Memory Algorithm for Bound Constrained Optimization. *SIAM Journal on Scientific and Statistical Computing*, 16(5):1190–1208, 1995.

[13] M. Carlier. *Hydraulique Générale et Appliquée*. Eyrolles, France, 1972.

[14] D. Caviedes-Voullième. *A Computational model for the simulation of multidimensional hydrodynamics and transport at the soil-surface interface*. Doctoral thesis, Universidad de Zaragoza, 2013.

[15] D. Caviedes-Voullième and G. Kesserwani. Benchmarking a multiresolution discontinuous galerkin shallow water model: Implications for computational hydraulics. *Advances in Water Resources*, 86:14–31, 2015.

[16] L. Cea, M. Garrido, and J. Puertas. Experimental validation of two-dimensional depth-averaged models for forecasting rainfallrunoff from precipitation data in urban areas. *Journal of Hydrology*, 382(1-4):88–102, Mar. 2010.

[17] L. Cea, J. Puertas, and M.-E. Vázquez-Cendón. Depth Averaged Modelling of Turbulent Shallow Water Flow with Wet-Dry Fronts. *Archives of Computational Methods in Engineering*, 14(3):303–341, Aug. 2007.

[18] L. Cea and M.-E. Vázquez-Cendón. Unstructured finite volume discretization of two-dimensional depth-averaged shallow water equations with porosity. *International Journal for Numerical Methods in Fluids*, 63:903–930, 2009.

[19] A. S. Chen, B. Evans, S. Djordjević, and D. a. Savić. A coarse-grid approach to representing building blockage effects in 2D urban flood modelling. *Journal of Hydrology*, 426-427:1–16, Mar. 2012.

[20] A. S. Chen, B. Evans, S. Djordjević, and D. a. Savić. Multi-layered coarse grid modelling in 2D urban flood simulations. *Journal of Hydrology*, 470-471:1–11, 2012.

[21] V. T. Chow. *Open-Channel Hydraulics*. McGraw-Hill, Singapore, 1959.

[22] P. Costabile, C. Constanzo, and F. Macchione. Two-dimensional numerical models for overland flow simulations. *River Basin Management*, 124:137–148, 2009.

[23] P. Costabile, C. Costanzo, and F. Macchione. Comparative analysis of overland flow models using finite volume schemes. *Journal of Hydroinformatics*, 14(1):122–135, Jan. 2012.

[24] Danish Hydraulic Institute. *MIKE 21 Hydrodynamic Module Users Guide and Reference Manual*, 1996.

[25] S. F. Davis. Simplified second-order Godunov-type methods. *SIAM Journal on Scientific and Statistical Computing*, 9:445–473, 1988.

[26] A. Defina. Two-dimensional shallow flow equations for partially dry areas. *Water Resources Research*, 36(11):3251–3264, Nov. 2000.

[27] A. Defina, L. D'Alpaos, and B. Matticchio. A new set of equations for very shallow flow and partially dry areas suitable to 2D numerical models. In *Proceedings of the Specialty Conference on "Modelling of Flood Propagation Over Initially Dry Areas"*, pages 72–81, New York, USA, 1994.

[28] O. Delestre, S. Cordier, F. Darboux, and F. James. A limitation of the hydrostatic reconstruction technique for Shallow Water equations. *Comptes Rendus Mathematique*, 350(13-14):677–681, July 2012.

[29] O. Delestre, F. Darboux, F. James, C. Lucas, C. Laguerre, and S. Cordier. Fullswof: A free software package for the simulation of shallow water flows. Technical report, University of Nice, 2014.

[30] S. Doocy, A. Daniels, S. Murray, and T. Kirsch. The human impact of floods: a historical review of events 1980-2009 and systematic literature review. *PLOS Current Disasters*, 1, 2013.

[31] F. Dottori, G. Di Baldassarre, and E. Todini. Detailed data is welcome, but with a pinch of salt: Accuracy, precision, and uncertainty in flood inundation modeling. *Water Resources Research*, 49(9):6079–6085, Sept. 2013.

[32] T. Dunne, W. Zhang, and B. F. Aubry. Effects of rainfall, vegetation, and microtopography on infiltration and runoff. *Water Resources Research*, 27(9):2271–2285, 1991.

[33] L. DAlpaos and A. Defina. Mathematical modeling of tidal hydrodynamics in shallow lagoons: A review of open issues and applications to the Venice lagoon. *Computers & Geosciences*, 33(4):476–496, May 2007.

[34] European Parliament and Council. Directive 2007/60/EC of the European Parliament and of the Council of 23 October 2007 on the assessment and management of flood risks, 2007.

[35] R. Falconer, B. Lin, E. Harris, and S. Kashefipour. *DIVAST model reference manual, Environmental Water Management Research Centre Report, Cardiff University, UK*, 2000.

[36] C. L. Farmer. Upscaling: a review. *International Journal for Numerical Methods in Fluids*, 40(1-2):63–78, Sept. 2002.

[37] M. Fišer, I. Özgen, R. Hinkelmann, and J. Vimmr. A mass conservative well-balanced reconstruction at wet/dry interfaces for the godunov-type shallow water model. *International Journal for Numerical Methods in Fluids*, 82(12):893–908, 2016.

[38] S. Fu, L. Cao, B. Liu, Z. Wu, and M. Savabi. Effects of DEM grid size on predicting soil loss from small watersheds in China. *Environmental Earth Sciences*, 73(5):2141–2151, 2015.

[39] M. Garrido, L. Cea, J. Puertas, and M.-E. Vázquez-Cendón. Porosity versus resolved approach in 2D shallow water models. Experimental

validation. In *Numerical Methods for Hyperbolic Equations: Theory an Applications. An international conference to honour Professor E.F. Toro*, volume di, Santiago, Spain, 2011.

[40] N. Gerhard, D. Caviedes-Voullième, S. Müller, and G. Kesserwani. Multiwavelet-based grid adaptation with discontinuious galerkin schemes for shallow water equations. *Journal of Computational Physics*, 301:265–288, 2015.

[41] M. O. Gessner, R. Hinkelmann, G. Nützmann, M. Jekel, G. Singer, J. Lewandowski, T. Nehls, and M. Barjenbruch. Urban water interfaces. *Journal of Hydrology*, 514:226–232, 2014.

[42] C. Geuzaine and J.-F. Remacle. Gmsh: A 3-d finite element mesh generator with built-in pre- and post-processing facilities. *International Journal for Numerical Methods in Engineering*, 79(11):1309–1331, 2009.

[43] M. J. Gibson, D. A. Savic, S. Djordjevic, A. S. Chen, S. Fraser, and T. Watson. Accuracy and computational efficiency of 2d urban surface flood modelling based on cellular automata. *Procedia Engineering*, 154:801 – 810, 2016.

[44] S. K. Godunov. A difference scheme for numerical computation of discontinuous solutions of hydrodynamic equations. *Matematicheskii Sbornik*, 47:271–306, 1959.

[45] S. Gottlieb and C.-W. Shu. Total variation diminishing Runge-Kutta schemes. *Mathematics of Computation*, 67(221):73–85, 1996.

[46] P. Gourbesville. Data and hydroinformatics: new possibilities and challenges. *Journal of Hydroinformatics*, 11(34):330–343, July 2009.

[47] V. Guinot. *Godunov-type schemes: an introduction for engineers*. Elsevier Science B.V., Amsterdam, the Netherlands, 2003.

[48] V. Guinot. Multiple porosity shallow water models for macroscopic modelling of urban floods. *Advances in Water Resources*, 37:40–72, Mar. 2012.

[49] V. Guinot and C. Delenne. Macroscopic modelling of urban floods. *La Houille Blanche – Revue internationale de l'eau*, 6:19–25, 2014.

[50] V. Guinot, B. Sanders, and J. Schubert. Dual integral porosity shallow water model for urban flood modelling. *Advances in Water Resources*, Accepted, nd.

[51] V. Guinot and S. Soares-Frazão. Flux and source term discretization in two-dimensional shallow water models with porosity on unstructured grids. *International Journal for Numerical Methods in Fluids*, 50(3):309–345, Jan. 2006.

[52] D. A. Haleem, G. Kesserwani, and D. Caviedes-Voullième. Haar wavelet-based adaptive finite volume shallow water solver. *Journal of Hydroinformatics*, 17(6):857–873, 2015.

[53] J. Henonin, M. Hongtao, Z.-Y. Yang, J. Hartnack, K. Havnø, P. Gourbesville, and O. Mark. Citywide multi-grid urban flood modelling: the July 2012 flood in Beijing. *Urban Water Journal*, 12(1):52–66, 2015.

[54] J. Hervouet. *Hydrodynamics of free surface flows: modeling with the finite element method*. Wiley & Sons, Inc., 2007.

[55] J.-M. Hervouet, R. Samie, and B. Moreau. Modelling urban areas in dam-break flood-wave numerical simulations. In *International Seminar and Workshop on Rescue Actions based on Dambreak Flood Analysis, Vol. 1*, Seinâjoki, Finland, 2000.

[56] R. Hinkelmann. *Efficient Numerical Methods and Information-Processing Techniques for Modeling Hydro- and Environmental Systems*. Springer Verlag, Berlin Heidelberg, 2005.

[57] R. Hinkelmann, E. Zehe, W. Ehlers, and M. Joswig. Special Section on Landslides: Setting the Scene and Outline of Contributing Studies. *Vadose Zone Journal*, 10(2):473, 2011.

[58] M. S. Horritt and P. D. Bates. Effects of spatial resolution on a raster based model of flood flow. *Journal of Hydrology*, 253:239–249, 2001.

[59] J. Hou. *Robust numerical methods for shallow water flows and advective transport simulation on unstructured grids*. Doctoral thesis, Technische Universität Berlin, 2013.

[60] J. Hou, Q. Liang, F. Simons, and R. Hinkelmann. A 2D well-balanced shallow flow model for unstructured grids with novel slope source term treatment. *Advances in Water Resources*, 52:107–131, Feb. 2013.

[61] J. Hou, Q. Liang, F. Simons, and R. Hinkelmann. A stable 2D unstructured shallow flow model for simulations of wetting and drying over rough terrains. *Computers & Fluids*, 82:132–147, Aug. 2013.

[62] J. Hou, Q. Liang, and X. Xia. Robust absorbing boundary conditions for shallow water flow models. *Environmental Earth Sciences*, Thematic issue:n/a, 2015.

[63] J. Hou, Q. Liang, H. Zhang, and R. Hinkelmann. An efficient unstructured MUSCL scheme for solving the 2D shallow water equations. *Environmental Modelling and Software*, 66:131–152, 2015.

[64] J. Hou, F. Simons, and R. Hinkelmann. Improved total variation diminishing schemes for advection simulation on arbitrary grids. *International Journal for Numerical Methods in Fluids*, 70(3):359–382, Sept. 2012.

[65] J. Hou, F. Simons, and R. Hinkelmann. A new TVD method for advection simulation on 2D unstructured grids. *International Journal for Numerical Methods in Fluids*, 71(10):1260–1281, Apr. 2013.

[66] J. Hou, F. Simons, Q. Liang, and R. Hinkelmann. An improved hydrostatic reconstruction method for shallow water model. *Journal of Hydraulic Research*, 52(June):1–8, 2014.

[67] J. Hughes, J. Decker, and C. Langevin. Use of upscaled elevation and surface roughness data in two-dimensional surface water models. *Advances in Water Resources*, 34(9):1151–1164, Sept. 2011.

[68] Intergovernmental Panel on Climate Change [Core Writing Team, R.K. Pachauri and L.A. Meyer (eds)]. Climate Change 2014: Synthesis Report, Summary for Policymakers. Contribution of Working Groups I, II and III to the Fifth Assessment Report of the Intergovernmental Panel on Climate Change, 2014.

[69] M. Jahanbazi, I. Özgen, R. Aleixo, and R. Hinkelmann. Development of a diffusive wave shallow water model with a novel stability condition and other new features. *Journal of Hydroinformatics*, online, 2017.

[70] M. K. Jain, U. C. Kothyari, and K. G. Ranga-Raju. A GIS based distributed rainfall–runoff model. *Journal of Hydrology*, 299(1-2):107–135, Nov. 2004.

[71] M. K. Jain and V. P. Singh. DEM-based modelling of surface runoff using diffusion wave equation. *Journal of Hydrology*, 302(1-4):107–126, Feb. 2005.

[72] E. Jones, T. Oliphant, P. Peterson, et al. SciPy: Open source scientific tools for Python, 2001–. [Online; accessed 2015-11-11].

[73] G. Kesserwani, D. Caviedes-Voullième, N. Gerhard, and S. Müller. Multiwavelet discontinuous galerkin h-adaptive shallow water model. *Computer Methods in Applied Mechanics and Engineering*, 294:56–71, 2015.

[74] G. Kesserwani and Q. Liang. RKDG2 shallow-water solver on non-uniform grids with local time steps: Application to 1D and 2D hydrodynamics. *Applied Mathematical Modelling*, 39(3-4):1317–1340, 2015.

[75] A. A. Khan and W. Lai. *Modeling Shallow Water Flows Using the Discontinous Galerkin Method*. CRC Press, Taylor & Francis Group, Abingdon, Oxfordshire, UK, 2014.

[76] B. Kim, B. F. Sanders, J. S. Famiglietti, and V. Guinot. Urban flood modeling with porous shallow-water equations: A case study of model errors in the presence of anisotropic porosity. *Journal of Hydrology*, 523:680–692, 2015.

[77] B. Kim, B. F. Sanders, J. E. Schubert, and J. S. Famiglietti. Mesh type tradeoffs in 2D hydrodynamic modeling of flooding with a Godunov-based flow solver. *Advances in Water Resources*, 68:42–61, June 2014.

[78] J. Kim and V. Y. Ivanov. A holistic, multi-scale dynamic downscaling framework for climate impact assessments and challenges of addressing finer-scale watershed dynamics. *Journal of Hydrology*, 522:645–660, 2015.

[79] J. Kim, A. Warnock, V. Y. Ivanov, and N. D. Katopodes. Coupled modeling of hydrologic and hydrodynamic processes including overland and channel flow. *Advances in Water Resources*, 37:104–126, Mar. 2012.

[80] A. Lacasta, M. Morales-Hernández, J. Murillo, and P. García-Navarro. An optimized GPU implementation of a 2D free surface simulation model on unstructured meshes. *Advances in Engineering Software*, 78:1–15, 2014.

[81] A. Lacasta, M. Morales-Hernández, J. Murillo, and P. García-Navarro. GPU implementation of the 2D shallow water equations for the simulation of rainfall/runoff events. *Environmental Earth Sciences*, 74(11):7295–7305, 2015.

[82] C. Lange, M. Schneider, M. Mutz, M. Haustein, M. Halle, M. Seidel, H. Sieker, C. Wolter, and R. Hinkelmann. Model-based design for restoration of a small urban river. *Journal of Hydro-environmental Research (JHER)*, 9(2):226–236, 2015.

[83] D. S. L. Lawrence. Macroscale surface roughness and frictional resistance in overland flow. *Earth Surface Processes and Landforms*, 22:365–382, 1997.

[84] M.-H. Le. *Modélisation multi-échelle et simulation numérique de l'érosion des sols de la parcelle au bassin versant. Equations aux dérivées partielles*. Doctoral thesis, Université d'Orléans, 2012.

[85] R. J. LeVeque. *Numerical methods for conservation laws*. Springer Basel AG, Basel, Switzerland, 2 edition, 1992.

[86] R. J. LeVeque. *Finite Volume Methods for Hyperbolic Problems*. Cambridge University Press, New York, USA, 2007.

[87] J. Lhomme. *One-dimensional, two-dimensional and macroscopic approaches to urban flood modelling*. Doctoral thesis, Université Montpellier 2, 2006.

[88] D. Liang, R. A. Falconer, and B. Lin. Coupling surface and subsurface flows in a depth averaged flood wave model. *Journal of Hydrology*, 337(1-2):147–158, Apr. 2007.

[89] D. Liang, I. Özgen, R. Hinkelmann, Y. Xiao, and J. M. Chen. Shallow water simulation of overland flows in idealised catchments. *Environmental Earth Sciences*, 74:7307–7318, 2015.

[90] D. Liang, X. Wang, R. A. Falconer, and B. N. Bockelmann-Evans. Solving the depth-integrated solute transport equation with a TVD-MacCormack scheme. *Environmental Modelling and Software*, 25(12):1619–1629, 2010.

[91] Q. Liang. Flood simulation using a well-balanced shallow flow model. *Journal of Hydraulic Engineering*, 136(9):669–675, Sept. 2010.

[92] Q. Liang and A. G. L. Borthwick. Adaptive quadtree simulation of shallow flows with wet-dry fronts over complex topography. *Computers and Fluids*, 38(2):221–234, 2009.

[93] Q. Liang and F. Marche. Numerical resolution of well-balanced shallow water equations with complex source terms. *Advances in Water Resources*, 32(6):873–884, June 2009.

[94] Y. Liu, J. Zhou, L. Song, Q. Zou, L. Liao, and Y. Wang. Numerical modelling of free-surface shallow flows over irregular topography with complex geometry. *Applied Mathematical Modelling*, 37(23), 2013.

[95] R. MacCormack. The effect of viscosity in hypervelocity impact cratering. In *Proceedings of the 4th Aerodynamic Testing Conference, Cincinnati, Ohio, USA*, 1969.

[96] K. Masatsuka. *I do like CFD*, volume 1. Katate Masatsuka, Virginia, USA, 2 edition, 2017.

[97] H. K. McMillan and J. Brasington. Reduced complexity strategies for modelling urban floodplain inundation. *Geomorphology*, 90(3-4):226–243, Oct. 2007.

[98] E. Mignot, A. Paquier, and S. Haider. Modeling floods in a dense urban area using 2D shallow water equations. *Journal of Hydrology*, 327(1-2):186–199, July 2006.

[99] C. G. Mingham and D. M. Causon. High-resolution finite-volume method for shallow water flows. *Journal of Hydraulic Engineering*, 124(June):605–614, 1998.

[100] K. Mohamed. A finite volume method for numerical simulation of shallow water models with porosity. *Computers & Fluids*, 104:9–19, Nov. 2014.

[101] H. Morvan, D. Knight, N. Wright, X. Tang, and A. Crossley. The concept of roughness in fluvial hydraulics and its formulation in 1D, 2D and 3D numerical simulation models. *Journal of Hydraulic Research*, 46(2):191–208, Mar. 2008.

[102] C. Mügler, O. Planchon, J. Patin, S. Weill, N. Silvera, P. Richard, and E. Mouche. Comparison of roughness models to simulate overland flow and tracer transport experiments under simulated rainfall at plot scale. *Journal of Hydrology*, 402(1-2):25–40, May 2011.

[103] S. Müller and Y. Stiriba. Fully adaptive multiscale schemes for conservation laws employing locally varying time stepping. *Journal of Scientific Computing*, 30(3):493–531, 2007.

[104] J. Murillo and P. Garcìa-Navarro. Wave Riemann description of friction terms in unsteady shallow flows: Application to water and mud/debris floods. *Journal of Computational Physics*, 231:1963–2001, 2012.

[105] J. Murillo, P. García-Navarro, J. Burguete, and P. Brufau. The influence of source terms on stability, accuracy and conservation in two-dimensional shallow flow simulation using triangular finite volumes. *International Journal for Numerical Methods in Fluids*, 54(5):543–590, June 2007.

[106] S. Néelz and G. Pender. Sub-grid scale parameterisation of 2D hydrodynamic models of inundation in the urban area. *Acta Geophysica*, 56(3):65–72, 2007.

[107] H. M. Nepf. Drag, turbulence, and diffusion in flow through emergent vegetation. *Water Resources Research*, 35(2):479–489, Feb. 1999.

[108] M. Nujič. *Hydro_AS-2D: Ein zweidimensionales Strömungsmodell für die wasserwirtschaftliche Praxis*, 2002.

[109] I. Özgen. A coarse grid approach-based model chain for fast rainfall-runoff predictions in natural and urban areas. In *Proceedings of the 37th IAHR World Congress, Kuala Lumpur, Malaysia*, 2007.

[110] I. Özgen, D. Liang, and R. Hinkelmann. Shallow water equations with depth-dependent anisotropic porosity for subgrid-scale topography. *Applied Mathematical Modelling*, 40:7447–7473, 2016.

[111] I. Özgen, S. Seemann, A. L. Candeias, H. Koch, F. Simons, and R. Hinkelmann. Simulation of hydraulic interaction between Icó-Mandantes bay and São Francisco river, Brazil. In G. Gunkel, J. A. A. Silva, and M. d. C. Sobral, editors, *Sustainable Management of Water and Land in Semiarid Areas*, chapter 1.2, pages 28–38. Editora Universitária UFPE, Recife, Brazil, 2013.

[112] I. Özgen, M. Serrano-Taslim, J. Zhao, D. Liang, and R. Hinkelmann. Coarse grid shallow water simulations of rainfall runoff in small catchments with modified friction law to account for unresolved microtopography. In *European Geosciences Union General Assembly*, Vienna, Austria, 2016.

[113] I. Özgen, K. Teuber, D. Liang, and R. Hinkelmann. Surface roughness parameterization to account for subgrid scale topography in shallow water flow modeling. In *Proceedings of the 36th IAHR World Congress*, The Hague, the Netherlands, 2015.

[114] I. Özgen, K. Teuber, F. Simons, D. Liang, and R. Hinkelmann. Upscaling the shallow water model with a novel roughness formulation. *Environmental Earth Sciences*, 74:7371–7386, 2015.

[115] I. Özgen, J. Zhao, B. Kim, D. Liang, and R. Hinkelmann. An anisotropic-porosity shallow water model with novel monotonicity treatment and subgrid-scale drag estimation. *International Journal for Numerical Methods in Fluids*, Submitted, nd.

[116] I. Özgen, J. Zhao, D. Liang, and R. Hinkelmann. Urban flood modeling using shallow water equations with depth-dependent anisotropic porosity. *Journal of Hydrology*, 541:1165–1184, oct 2016.

[117] S. Panday and P. S. Huyakorn. A fully coupled physically-based spatially-distributed model for evaluating surface/subsurface flow. *Advances in Water Resources*, 27(4):361–382, 2004.

[118] G. Petaccia, L. Natale, F. Savi, M. Velickovic, Y. Zech, and S. Soares-Frazão. Flood wave propagation in steep mountain rivers. *Journal of Hydroinformatics*, 15(1):120, 2013.

[119] G. Petaccia, S. Soares-Frazão, F. Savi, L. Natale, and Y. Zech. Simplified versus detailed two-dimensional approaches to transient flow modeling in urban areas. *Journal of Hydraulic Engineering*, 136:262–266, 2010.

[120] O. Planchon, M. Esteves, N. Silvera, and J.-M. Lapetite. Microrelief induced by tillage: measurement and modelling of Surface Storage Capacity. *Catena*, 46:141–157, 2001.

[121] F. W. Platzek, G. S. Stelling, J. A. Jankowski, R. Patzwahl, and J. D. Pietrzak. An efficient semi-implicit subgrid method for free-surface flows on hierarchical grids. *International Journal for Numerical Methods in Fluids*, 80(12):715–741, 2016. fld.4172.

[122] A. Pradhan and Y.-T. Kim. Application and comparison of shallow landslide susceptibility models in weathered granite soil under extreme rainfall events. *Environmental Earth Sciences*, 73(9):5761–5771, 2015.

[123] U. Razafison, S. Cordier, O. Delestre, F. Darboux, C. Lucas, and F. James. A Shallow Water model for the numerical simulation of overland flow on surfaces with ridges and furrows. *European Journal of Mechanics - B/Fluids*, 31:44–52, Jan. 2012.

[124] B. Riemann. Über die Fortpflanzung ebener Luftwellen von endlicher Schwingungsweite. *Abhandlungen der Königlichen Gesellschaft der Wissenschaften zu Göttingen*, 8:1–30, 1860.

[125] B. F. Sanders, J. E. Schubert, and H. A. Gallegos. Integral formulation of shallow-water equations with anisotropic porosity for urban flood modeling. *Journal of Hydrology*, 362(1-2):19–38, Nov. 2008.

[126] J. E. Schubert and B. F. Sanders. Building treatments for urban flood inundation models and implications for predictive skill and modeling efficiency. *Advances in Water Resources*, 41:49–64, June 2012.

[127] J. E. Schubert, B. F. Sanders, M. J. Smith, and N. G. Wright. Unstructured mesh generation and landcover-based resistance for hydrodynamic modeling of urban flooding. *Advances in Water Resources*, 31(12):1603–1621, Dec. 2008.

[128] F. Simons, T. Busse, J. Hou, I. Özgen, and R. Hinkelmann. A model for overland flow and associated processes within the Hydroinformatics Modelling System. *Journal of Hydroinformatics*, 16(2):375–391, Mar. 2014.

[129] L. S. Smith and Q. Liang. Towards a generalised GPU/CPU shallow-flow modelling tool. *Computers & Fluids*, 88:334–343, Dec. 2013.

[130] M. W. Smith. Roughness in the Earth Sciences. *Earth-Science Reviews*, 136:202–225, Sept. 2014.

[131] M. W. Smith, N. J. Cox, and L. J. Bracken. Applying flow resistance equations to overland flows. *Progress in Physical Geography*, 31(4):363–387, Aug. 2007.

[132] S. Soares-Frazão, J. Lhomme, V. Guinot, and Y. Zech. Two-dimensional shallow-water model with porosity for urban flood modelling. *Journal of Hydraulic Research*, 46(1):45–64, Jan. 2008.

[133] S. Soares-Frazão and Y. Zech. Dam-break flow through an idealised city. *Journal of Hydraulic Research*, 46(5):648–658, 2008.

[134] S. Soares-Frazão. Experiments of dam-break wave over a triangular bottom sill. *Journal of Hydraulic Research*, 45(Extra Issue):19–26, 2007.

[135] L. Song, J. Zhou, J. Guo, Q. Zou, and Y. Liu. A robust well-balanced finite volume model for shallow water flows with wetting and drying over irregular terrain. *Advances in Water Resources*, 34(7):915–932, July 2011.

[136] V. Souchere, D. King, J. Daroussin, F. Papy, and A. Capillon. Effects of tillage on runoff directions: consequences on runoff contributing area within agricultural catchments. *Journal of Hydrology*, 206(3-4):256–267, May 1998.

[137] L. Stadler, R. Hinkelmann, and R. Helmig. Modeling macroporous soils with a two-phase dual-permeability model. *Transport in Porous Media*, 95:585–601, 2012.

[138] G. S. Stelling. Quadtree flood simulations with sub-grid digital elevation models. *Proceedings of the ICE - Water Management*, 165(10):567–580, Nov. 2012.

[139] G. Testa, D. Zuccalà, F. Alcrudo, J. Mulet, and S. Soares-Frazão. Flash flood flow experiment in a simplified urban district. *Journal of Hydraulic Research*, 45(sup1):37–44, dec 2007.

[140] K. Teuber, I. Özgen, D. Liang, and R. Hinkelmann. [Entwicklung eines Skalierungsansatzes zur Berücksichtigung von Mikrotopographie in den Flachwassergleichungen]. Unpublished.

[141] S. E. Thompson, G. G. Katul, and A. Porporato. Role of microtopography in rainfall-runoff partitioning: An analysis using idealized geometry. *Water Resources Research*, 46(7), July 2010.

[142] E. F. Toro. *Shock-Capturing Methods for Free-Surface Shallow Flows*. John Wiley & Sons, Ltd., West Sussex, UK, 2001.

[143] E. F. Toro, M. Spruce, and W. Speares. Restoration of the contact surface in the HLL-Riemann solver. *Shock Waves*, 4(1):25–34, July 1994.

[144] V. A. Tsihrintzis, F.-C. Wu, H. W. Shen, and Y.-J. Chou. Discussion and Closure: Variation of Roughness Coefficients for Unsubmerged and Submerged Vegetation. *Journal of Hydraulic Engineering*, 127(3):241–245, 2001.

[145] United Nations, Department of Economic and Social Affairs, Population Division. World Urbanization Prospects: The 2014 Revision, Highlights, 2014.

[146] United Nations, Department of Economic and Social Affairs, Population Division. World Population Prospects: The 2015 Revision, Key Findings and Advance Tables, 2015.

[147] United Nations, Department of Economic and Social Affairs, Population Division [D. Satterthwaite]. Climate Change and Urbanization: Effects and Implications for Urban Governance, 2007.

[148] A. Valiani and L. Begnudelli. Divergence Form for Bed Slope Source Term in Shallow Water Equations. *Journal of Hydraulic Engineering*, 132(7):652–665, July 2006.

[149] S. van der Walt, C. S. Colbert, and G. Varoquaux. The NumPy array: A structure for efficient numerical computation. *Computing in Science & Engineering*, 13:22–30, 2011.

[150] B. van Leer. Towards the ultimate conservative difference scheme V: A second order sequel to Godunov's method. *Journal of Computational Physics*, 32:101–136, 1979.

[151] M. Velickovic. *Macroscopic modeling of urban flood by a porosity approach*. PhD thesis, Université catholique de Louvain, Louvain-la-Neuve, Belgium, 2012.

[152] M. Velickovic, S. van Emelen, Y. Zech, and S. Soares-Frazão. Shallow-water model with porosity: sensitivity analysis to head losses and porosity distribution. In A. Dittrich, editor, *River Flow 2010: Proceedings of the International Conference on Fluvial Hydraulics*, pages 613–620, Braunschweig, Germany, 2010. Bundesanstalt für Wasserbau.

[153] D. P. Viero, A. DAlpaos, L. Carniello, and A. Defina. Mathematical modeling of flooding due to river bank failure. *Advances in Water Resources*, 59:82 – 94, 2013.

[154] D. P. Viero, P. Peruzzo, L. Carniello, and A. Defina. Integrated mathematical modeling of hydrological and hydrodynamic response to rainfall events in rural lowland catchments. *Water Resources Research*, July 2014.

[155] N. D. Volp, B. C. van Prooijen, and G. S. Stelling. A finite volume approach for shallow water flow accounting for high-resolution bathymetry and roughness data. *Water Resources Research*, 49(7):4126–4135, July 2013.

[156] Y. Wang, Q. Liang, G. Kesserwani, and J. W. Hall. A 2d shallow flow model for practical dam-break simulations. *Journal of Hydraulic Research*, 49(3):307–316, 2011.

[157] A. Warnock, J. Kim, V. Ivanoc, and N. D. Katopodes. Self-adaptive kinematic-dynamic model for overland flow. *Journal of Hydraulic Engineering*, 140:169–181, 2014.

[158] A. Yörük. *Unsicherheiten bei der hydrodynamischen Modellierung von Überschwemmungsgebieten*, volume 99 of *Mitteilungen / Institut für Wasserwesen*. Universität der Bundeswehr München, 2009.

[159] C. Yu and J. Duan. Two-dimensional hydrodynamic model for surface-flow routing. *Journal of Hydraulic Engineering*, 140(9):13, 2014.

[160] D. Yu and S. N. Lane. Urban fluvial flood modelling using a two-dimensional diffusion-wave treatment, part 1: mesh resolution effects. *Hydrological Processes*, 20(7):1541–1565, Apr. 2006.

[161] D. Yu and S. N. Lane. Urban fluvial flood modelling using a two-dimensional diffusion-wave treatment, part 2: development of a sub-grid-scale treatment. *Hydrological Processes*, 20(7):1567–1583, Apr. 2006.

[162] W. Zhang and T. W. Cundy. Modeling of two-dimensional overland flow. *Water Resources Research*, 25(9):2019–2035, Sept. 1989.

[163] M. Zhao, T. Yue, N. Zhao, X. Yang, Y. Wang, and X. Zhang. Parallel algorithm of a modified surface modeling method and its application in digital elevation model construction. *Environmental Earth Sciences*, pages 1–11, 2015.

[164] C. Zhu, R. H. Byrd, and J. Nocedal. L-BFGS-B: Algorithm 778: L-BFGS-B, FORTRAN routines for large scale bound constrained optimization. *ACM Transactions on Mathematical Software*, 23(4):550–560, 1997.

[165] C. Zoppou and S. Roberts. Numerical solution of the two-dimensional unsteady dam break. *Applied Mathematical Modelling*, 24(7):457–475, June 2000.